MODELING OF ELECTROCHEMICAL ENERGY STORAGE AND ENERGY CONVERSION DEVICES

A Dissertation
Presented to
The Academic Faculty

by

Rajeswari Chandrasekaran

In Partial Fulfillment
of the Requirements for the Degree
Doctor of Philosophy in the
School of Chemical and Biomolecular Engineering

Georgia Institute of Technology
December 2010

MODELING OF ELECTROCHEMICAL ENERGY STORAGE AND ENERGY CONVERSION DEVICES

Approved by:

Dr. Thomas F.Fuller, Advisor
School of Chemical & Biomolecular Engineering
Georgia Institute of Technology

Dr. Paul Kohl
School of Chemical & Biomolecular Engineering
Georgia Institute of Technology

Dr. Dennis Hess
School of School of Chemical & Biomolecular Engineering
Georgia Institute of Technology

Dr. Gabriel A. Rincón-Mora
School of Electrical and Computer Engineering
Georgia Institute of Technology

Dr. Dimitri Mavris
School of Aerospace Engineering
Georgia Institute of Technology

Date Approved: July 15, 2010

To

அம்மா, அப்பா, தம்பி

Mom, Dad & Brother

Shuklaambara Dharam Vishnum Shashi Varnam Chatur Bhujam

Prasanna Vadanam Dhyaayet Sarva Vighna Upashaanthaye.

ACKNOWLEDGEMENTS

I am grateful to my PhD Thesis Advisor, Prof. Thomas F. Fuller for giving me the opportunity to work with him in the field of batteries and fuel cells. I appreciate the freedom and the time he gave me to work on mathematical models varying in complexity and scale. The freedom to be part of the Ecocar Challenge of which Prof. Fuller is the faculty advisor and to do summer internship at Ford Motor Company paved way for a first-hand experience to correlate the relevance of fundamental research to real world applications. His clarity of thoughts and attention to detail has always been an inspiration. Drafting manuscripts under his guidance has been a real pleasure. I hope to carry forward the lessons I learnt in the process. Apart from research work, I thoroughly enjoyed my interaction with him in my capacity as teaching assistant for his undergraduate transport phenomena course for two semesters. The opportunity to review manuscripts with Prof. Fuller at early stages of my PhD helped me understand the peer review process better.

I am thankful to each of the professors serving on my thesis committee for their time and suggestions. It's always a delight to talk to Prof. Paul Kohl and I enjoyed his electrochemistry class in my first semester at Tech as well as the end of semester parties he hosted for all of us. I enjoyed listening Prof. Dennis Hess talk on different topics such as lab safety, service to the Electrochemical Society from the very first luncheon the department hosted for our incoming graduate class in 2005 till date. Prof. Dimitri Mavris is sincerely acknowledged for the interesting course on Advance Systems Design which helped me in understanding the statistical approaches used in this thesis. Thanks also to Prof. Gabriel Rincón-Mora for his comments on my thesis. I am grateful to GTRI and

NASA Glenn Research Center for the financial support. The Electrochemical Society (ECS), WIC of the AIChE, SGA and COE at Georgia Tech are all sincerely acknowledged for the various travel grants to attend conferences and present my work.

Special mention should go to my officemates Kevin and Brian, labmates Cheng, Wu, Norm, and Jonathan for their company and support over the years. Thanks also to Eric, Erin, Vyran, Tom, Panos, Kara, Todd, Xiaoyu, Kevin Davies, Aurore, Gigi, Michael, Jina, David and Shrayesh for the pleasant experience that I had within the Fuller research group. I am grateful to the faculty members at Georgia Tech whose teaching made the courses I took interesting and the exams simpler. It has also been a pleasure to interact with Prof. Carsten Sievers and Prof. Dan Tedder while I served as the teaching assistant for the courses they offered. Thanks are due to Prof. Peter Hesketh who has served as the faculty advisor for the ECS student chapter at Georgia Tech. The assistance from the professors across different departments and the efforts of the student office bearers has made the chapter's events successful so far. I also thank all the administrative and support staff at ChBE, GTRI, OIE, registrar's office and graduate studies office at Tech for their help during my stay here.

I thank Wu Bi for the platinum catalyst dissolution data for the work discussed in Chapter 4. I also thank Tommer Ender for useful discussions on surrogate modeling techniques. Acknowledgements are due to Gary Gray, Cheng Chen, Norimitsu Takeuchi and Tom Bradley for their comments on this work. I am appreciative of the friendly staff at GTRI facility on North Avenue for their support while I carried out experiments described in Chapter 5 there. Prof. Peter Hesketh is acknowledged for allowing me to use

equipments in his lab for some of the work related to Chapter 5. The technical support offered by Kevin Duff at Arbin is simply great. My heartfelt appreciation is due to the enthusiastic undergraduate, Jonathan Denis (and Michael Skinner) who performed experiments mentioned in Chapter 6. I would like to thank Ryan Melsert, Prof. Jerome Meisel, Prof. David Taylor, and the entire Ecocar Challenge team for the collaborative work detailed in Appendix B. I express my gratitude to Prof.Gleb Yushin and Alexandre Magasinski for the experimental data and comments in Chapter 8 and it has been a pleasure interacting with them on the silicon project. I am grateful to Ted for the opportunity to pursue summer internship at Ford Motor Company. My sincere thanks to Dawn for the stimulating discussions while at Ford; Jagjit, Jeff, Ann and Ken for giving me an opportunity to work on in-situ Raman technique for analysis of electrodes; Kent, Renata, Xiao and Chul for explaining to me in detail about their work and to everyone for making my stay memorable. Thanks are due to researchers at ORNL for giving me an insight, during my short visit there, into their various battery related activities.

The support and encouragement extended by many friends from school days in India, CECRI, South Carolina, ChBE/Gatech and other friends around the globe is amazing and many thanks for the same. The list is endless. All my teachers from school days, undergraduate college and masters program are acknowledged for their inspiring lectures and challenging problems which has paved way for my analytical and mathematical skills. Credits are also due to Profs. TRS, Balsu and Santhanam for the same. Sincere thanks for the wishes of my huge circle of relatives including my grandma.

I am heartily thankful to Godfrey Sikha for his encouragement, good will, strong support and stimulating scientific discussions (in particular, in the wide field of electrochemical engineering), all of which have made this dissertation possible. The help he has offered in my life outside research, in spite of his busy schedule is highly appreciated.

Finally, my entire career, including this PhD dissertation, is solely possible due to the sacrifices, blessings, prayers, help, hard work, thoughts, patience, understanding, encouragement, love and affection of my parents (Mr. Chandrasekaran and Mrs.Gowri) and my younger brother, Manikandan. All these and their undying confidence in my abilities have always taken me through tough times and enabled me to complete the task in hand successfully. I sincerely thank the Almighty for making this dissertation possible and also for taking care of my family who are thousands of miles away in India.

TABLE OF CONTENTS

LIST OF TABLES

Page

LIST OF FIGURES

Page

LIST OF ABBREVIATIONS

CHAPTER 3

RDS	Robust Design Simulation
DOE	Design of Experiments
RSM	Response Surface Methodology
RSE	Response Surface Equation
PSAT	Powertrain Systems Analysis Toolkit
ABTS	Arbin Battery Test System

CHAPTER 4

SOC	State of Charge
FTP	Federal Test Procedure
PEMFC	Polymer Electrolyte Membrane Fuel Cell
MEA	Membrane Electrolyte Membrane
RSM	Response Surface Methodology
CCD	Central Composite Design
MFE	Model Fit Distribution
RSE	Response Surface Equation

CHAPTER 6

UDDS	Urban Dynamometer Driving Schedule
HWFET	Highway Fuel Economy Test
SOC	State of Charge

PDF	Probability Density Function
CDF	Cumulative Distribution Function
LH	Latin Hypercube
MFE	Model Fit Error
MRE	Model Representation Error

CHAPTER 7

FEM	Finite Element Method
FEA	Finite Element Analysis

LIST OF SYMBOLS

CHAPTER 3

y response variable

x regressor variable

β regression coefficient

ε error variable

CHAPTER 4

Pt Platinum

CHAPTER 8

A charge transfer area, m^2

c concentration of Li in the particle, mol/m^3

c' concentration of Li in the particle with respect to initial volume of the particle, mol/m^3

c_e concentration of electrolyte, mol/m^3

c_s concentration of Li on the surface of the particle, mol/m^3

$c_{280\%}$ maximum concentration of Li in the particle based on 280% volume expansion;

$$c_{280\%} = \frac{N_{tot}}{\frac{4}{3}\pi\left(3.8^{\frac{1}{3}} R_{p_0}\right)^3}$$; 81923 mol/m^3 (can also be denoted as c_{max})

$c_{r=0}$ concentration of Li at the center of the particle, mol/m^3, assumed (0.5 x 81923) mol/m^3 in Appendix C for calculation of $S_{D\text{-}T\,flux}$ and $S_{D\text{-}C\,flux}$

C_{tot} 1C-rate current per unit mass of silicon, 3579 A/kg; (based on specific capacity of silicon of 3579 mAh/g)

C_O concentration of oxidizing species in solution, mol/m^3

D_{Li} diffusion coefficient of Li in silicon as measured by experiments, m^2/s

$\mathscr{D}_{\mathrm{Li}}$ binary interaction parameter (or diffusion coefficient of Li in Si for thermodynamic driving force), m^2/s

D_O solution phase diffusion coefficient of oxidizing species, m^2/s

F Faraday's constant, 96487 coulombs/mol

i current density, A/m^2

i' normalized current density, A/m^2

I constant applied current in galvanostatic simulations and varying response current in CV simulations, Amperes

i_0 exchange current density, A/m^2

I_p peak current, A

J_{Li} diffusive molar flux, mol/m^2/s

k kinetic rate constant, $(m/s)\,(mol/m^3)^{-\alpha_a}$

n number of electrons transferred, taken to be one for the reduction of Li^+ to Li

N_{Li} molar flux of lithium with respect to fixed co-ordinates, mol/m^2/s

N_{tot} total number of moles of Li that can be inserted in the silicon electrode particle, mol

R_p radius of the particle, m

R_{p0} initial radius of the particle, m

R gas constant, 8.314 J/K/mol

r radial distance within the particle, m

S_s dimensionless parameter defined in Equation 18

$S_{D\text{-}T\ flux}$ dimensionless parameter for ratio of diffusive flux to total flux defined in Appendix C

$S_{D\text{-}C\ flux}$ dimensionless parameter for ratio of diffusive flux to convective flux defined in Appendix C

t time, sec

T temperature, 298 K

U pseudo-thermodynamic potential, V

U_c peak (pseudo-thermodynamic) potential during lithiation, V

U_a peak (pseudo-thermodynamic) potential during de-lithiation, V

V_0 initial applied potential, V (equal to the initial pseudo-thermodynamic potential)

V_{app} applied potential, V

$v^{\square}$ volume average velocity, m/s

$\overline{V}_{Li}$ partial molar volume of Li, m^3/mol

$\overline{V}_{Si}$ partial molar volume of Si, m^3/mol

V_p volume of the particle, m^3

V_{p_0} initial volume of the particle, m^3

x x in $Li_xSi_{4/15}$ (represents dimensionless lithium concentration or local composition or local state of charge in silicon electrode)

x_s dimensionless surface concentration of Li

$\langle x \rangle$ dimensionless volume average concentration (or state of charge) of the entire particle

α_a anodic transfer coefficient

α_c cathodic transfer coefficient

η overpotential, V

η_a overpotential during de-lithation, V

η_c overpotential during lithiation, V

φ_1 metal potential, V

φ_2 solution potential, V

υ scan rate, V/s

$\varphi_{1,c}$ peak metal potential during lithiation, V (for simplicity, only one pair of peak considered)

$\varphi_{1,a}$ peak metal potential during de-lithiation, V

$\Delta\varphi_1$ peak potential separation, V

ρ_{Si} density of silicon, 2.33 x 10^3 kg/m^3

γ_{Li} mole-fraction activity coefficient of Li

χ_{Li} mole fraction of Li

CHAPTER 9

a specific interfacial area, m^2/m^3

c_i concentration of species i, mol/m^3

c concentration of the electrolyte, mol/m^3

c_s concentration of lithium in the solid particle phase, mol/m^3

$c_{initial}$ initial salt concentration, mol/m^3

$c_{s_{initial}}$ initial concentration of lithium in solid phase, mol/m^3

c_{max} maximum lithium concentration in solid phase, mol/m^3

$D(c)$ bulk diffusion coefficient of the salt, m^2/s

D_{eff} effective diffusion coefficient of the salt, m^2/s

D_s diffusion coefficient of lithium in the solid phase, m^2/s

f_A activity coefficient of the salt

F Faraday's constant, 96487 C/eq

$\mathbf{i}$ current density , A/m^2

$\mathbf{i_2}$ solution phase current density, A/m^2

i_n transfer current per unit of interfacial area, A/m^2

i_0 exchange current density for lithium insertion in silicon electrode, A/m^2

i_{01} exchange current density for the electrochemical reaction at the lithium foil, A/m^2

I superficial current density, A/m^2

j_n pore-wall flux of lithium ions, mol/m^2/s

K_{ij} frictional coefficients, J.s/m^5

k reaction rate constant

L_c length of the composite electrode, m

L_s length of the separator, m

M_i molecular weight of species i, g/mol

n number of electrons transferred in the electrode reaction, n=1 in this work

N_i molar flux of species i in z direction, mol/m^2/s

R universal gas constant, 8.314 J/K/mol

r radial distance in a particle of active material, m

R_s radius of solid spherical particles (here taken to be constant), m

R_{sp} varying radius of solid spherical particles used in the expression for 'a', m

s_i stoichiometric coefficient of species i in electrode reaction

S_c dimensionless parameter to assess the importance of diffusion in the solid

S_s dimensionless parameter relating the time constant for transport of the electrolyte to the time of discharge

t_i^0 transference number of species i relative to the solvent

t time, sec

T temperature, K

U' open-circuit potential of lithium foil *vs.* Li/Li^+ ref., V

$U(x_s)$ open-circuit potential of silicon composite electrode *vs.* Li/Li^+ ref. , V

$\mathbf{v_i}$ velocity of species i, m/s

$\boldsymbol{v}^{\square}$ superficial volume average velocity, m/s

$\tilde{V}_{LiSi_{4/15}}$ molar volume of $Li_xSi_{4/15}$, m^3/mol

$\tilde{V}_{Si}$ molar volume of Si, 12 x 10^{-6} m^3/mol

$\overline{V}_{Si}$ partial molar volume of Si in the electrode, 12 x 10^{-6} m^3/mol

$\overline{V}_{Li}$ partial molar volume of Li in the electrode, 8.8 x $10^{-6}m^3/mol$

$\overline{V}_e$ partial molar volume of the electrolyte, m^3/mol

$\overline{V}_0$ partial molar volume of the solvent, m^3/mol

$\langle x \rangle$ dimensionless average solid phase concentration (i.e. within the particle) along the porous electrode

z co-ordinate along the cell sandwich direction (distance from the current collector, m)

z_i charge number of species i

μ_i electrochemical potential of species i, J/mol

ε porosity of the electrode

ε_{bf} combined volume fraction of the binder and inert filler in the composite electrode

υ_+, υ_- number of cations and anions into which a mole of electrolyte dissociates (In this work, each equals one)

ρ_i density of species i, kg/m^3

Φ_2 solution phase electrical potential, V

Φ_1 matrix phase electrical potential, V

η_{s1} surface overpotential at the lithium foil, V

η surface overpotential in the composite electrode, V

α_{a1}, α_{c1} anodic and cathodic transfer coefficients for the electrochemical reaction at the lithium foil, each taken to be 0.5 in this work

α_a, α_c anodic and cathodic transfer coefficients for the electrochemical reaction at the composite electrode, each taken to be 0.5 in this work

κ_{eff} effective conductivity of the electrolyte, S/m

κ conductivity of the electrolyte, S/m

σ_b bulk conductivity of solid matrix, S/m

σ_{eff} effective conductivity of the solid matrix, S/m

SUMMARY

With increasing interest in energy storage and conversion devices for automobile applications, the necessity to understand and predict life behavior of rechargeable batteries, PEM fuel cells and super capacitors is paramount. These electrochemical devices are most beneficial when used in hybrid configurations rather than as individual components because no single device can meet both range and power requirements to effectively replace internal combustion engines for automobile applications. A system model helps us to understand the interactions between components and enables us to determine the response of the system as a whole. However, system models that are available predict just the performance and neglect degradation. In the first part of the thesis, a framework is provided to account for the durability phenomena that are prevalent in fuel cells and batteries in a hybrid system. Toward this end, the methodology for development of surrogate models is provided, and Pt catalyst dissolution in PEMFCs is used as an example to demonstrate the approach. Surrogate models are more easily integrated into higher level system models than the detailed physics-based models. As an illustration, the effects of changes in control strategies and power management approaches in mitigating platinum instability in fuel cells are reported. A system model that includes a fuel cell stack, a storage battery, power-sharing algorithm, and dc/dc converter has been developed; and preliminary results have been presented. These results show that platinum stability can be improved with only a small impact on system efficiency. Thus, this research will elucidate the importance of degradation issues in system design and optimization as opposed to just initial performance metrics.

In the second part of the thesis, modeling of silicon negative electrodes for lithium ion batteries is done at both particle level and cell level. The dependence of the open-circuit potential curve on the state of charge in lithium insertion electrodes is usually measured at equilibrium conditions. Firstly, for modeling of lithium-silicon electrodes at room temperature, the use of a pseudo-thermodynamic potential *vs.* composition curve based on metastable amorphous phase transitions with path dependence is proposed. Volume changes during lithium insertion/de-insertion in single silicon electrode particle under potentiodynamic control are modeled and compared with experimental data to provide justification for the same. This work stresses the need for experiments for accurate determination of transfer coefficients and the exchange current density before reasoning kinetic hysteresis for the potential gap in Li-Si system. The silicon electrode particle model enables one to analyze the influence of diffusion in the solid phase, particle size, and kinetic parameters without interference from other components in a practical porous electrode. Concentration profiles within the silicon electrode particle under galvanostatic control are investigated. Sluggish kinetics is established from cyclic voltammograms at different scan rates. Need for accurate determination of exchange current density for lithium insertion in silicon nanoparticles is discussed. This model and knowledge thereof can be used in cell-sandwich model for the design of practical lithium ion cells with composite silicon negative electrodes. Secondly, galvanostatic charge and discharge of a silicon composite electrode/separator/ lithium foil is modeled using porous electrode theory and concentrated solution theory. Porosity changes arising due to large volume changes in the silicon electrode with lithium insertion and de-insertion are included and analyzed. The concept of reservoir is introduced for lithium ion cells to

accommodate the displaced electrolyte. Influence of initial porosity and thickness of the electrode on utilization at different rates is quantitatively discussed. Knowledge from these studies will guide design of better silicon negative electrodes to be used in dual lithium insertion cells for practical applications.

CHAPTER 1

INTRODUCTION

The global population is projected to increase from 6 billion in 2001 to 10 billion and the number of vehicles from 700 million to 2.5 billion by 2050 [1]. If all these vehicles are propelled by internal combustion engines, then the oil reserves are sure to diminish. Moreover, the exhaust emissions will significantly contribute to global warming. Therefore sustainable road transportation for the 21st century is needed. Hence electric vehicles (EV) and hybrid electric vehicles (HEV) powered by alternate energy sources are the need of the hour. Alternate energy storage and energy conversion devices include, batteries, fuel cells supercapacitors, flywheels, solar cells, etc. Batteries and fuel cells are the focus of this dissertation.

1.1. Background

1.1.1. Fuel Cells

Sir William Grove invented the fuel cell in 1839 and Dr. Harry Karl Ihring of Allis-Chalmers Manufacturing, a U.S. company, first built a fuel cell tractor in 1959 [2]. Fuel cells were subsequently used by NASA in manned space missions. In recent years, many auto manufacturers have either a fuel cell vehicle or a fuel cell battery hybrid vehicle in demonstration and research stage [3].

A fuel cell is an electrochemical device wherein fuel and oxygen can combine to produce water and electricity. Different types of fuel cells are: alkaline fuel cell (AFC), phosphoric acid fuel cell (PAFC), solid oxide fuel cell (SOFC) and proton exchange membrane (PEM) fuel cells (also called polymer electrolyte fuel cells). Among these, the PEMFC is the most suited for

automobiles because of its low operating temperature, large power density compared to PAFC and the ability to survive a large number of starts and stops relative to SOFC [2].

Hydrogen storage, durability and cost are major areas of research prior to commercial deployment of PEMFC for automobile applications.

1.1.2. Batteries

The invention of the (primary) battery can be attributed to Alessandro Volta, who in 1800 described an assembly consisting of plates of two different metals, such as Zn and Cu, placed alternately in a stack-like fashion separated by paper soaked in an aqueous solution, such as brine or vinegar [4]. Silver-Zinc was the first (primary) battery to be deployed on space mission in 1956 [5]. Primary battery is one which can be used only once to do useful work.

A rechargeable battery is an electrochemical energy storage device wherein chemical energy is converted to electrical energy upon discharge and vice versa upon charge. Lead-acid batteries are the oldest type of rechargeable battery and have been used in automobiles for starting motors, lighting and ignition. In recent years, commercial hybrid vehicles have predominantly used nickel-metal hydride batteries. Apart from hybrid and all-electric vehicles, widespread use of intermittent renewable sources such as solar and wind power all rely on efficient energy storage. Secondary (or re-chargeable) batteries are preferred for the same, justifying the attention given to these systems in recent years.

Among the different types of batteries available [6], [7] lithium-ion cells have high specific energy, high specific power, high energy efficiency, low self-discharge. These factors make them highly suitable for EV and HEV and portable electronics as seen in Figure 1.1 [8].

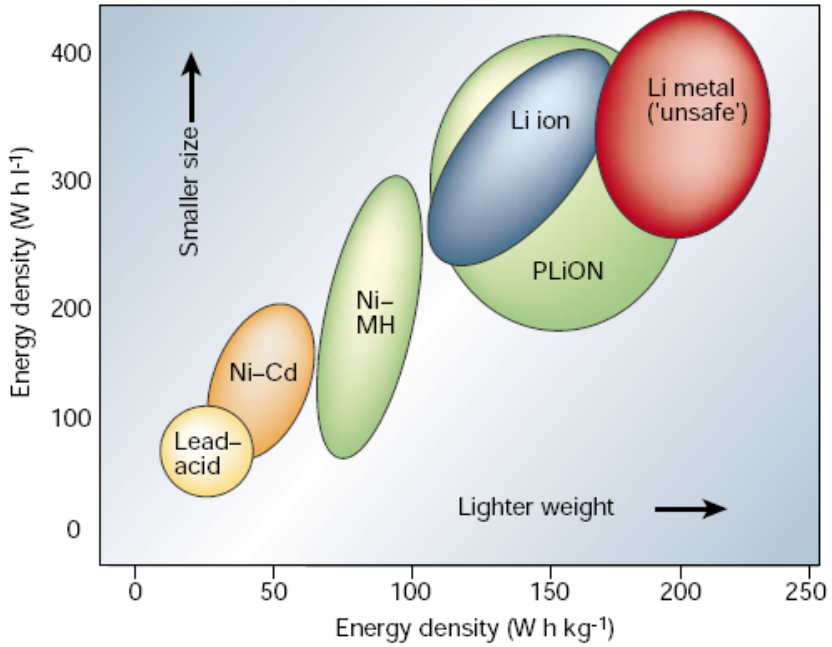

Figure 1.1. Comparison of different battery technologies (Adapted by permission from Macmillan Publishers Ltd: *Nature*, copyright (2001)) (Ref: 8).

In a lithium ion cell, lithium ions shuttle back and forth between intercalation or insertion compounds during charge/discharge cycles and hence called "rocking chair" cells [9]. The first commercial Li-ion rechargeable battery developed by Sony used the layered $LiCoO_2$ intercalation compound as the positive electrode and a form of carbon (petroleum coke) as the negative intercalation electrode. [10] Following Sony's success, rechargeable lithium ion batteries got more attention, and are the principal research focus for rechargeable batteries. The advantage of using a negative intercalation electrode over lithium metal is that the formation and growth of dendrites and hence short-circuit is avoided.

Different chemistries have been explored for the positive electrode and the negative electrode in lithium ion batteries. Positive electrode materials include $LiCoO_2$, $LiNiO_2$, $Li_xMn_2O_4$ $LiFePO_4$, TiS_2, VSe_2, V_2O_5, etc. Negative materials include lithium metal, various

forms of carbon such as graphite, coke, TiO_2, tin composite oxides, alloys such as Li-Al and Li-Si. Recently rechargeable Li-air batteries are also being explored.

Safety, cycle and storage life, low temperature performance, and cost are major concerns for successful commercialization of lithium ion batteries. Recent review articles [11], [12] discuss the challenges facing lithium-ion batteries and means to mitigate them. With lots of research addressing each of these issues and the progresses made, many auto manufacturers have already begun production of HEVs and EVs with lithium ion battery packs. For example, Nissan Leaf ,Chevy Volt and Ford Focus Electric are all- electric cars with lithium ion battery packs that will be available in late 2010/ 2011 [13], [14], [15].

1.1.3. Hybrids

Figure 1.2 shows the Ragone plot [16] for various energy storage and energy conversion devices. As can be seen, no single electrochemical device can effectively replace the internal combustion engine (ICE). Hence hybrid configurations are sought for transportation applications. The fuel cell has the capability to provide the same range as ICE, but has lower specific power. It can also be seen, as compared to supercapacitors, batteries have higher energy density, and hence the vehicle can run on batteries alone for at least a limited range, though not as far as that propelled by ICE. From Figure 1.2, it is evident that the supercapacitors can also be used in hybrid configurations along with fuel cells and batteries for power boosts. Significance of hybrid systems can be understood from its use over a wide spectrum of applications extending all the way down to wireless micro-sensors [17].

1.1.4. Modeling

Modeling of electrochemical energy storage and energy conversion devices is needed for their design and optimization of performance, effective scale-up, and also for the prognostics and

diagnostics of their cycle life and storage life issues. Detailed physics-based, mathematical modeling of dual lithium insertion cell, proton exchange membrane fuel cells, supercapacitors and hybrids have been developed by several research groups as discussed in Chapter 2. Vehicle level system models include electrical circuit models, look-up table based models or empirical models for different components such as batteries, fuel cells and supercapacitors, DC/DC converters, etc. They also include power management algorithms. These higher level models enable one to determine the performance of the system in response to different driving patterns, optimize the different parameters and control algorithms and arrive at trade-offs between different objectives. Chapter 2 provides a review of different types of models that have been developed for batteries, fuel cells, and hybrid systems. But most vehicle level systems models do not include degradation issues in these energy storage and energy conversion devices. A systematic methodology does not exist to transfer the knowledge from detailed physics-based models and experiments to system level models. This is the focus of the first part of this dissertation. Chapter 3 discusses the modeling and experimental techniques employed in the first part of the thesis.

In Chapters 4, the necessity to include the Pt catalyst degradation in PEMFC in the hybrid model and the influence of power management and control algorithms in mitigating Pt catalyst dissolution with negligible loss in efficiency is shown quantitatively. The cycling and self-discharge experiments on commercial lithium ion cells at different temperatures and conditions discussed in Chapter 5 underline the need for a battery performance model that includes temperature and rate capability effects. In Chapter 6, the battery surrogate model as a function of temperature and discharge rate has been developed using response surface techniques. These

were further analyzed using goodness of fit tests and validated in a hybrid model, using the Powertrain Systems Analysis Toolkit (PSAT).

As new materials are discovered and used in these energy storage and energy conversion devices, fundamental understanding of the thermodynamic, kinetic and transport of these materials is paramount and the existing physics-based models will have to be re-visited as needed. One such system is Li-Si negative electrode material, which is being re-visited in recent years for lithium ion batteries because of its high theoretical specific energy (4200 mAh/g) and is the focus of the second part of this dissertation. Chapter 7 provides a detailed literature review of the Li-Si system and also discusses briefly the modeling techniques employed in the analysis of silicon electrodes in this work. In Chapter 8, the Li-Si electrode is theoretically analyzed at the particle level during galvanostatic and potential sweep simulations, and the influence of different parameters is studied. Justification is provided by comparison with experimental data for the inclusion of path dependence in the pseudo-thermodynamic potential *vs.* composition curve associated with the metastable phase transitions. The knowledge from the particle model is then carried further in the development of cell level model in Chapter 9. Porosity variation arising due to volume changes in silicon electrode with lithium insertion/de-insertion have been studied under galvanostatic conditions. Chapter 10 concludes this dissertation work and provides recommendations for future work.

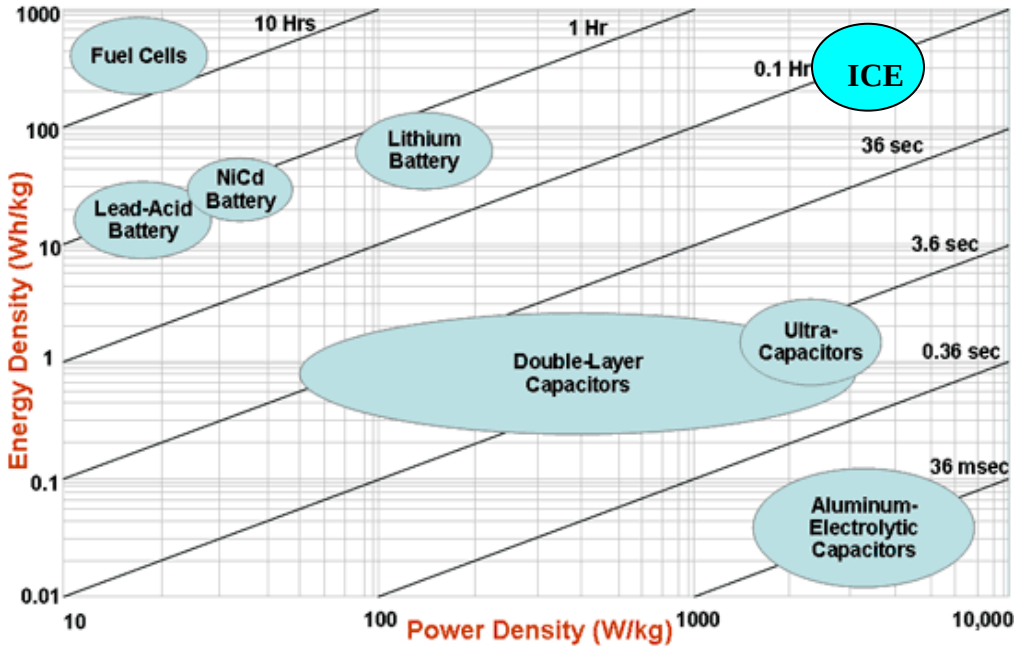

Figure 1.2. Ragone plot for various energy storage and energy conversion devices.

Courtesy: http://www.mpoweruk.com/performance.htm, Source: US Defense Logistics Agency

1.2. References

[1] C.C. Chan, K.T.Chau, *Modern Electric Vehicle Technology*, Monographs in electrical and electronic engineering, Oxford Science Publications, 2001.

[2] Daniel Sperling, *Future Drive, Electric Vehicles and Sustainable Transportation*, Island Press, Washington DC.

[3] http://www.fuelcells.org/info/charts/carchart.pdf

[4] Daniel A. Scherson and Attila Palencsár, *The Electrochem. Soc. Interface*, Spring 2006.

[5] Gerald Halpert, Harvey Frank, Subbarao Surampudi, *The Electrochem. Soc. Interface*, Fall 1999.

[6] Michael H.Westbrook, *The Electric Car*, IEE Power & Energy Series 38, London, UK.

[7] Iqbal Husain, *Electric and Hybrid Vehicles, Design Fundamentals*, CRC Press.

[8] J.M. Tarascon, M. Armand, *Nature*, 414 (2001), 359-367.

[9] Bruno Scrosati, *J. Electrochem. Soc.*, 139 (10) (1992), 2776-2781.

[10] J. M.Tarascon, D. Guyomard, *Electrochim.Acta*, 38(9) (1993), 1221-1231.

[11] J.B.Goodenough, Y.Kim, *Chem.Mat.* (review), 22 (2010), 587-603.

[12] J.M.Tarascon, *Phil.Trans .R. Soc. A ,* 368 (2010), 3227- 3241.

[13] http://www.nissanusa.com/leaf-electric-car/index#/leaf-electric-car/index

[14] http://www.chevrolet.com/pages/open/default/future/volt.do

[15] http://www.thefordstory.com/green/ford-focus-electric-coming-soon/

[16] Thomas Christen, Martin W. Carlen, *J.Power Sources*, 91 (2) (2000), 210-216.

[17] Erick O. Torres, Lucas A. Milner, Gabriel A. Rincón-Mora, *The Electrochem.Society Interface*, Fall 2008.

CHAPTER 2

LITERATURE REVIEW ON HYBRID SYSTEMS COMPONENTS AND MODELING

2.1. Introduction

Environmental pollution not only accelerates climate change but also aggravates serious health concerns, and a major cause is emission from motor vehicles [1]. Pressure from governmental agencies and environmental groups has driven the car manufacturers and energy companies to look for cleaner energy conversion and storage devices. Among the alternatives for transportation are electric vehicles, fuel cell-battery hybrids, fuel cell –super-capacitor (and battery) hybrids. Neither the fuel-cell hybrid vehicle nor other hybrid vehicles are anticipated to compete with the internal combustion engine on cost or performance alone. Their value is in increasing efficiency and thereby reducing emissions of carbon-dioxide.

Hybrid configurations are generally sought to provide both high specific power and specific energy [2-7]. A hybrid configuration is preferred over an all electric or pure fuel cell vehicles in order to combine the advantages of both the technologies and eliminate their individual disadvantages. A battery is essential in recovering the braking energy and in providing start-up power [8], whereas the fuel cell has the principal advantage of being a range extender.

The main challenges for commercializing Proton Exchange Membrane Fuel Cells (PEMFC) systems for automobile applications are: hydrogen storage, durability, and cost. Durability concerns, such as platinum catalyst degradation [9], [10] carbon catalyst support corrosion [11], [12], and membrane chemical attack [13, 14] are key challenges [15] because they affect not only the performance of the fuel cell but also the economics and the reliability of

the fuel cell technology and its commercialization for automotive applications. Similarly, for secondary batteries, capacity degradation under both cyclic and storage conditions have to be considered for both long term safe performance and also life-cycle cost analysis. The aging mechanisms in lithium ion batteries in different components have been extensively discussed in literature [16-18].

Mathematical modeling of fuel cells, batteries and the hybrid systems with different levels of complexity has been pursued to understand the system, optimize the performance, scale-up and mitigate some of the durability and degradation issues.

2.2. Fuel Cell Modeling

Several electrochemistry based models exist in literature for the modeling of PEMFC [19-24]. These models help to gain understanding of the underlying fundamental transport processes and simulate performance. They could be 1D, 2D, computational fluid dynamic models, etc. Empirical and simplified mechanistic models also exist for performance analysis and parameter estimation of PEMFC [25-30]. These simple models are valuable for determining kinetic parameters as well as comparing the various losses in the system to one another. Transient phenomena in fuel cells arises due to step changes in potential (start-up, shut down, etc.) and related phenomena (such as gas flow rates, water production, current density) is studied [31], [32]. Non-isothermal effects [22], [33] have also been considered in some of these models. Stack level models that focus on temperature distribution and determination of appropriate coolant flow have been developed [34], [35]. Complete fuel-cell power system models have the benefit of examining true designs of operating systems and the interconnections between components. Sensitivity analysis can be done for modeling parameters that are used in the simulation of fuel cell and thus can deduce the relative importance of each parameter on model

results [36]. Moreover, fuel cell model have also been incorporated in vehicle simulation software [37]. This allows the investigation of fuel cell operation during driving cycle conditions.

Failure mechanisms have also been studied by few modeling groups using physics-based models. Pt catalyst degradation with potential cycling [9] and other potential dynamic conditions [38] have been modeled. Carbon support corrosion [39], [40] and membrane degradation [41] have also been modeled. But there are few studies that view these durability issues in the context of the system model. The reason is that integration of detailed electrochemical degradation models is complex and simulation times can be excessive. On the other hand, there are hardly any empirical models that capture the different durability issues with fidelity. Fowler *et al.* [42] have incorporated voltage degradation into a generalized steady state electrochemical model for a PEM fuel cell. The authors have considered degradation with aging and not cycling. Liu and Case [43] have developed a semi-empirical phenomenological durability modeling for PEMFC under both cyclic and constant aging conditions to incorporate observed aging phenomena and describe the cell performance at different time periods.

2.3. Battery Modeling

Reliable battery models must exist when developing both battery and vehicle level control strategies. Battery models must be computationally fast in order to be applicable to dynamic HEV applications. For automotive applications, modeling in MATLAB is desirable, because it is already a familiar tool in vehicle development [44].

2.3.1. Types of battery models

Several types of battery models are available in literature: electrochemical models [45-47], analytical models involving parameter estimation to predict remaining capacity of battery

taking into account cycle-aging and temperature effects [48], electrical circuit models [49], [50], resistance models (described in ADVISOR), computational fluid dynamics (CFD) based models [51] and other simplified models [52]. A kinetic battery model has been used in the HOMER (micro power optimization model) software in NREL [53]. An extended kinetic battery model is used in Hybrid2 software from NREL, which is used to perform detailed long-term performance and economic analysis on a wide variety of hybrid power systems. Some of the battery component models in fuel cell/battery hybrid system models such as in ADVISOR have been predominantly based on equivalent circuits approach and look-up tables [54]. A lower order real time simulation model [55] is developed using a combination of techniques to simulate the discharge profile of a lithium-ion system in time scales of milliseconds. Other reduced order models arrived at from physics based models [56-58] exist in literature for lithium ion batteries. A detailed physics-based model for the performance of a battery/super capacitor hybrid system exists in literature [59]. Simple vehicle-battery performance modeling is also available in literature [52] where the vehicle model calculates the total power demand from the vehicle and accordingly determines the power demand from the energy storage device.

2.3.2. Parameters and uncertainties

One of the main parameters in battery operation and modeling is state of charge (SOC). SOC is the capacity of the battery expressed as the percentage of a nominal value and corresponds to the stored chemical energy available to do work. State of Health (SOH) is used to imply that one could deduce how well the battery system is functioning relative to its nominal (rated) and end (failed) states. SOH is also relevant to on-board diagnostics [60]. Several studies have focused in the estimation of these important parameters online [61], [62]. SOC can be viewed as a thermodynamic quantity, enabling one to assess the chemical energy of the system.

But onboard a vehicle, the SOC is not very close to a thermodynamic property because there is no steady state. A simple way of measuring state of charge of the battery onboard a vehicle is by coulomb counting. But it is difficult to know the exact state of charge because the remaining usable capacity is dependent on several factors such as the discharge rate, temperature, number of cycles and self-discharge. Unless the influence of each of these factors is clearly understood and accurately predicted, estimation of state of charge precisely is not possible. This leads to over-design of battery systems for vehicular applications. The weight of the additional batteries leads to both increased cost and additional fuel usage. In spite of the fact that larger difference between the maximum state of charge SOC and minimum SOC level aids in effective absorbing of the regenerative braking energy, this would also reduce the life of the battery, which is affected by the depth of discharge (DOD) [63]. The hybrid power control strategy employed by Hyoung *et al.* [63] can be employed especially at medium power modes to strike a balance between regenerative braking energy and battery life. It has to be borne in mind that braking operations are typically characterized by high currents and short time intervals. Apart from SOC and regenerative braking inter-dependency considerations, as mentioned before, the impact of drivability on power distribution can also be considered. Typically, the method for most efficiently recapturing regenerative power to an energy storage device does not coincide with the smoothest method of decelerating the vehicle. Often, the regenerative power must be limited, i.e. more must be wasted in the friction brakes, to preserve the smooth ride that a consumer expects from a vehicle [64]. State of charge balancing is an important aspect of hybrid vehicle analysis [65], [52]. If the change in SOC of the battery between the beginning and the end of a cycle is too large, the vehicle fuel economy may artificially be very high or very low due to the battery net discharge or charge, respectively. Packages like Powertrain Systems Analysis Toolkit

(PSAT) and ADVISOR offer two methods for SOC balancing (to avoid an artificially high fuel economy within a single cycle)- linear approximation method and an iterative zero-delta approach for SOC balancing wherein the iteration routine is performed on the initial SOC until the final SOC is within some tolerance (0.5%) [65], [66]. Gielniak and Shen [64] suggest that there are number of ways to achieve SOC balancing in practice and they are: (a) modify the control strategy, (b) iterate the simulation (like in zero-delta approach) (c) restrict operation within the cycle to ensure that the SOC ends within tolerance and altering the profile until SOC matches. It is suggested that SOC balancing routine can also be done such that the equivalent fuel energy of the change in SOC of the battery pack is less than a specified percentage of the total fuel consumed during a cycle. This approach will eliminate fluctuations in results due to variations in total battery pack capacity among vehicles (e.g. 5% SOC change in a 50 Ah pack is ten times more energy than a 5% SOC change in a 5 Ah battery pack).

Multiple responses are of interest in batteries–namely, specific power, specific energy, capacity, cost, calendar life and cycle life. It is also desirable to reduce cell-to-cell variation within a battery module (or pack) by means of a proper battery management system. Variations in cell could arise from differences in active material loading [67, 68], which come from the stage of manufacturing and/or develop during operation. Thaller [69] discusses that the stochastic variations associated with the grouping of cells can easily lead to cell reversal, overcharging or other undesirable occurrences on the overall cycle life of the battery pack and hence in multicell strings, the standard deviation plays an important role in determining overall battery life and had assigned normal distributions to parameters. Sastry *et al.* [68], in order to develop a battery management technique, captured the dynamic uncertainties arising from cell-to-cell variation by randomly varying the parameters of their battery model within a few percent

of their nominal values and the uncertainties arising from manufacturing by random variation of the initial capacities within few percent.

2.3.3. Capacity fade and thermal effects

The acceptable amount of irreversible capacity loss varies widely depending on the application. In consumer electronics, such as personal computers and cellular phones, batteries are typically expected to last a two or three years. So, an irreversible capacity loss of > 20% over 1–2 years would be acceptable for batteries used in many small, portable electronic devices. On the other hand, a satellite battery might be required to retain 80% of its initial capacity after 18 years or more. Automakers have set a 15 years life (or 1000 cycles at 80% depth of discharge) as a goal for batteries in hybrid and full electric vehicles [18]. Thus one could say the number of years a battery pack in a hybrid system can continue providing a minimum "up-time" can define the life of the battery pack for the particular application [70]. Battery pack reliability relates to both normal "wear out" factors inherent in the operation of the electrochemical cell itself and to failure mechanisms from manufacturing defects and component failures that cause a cell in the battery to go open circuit or short circuit. The decreased reliability due to wear out is due to gradual increased variation in the capacity of individual cells in the battery with age. There could also be series connection problems, and so to avert these issues battery packs have charge balancing circuits. Thus cell-to-cell variation can be neglected in system models. But models for degradation of a cell from irreversible capacity losses due to various phenomena such as poor solid electrolyte interphase (SEI), huge volume changes and associated stress has to be captured in system models. Since understanding and capturing thermal effects are also important for cell safety and better thermal management, this is also discussed briefly here. Botte *et al.* [71], Gomadam *et al.* [72] and Bandhauer *et al.* [73] have reviewed the electrochemical and thermal

models for secondary lithium batteries. Heat losses are encountered in lithium ion cell because of ohmic drop and other overpotentials during the course of operation. This is especially significant for high rates of operation typical of automobile applications during peak power demand. Moreover, phenomena like thermal runaway under abuse conditions should also be explored in a thermal model. The batteries used in camcorders and other such electronics have spiral geometries (for e.g. Sony 18650 cells) whereas for automobile applications, prismatic geometries are preferred so that the battery pack satisfies both volumetric and weight demands. As much as thermal management within an individual cell is desired, thermal management of the entire battery pack is also essential. The reason is these thermal variations could also lead to an early failure of the entire pack. Heat generation can be treated by means of a lumped parameter model or one could consider localized energy balance and from there arrive at the temperature and energy distributions. In the lumped parameter approach (or the lumped heat generation method), cell can be considered to be at a constant temperature and then the thermal balances corresponding to the rate of charge/discharge, etc. can be arrived at. In other models the electrochemical reactions and the thermal effects are coupled, i.e. the electrochemical and transport parameters and the reactions rates are considered functions of temperature and hence thermal differences at different regions in the cell have an effect on the electrochemical behavior of the cell simultaneously as well. Hence modeling has been pursued at varying degrees of complexity [74-93] to understand these processes in order to develop a good thermal management system for better cell life and safety. Also, once thermal effects in a battery are captured, mitigation approaches, such as the use of phase-change material [94], can be developed.

2.4. DC/DC converter modeling

It is desired to maintain the dc bus at a constant voltage because constant voltage output is preferred for the load. The output current of the fuel cell will vary with power demand and hence its voltage is also strongly dependent on power demand. Hence the fuel cell cannot be directly connected to the dc bus and the load. Hence it is necessary to use a dc/dc converter between fuel cell and dc bus to elevate and stabilize the output voltage of the fuel cell [95]. Thus an actively controlled hybrid system [96] has advantages over a passive hybrid system. This dc/dc converter can be unidirectional or bi-directional [97]. Several reports are available for modeling of dc/dc converters [98], [99]. DC/DC converter has been described by a second order dynamic system by Kim *et al.* [100] The DC/DC converter is described as a static device with efficiency loss, which is a function of the fuel cell output power. Integrated modeling of a fuel cell subsystem and DC/DC converter is available in literature [101].

2.5. Fuel Cell/Battery Hybrid System

The fuel cell/battery hybrid system is a case of series hybrid system [102] because the power from both the fuel cell and the batteries flow through the electric motor which then provides the traction to the wheels. In an active hybrid, the fuel cell and battery are connected through a uni-directional dc/dc converter and the load is directly connected to the battery as shown in Figure 2.1. [96]. The objectives of the power management strategies have so far been to improve system efficiency, to effectively capture regenerative energy by optimally controlling state of charge and also to strike a balance with battery life, to include drivability considerations on power distribution and to avoid fuel starvation problems, etc. [63], [103], [104]. One could arrive at different levels of optimal power split (degree of hybridization) and control parameters in fuel cell hybrid electric vehicle with different battery sizes, drive cycles and objectives [105], [106].

The paragraph below gives a snapshot of the different issues in arriving at an optimized hybrid system.

For applications where fuel cell cannot respond fast enough, additional batteries is required. Added weight of batteries makes the configurations with larger batteries perform worse. Having a large number of cells or very big size batteries than optimal solution will only add extra mass to the system and hence will affect fuel consumption, cost, etc. It is therefore crucial to increase the power-to-weight ratio of the batteries. Battery sizing is complicated because if one focuses on just the short-time assistance [107] from battery, one can downsize the battery, but at the same time, cannot operate the vehicle as an all-electric drive when it is advisable to do so. The fuel cell can be made to ensure that a target SOC is maintained for the battery, which is the average of the operating band of the SOC. So the fuel cell sometimes is required to provide both the load power demand and also the additional power to maintain the target SOC [64]. Moreover, the rate at which the fuel cell can come to the operating point to deliver the demanded power also affects battery sizing. An optimized hybrid design can nullify the effects of fuel cell transient response.

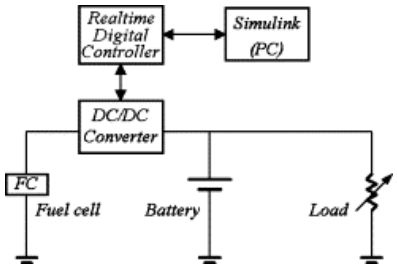

Figure 2.1. Block diagram of active fuel cell/battery hybrid system (Reprinted from *J.Power Sources*, 130 (1-2), copyright (2004) with permission from Elsevier) (Ref. 96).

Though the base control scheme could have constant accessory load of say 300-700 W on an average, it can be modified to accommodate the inclusion of other loads such as adaptive

suspension system, electric power steering, coolant pump and high voltage accessory loads [64] such as electric air conditioning, fuel cell air compressor, *etc*. Depending on vehicle architecture, adaptive suspension system can sometimes be classified under high voltage accessories. Based on the power requirements for these devices, there could be a peak accessory load and an average accessory load and hence one could have an accessory load profile also.

2.6. Response Surface Methodologies

The Response Surface Methodology (RSM), by careful design and analysis of experiments, seeks to relate a response or output variable to the levels of a number of predictors, or input variables [108, 109].

Since in many cases, such as electrochemical systems, the relationship between response and predictors is either too complex to determine or unknown, deterministic relationships may not be possible and an empirical approach is necessary to determine the behavior. Thus this methodology can be used in lieu of standard, sophisticated parametric approaches to design space search and complex iterative optimization routines which are time consuming. Moreover the problem of program crashing due to non-convergence in any of the sub-programs is eliminated. Since the RSE is a regression curve, though, a set of experimental or computer simulated data must be available.

One organized way of obtaining the data is design of experiments (DOE). A full factorial design, in most cases, leads to an impractical level of runs. To perform fewer simulation or experimental runs, a fractional factorial design can be adopted. Fractional factorial DOEs use less information to come up with results similar to full factorial designs. This is accomplished by reducing the model to only account for parameters of interest. Therefore, fractional factorial designs neglect third or higher order interactions for an analysis accounting only for main and

quadratic effects and second order interactions. Thus, a tradeoff exists in fractional factorial designs. Alexander discusses Response Surface Optimization using JMP software [110]. A uniform framework of quantification of uncertainties is provided by probabilistic design methods [111, 112]. The objective of probabilistic design is to analytically quantify the impact of uncertainty in terms of probabilities by describing design performance in terms of distributions instead of point values.

2.7. References

[1] B.Johnston, M.C. Mayo, A.Khare *Technovation*, 25(6) (2005), 569-585.

[2] K. T. Chau, Y. S. Wong, *Energy Convers. Mgmt.*, 42 (9) (2001), 1059-1069.

[3] Yap, H. T., Schofield, N., Bingham, C. M., IEEE *Conference Publication* 498(1) (2004), *Power Electronics, Machines and Drives*, 61-66.

[4] R. Kötz, M. Carlen, *Electrochim. Acta*, 45 (15-16) (2000), 2483–2498.

[5] Peter Van den Bossche, Frédéric Vergels, Joeri Van Mierlo, Julien Matheys and Wout Van Autenboer, *J. Power Sources*, 162 (2) (2006), 913–919.

[6] W. G. Pell, B. E. Conway, *J. Power Sources*, 63 (2) (1996), 255-266.

[7] T.Christen, M.W. Carlen, *J. Power Sources*, 91 (2) (2000), 210–216.

[8] G. Pede, A. Iacobazzi, S. Passerini, A. Bobbio, G. Botto, *J. Power Sources*, 125 (2) (2004), 280–291.

[9] R.M. Darling ,J.P. Meyers, *J. Electrochem. Soc.,*150(11) (2003), A1523-A1527.

[10] Wu Bi, PhD Dissertation, Georgia Institute of Technology, 2008.

[11] J.P. Meyers, R.M. Darling, *J. Electrochem. Soc.,* 153(8) (2006), A1432-A1442.

[12] Kevin Gallagher, PhD Dissertation, Georgia Institute of Technology, 2009.

[13] H.Tang, S.Peikang, S.P.Jiang, F.Wang , M.Pan, *J .Power Sources*, 170(1) (2007),85-92.

[14] Cheng Chen, Galit Levitin, Dennis W. Hess, Thomas F. Fuller, *J. Power Sources*, 169(2) (2007), 288-295.

[15] Steven G. Chalk, James F. Miller, *J. Power Sources*, 159(1) (2006), 73–80.

[16] J. Vetter, P. Novák, M.R. Wagner, C. Veit, K.-C. Möller, J.O. Besenhard, M. Winter, M. Wohlfahrt-Mehrens, C. Vogler and A. Hammouche, *J. Power Sources*, 147(1-2) (2005), 269–281.

[17] P. Arora, Ralph E. White, Marc Doyle, *J. Electrochem.Soc.,* 145 (10) (1998), 3647-3667.

[18] R. Spotnitz, *J. Power Sources*,113(1)(2003), 72-80.

[19] T. E. Springer,T. A. Zawodzinski, S. Gottesfeld, *J. Electrochem. Soc.*, 138(1991), 2334.

[20] Dawn M. Bernardi and Mark W. Verbrugge, *J. Electrochem. Soc.* 139(1992), 2477.

[21] Thomas F. Fuller and John Newman, *J. Electrochem. Soc.,* 140(1993), 1218.

[22] Trung V. Nguyen and Ralph E. White , *J. Electrochem. Soc.,*140 (1993), 2178.

[23] T.E. Springer, M. S. Wilson, and S. Gottesfeld, *J.Electrochem. Soc.,* 140 (1993), 3513.

[24] Andrew Rowe, Xianguo Li , *J.Power Sources*,102 (2001),82-96.

[25] J.Kim, S.Lee, S.Srinivasan, C.E. Chamberlin, *„J. Electrochem. Soc.*142 (1995), 2670.

[26] J. C. Amphlett, R. M. Baumert, R. F. Mann, B. A. Peppley, P. R. Roberge, and T. J. Harris, *J. Electrochem. Soc*. 142(1) (1995).

[27] J. C. Amphlett, R. M. Baumert, R. F. Mann, B. A. Peppley, P. R. Roberge, T. J. Harris, *J. Electrochem. Soc*., 142(9)(1995).

[28] R.Tirnovan, et.al., Automation Quality and Testing, Robotics, IEEE International Conference, May 2006 Volume: 1.

[29] M.G.Santarelli, M.F.Torchio, P.Cochis, *J.Power Sources*,159 (2006),824-835.

[30] R.F.Mann, J.C. Amphlett, M.A. I. Hooper, H.M. Jensen, B.A. Peppley, P.R. Roberge, *J.Power Sources*, 86(2000),173-180.

[31] van Bussel, H.; Koene, F. G. H.; Mallant, R. , *J. Power Sources*, 71 (1998), 218.

[32] Amphlett, J. C.; Mann, R. F.; Peppley, B. A.; Roberge, P. R.; Rodrigues, A. *J. Power Sources*, 1996, 61, 183.

[33] Wohr, M.; Bolwin, K.; Schnurnberger, W.; Fischer, M.; Neubrand, W.; Eigenberger, G. *Int. J. Hydrogen Energy* 1998, 23, 213.

[34] Maggio, G.; Recupero, V.; Mantegazza, C. *J. Power Sources* 1996, 62, 167.

[35] Lee, J. H.; Lalk, T. R.; Appleby, A. J. *J. Power Sources* 1998, 70, 258.

[36] Jeferson M.Corrêa et.al., IEEE Transactions on Energy Conversion , 20(1)(2005).

[37] Christos N.Maxoulis,Dimitrios N.Tsinoglou,Grigorios C.Koltsakis, Energy Conversion and Management, 45(2004),559-573.

[38] Wu Bi and T.F. Fuller, J. Power Sources, 2008. 178: p. 188.

[39] K.G. Gallagher, T. F. Fuller, *Phys. Chem. Chem. Phys.*, 11, 11557–11567 (2009).

[40] Norimitsu Takeuchi, T. F. Fuller, *J. Electrochem. Soc.,* 157, B135-B140 (2010).

[41] Cheng Chen, T. F. Fuller, *Electrochim. Acta*, 54, 3984-3995 (2009).

[42] Michael W.Fowler, Ronald F.Mann,John C.Amphlett,Brant A.Peppley,Piere R.Roberge, *J.Power Sources*,106(2002),274-283.

[43] D.Liu, S.Case, *J.Power Sources*, 162 (1)(2006),521-531.

[44] Ted J.Miller, *J.Power Sources*, 110 (2002) 475-476.

[45] Marc Doyle, Thomas F Fuller, John Newman, *J.Electrochem.Soc.*, 140(6) (1993).

[46] Thomas F. Fuller, Marc Doyle, John Newman, *J.Electrochem.Soc.,* 141(1) (1994).

[47] Thomas F.Fuller, Marc Doyle, John Newman, *„J.Electrochem.Soc.,*141(4)(1994).

[48] Peng Pong, Massoud Pedram, *IEEE Trans.Very Large Scale Integration (VLSI) Systems*, 14(5) (2006), 441- 451.

[49] Min Chen, Gabriel A. Rinćon-Mora, *IEEE Trans. Energy Conversion*, 21 (2), June 2006, 504-511.

[50] Lijun Gao, Shengyi Liu, Roger A.Dougal, *IEEE Trans.Components and Packaging Technologies*,25(3) (2002).

[51] Bor Yann Liaw, Wen-Bin Gu, Chao-Yang Wang, Proceedings of the 32nd Intersociety Energy Conversion Engineering Conference, 2, 1997,899 – 903.

[52] Fellner and Newman, *J.Power Sources*, 85(2)(2000), 229-236.

[53] James F.Manwell, Jon G. McGowan, *Solar Energy*, 50 (5) (1993), 399-405.

[54] V.H. Johnson , *J.Power Sources* 110 (2002), 321–329.

[55] V.R.Subramanian,V.Boovaraghavan, V.D. Diwakar, *Electrochem.Solid State Letts.* , 10 (11) (2007), A255-A260.

[56] B.Bhikkaji, T.Soderstrom, *Int.J.Control*, 74 (2001), 1543.

[57] K.A.Smith, C.D.Rahn,C.Y.Wang, *J.Dyn.Syst.Meas.Control*, 130 (2008).

[58] Long Cai, Ralph White, *J.Electrochem.Soc.* 156 (3) (2009), A154-A161.

[59] Godfrey Sikha, Ralph E. White, Branko N. Popov, *J.Electrochem.Soc.* 152 (8) (2005). A1682-A1693.

[60] Mark Verbrugge,Edward Tate, *J.Power Sources*,126(2004), 236-249.

[61] Gregory L.Plett, *J.Power Sources*,134(2004),262-276.

[62] S.Santhanagopalan,Ralph E.White, *J. Power Sources*, 161(2)(2006), 1346-1355.

[63] Hyoung Yeon Cho, Wenzhong Gao, Herbert L.Ginn (III),*Power Electronics in Transportation*, 21-22 (2004), 159 – 166.

[64] Michael J. Gielniak, Z.John Shen, IEEE 60th Vehicular Technology Conference, 6(26-29), 2004, 4422 – 4426.

[65] M.Amrhein, P.T.Krein, *IEEE Trans.Vehicular Technology*, 54(3) (2005), 825-836.

[66] T. Markel, A. Brooker, T. Hendricks, V. Johnson, K. Kelly, B. Kramer, M. O'Keefe, S. Sprik, K. Wipke, *J.Power Sources*, 110 (2002) 255–266.

[67] M.Dubarry, N.Vuillaume, Bor Yann Liaw, *J.Power Sources* 186 (2009) 500-507.

[68] S.Sastry, O.Gimdogmus, T.Hartley, R.J. Veillette, *J.Power Sources* 166(2007) 284-296.

[69] Lawrence H.Thaller, *J.Electrochem.Soc.*, 130(5) (1971) 986-990.

[70] W.A.Adams et.al., Telecomm.Energy Conference,19-23 ,Sept. 2004, 73- 82.

[71] G.Botte,V.R.Subramanian,R.E.White, *Electrochim. Acta*, 45(2000), 2595-2609.

[72] P.M.Gomadam,J.W.Weidner,R.A.Dougal,R.E.White, *J.Power Sources* ,110 (2002) 267-284.

[73] Todd Bandhauer, T. F. Fuller, Srinivas Garimella, Critical Reviews in Electrochemistry and Solid State Science and Technology, CRES3T, *J. Electrochem. Soc.*(submitted).

[74] D.Bernardi, E.Pawlikowski, J.Newman, *J.Electrochem.Soc.,* 132(1) (1985).

[75] T.I.Evans and R.E.White, *J.Electrochem.Soc.*,136(8) (1989).

[76] Yufei Chen and James W.Evans, *J.Electrochem.Soc.,* 140(7)(1993).

[77] Yufei Chen and James W.Evans, ,J.Electrochem.Soc.,141(11)(1994).

[78] Yufei Chen,James W.Evans, *Electrochim.Acta*,39(4),517-526,1994.

[79] John Newman, William Tiedemann, *J.Electrochem.Soc.*, 142(4) (1995).

[80] Carolyn R.Pals, John Newman, *J.Electrochem.Soc.,*142(10) (1995), 3274-3281.

[81] Carolyn R.Pals, John Newman, *J.Electrochem.Soc.,*142(10) (1995),3282-3288.

[82] Yufei Chen and James W.Evans, *J.Electrochem.Soc.*,143(9) (1996), 2708-2712.

[83] Lin Rao, John Newman, *J.Electrochem.Soc.,*144(8)(1997).

[84] Li Song and James W.Evans, J.Electrochem.Soc., 145(7)(1998), 2327-2334.

[85] Li Song, James W Evans, *J.Electrochem.Soc.*,147(6) (2000), 2086-2095.

[86] Mark W.Verbrugge Robert.S.Conell, *J.Electrochem.Soc.,* 149(1) (2002), A45-A53.

[87] Gerardine G.Botte,Bradley A.Johnson, Ralph E.White, *J.Electrochem.Soc.,*146(3) (1999),914-923.

[88] P.Baudry,M.Neri,M.Gueguen,G.Lonchampt*, J.Power Sources* ,54(1995), 393-396.

[89] Said Al-Hallaj,J.R.Selman, *J.Power Sources*,110 (2002),341-348.

[90] S.C.Chen, C.C.Wan,Y.Y Wang, *J.Power Sources*,140(2005), 111-124.

[91] Kandler Smith,C.Y.Wang, *J. Power Sources*,160 (2006) ,662-673.

[92] Kazuo Onda, Takamasa Ohshima, Masato Nakayama, Kenichi Fukuda, Takuto Araki, *J. Power Sources* ,158 (2006), 535-542.

[93] D.H.Doughty, P.C.Butler, R.G.Jungst, E.PeterRoth, *J. Power Sources*,110 (2002), 357-363.

[94] S.A.Khateeb, S.Amiruddin, M.Farid, J.Robert Selman, Said Al-Hallaj, *J.Power Sources*,142(2005) 345-353.

[95] R.Rizzo and L.Piegari, IEEE Bologna PowerTech Conference, June23-26, Bologna, Italy, 2003.

[96] L.Gao, Z.Jiang R.A. Dougal, *J. Power Sources*, 130(1-2)(2004), 202-207.

[97] L.Gao, Z.Jiang, R.A.Dougal, 35th Annual IEEE Power Electronics Specialists Conference, Aachen, Germany, 2004.

[98] M. Marchesoni, C. Vacca, *IEEE Trans. Power Electronics*, 22(1), Jan 2007.

[99] Chih-Chiang Hua, Chih-Wei Chuang, Chi-Lun Huang, 37th IEEE Power Electronics Specialists Conference, June 2006.

[100] Min Joong Kim, Huei Peng, Chan-Chaio Lin, Euthie Stamos, Doanh Tran, 2005 American Control Conference, June 8-10 2005,Portland,OR,USA.

[101] Song-Yul Choe, Jung-Gi Lee, Jong-Woo Ahn, Soo-Hyun Baek, *J. Power Sources*, 164 (2007), 614-623.

[102] G. Maggetto, J. Van Mierlo, Electric, Hybrid and Fuel Cell Vehicles IEE Seminar, 2000.

[103] M.Amirabadi, S.Farhangi, Industrial Electronics and Applications, 1st IEEE Conference, May 2006.

[104] Kwi-Seong Jeong, Won-Yong Lee, Chang-Soo Kim, *J.Power Sources*, 145 (2005), 319-326.

[105] O.Sundström, A.Stefanopoulou, IEEE International Conference on Control Applications, October 2006.

[106] A.Jossen, J.Garche, H.Doering, M.Goetz, W.Knaupp, L.Joerissen, *J.Power Sources*, 144(2005), 395-401.

[107] SM Nayeem Hasan, Sikyung Kim,Iqbal Husain, Applied Power Electronics Conference and Exposition, 19th Annual IEEE,Vol:2,2004.

[108] Jimmy C.Tai, Dimitri N.Mavris, Daniel P.Schrage, *AIAA Paper* , 95 (1995).

[109] Daniel DeLaurentis, Dimitri N. Mavris, Daniel P. Schrage, 20th Congress of the International Council of the Aeronautical Sciences, Sorrento, Italy, Sept. 8-13, 1996.

[110] Melvin T.Alexander, SAS Proceedings.

[111] Dimitri Mavris, Bryce Roth Noel Macsotai 14th ISABE, Florence, Italy, Sept. 1999.

[112] A.A.Giunta, M. S. Eldred, J.P.Castro, 9th ASCE Specialty Conference on Probabilistic Mechanics and Structural Reliability, 2004, 1-7.

CHAPTER 3

MODELING & EXPERIMENTAL TECHNIQUES FOR STUDY OF ROBUST HYBRID SYSTEM DESIGN

A brief overview of the modeling tools and experimental techniques used in this thesis is presented in this chapter.

3.1. Robust Design and surrogate modeling techniques

System design should involve a decision process that focuses not merely on optimization, but also on obtaining a robust solution to maximize affordability [1]. Robust Design is one in which levels of controllable factors are chosen such that the responses are made insensitive to noise or uncontrollable factors. Surrogate models are key enabler for a robust design simulation (RDS). Surrogate modeling can be considered as an approach to create a model of a model. In this method, a model is first constructed from data obtained from a physics-based model or from experiments by employing a design of experiments (DOE). When there are many design variables, a screening test is conducted to identify the variables that make the greatest contribution to the response of the system. The simple model is then validated using different statistical techniques and with data not used for model construction. Surrogate models are otherwise called meta-models. After the surrogate models are developed, the effect of uncertainty in variables can be incorporated into a systems level design through the use of Monte Carlo Simulation [1]. These models can be constructed by either parametric or non-parametric approaches and can be either linear or non-linear in the parameters. Response surface methodology, kriging, neural networks are some of the metamodeling techniques. In this dissertation, RSM with linear regression models with respect to the parameters is used. Response surface methodology (RSM) could typically handle up to eight or nine variables. In other

instances, neural networks technique is sometimes used in place of RSM. This helps in solving prediction problems as opposed to the formal model-building as done in RSM. When meta models for multiple responses are created, one can adopt the desirability function approach [2] to simultaneously optimize these several response variables when they are uncorrelated. When correlated, alternative approaches, such as generalized distance measure, etc. have to be adopted [3].

3.2. RSM-Brief Explanation of the methodology

Box and Wilson [4] laid the foundations for Response Surface Methodology (RSM) by outlining a sequential philosophy of experimentation that encompasses experiments for screening, region seeking (such as steepest ascent), process/product characterization and process/product optimization. RSM encompasses statistical experimental design techniques, regression modeling techniques and elementary optimization methods.

Response Surface Methodology (RSM) is a collection of statistical and mathematical techniques useful for developing, improving, and optimizing processes [5]. It provides a way to develop surrogate models for complex life models such as those for capacity fade in batteries [6], Pt catalyst degradation model [7], carbon corrosion model in PEMFC [8], etc. in a statistical framework. These surrogate models facilitate a robust design space solution. In robust parameter design methodology, product or process variations are reduced by choosing levels of controllable factors (or parameters) that make the system less sensitive (or robust) to changes in a set of uncontrollable factors. The simplest of Response Surface Equations (RSE) is a quadratic equation based on Taylor series approximation,

$$y = \beta_0 + \sum_{i=1}^{k} \beta_i x_i + \sum_{i=1}^{k} \beta_{ii} x_i^2 + \sum_{i=1}^{(k-1)} \sum_{j=i+1}^{k} \beta_{ij} x_i x_j + \varepsilon .$$

It is a multiple linear regression model with k –regressor variables. The Goodness of Fit procedures in statistics are used to test the surrogate model so obtained. Since these equations take much less computation time than the detailed physics-based model, probabilistic analyses of the system can be done relatively quickly.

Second -order model is used for RSM widely because it is very flexible as it can take a wide variety of functional forms and so it often works well as an approximation to the true response surface [9]. Both control and noise variables are considered in the same equation. The method of least squares is used to estimate the parameters. The errors are uncorrelated random variables. JMP software [10] from SAS (Statistical Analysis Software) [11] is used to create DOE and develop RSM models in Chapter 4 and Chapter 6.

3.3. MATLAB for hybrid system model

The vehicle level hybrid system model described in Chapter 4 comprising fuel cell, battery, DC/DC converter, power sharing algorithm is written in MATLAB. The overall code is written as an M-file function.

3.4. Powertrain Systems Analysis Toolkit (PSAT)

This is a forward-looking modeling and simulation tool developed at Argonne National Laboratory to meet the requirements of automotive engineering throughout the development process. It is used to analyze fuel economy, performance, comparison of component technologies, analyze transmission ratios, impact of drive cycle, component sizing, development of control strategies, comparison of drivetrain configurations, validation of models and analysis of test data. PSAT is used in Chapter 6.

3.5. Experimental Techniques

Experimental techniques such as galvanostatic charge-discharge, self-discharge have been used to study lithium ion batteries in this work. The testing equipment and a short description of the lithium-ion batteries that were tested are provided in the next section.

3.5.1. Galvanostatic charge-discharge

This technique is used to do capacity check, cycling and rate capability studies in lithium ion batteries in this work. Constant Current-Constant Voltage (CC-CV) is the protocol used to charge the cells. Under this protocol, the cell is charged at constant current until a set upper potential is reached. It is then held at that potential until the current tapers to few millamperes. The cell is subsequently discharged at constant current to a pre-determined cut-off potential. The Arbin battery cycler described below is used for these tests.

3.5.2. Self-discharge

In this technique, the cell is left at open circuit at a certain state of charge for desired number of hours. The observed decrease in potential as a function of time is the self-discharge occurring in the system at given conditions.

3.6. Equipments and Lithium-ion Cells

3.6.1. Arbin Battery Cycler

The system used to collect data for Chapter 5 consists of a test stand with multiple output channels, a Windows NT™ software application, and one or more custom I/O cards for the PC running the application. There are eight channels , four of which are capable of testing up to a maximum of 25 A and the other four up to a maximum of 1 A. Temperature control is possible.

The eight temperature channels can be assigned to the desired voltage/current channels for temperature measurements during battery testing. The Red LED, when on, indicates that the corresponding test channel is in use. When it is not glowing, it implies either no test is conducted or open circuit step is in progress. Figure 3.1 shows the Arbin battery cycler. The Arbin Battery Test System (ABTS) is designed with a convenient, user-friendly software interface. This is an advanced system that features many helpful functions for battery research and testing. All major system functions are defined, controlled and monitored through this Microsoft Windows NT™ interface. The ABTS software enables a battery test engineer to program multiple custom test schedules that can be applied concurrently to different batteries, and provides the means to acquire and analyze the test results automatically. The Arbin cycler that is used to collect experimental data for Chapter 6 is the newer version called BT2000 with MITSPRO testing software.

3.6.2. Lithium ion cells

Figure 3.2 shows a single LM4 GS-Yuasa 4 Ahr lithium ion cell. This rechargeable cell is packed in a prismatic pouch. The case is made of aluminum and resin laminated film. The nominal voltage is 3.8 V. The outer dimensions (except the length of the terminals) are 115 × 65 × 11.3 mm. The weight of the single cell is about 132 g. The positive terminal is aluminum and negative terminal is nickel. The positive and negative electrodes are metallic oxides and carbon respectively. This cell is mainly used for experiments in Chapter 5. Other lithium ion cells that were used in Chapter 6 include K2 and Valence cells with 3.2 Ah and 1.1 Ah nominal capacities respectively.

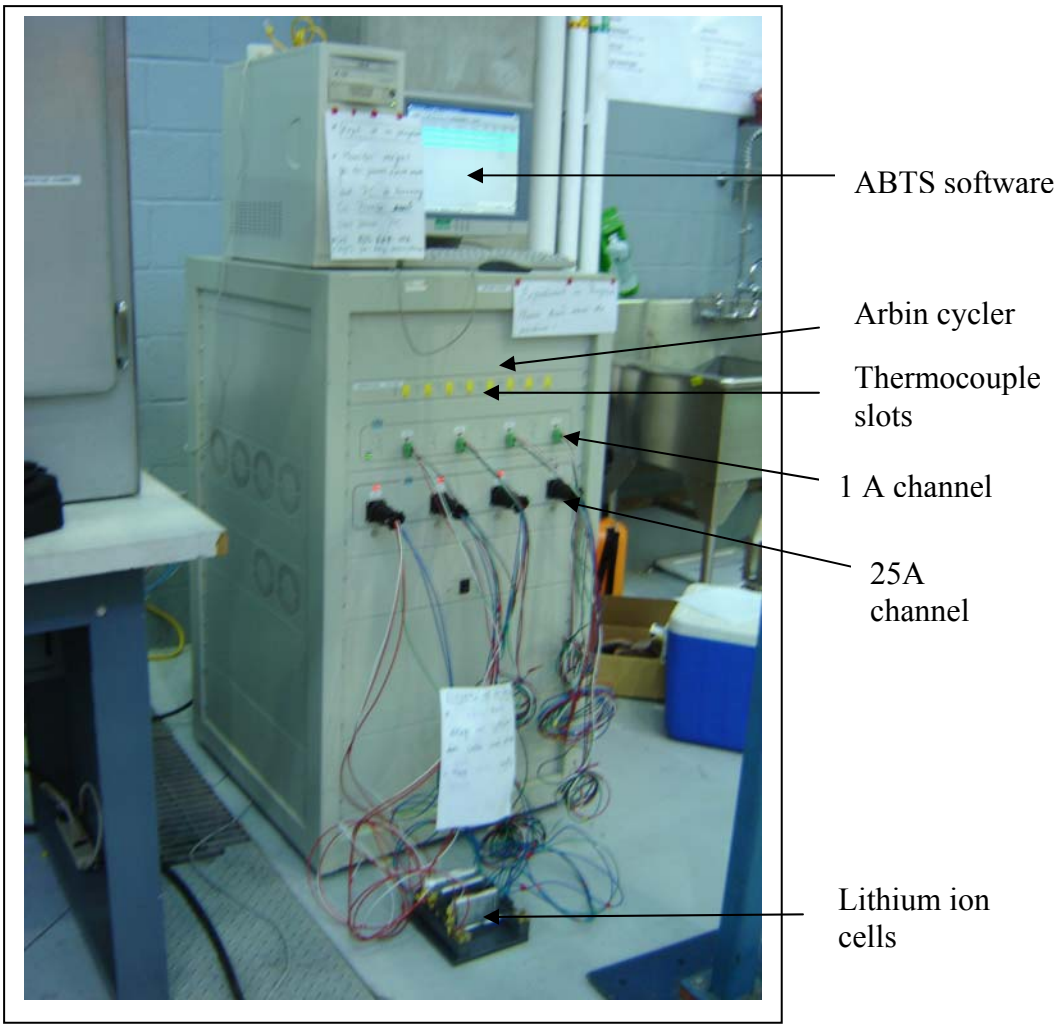

Figure 3.1. Arbin Battery Cycler Model BT-2043.

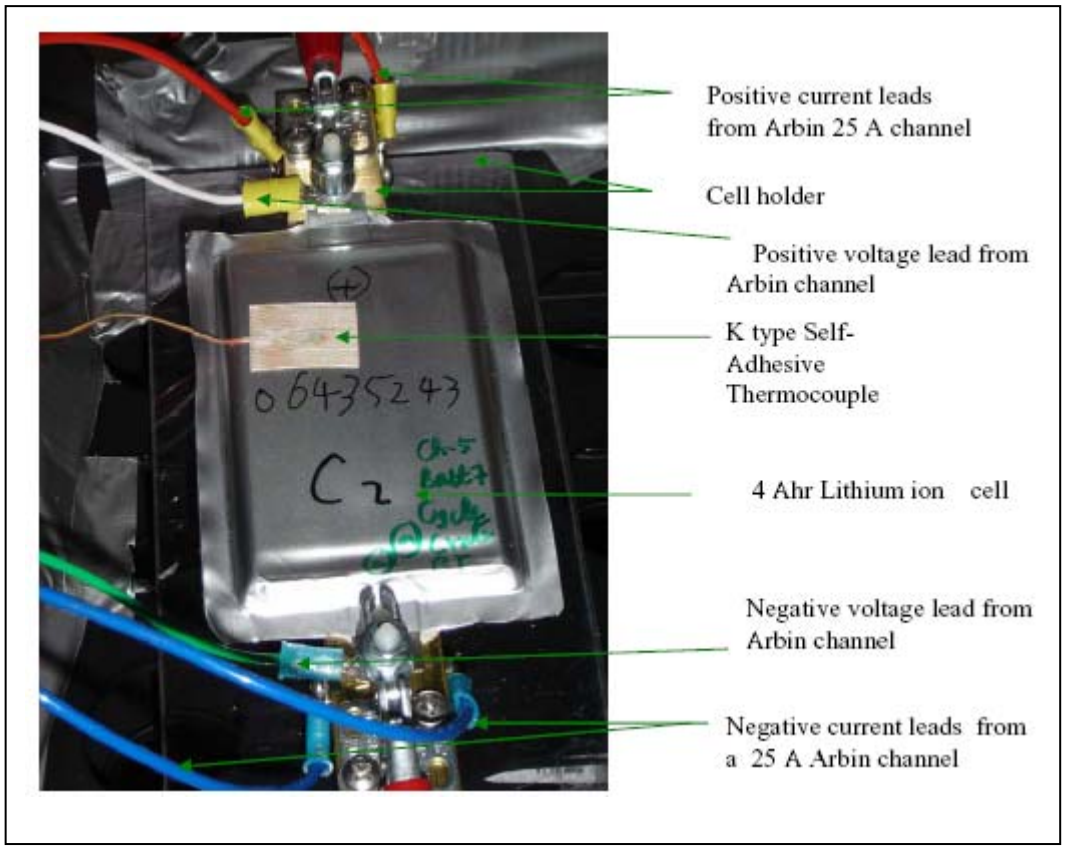

Figure 3.2. GS Yuasa 4 Ahr Lithium Ion Cell.

Figure 3.3. K2 and Valence cells with 3.2 Ah and 1.1 Ah nominal capacities respectively.

3.7. References

[1] Dimitri N. Mavris, Oliver Bandte, AIAA and SAE, 1997 World Aviation Congress, Anaheim, CA; UNITED STATES; 13-16 Oct. 1997.

[2] Derringer, G.C. and Suich, R, *J.Quality Technology*,12 (1980),214-219.

[3] Raymond H. Myers, Douglas C. Montgomery, G.Geoffrey Vining, Connie M. Borror, Scott M. Kowalski, *J.Quality Technology*, 36(1) (2004), 53-77.

[4] Box, G.E.P and Wilson, K.B. *J.Royal Statistical Society B*, 13(1951), 335-341.

[5] Raymond H. Myers, Douglas. C. Montgomery, Response Surface Methodology, Second Ed., Wiley, New York, 2002, pp. 1.

[6] Pankaj Arora, Ralph White, *J.Electrochem.Soc.*, 145 (10) (1998), 3647-3667.

[7] Wu Bi, Thomas F. Fuller, *J.Power Sources*, 178(1) (2008),188-196.

[8] Norimitsu Takeuchi, T. F. Fuller, *J. Electrochem. Soc.,* 157 (2010), B135-B140.

[9] Response Surface Methodology, Process and Product Optimization Using Design of Experiments, Raymond H. Myers, Douglas C.Montgomery, Wiley Series in Probablity and Statistics.

[10] http://www.jmp.com/

[11] http://www.sas.com/

CHAPTER 4

ROBUST DESIGN OF BATTERY/FUEL CELL HYBRID SYSTEMS METHODOLOGY FOR SURROGATE MODELS OF PT STABILITY AND MITIGATION THROUGH SYSTEM CONTROLS

4.1. Introduction

With increasing interest in energy storage and conversion devices for automobile applications, such as rechargeable batteries, proton exchange membrane fuel cells (PEMFCs) and super capacitors, the necessity to understand and predict not just their initial performance but their life behavior is paramount. A system model elucidates the interactions between components, and enables the response of the system as a whole to changing load demands to be determined. However, system models that are available in the literature predict just the performance and do not include the durability and degradation phenomena associated with both fuel cells and batteries.

As illustrated by two recent articles on hybrid vehicles systems, the foremost design goal has been minimizing fuel consumption [1], [2]. To their credit, these investigators recognized that multiple objectives must be considered for a robust design. Furthermore, Kim and Peng highlight that the components of the system must be evaluated and the control strategy scrutinized simultaneously. What's missing is any consideration of the durability of the electrochemical devices. Their life and the associated failure mechanisms are strongly dependent on the architecture, load profile, and control strategies.

Furthermore, although efficiency is an important design objective, the small increases in efficiency that are envisaged will have little effect on the commercialization of these fuel-cell

hybrid systems. In fact, independent "wells to wheels" analysis by Toyota and Argonne National Laboratory have underscored that efficiency for these systems is only slightly better than an internal combustion engine hybrid. The greater impetus for hydrogen fuel-cells hybrids, plug-in hybrids, or all electric vehicles will be the elimination of the source of carbon dioxide emission from the vehicle. Therefore, reducing the life-cycle cost of the electrochemical storage and conversion devices is the primary technical barrier; and one of the best ways to attack the cost is to improve durability.

Traditionally, durability is not considered in detail until well into the design process. As a result it is usually too late to account for these phenomena in the design optimization. The flaws in this approach are acknowledged, but there is no established methodology to treat durability of the electrochemical systems in the conceptual design phase in anything more than a superficial manner. This research seeks to change fundamentally this pattern—in short, to develop a framework that allows life or durability constraints of the electrochemical components to be traded against other design objectives, such as weight, efficiency and cost early in the design phase. Similarly, approaches to infuse knowledge about new technologies early in the design phase have been described by Mavris *et al.* [3]. There are three required elements: 1) development of scalable subsystem models, 2) establishment of framework for design optimization, and 3) creation of surrogate models for degradation phenomena from the detailed physics based models.

A framework is provided in this chapter that allows designers to explore how changes in hybrid control strategies, system architecture, power management approaches and degree of hybridization impact the degradation of the electrochemical devices. Hence, a robust design methodology allows broader exploration of the design space to arrive at a trade-off between

performance metrics—such as hydrogen used, specific energy/specific power, efficiency, cost, size, weight and degradation challenges. To illustrate the methodology, one specific degradation phenomena is considered: platinum stability. For a given driving schedule, the effects of changes in the power sharing between the battery and fuel cell on hydrogen consumption and platinum stability are presented.

4.2. Baseline Fuel Cell-Battery Hybrid Vehicle Model Description

4.2.1. Vehicle Model

The hybrid system conceptualized for this study is shown in Figure 4.1a and is comprised of the following subsystems: PEM fuel cell, Li-ion battery pack, DC/DC converter, and power management. A vehicle model (Appendix A.1) is used to determine the power required to supply the accessories and the electric motor drives, but these devices are not part of the model. In brief, from a prescribed driving schedule, speed *vs.* time, the net power to overcome rolling resistance & aerodynamic drag, accelerate the vehicle, and supply accessories is calculated.

(a)

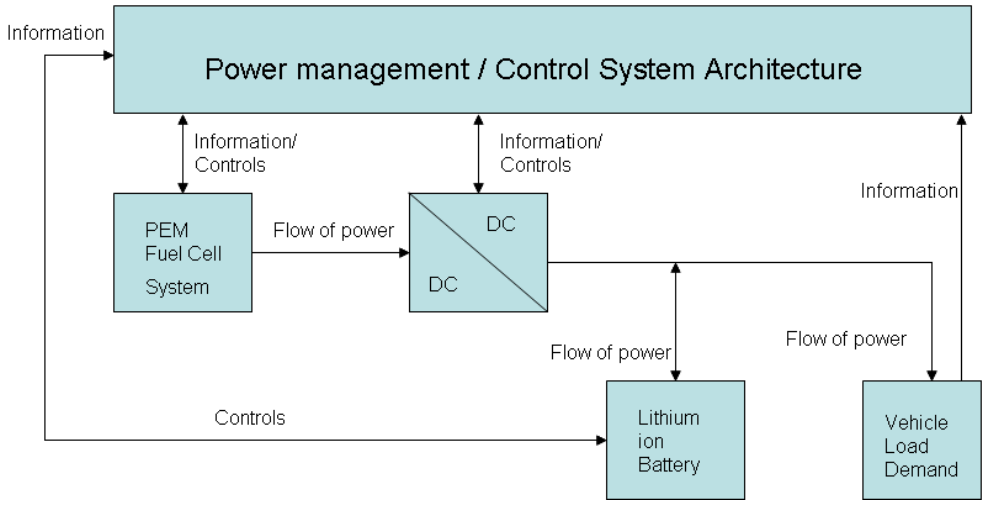

Figure 4.1. a) Structure of the hybrid system b) Reasonable States.

(b)

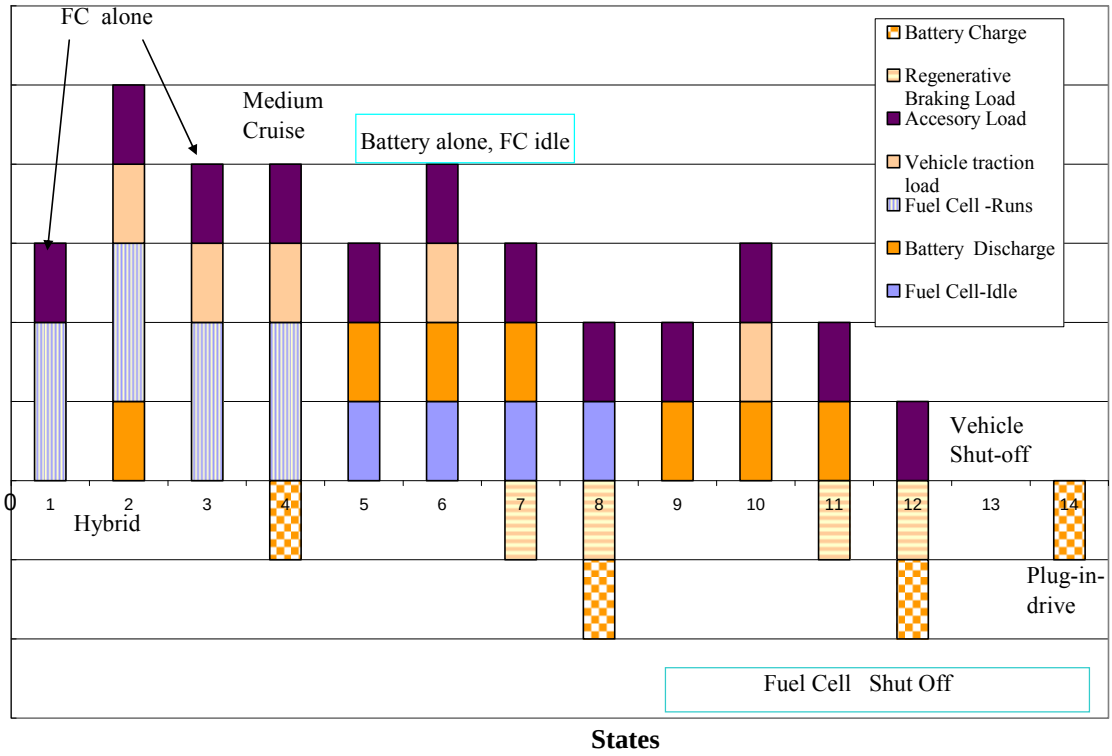

Figure 4.1. continued

4.2.2. Fuel Cell Model

The empirical fuel-cell performance model [4] used in this work is that of Kim *et al.*;

$$E = E_o - b\ln i - Ri - m\exp\{ni\} \quad (1)$$

This empirical equation has been fitted to experimental data from our research group that are more representative of typical fuel cell performance. The corresponding parameters used in this study are provided in Table 4.1. Future work will provide these parameters as a function of temperature and reactant pressures. Appendix A.2 gives fuel-cell system design specifications.

A fuel-cell subsystem, consists of an air compressor, humidifier, radiator and hydrogen tanks and is required to supply reactants and control the temperature of the cell stack. The

subsystem requires electrical power for its operation, which is usually provided by the fuel-cell system itself. The presence of these subsystems also implies additional mass and consequently less specific energy of the fuel cell system. Whereas the mass of the subsystem is included, their impact on system efficiency is not accounted for here. A constant accessory power level has been assumed. Hydrogen utilization is assumed to be constant (90%) when calculating the hydrogen used under given driving conditions, and it acts simply as a scaling factor (see Appendix A.2). The fuel-cell system efficiency, thus, in the present model is a function of the potential of the fuel cell only.

4.2.3. Battery Model

Fellner and Newman's [5] simplified battery model is used. It assumes that the system is ohmically limited, resulting in a linear relationship between the over potential and the current segment. This is a reasonable assumption for hybrid vehicle system where

Table 4.1. Parameters for the PEMFC empirical equation

Parameters	**Units**	**Value**
E_0	mV	1128.4602
R	Ohm*cm^2	0.0692
b	mV	61.1344
m	mV	7.6401
n	cm ^{2}/mA	0.0003

short current pulses are demanded; but as the reliance on the battery increases, this assumption is less appropriate. The capacity of each electrode is updated using Faraday's law.

It is understood that the battery will have an effective thermal management system and this is not dealt with in detail in this study. In the present work, the open-circuit potential as a function of state of charge for the $LiMn_2O_4$ (positive) [6] and carbon (negative) [7] electrodes are estimated from the literature.

Depending on the power demanded, the state of charge (SOC) of the battery, and the power management algorithm (including voltage restrictions), the response of the battery is determined. The charging rate is limited to the C rate. Though the chances of the battery going to constant-voltage charge mode may be small in hybrid operation due to continuous change in power demanded, the model still allows for constant voltage (CV) charging when required.

The SOC can be estimated by counting the coulombs passed (current and time) or from the open-circuit potential, whereas the model needs individual intercalation co-efficients to determine the limiting electrode to calculate the overall capacity of the battery at each time step. For the present study, the battery consisted of 25 Ah lithium ion cells connected in series. Appendix A.3 provides the battery design specifications and model equations including the conversion of SOC to the individual electrode intercalation co-efficients and vice versa. SOC is difficult to determine accurately in the vehicle and is a source of uncertainty. The surrogate model methodology described in this work can be used to arrive at a robust design that is less sensitive to this uncertainty.

4.2.4. DC/DC Converter Model

The DC/DC converter efficiency is the ratio of output power to input power. A sixth order polynomial equation was fitted in this proposed work for the DC/DC converter performance curve obtained experimentally by Pei *et al*. [8] and used in this system model. This is provided in Appendix A.4.

4.2.5. Power Sharing Algorithm of the Baseline Model

In order to develop a power management algorithm, the different conditions of the individual components have to be identified. These conditions then determine the possible states of the hybrid system. The major components and the conditions considered for the algorithm are shown in Table 4.2. Of the 54 permutations, just 14 reasonable states emerged as shown in Figure 4.1b. For instance, a situation that simultaneously uses the fuel cell and regenerative braking to charge the battery is not considered. It is assumed that whenever the vehicle is on, there is some nonzero net load, *i.e.,* the accessories load is always required.

The transition between these different states in the power sharing algorithm is based on the traction load power demand, accessories power demand, battery state of charge and voltage

Table 4.2. Different possible condition of the individual components

Battery	**Fuel Cell**	**Traction Load**	**Accessory Load**
Charge	Runs	Traction	On
Idle	Idle	Zero	Off
Discharge	Off	Regenerative Braking	

limits, and the rated fuel cell power (maximum power from the fuel cell) as well as the minimum power permitted. This minimum fuel-cell power is established as that power below which leads to an unacceptably low fuel-cell system efficiency. As will be demonstrated later, there is another perspective to consider when establishing this minimum power. As we operate the fuel cell at lower current densities, the corresponding potential of the fuel cell will increase and

approach the open-circuit value. This higher potential will accelerate platinum catalyst dissolution and carbon catalyst support corrosion in the fuel cell stack.

The power sharing algorithm is developed for three cases.

- Traction power demand is greater than or equal to zero and accessories power demand is positive
- Traction load is negative and accessories power demand is positive
- Both the traction and accessories power demand is zero.

As seen from Table 4.2, the above cases arise from the reasonable combination of the individual conditions of traction load and accessories load.

In the first case, both the fuel cell and the battery provide power, and the balance between them depends on the SOC of the battery. Whereas in the next case, if its SOC is low, the battery is charged with power from regenerative braking. The third case corresponds to when the vehicle power demand is zero, and so it is either at a standstill—where all energy sources are shut-off—or using the plug-in-drive mode, where the battery is getting charged from an external source. For the baseline model, a constant positive accessories load demand is assumed. The power sharing algorithm for this case is given in Appendix A.5.

4.2.6. Influence of Control Algorithms

The control algorithm establishes the power sharing between the fuel cell and battery and also influences their life-times. The effect on the fuel-cell catalyst stability is addressed in this work—future work will investigate other fuel cell and battery degradation mechanisms.

When the power demanded by the vehicle from the fuel cell is zero, the fuel cell can be put in a variety of conditions, such as 1) at open circuit with reactants still provided (idling), 2) operating to supply just enough power for the balance of plant (BoP), 3) completely shut-off,

including BoP components, or 4) an off state where some of the BoP components are turned off and the others are powered from the battery. This choice would in turn determine the potential window of the fuel cell cycling and thus affect the degradation phenomena in the fuel cell.

The upper fuel cell voltage limit determines the lower power limit for the fuel cell operation. The upper fuel cell voltage could be set at different levels, for example, 0.8 or 0.9 or 1 V. The lower limit of fuel cell potential is set such that mass transfer losses are minimized by avoiding excursions to higher current densities. Under the present control strategy, the higher the upper voltage limit of the fuel cell, the higher the rate of platinum catalyst degradation. If the upper voltage limit is lowered, the fuel cell would be operating less efficiently and negate one of its key advantages. First the results from the baseline model are presented, and then in section 1.4 the influence of control algorithm on fuel cell durability and hydrogen consumption are discussed.

4.3. Baseline model results

4.3.1. Vehicle Model

Baseline results are developed for a fuel cell rated at 90 kW and a 20 kW battery. Thus, the maximum power for the vehicle is 110 kW. The battery consists of 53 lithium ion cells of 25 Ahr connected in series. The mass of each lithium-ion cell is 0.908 kg. The voltage range of the battery pack is 146-217 V, and that of the fuel stack is 214-427 V. The total power demanded based on the Federal Test Procedure (FTP) driving cycle [9] is computed from the vehicle model. This FTP was intended to represent typical driving patterns in primarily urban areas. The simulation was done for 5624 seconds, which is the time required for going through the FTP cycle thrice, and thus ensures that there is sufficient time for noticeable initial rates of degradation in the cell stack to be established. Figure 4.2a shows the vehicle load demand for a

portion of the schedule for better readability. The power profile is lower than 110 kW range because of the relatively mild driving conditions.

4.3.2. Power Sharing

Figure 4.2b shows the voltage profile of a single fuel cell for the baseline control algorithm. Figure 4.2c shows the corresponding battery power. Due to mild driving conditions, initial SOC of the battery chosen for this simulation (0.8), and the control algorithm, the battery predominantly gets charged, which is evident from the SOC profile seen in Figure 4.2d. The initial SOC of the battery was chosen as 0.8 because it is reasonable to assume that the battery is left at a SOC that is sufficiently high to allow hybrid drive conditions even early in the driving schedule. The control algorithm can handle any SOC value as input parameter; however, choosing a value of 0.8 resulted in a negligible change in the SOC over the selected driving schedule, thus simplifying the efficiency comparisons between control strategies. But in the long run, the chosen power management strategy will decide if a net neutral SOC is obtained. Also if the initial SOC chosen is different, then again net neutral SOC need not be obtained. In these cases, adjustments will have to be made to account for the net change in SOC before proceeding to compare between different control strategies. The potential of the lithium ion cell, seen in Figure 4.2e (for the entire time span), is obtained from the difference between the open circuit potential and the over potential of the battery.

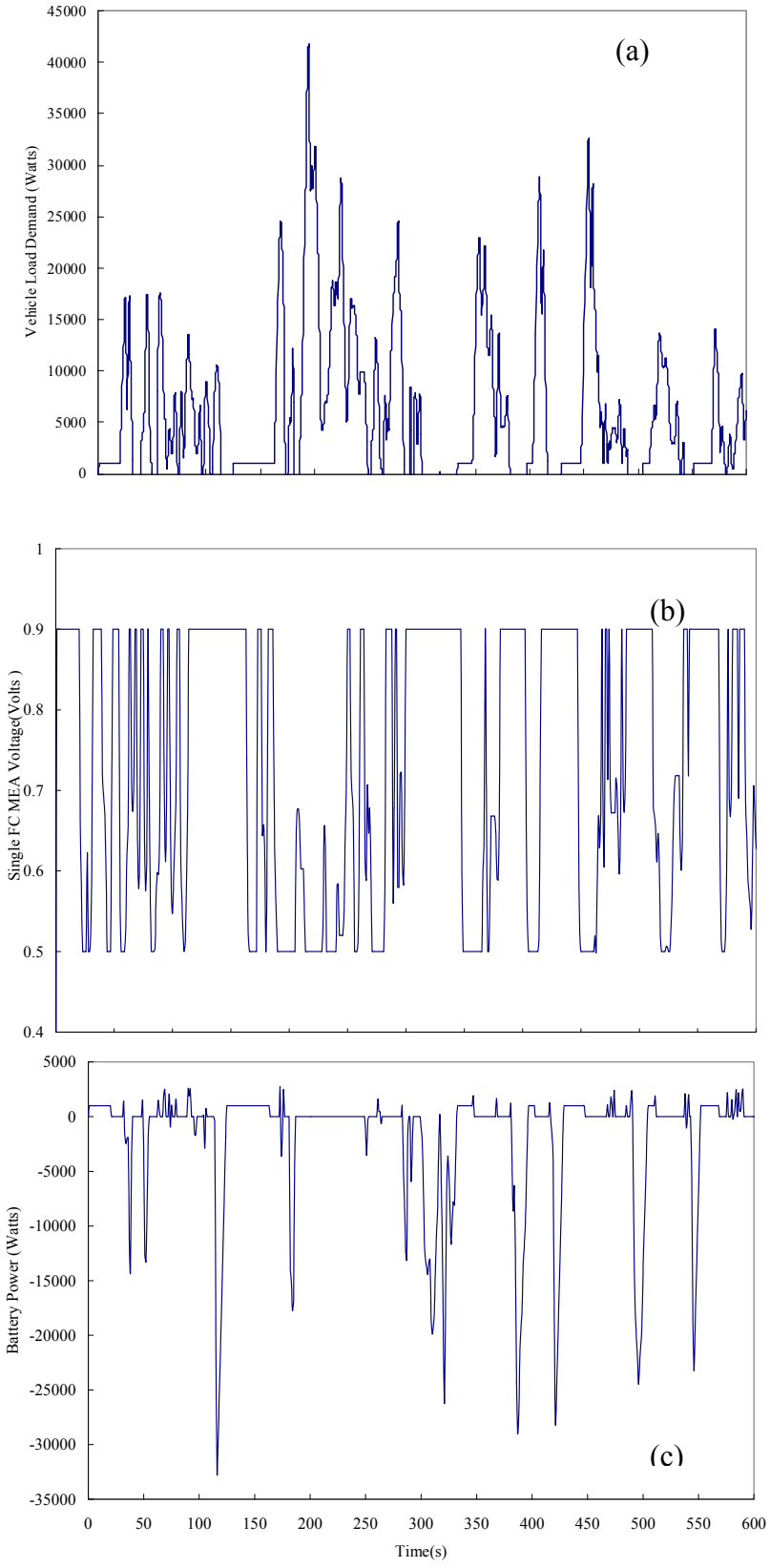

Figure 4.2. Baseline Model Results.

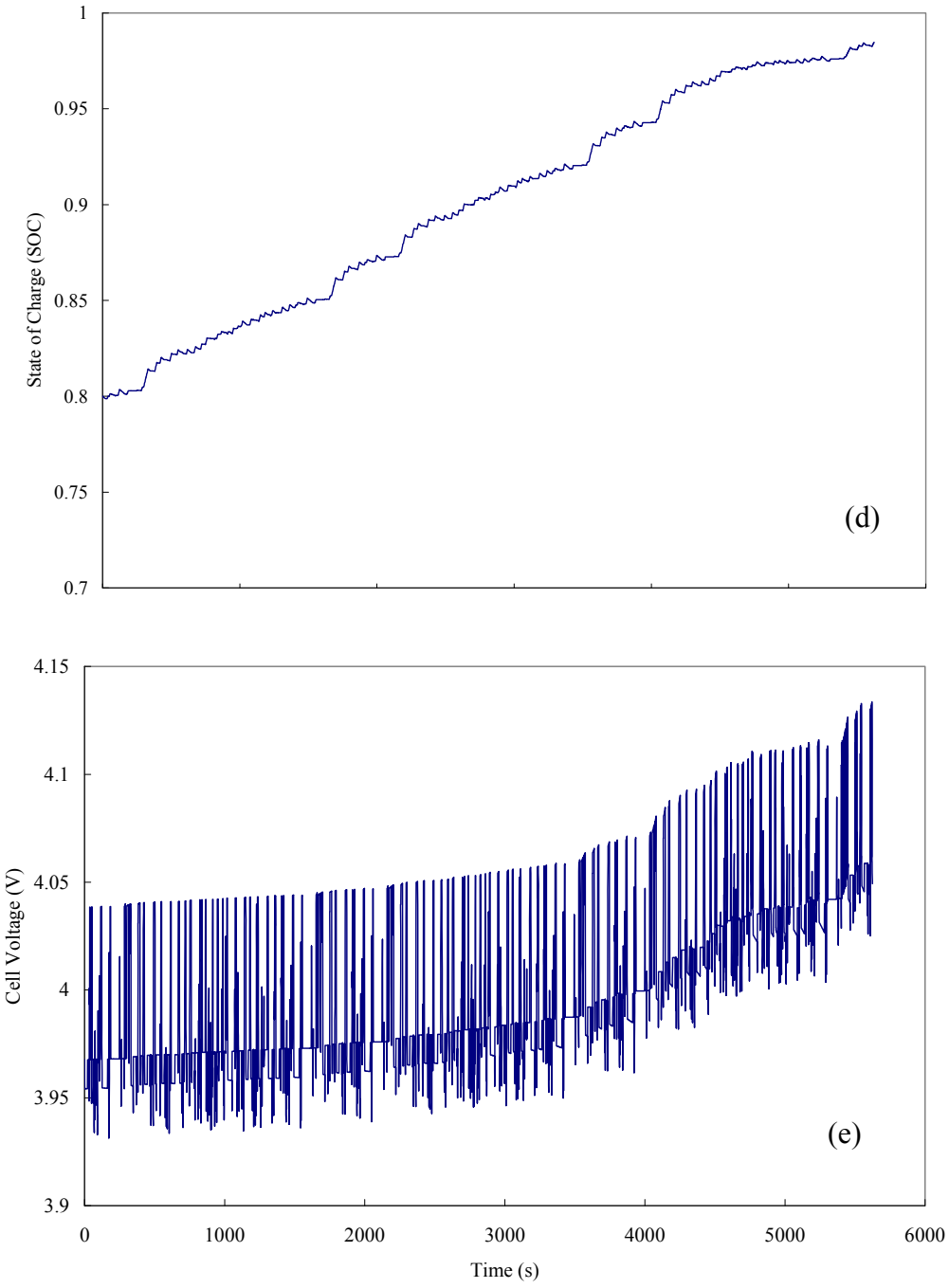

Figure 4.2. continued

4.4. Proof of concept for the need for robust design

To understand better how different power management algorithms affect efficiency and durability, the allowed upper potential of the fuel cell was varied. The responses (loss terms) vs.

hydrogen used (kg) for the prescribed driving schedule are plotted in Figure 4.3.The Pt surface area loss rate and the radius growth rate shown in the figure are simply the net change in the variable divided by the elapsed time. Pt mass loss rate is further normalized with respect to the MEA area. Figure 4.3 shows that as the upper potential is lowered, the hydrogen required increases (because of lower fuel-cell efficiency). At the same time, the rate of Pt degradation is reduced dramatically. If one were to extrapolate the results for a 5000 hr driving cycle, it is observed that Pt surface area loss is the dominant issue in catalyst durability. For the case with fuel cell upper potential of 0.9 V, extrapolation to 5000 hours is not meaningful, and longer simulations would be required to account for the fact that the rate of surface area loss will decrease over time. For the ranges of upper potential examined, there is an imperceptible Pt mass loss. It is expected that if start-stop losses were also treated, or if the upper potential were raised further, platinum mass loss from the electrode would be significant. Most important, these results provide the framework to make trade-offs between performance and durability. They signify the need to have robust design methodologies as part of degradation mitigation efforts in the early design phases.

Under the prescribed driving conditions, the battery is not exerted much, and there is a net increase in SOC. The percent of the net energy that goes to charge the battery is about 1.6 % of the total energy provided by the fuel cell. Thus, it is justified not to make any adjustment for changes in SOC when calculating hydrogen used for this preliminary analysis. If the parasitic power to operate ancillary devices in the fuel cell system and variations in utilization of hydrogen with power level are included, the increase in hydrogen consumption will be diminished as the upper-potential limit is lowered. This affirms that power management

strategies and control strategies in the hybrid systems can be used to arrive at a trade-off between performance and degradation. Surrogate Models are key enablers for this vision.

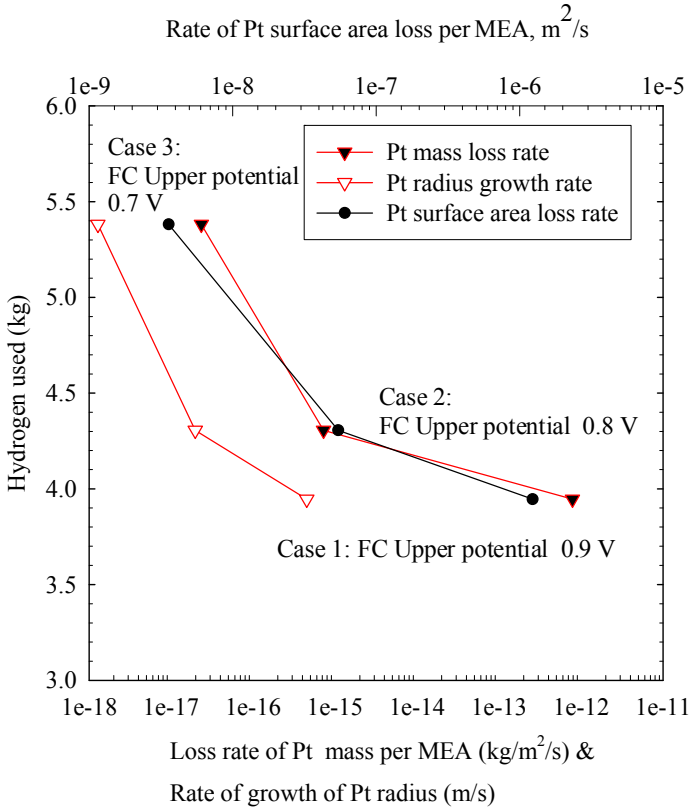

Figure 4.3. Pt stability in PEMFC *vs.* Hydrogen used (kg) [10].

4.5. Response Surface Methodology (RSM) for surrogate life model of PEMFC

4.5.1. Need for RSM for fuel cell and battery life models

Present hybrid system models do not capture degradation phenomena associated with batteries and fuel cells. This is partly because a framework does not exist to make quantitative trades between life time issues, performance, and cost in the conceptual and preliminary design phases. This can lead to designing the system principally focused on performance and capital cost. What's more, when efforts are made to incorporate life issues in system design at later

stages, it actually becomes difficult to make large changes. Re-designing at this stage would require lots of effort in terms of time and cost. Neglect of life-time issues is also undesirable because of the costs associated with the loss of costly materials like Pt catalyst, Nafion® membrane in PEMFCs or those of lithium ion cell components. Moreover, system models without the incorporation of life models can lead to over prediction of performance in real time, which also creates safety concerns in case of an unexpected, early failure. Hence, it is paramount that life models are incorporated in hybrid system models. But detailed physics-based models are difficult to integrate with higher level system models, both in terms of different languages in which they are coded and also the variation in complexity levels. Another disadvantage is that complex physics-based life models require larger computation time. Hence, simpler life models are desired that can be integrated in hybrid system model without losing much of the fidelity of the original physics-based models.

Surrogate models are a step in this direction. These models are important in the robust design strategy wherein the response of the system can be made less sensitive to noise factors. Response Surface Methodology (RSM) is the tool used for this purpose. So far, surrogate models have been used for PEMFC performance [11] and compressor characteristics, [12] but not for degradation and durability phenomena in electrochemical energy storage and conversion devices. Moreover, the surrogate models developed by Tirnovan *et al.* are derived from experimental data and not from physics based models. Though experimental data averts the need for the assumptions made with physics-based models, data derived from physics-based models are a necessity in situations where sufficient historical (or experimental) data are not available.

4.5.2. Application of RSM to Pt catalyst dissolution

Among the degradation processes in PEMFCs, platinum catalyst dissolution and degradation is a major cause of loss of fuel-cell performance. Driving conditions such as idling (which results in the operation of PEMFCs at high potentials), city driving (which results in frequent potential cycles), or frequent starting and stopping of the fuel cell accelerate the Pt catalyst degradation processes. Hence, an effort is being made to develop surrogate model for Pt catalyst dissolution process.

Two variables that can be set in the control architecture are the upper and lower potential limits of the fuel cell. Other variables, such as the durations of the time step, and number of cycles (these variables define the driving schedule) are not known *a priori* and are in the hands of the driver. Additional variables, such as the particle size of the platinum catalyst, will have a distribution of values from the manufacturing processes. If the number of variables is large, a 2-level design of experiments is typically done to perform a screening analysis. The variables that have the most influence are then used to create RSEs.

In this initial study, just four variables are considered: upper and lower potential limits for the fuel cell, the number of cycles, and the time step. A square wave potential was used to generate the responses from the detailed physics-based model for platinum catalyst dissolution developed by Bi and Fuller [13]. Hence, the potential step in this case is simply the difference between the upper and lower fuel-cell potential. The responses from the model are the rates of platinum mass loss from the catalyst, reduction in electrochemical surface area, and growth in particle radii.

The upper and lower levels of each of the four variables were chosen as given in Table 4.3. Central Composite Design (CCD) of Experiments was chosen to select the different cases to

be run in the detailed model and obtain responses. Quadratic RSEs were created for each of the responses with the data obtained. A total of 32 "experiments" were run (27 cases were derived from Central Composite Design of Experiments and 5 extra cases were run using a time step of 25 seconds instead of the mid level of 35 seconds). The extra cases can not only help us increase the fidelity of the model but also lessen high correlation between independent variables when certain cases (outliers) have to be deleted. For the two cases with 200 cycles and 60 s time step, the physics-based model did not give any responses. The reason is that, in the physics based model with a bi-modal particle size distribution, as small particles dissolved, their radius became vanishingly small. The associated shift in equilibrium potential with radius was so large that the particle surface completely oxidized before the completion of the simulation for these two cases [13] .It is acknowledged that the effect of creating the RSEs with less than two cases as required by CCD design will lead to some correlation between the independent variables. In this instance, we believe that the underlying physics-based model requires improvement, which is an on-going effort, and not a failing in the methodology proposed here.

Table 4.3. Independent variables and the corresponding levels chosen for the surrogate model development

Variables	Upper Level	Middle Level	Lower level
Upper potential (V)	1	0.9	0.8
Lower potential (V)	0.7	0.6	0.5
Number of cycles	200	150	100
Time step (s)	60	35	10

4.5.3. Goodness of Fit Tests

Since each response varied amongst different cases by orders of magnitudes, the responses were transformed from ‘y’ to ‘exp (y)’ before the RSEs were created. Moreover, the potential term in the Butler-Volmer equation highlights the exponential dependence of the Pt catalyst dissolution process in PEMFCs on cell potential. Hence, RSEs for the transformed metrics as a function of lower potential, number of cycles, time step and exponential of upper potential were obtained with R^2 >0.9. The residual *vs*. predicted is shown in Figure 4.4. The scale of magnitude of the error is less than 2.5 % of the predicted value for each of these responses, and the error distribution does not show any distinguishable pattern. However, the error distribution plot for the data points used for the development of RSEs, called the Model Fit Distribution (MFE), and the error distribution plot for the validation points (data points not used for surrogate model) showed high standard deviations and error ranges. Data points that cause a large variance, called outliers, were deleted. Ideally, no more than 7-8 % outliers should be deleted to minimize correlation between the independent variables. In the present results, 10 % of the outliers were deleted to reduce the error distribution. These indicate that the present surrogate model cannot fully replicate the dissolution process. Nonetheless, the framework is established for a PEMFC life surrogate model. One could observe data clumping in actual *vs*. predicted plot as seen in Figure 4.5. Data clumping usually means that at the current settings, a single variable is primarily driving the response.

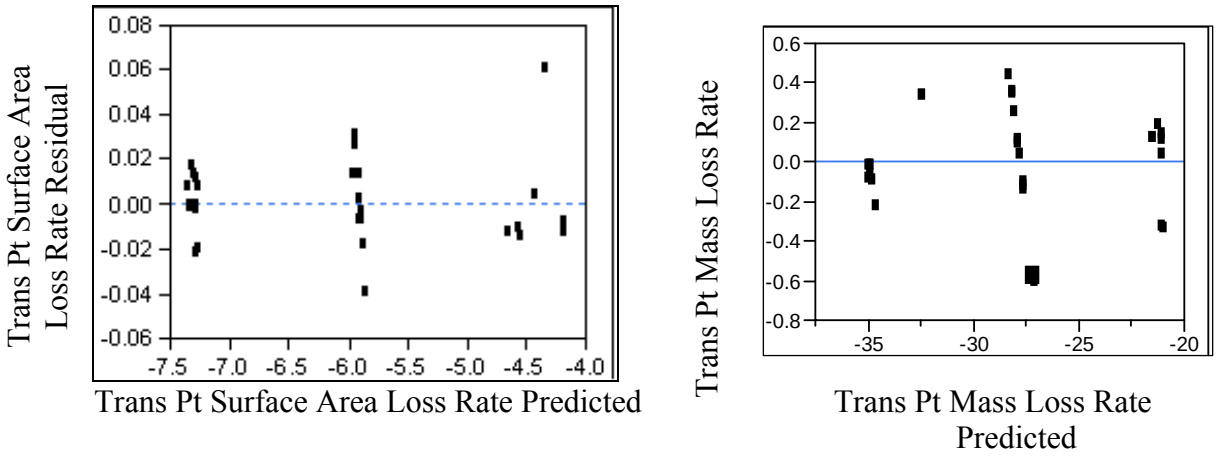

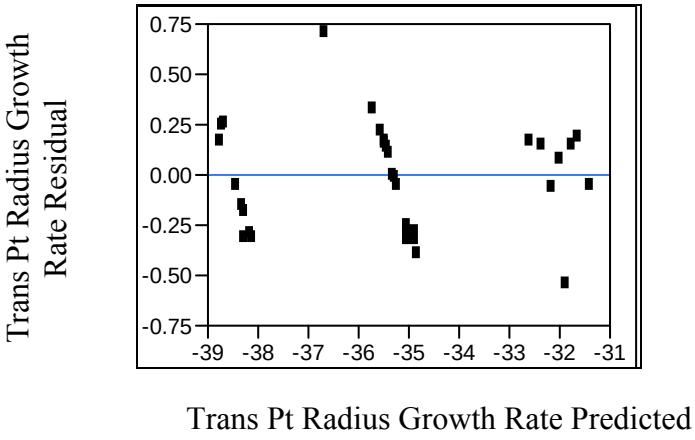

Figure 4.4. Residual *vs.* Predicted.

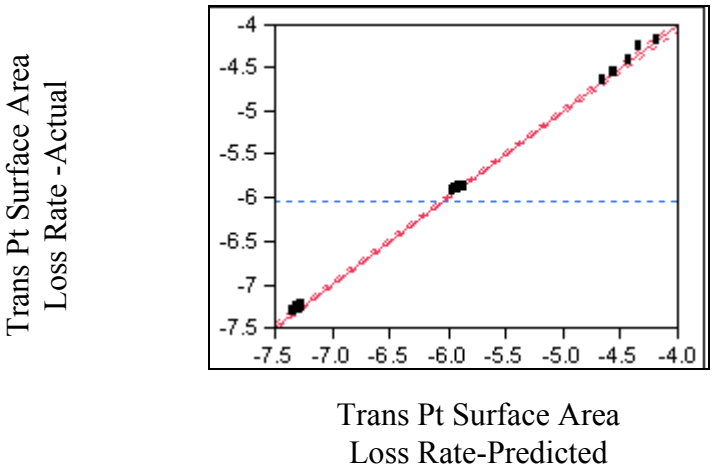

Figure 4.5. Actual *vs.* Predicted Plot.

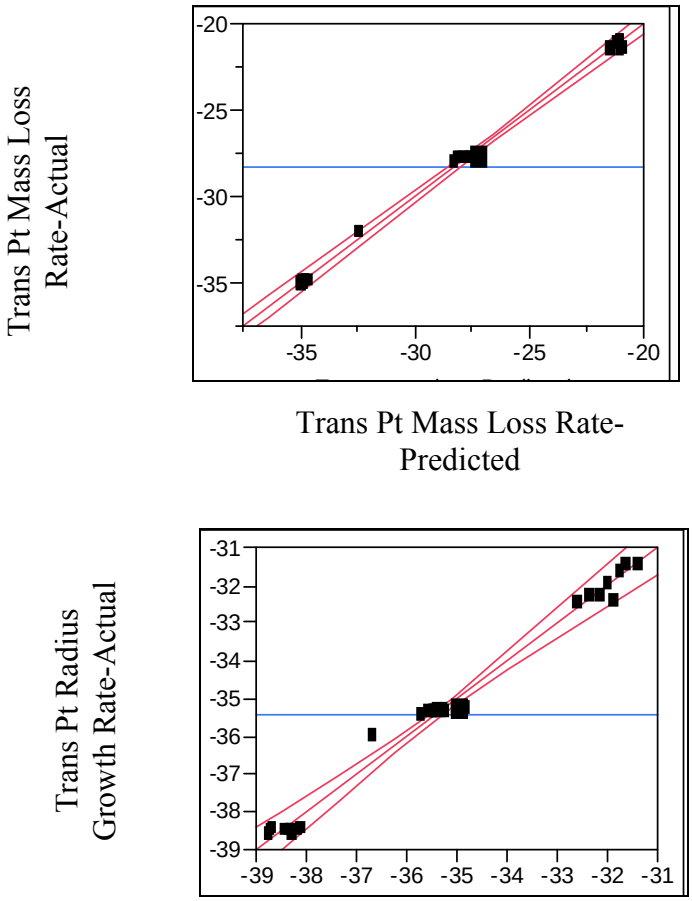

Figure 4.5. continued

4.5.4. Pareto Plots and Scatter Plot Matrix

To further analyze the sensitivity of the variability in response metrics to the independent factors, Pareto plots for all responses (Figure 4.6) were created. The larger the value, the greater the sensitivity of the results to that variable. These plots show that the "upper potential" contributes to more than 60 % of the variability in the Pt catalyst dissolution responses in PEMFCs. Figure 4.7 shows the scatter plot matrix between the independent variables and the metrics for the Pt catalyst dissolution process. The density ellipses for the metrics as a function of the upper potential, and also the random scatter of the data points for the metrics with respect

to time step, number of cycles and lower potential also re-emphasize the dominant role of upper potential in the durability of PEMFC catalysts. These indicate that controlling the upper potential of the fuel cell in the hybrid system power management and control architecture is a positive direction towards addressing durability issues in PEMFC. The durability of the fuel-cell system may be improved by using fuel cell as principally a battery charger or range extender, and thus operating it only at relatively low potentials with a reduced number of starts and stops. Better RSEs will be developed in future to arrive at a robust design such that the degradation issues are made less sensitive to the uncertainties (not known *a priori*) associated with driving cycle such as time steps, number of cycles and potential steps and also to the variation in particle size distributions of the platinum catalyst particles. This work provided the framework for analysis, but other degradations mechanism for fuel cell durability, and cycle and calendar life of the battery pack will be included in future work.

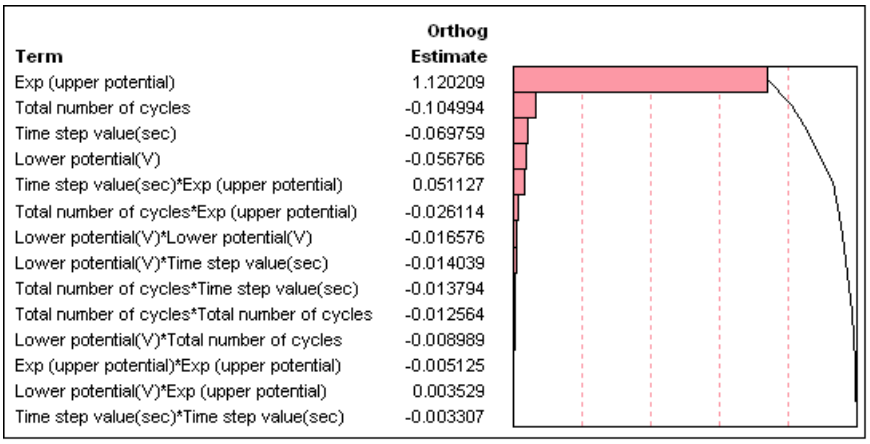

Figure 4.6. Pareto Plot for a) Pt surface area loss b) Pt mass loss c) Pt particle radius growth rate (after transformation).

Term	Orthog Estimate
exp(upper potential)	5.288554
Total number of cycles*Time step value(sec)	0.450089
Lower potential(V)	-0.331100
exp(upper potential)*exp(upper potential)	-0.211854
Time step value(sec)	-0.154795
Total number of cycles	-0.110767
Total number of cycles*exp(upper potential)	-0.054164
Time step value(sec)*Time step value(sec)	0.038905
Lower potential(V)*Total number of cycles	0.029183
Lower potential(V)*Time step value(sec)	0.027993
Total number of cycles*Total number of cycles	-0.026700
Lower potential(V)*Lower potential(V)	-0.018302
Time step value(sec)*exp(upper potential)	-0.014045
Lower potential(V)*exp(upper potential)	0.012547

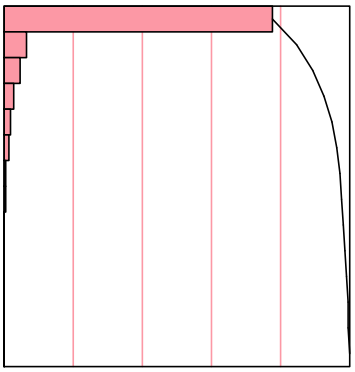

Term	Orthog Estimate
exp(upper potential)	2.535124
Lower potential(V)	-0.248663
Lower potential(V)*Time step value(sec)	-0.200523
Total number of cycles*Time step value(sec)	0.197444
Lower potential(V)*Total number of cycles	-0.142700
Total number of cycles*exp(upper potential)	-0.095773
Lower potential(V)*exp(upper potential)	0.095363
Total number of cycles	-0.094199
Time step value(sec)*Time step value(sec)	0.056151
Time step value(sec)*exp(upper potential)	0.027132
Total number of cycles*Total number of cycles	0.022409
Time step value(sec)	0.021677
Lower potential(V)*Lower potential(V)	-0.005048
exp(upper potential)*exp(upper potential)	-0.002916

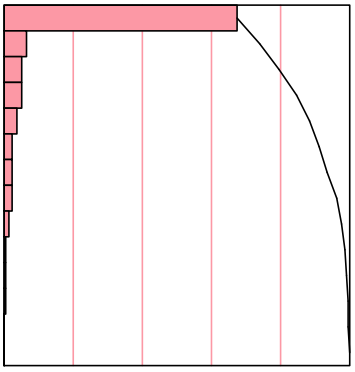

Figure 4.6. continued

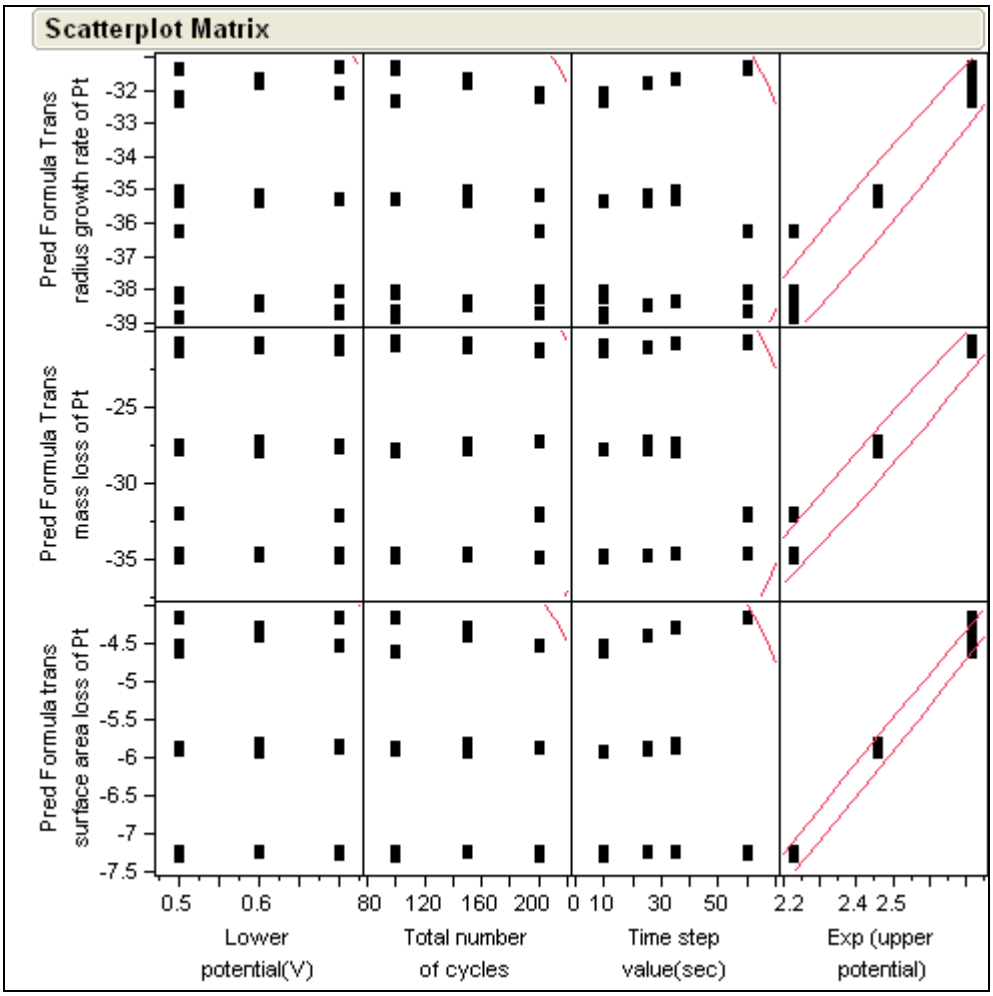

Figure 4.7. Scatter Plot Matrix of the Pt catalyst dissolution metrics against the four independent variables.

4.6. Conclusions and Future Work

A framework for the surrogate model of Pt catalyst dissolution of PEMFC is developed. The effectiveness and importance of Response Surface Methodology in electrochemistry degradation models is discussed. An indication about the relative importance of different variables that influence platinum catalyst dissolution is obtained and this knowledge could also be employed to design control architecture and power management strategies that help mitigate platinum catalyst degradation in hybrid systems and also to arrive at a trade-off between

performance and degradation of the hybrid system. Better RSEs will be developed and integrated in the hybrid system model. A key enabler for developing more accurate RSEs will be a computationally efficient physics-based model for Pt degradation that takes into consideration different degradation mechanisms with minimal assumptions. The procedure and the methodology could also be extended to develop surrogate model for carbon corrosion in PEMFC from the electrochemistry models and also for the incorporation of battery degradation models in hybrid system framework. Ultimately, a robust design will evolve that makes the hybrid system less sensitive to uncertainties by controlling other independent variables and operating in a regime (through power management algorithms) that will be an optimized trade-off between different performance metrics and durability issues.

4.7. References

[1] M. J. Kim and H. Peng, *J. Power Sources,* 165(2) (2007), 819-832.

[2] W. Na and B. Gou, *J. Power Sources,* 166(2) (2007), 411-418.

[3] D. N. Mavris, D. A. DeLaurentis, O. Bandte, M. A. Hale, AIAA98-0912, 36th Aerospace Sciences Meeting and Exhibit, Reno, NV, January 12-15, 1998.

[4] J.Kim, Seong-Min Lee, S.Srinivasan, C.E.Chamberlin, *J. Electrochem. Soc.,* 142(8) (1995), 2670-2674.

[5] C. Fellner , John Newman, *J. Power Sources*, 85(2) (2000), 229-236.

[6] Doyle , Newman, Antoni S. Gozdz, Caroline N. Schmutz , Jean-Marie Tarascon, *J. Electrochem. Soc*., 143(6) (1996), 1890-1903.

[7] Godfrey Sikha, Branko N. Popov and Ralph E. White, *J.Electrochem.Soc.*, 151 (7) (2004), A1104-A1114.

[8] P.Pei, M.Ouyang, Q.Lu, H.Huang Xihao Li, *Int. J. Hydrogen Energy*, 29 (10) (2004), 1001-1007.

[9] http://www.epa.gov/otaq/sftp.htm

[10] Rajeswari Chandrasekaran, Wu Bi, Thomas F. Fuller, *J.Power Sources* 182 (2008), 546–557.

[11] R. Tirnovan, S. Giurgea, A. Miraoui, M.Cirrincione, *J. Power Sources*, 175 (2) (2008), 773-778.

[12] R. Tirnovan, S. Giurgea, A. Miraoui, M. Cirrincione, *Applied Energy*, 86 (7-8), (2009), 1283-1289.

[13] Wu Bi and Thomas F. Fuller, *J. Power Sources*, 178 (2008), 188-196.

CHAPTER 5

DIAGNOSTIC AND LONG TERM TESTING OF LITHIUM-ION CELLS

5.1. Introduction

Capacity fade in lithium ion batteries under cycling and storage conditions has been studied before and the effect of different parameters analyzed [1, 2, 3]. This chapter aims to briefly analyze the effect of temperature, cycling, storage and overcharge on the performance and degradation in lithium ion batteries. The results will justify the need for surrogate models for lithium ion batteries, to capture the influence of different parameters on their performance and degradation in hybrid level system models.

5.2. Experiments

5.2.1. Capacity check

4 Ahr GS-Yuasa LM4 lithium ion cells were charged at constant current (CC) at C rate (4 A) until the cell potential reaches 4.1 V, followed by constant voltage (CV) charging at 4.1 V until the current tapers off to 50 mA. The cells were then discharged at C rate until the potential reaches the cut-off voltage of 2.75 V. This capacity check was done both initially and also after prolonged testing. Arbin battery cycler Model BT-2043 with Arbin Battery Testing System (ABTS) software Version 2.1.0 was used for the capacity check and cycling/storage studies.

5.2.2. Long term performance testing

The cells were cycled using the above mentioned CC-CV charging followed by constant current discharge at C rate up to 2.75V, both at room temperature and at 50 °C. The cells were also stored at open circuit at room temperature and at 50 °C at different state of charges. Table 5.1 shows the details of the cycling/storage test details that have been conducted.

5.3. Results and Discussion

The storage tests indicate that the decrease in open-circuit potential is greater at higher temperature (50 ^{o}C) than at room temperature. This is shown in Figure 5.1. This can be correlated to the higher capacity fade of cells stored at high temperatures than at room temperature (Table 5.1). Table 5.1 also shows that the cell stored at slight overcharge has a slightly higher capacity fade than the cell stored at fully charged condition at 50 ^{o}C.

The tests show that all the cells demonstrate a decrease in capacity with storage and cycling (Table 5.1). The cells that were cycled at higher temperature (50^{o}C) showed the highest capacity fade. Among the two cells cycled at 50 ^{o}C, the one that was cycled up to 292 cycles showed higher fade than the one that was cycled up to 271 cycles. Figure 5.2 shows the discharge curves and capacity check curves for a lithium ion cell cycled at 50 ^{o}C. It can be seen that the voltage plateau is at higher potentials while cycling at 50 ^{o}C. This can be understood from the fact that at higher temperatures ionic conductivity increases, and the reaction kinetics tend to be faster. But at higher temperature, degradation mechanisms are also accelerated. Figure 5.3 shows the discharge curves and capacity check curves for a lithium ion cell cycled at room temperature. This figure shows that the discharge curves during cycling at C rate and the capacity check curves are identical at room temperature.

Table 5.1. Capacity Fade Analysis of lithium ion cells

Test	Rate or Condition	Temperature	# cycles	# hours	Capacity Fade (%)
Cycle	C-rate	50^{o} C	292	-	20.87
Cycle	C-rate	50^{o} C	271	-	17.98
Cycle	C-rate	25^{o} C	242	-	7.54

Table 5.1. continued

Cycle	C-rate	25^{o} C	269	-	6.65
Storage	Overcharge (at 4.2 V)	50^{o} C	-	659	10.21
Storage	100 SOC (fully charged)	50^{o} C	-	659	8.84
Storage	100 SOC (fully charged)	25^{o} C	-	659	2.89
Storage	0 SOC (fully discharged state)	25^{o} C	-	659	5.07

Note: 25^{o} C denotes room temperature

5.4. Conclusions

Temperature has a significant effect on degradation of lithium ion cells. The worst case scenario in the present study is cycling at high temperatures. Overcharging will accelerate the degradation process in a lithium-ion cell more than when it is kept within normal potential window.

This study indicates that it is necessary to create surrogate models of lithium ion batteries to capture the influence of parameters such as temperature on the performance at first and later on degradation such that these can then be used at higher level system models. Hence, as a first step, in the next chapter (Chapter 6), design of experiments is used to collect data systematically on the performance of lithium ion batteries as a function of temperature and rate capability to create the RSEs.

5.5. References

[1] P. Ramadass, B.Haran, R.White, B.N. Popov, *J.Power Sources*, 112(2), 614-620 (2002).

[2] P. Ramadass, B.Haran, R.White, B.N. Popov, *J.Power Sources*, 112(2), 606-613 (2002).

[3] R. Chandrasekaran, G.Sikha, B.N.Popov, *J.Applied Electrochemistry*, 35(10), 1005-1013 (2005).

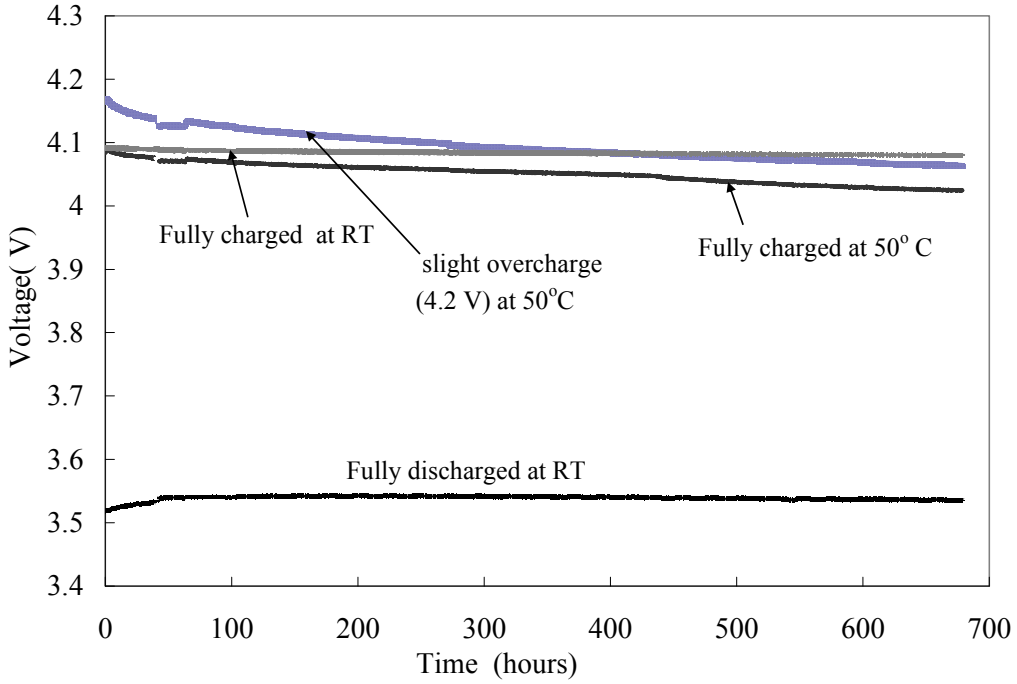

Figure 5.1. Open circuit potential *vs.* time for lithium ion cells at both 50°C and at room temperature.

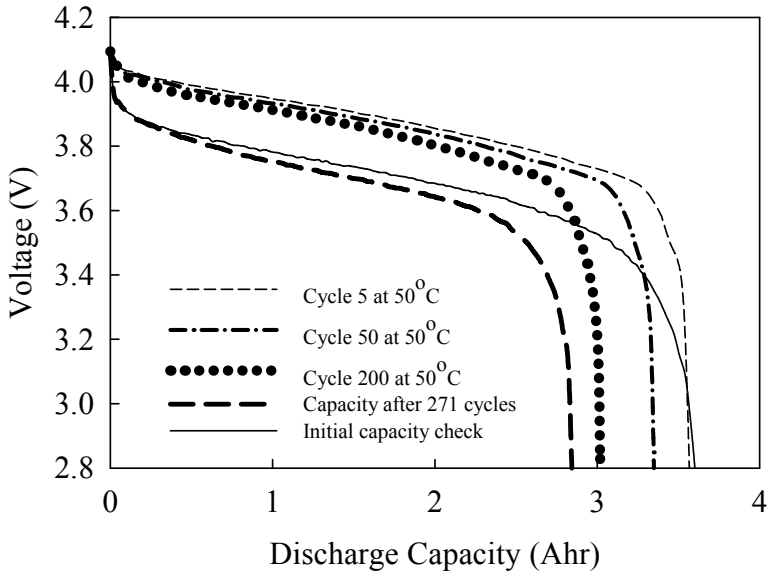

Figure 5.2. Discharge and capacity check curves of a lithium ion cell cycled at 50°C.

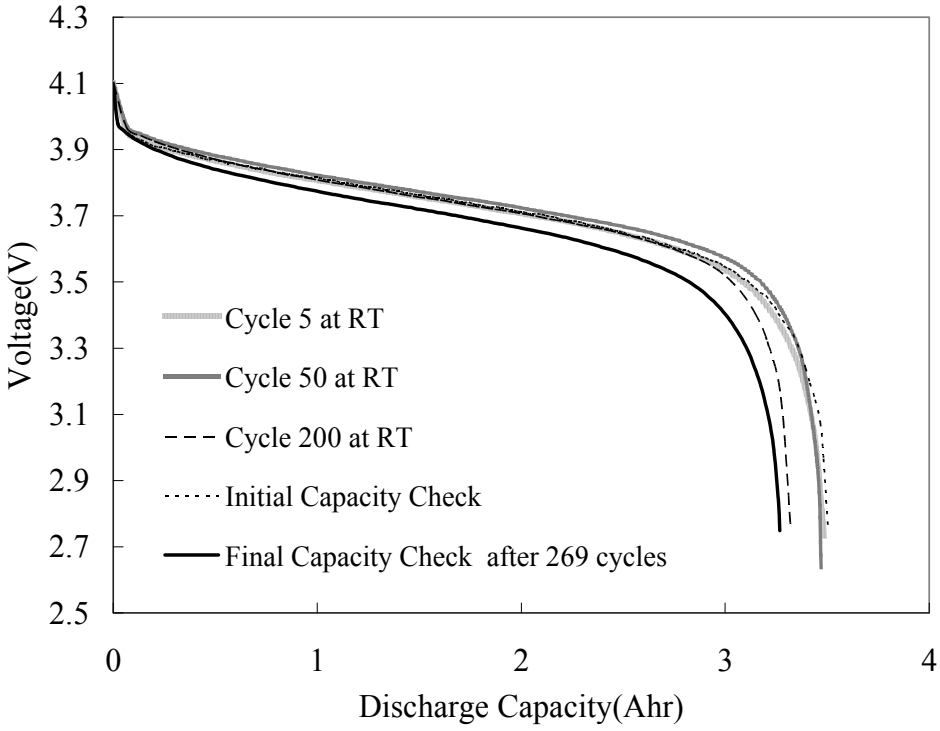

Figure 5.3. Discharge and capacity check curves of a lithium ion cell cycled at room temperature.

CHAPTER 6

METAMODELS AND UNCERTAINTY ANALYSES IN LITHIUM ION BATTERIES FOR ROBUST BATTERY/FUEL CELL HYBRID SYSTEM DESIGN

6.1. Introduction

The importance of hybrid systems in automobile applications, challenges for commercializing PEMFC systems, the necessity to include durability issues such as Pt stability and the robust surrogate model methodology enabling uncertainty analyses for the same has been discussed in Chapter 4 [1]. This chapter focuses on the need for good performance models of batteries in order to achieve a robust design of fuel-cell/battery hybrid systems. Multiple responses are of interest in the overall fuel-cell/battery hybrid system as well –namely, fuel economy [2], emissions, system efficiency, cost [3], other performance and durability issues in fuel cells such as Pt catalyst degradation, carbon support, membrane degradation and degradation in batteries such as capacity fade, power fade, etc. A robust design is one wherein the system is operated in a design space such that the responses are made insensitive to factors that are difficult to control. For achieving both a reliable and a robust design in the multidisciplinary problem of hybrid system modeling and arrive at trade-off between different responses or metrics, the approach should be to first to identify the robust design space with respect to the regressor variables for all the responses of interest. One can later explore within this region to find an optimal solution space.

Equivalent circuit models based on look-up tables are advantageous because they take less time for computation [4] and are easier for integration. But these do not have the high

fidelity of the physics-based models in the entire design space. Good fidelity of the cell-level model is essential for predicting battery pack performances accurately. Most of the hybrid power systems models do not capture the uncertainty associated with the cell-to-cell variation in a battery pack, and hence the cell model is simply linearly scaled to the pack level [5]. The fidelity of the battery models themselves is not extensively discussed. On the other hand, detailed physics-based models for individual cells [6] need greater time, higher computational resources and are complex to run battery-pack simulations [7] and also challenging to integrate with system level models. Sikha *et al.* developed a detailed physics-based model for the performance of a battery/super capacitor hybrid system [8]. But again, this detailed model has not been integrated in a vehicle level system model. A battery model that is employed in a hybrid system model should have good fidelity, ease of integration, capture the uncertainty associated with the cell-to-cell variation within the battery pack and have less computational time. Lower order real time simulation models [9] require considerable preprocessing. The ease of integration of these models with the hybrid models will be a deciding factor.

Moreover, several uncertainties are associated with the operation of batteries. Uncertainties arise because of variations introduced during manufacturing steps, experimental errors, external noise factors, parameter estimation techniques employed, model assumption, cell-to-cell variations within a battery pack, etc. Though the effect of uncertainty in particle size of the electrodes on the discharge response of the lithium ion cell using polynomial chaos theory and single particle model has been captured [10], this uncertainty analyses is again not taken all the way upto a system model. Ease of integration of single particle model in hybrid system model might not be straightforward. Also, other uncertainties will have to be considered to obtain a robust solution.

Meta modeling (or surrogate modeling) techniques using response surface methodologies are key enablers to obtain a robust design [11]. Hence surrogate models have higher fidelity than other simpler models. These techniques take a probabilistic approach for modeling the responses and enable uncertainty analyses. First, a quantitative proof for the need for robust design in batteries for hybrids is presented. Second, surrogate modeling techniques for capacity predictions of batteries as a function of temperature and rate of discharge from experimental data are discussed. Finally uncertainty analyses are illustrated. The advantage of the response surface methodology is that it can be easily adopted by any research group to create their own surrogate models and incorporate in their higher system-level models. Since response surface models have good fidelity and have lesser computation time, the cell level model can be used to construct the pack level model by incorporating cell-to-cell variations by means of distributions. In future, data from physics based models can be used to analyze multiple responses in a battery as a function of other independent variables like the charging rate, depth of discharge, cell parameters such as porosity of the electrodes [12], etc. The surrogate model methodology should be extended in future to capture degradation mechanisms in these energy storage devices in hybrid system so that novel system control strategies can be arrived at for the mitigation of these issues.

6.2. Proof of concept for the need for robust design

Figure 6.1 shows a fuel cell /battery hybrid vehicle model developed using Argonne National Laboratory's Powertrain Systems Analysis Toolkit (PSAT) [5]. GM's Saturn VUE is chosen as the base vehicle, and a 2 wheel-drive, series, fuel-cell hybrid configuration with an automatic transmission is modeled. The component details are given in Table 6.1. The limits for peak power of the battery pack at 100% depth of discharge were varied for three different cases: 29 kW, 22 kW and 11 kW. Parameters in the control strategy are given in Table 6.2. Simulations

were performed for city (UDDS) and highway (HWFET) driving cycles. SOC correction was employed using the dichotomy method. Time taken for acceleration between 0-60 mph, 50-70 mph and also time for quarter mile distance are evaluated. The detailed approach to design a hybrid electric vehicle using PSAT is provided in Appendix B.

All the results are shown in Table 6.3. The battery pack is air cooled, and a simple thermal model in PSAT captures the rise in temperature of the battery pack during operation as shown in Figure 6.2. Table 6.2 shows that as the battery peak power increases, vehicle mass increases slightly, fuel economy increases especially in city driving, performance as reflected by time to acceleration and time for quarter mile distance improves, hydrogen needed (for fuel cell) to cover a range of 320 miles especially with city driving decreases, and the percentage of regenerative braking energy that is recovered increases. But as seen in Figure 6.2, the temperature of the battery pack also increases with increasing battery peak power. The increase is more pronounced in city driving. This implies as the degree of hybridization with respect to batteries increases, thermal considerations are important as they affect not just the initial performance, but also the capacity fade of the batteries [12, 13, 14]. Even though the temperature of operation is usually assumed to be set and hence deterministic, as seen above, uncertainty in the temperature of the batteries could arise with operation that could lead to risks later unless uncertainty is captured earlier in the design phase and steps taken to counter its effect. Thus the need for a robust multi-objective optimal design space that not only allows for a good initial performance of the battery, but also minimizes the heat effects [15], [16] and mitigates life (both calendar and cycle life) issues. On the other end, at low peak power of batteries, the temperature rise is less in batteries, but they are more of a dead weight. Moreover, the hybrid controller strategy can

Table 6.1. Component specifications in the vehicle

Components	Values
Vehicle body mass	1180 kg
Fuel Cell Power	50 kW
Electric motor peak power	85 kW

Table 6.2. Controller Strategy

Propelling Control Strategy	**Values**
SOC below which fuel cell is activated	50%
SOC above which the fuel cell is idled	70%
Vehicle speed above which fuel cell can be activated	4.47 mph
Vehicle speed below which fuel cell is idled	1.12 mph
Regenerative Control Strategy	**Values**
SOC above which regenerative braking is turned off	90%
SOC below which regenerative braking is turned on	80%
Vehicle speed below which charging of the batteries is forbidden	2.24 mph

be manipulated such that the design space is robust not just between different responses of interest, but also in conjunction with different driving patterns. This chapter presents a methodology or framework in these directions.

6.3. Response Surface Methodology for meta-modeling of capacity predictions of lithium ion batteries

6.3.1. Application of RSM for battery surrogate models

Commercial lithium ion cells with rated capacities of 1.1 Ah (C rate) and 3.2 Ah (C rate) are chosen for the experiments. The controllable factors chosen are temperature of operation and rate of discharge. It should be noted that as the experiment proceeds, there will be a change in temperature of the battery, especially at high rates of discharge, and there will definitely be a temperature gradient within the battery. In this way, the temperature of the battery is also a noise or uncontrollable factor. Once a good response surface model is developed, it can be combined with Monte Carlo simulations to construct the probability density functions (PDFs), and the cumulative distribution functions (CDFs) of the objective and constraints. These can guide the designer in making decisions and trade-offs at the system level.

For each independent variable, three levels are chosen. A central composite design of experiments is created, and total of 9 runs were conducted using an Arbin battery cycler (BT-2000) and HD-508 environmental chamber from Associated Environmental Systems. Central composite design and Latin hypercube sampling are used to obtain capacity data for creating the surrogate model. The CCD design gives the same number of runs as a full factorial in this work since there are only two independent variables. To fill the inner design space, latin hypercube sampling with 10 data points was carried out. The design of experiments is shown in Table 6.4. All rates of discharge are denoted in reference to the respective C rates. Table 6.5 gives the experimental runs used for model validation. As a rule of thumb, the number of runs needed for model validation is 20% of the cases used for model creation.

Table 6.3. PSAT Simulation Results

Configuration :	Fuel Cell power: 50 kW Li-ion Battery Peak Power : 29.276 kW	Fuel Cell power : 50 kW Li-ion Battery Peak power: 11.208 kW	Fuel Cell power : 50 kW Li-ion Battery Peak Power : 21.876 kW
Total Vehicle mass (static) (kg)	1655.47	1629.10	1638.18
Fuel economy (miles per gallon gasoline equivalent)	62.39 (UDDS) 60.81(HWFET)	55.49(UDDS) 59.71(HWFET)	59.34(UDDS) 60.68(HWFET)
Hydrogen used (kg) for 1 cycle	0.12 (UDDS) 0.17 HWFET)	0.13(UDDS) 0.17(HWFET)	0.13(UDDS) 0.17(HWFET)
Fuel (hydrogen) needed to travel 320 miles (kg)	5.16 (UDDS) 5.30 HWFET)	5.80 (UDDS) 5.39(HWFET)	5.43(UDDS) 5.31(HWFET)
Percentage Braking Energy Recovered	67.18 %(UDDS) 63.34 % (HWFET)	32.21 % (UDDS) 32.22 % (HWFET)	49.85% (UDDS) 48.34 % (HWFET)
Time for Acceleration (0-60 mph) (sec)	14.7	19	17.1

Table 6.3. continued

Acceleration (50-70 mph) (sec)	11.1	16	13.8
Time to 0.25 mile(sec)	19.8	21.3	20.7

Table 6.4. Design of Experiments

Central Composite Design (CCD design)			
Temperature (^{o}C)	**Rate of Discharge (C rates)**	**Actual Capacity (Ah) of the cell with nominal capacity of 1.1 Ah**	**Actual Capacity (Ah) of the cell with nominal capacity of 3.2 Ah**
0	0.1	1.230	2.547
0	1.55	0.860	1.854
0	3	0.877	1.858
25	0.1	1.504	3.139
25	1.55	1.175	2.430
25	3	1.318	2.583
50	0.1	1.477	3.043
50	1.55	1.398	2.629
50	3	1.404	2.841
Latin Hypercube Space Filling Design			
11	2.03	1.074	2.153
6	1.07	1.061	2.163

Table 6.4. continued

22	0.74	1.306	2.752
28	1.71	1.306	2.569
33	2.68	1.324	2.409
39	0.42	1.392	2.922
44	1.39	1.377	2.722
50	2.36	1.385	2.547
18	3	1.182	2.027
0	0.1	Included in CCD design	Included in CCD design

Table 6.5. Experimental runs for model validation (Model Representation Error)

Temperature (^{o}C)	**Rate of Discharge (C rates)**	**Actual Capacity (Ah) (nominal capacity: 1.1 Ah)**	**Actual Capacity (Ah) (nominal capacity: 3.2 Ah)**
0	0.5	1.021	2.006
0	1.75	0.850	1.685
25	0.5	1.366	2.882
25	1.75	1.302	2.615
50	0.5	1.440	3.068
50	1.75	1.418	2.771
0	1	0.850	1.679
0	2	0.801	1.625
25	1	1.284	2.712
25	2	1.301	2.452

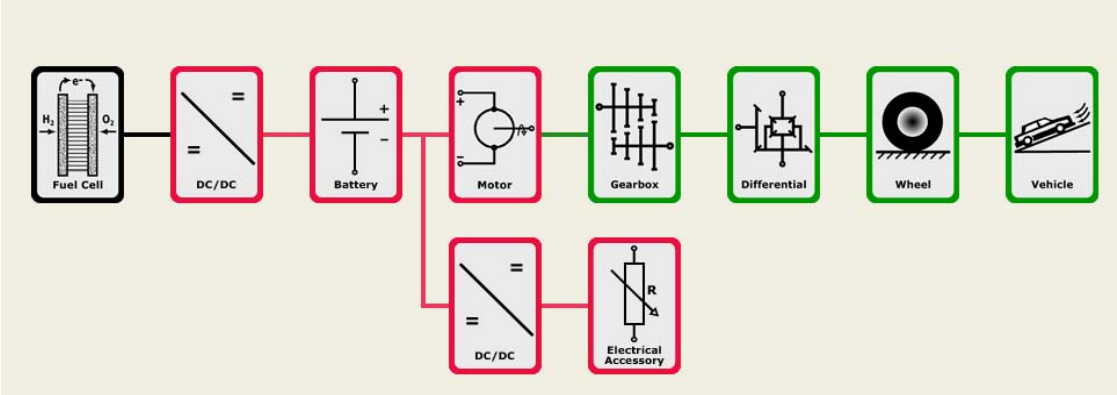

Figure 6.1. Fuel Cell/Battery Series Hybrid Configuration.

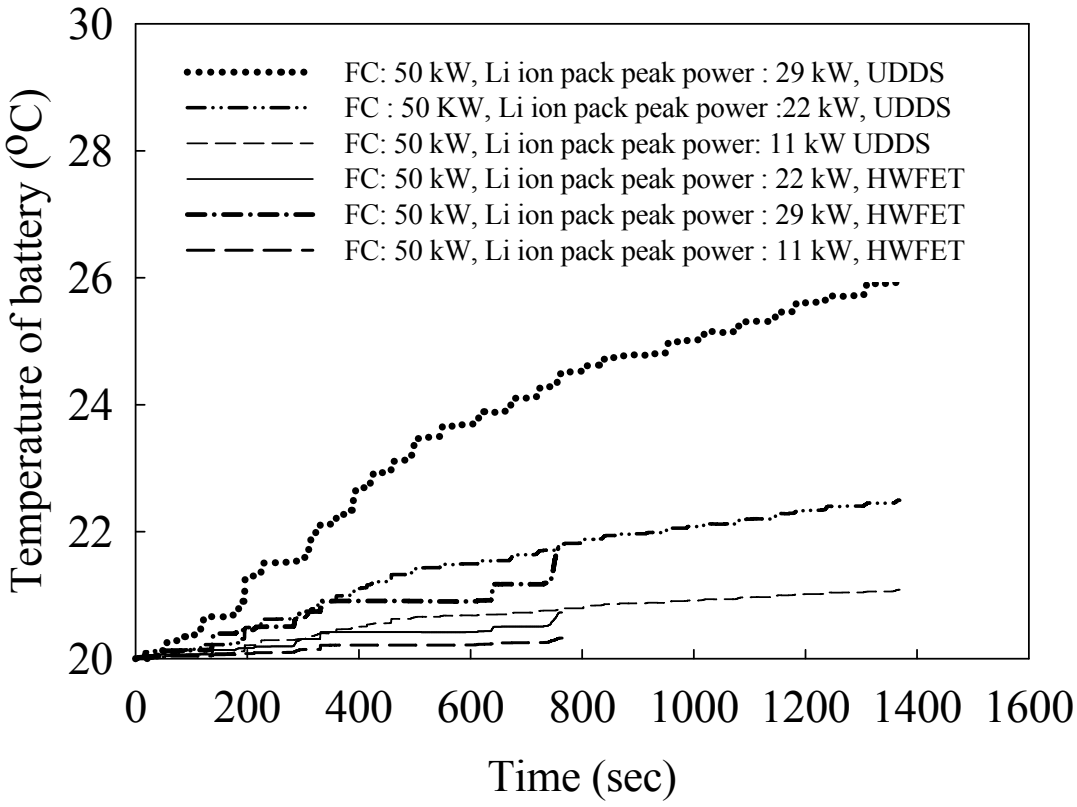

Figure 6.2. Temperature rise in battery pack.

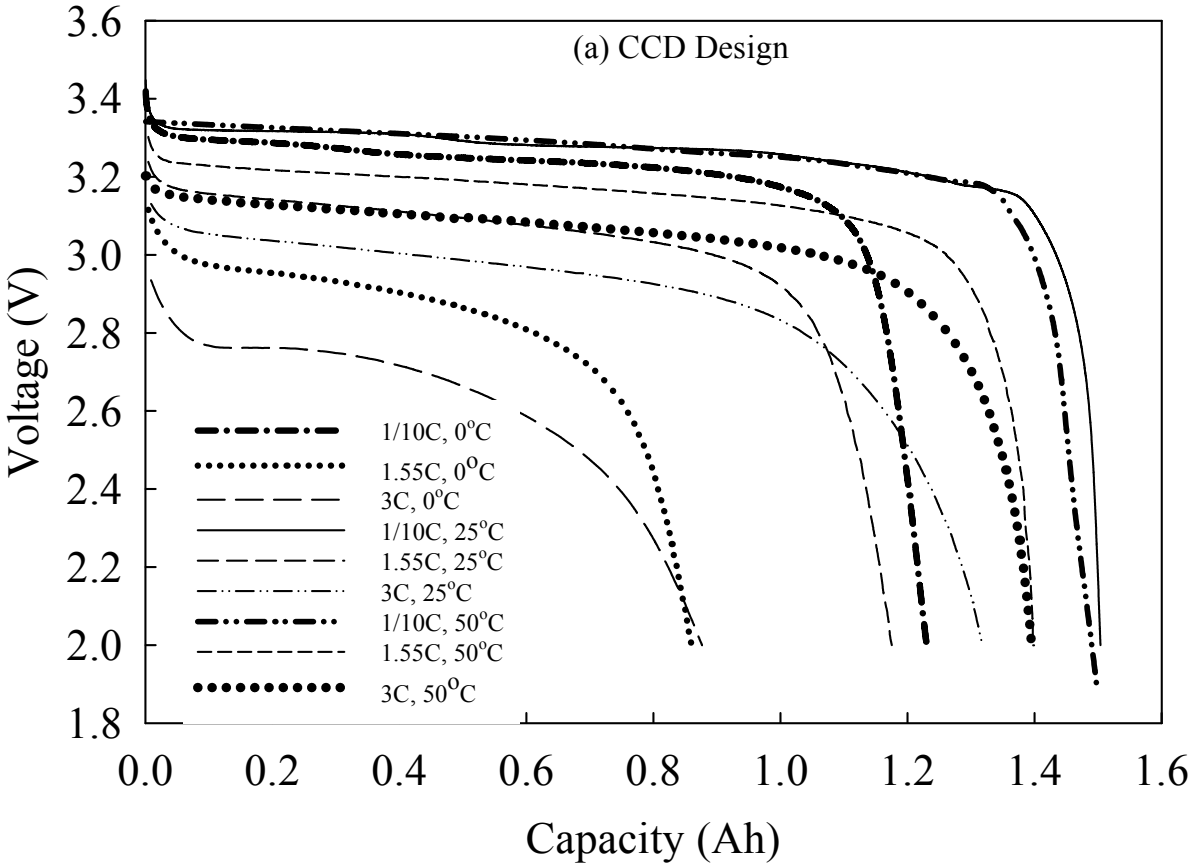

Figure 6.3. Discharge curves for the 1.1 Ah Lithium ion cell (a) CCD design (b) Latin Hypercube design.

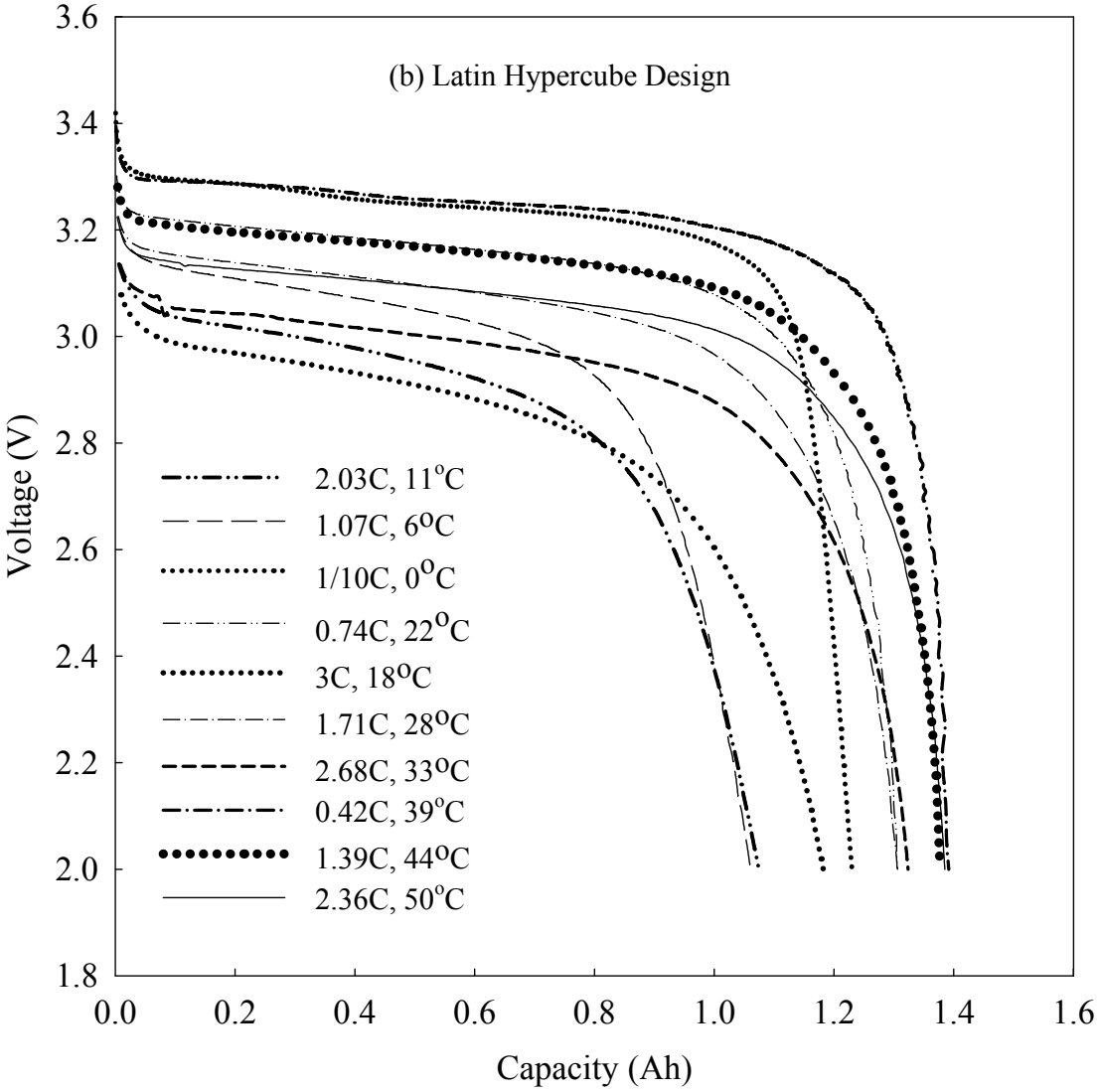

Figure 6.3. continued

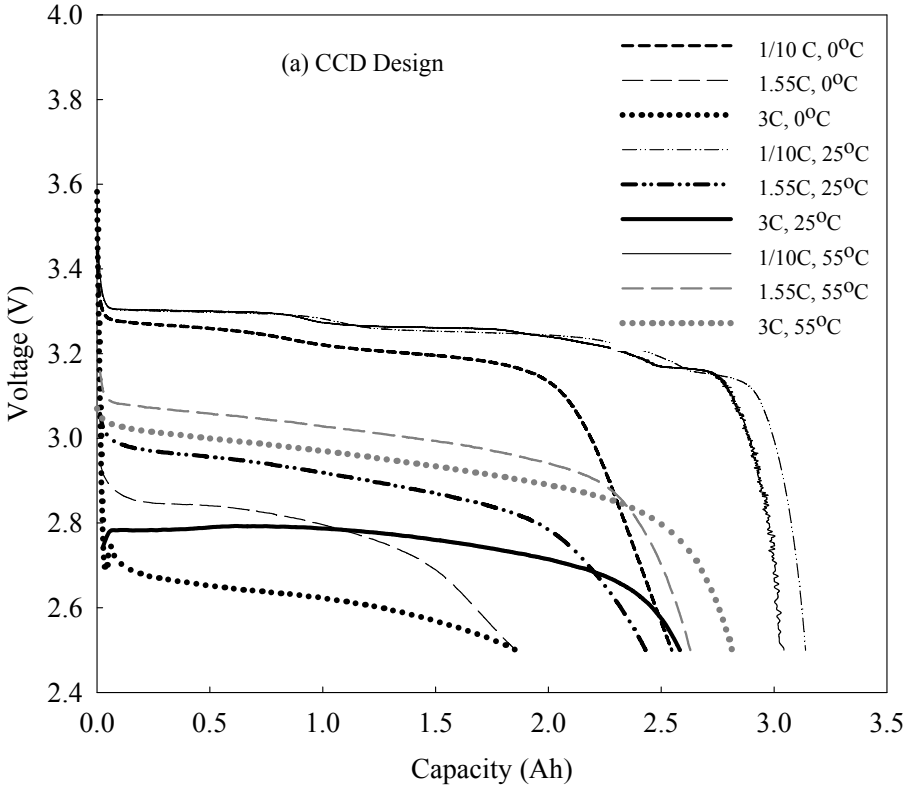

Figure 6.4. Discharge curves for 3.2Ah Lithium ion cell (a) CCD design (b) Latin Hypercube Design.

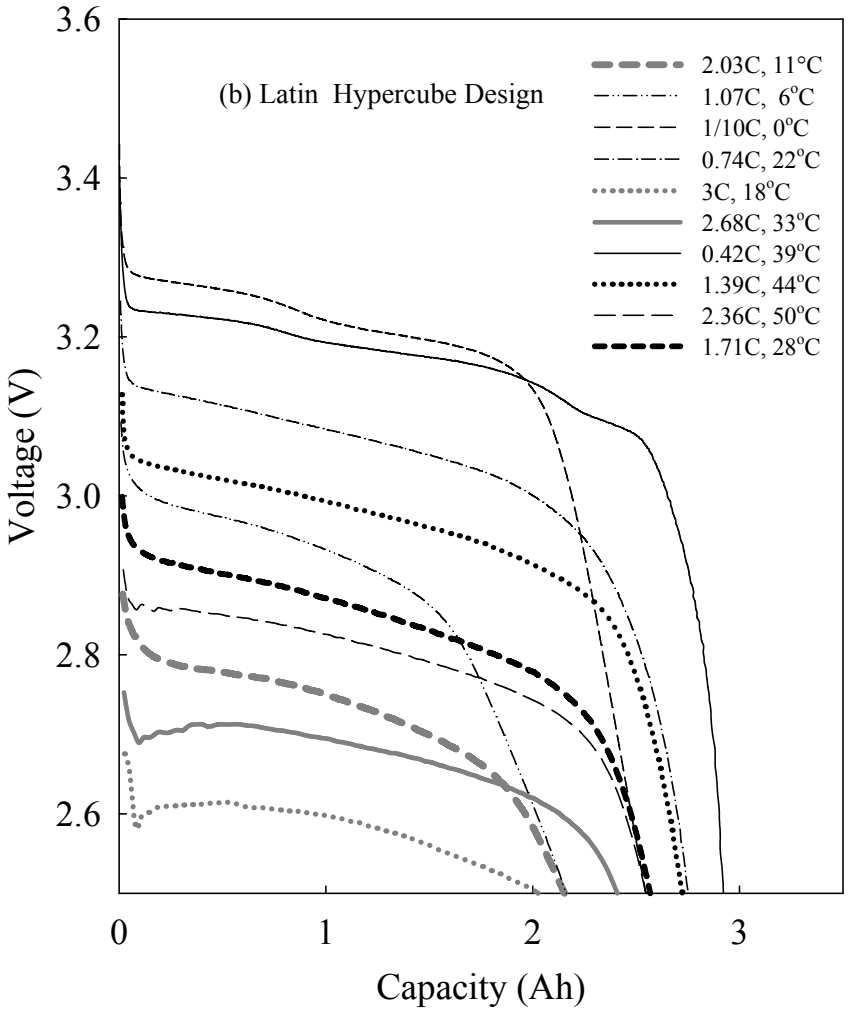

Figure 6.4. continued

6.3.2. Results and Discussions

The discharge curves for the above DoE cases for the two cell are given in Figures 6.3 and 6.4. Response surfaces are created for the capacity obtained in the above runs as a function of temperature and rates of discharge. The results are now analyzed using statistical goodness of fit tests.

6.3.2.1. Actual *vs.* Predicted Plot

Figure 6.5 gives the actual *vs.* predicted plot for the capacity (Ah) for both the commercial cells. The R^2 values are 0.961 and 0.929 respectively. The high R^2 values imply that the variables, as well as the order of the regression polynomials, do account for most of the variation in responses. Since R^2 values can increase as the number of independent variables increases, adjusted R^2 values are also considered and they are 0.946 and 0.8999 respectively. Adjusted R^2 is a modification of R^2 that accounts for the number of regressors (or independent variables or explanatory terms) in a model by the formula below:

$$\text{Adjusted } R^2 = 1 - (1 - R^2)\frac{n-1}{n-p-1}$$

where n is the sample size and p is the number of regressors in the model.

All data points lie close to the Perfect Fit line (diagonal), but since there is a slight spread, it might indicate that the assumed second order model might be inadequate. The mean of the response is also slightly shifted upwards in the case of 1.1Ah cells because of the slightly uneven distribution. The dashed lines are the 95% confidence lines.

6.3.2.2. Residual *vs.* Predicted Plot

Figure 6.6 gives the residual *vs.* predicted plot for both the commercial cells. There is no distinguishable pattern observed in the residual by predicted plot. A good random distribution of the error implies that it is acceptable to have discarded the higher order terms and interaction terms from the Taylor series expansion for the assumed model. The total span of error is 18.75 % of the minimum of the predicted capacity values in case of 1.1 Ah cells and 30 % in case of 3.2 Ah cells. As a rule of thumb it is desirable to have this as low as 5% for validity of the second order meta model. But the residual is an order of magnitude lesser than the predicted values.

Also there is no clumping of the data in both Figure 6.5 and Figure 6.6 and hence a second order model could still be valid.

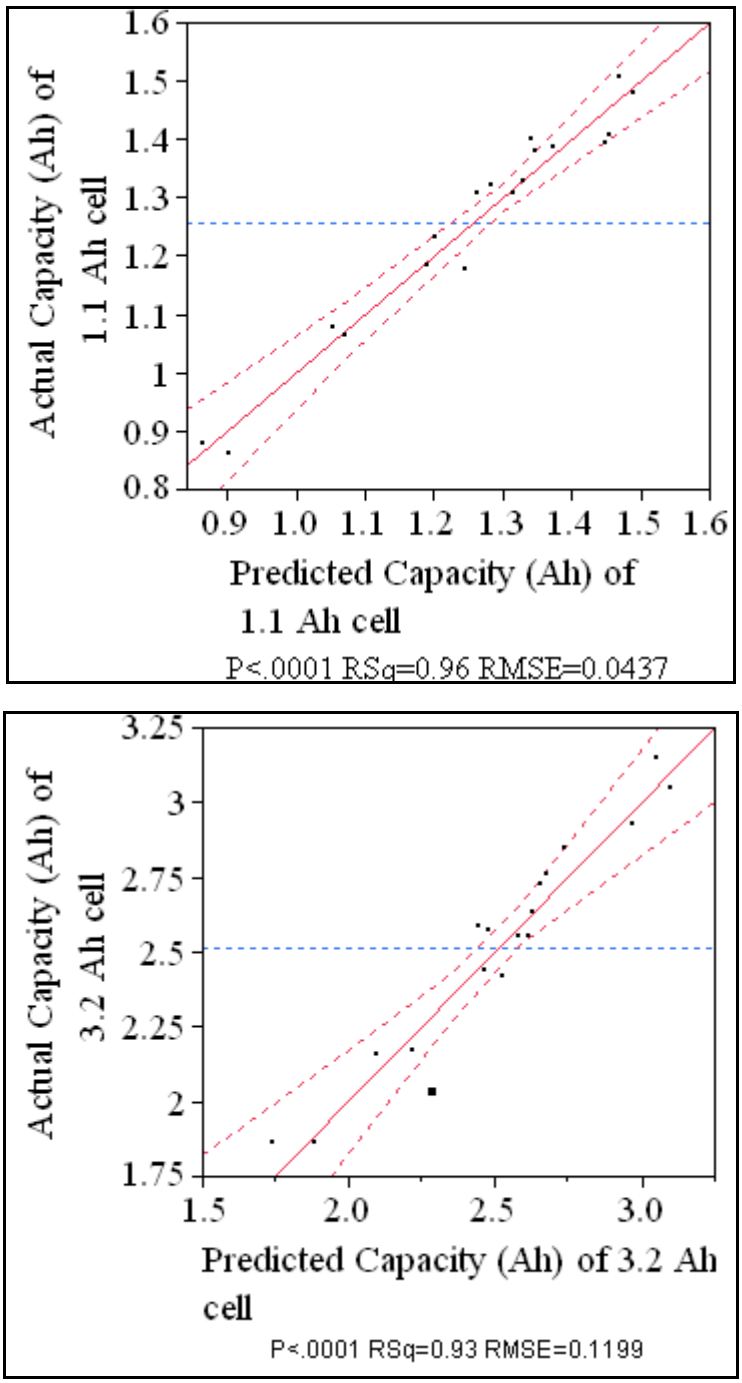

Figure 6.5. Actual vs. Predicted Capacity plot for (a) 1.1 Ah cell (b) 3.2 Ah cell.

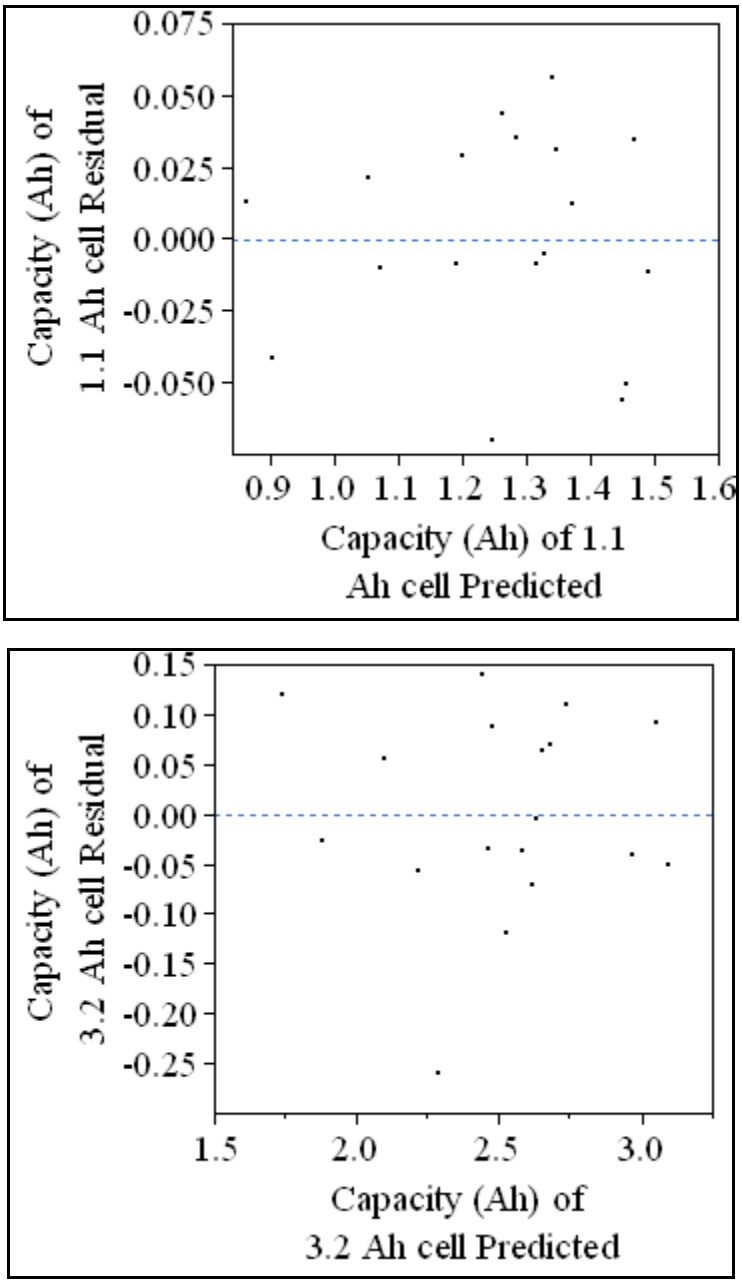

Figure 6.6. Residual *vs.* Predicted Capacity plot for (a) 1.1 Ah cell (b) 3.2 Ah cell.

6.3.2.3. Model Fit Error

The error distribution, which is called the model fit error, gives an idea of how well the model fits the data points within the design of experiments. Ideally, it is desired that the model fit error resemble a normal distribution with mean of zero and standard deviation of one. Figure 6.7 gives

the model fit error for the predicted capacities. As can be seen in Figure 6.7, the upper and lower bounds of the error for 1.1 Ah cells are approximately 4 and -6%. Typically these values are desired to be less than an absolute value of 5 %, i.e., it is desirable to minimize the bounds. The mean and standard deviation of the above distribution are -0.098 and 2.958 respectively. For 3.2 Ah cells, the upper and lower bounds of error are 6.36 % and -12.9 5%. The mean and standard deviation of the error distribution for 3.2 Ah cells are -0.15 and 4.48. In the above distribution, if one outlier is neglected for the 3.2 Ah cell, then the standard deviation reduces to 3.2 (and the mean has changed to 0.6) and the error bounds are also minimized to 6.35 % and -5.05 % respectively. But caution has to be applied when neglecting outliers to avoid significant correlation between the independent variables. Usually, a maximum of about 7-8% of the data can be neglected as outliers, and hence we have ignored only 1 data in 3.2 Ah cell as outlier out of a total of 18 cases. Multivariate analysis yields the correlation matrix where the correlation between the cross terms in the 1.1 Ah cell is found to be 0.0107, and that for the 3.2 Ah cell (with one outlier data excluded) as 0.0515. In both cases it is less than 0.1, which is a rule of thumb to avoid any correlation between independent variables. A point to be noted above is that there were fewer runs and hence the normal distribution of the error within this small set of data might be slightly difficult.

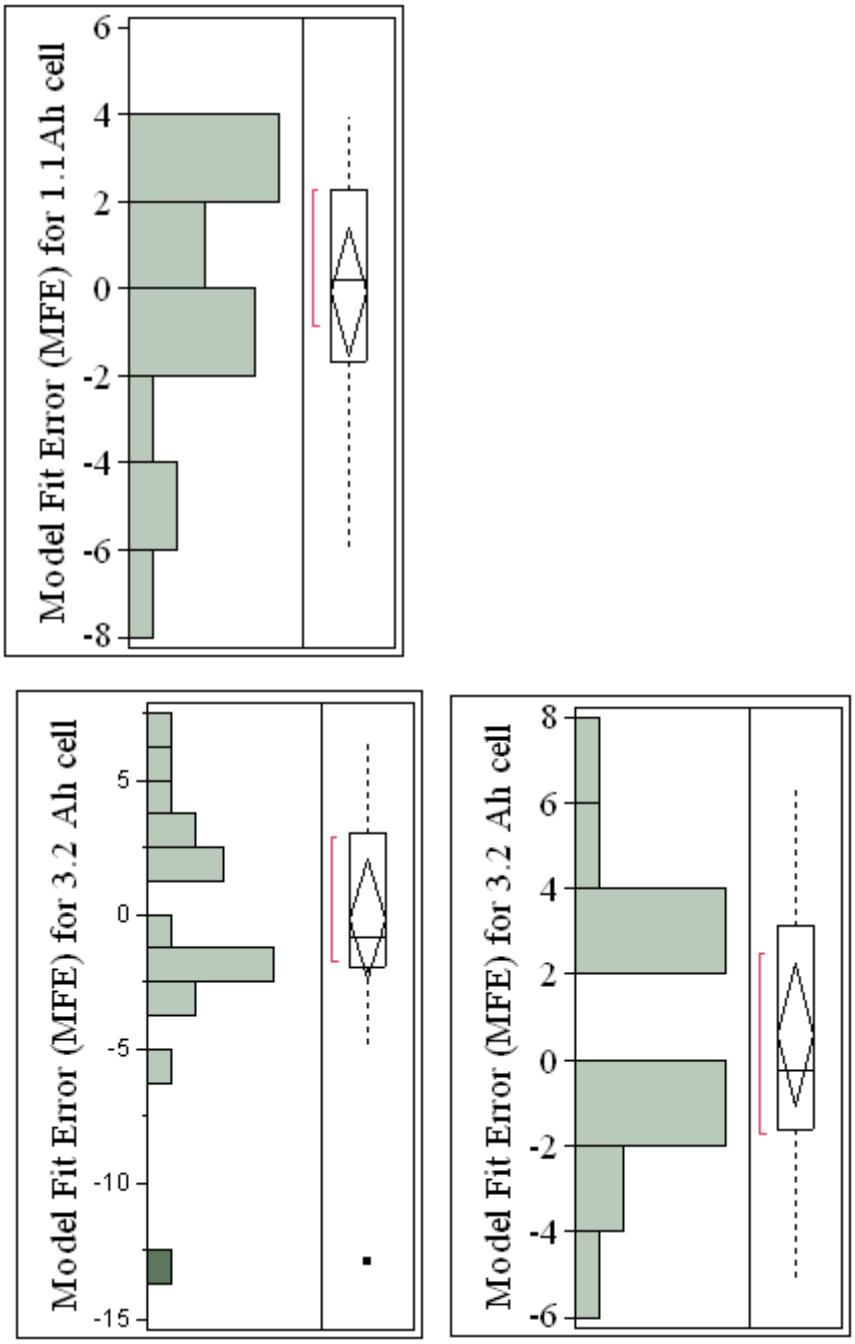

Figure 6.7. Model Fit Error (MFE) plot for (a) 1.1Ah cell (b) 3.2Ah cell.

6.3.2.4. Model Representation Error

This statistic shows how well the assumed model predicts the actual response for the design settings not used in the creation of model within the design range of interest. For this, random

settings of the independent variables are chosen and experiments performed. Usually it is desired to have at least 20 % of the original number of runs to have a sufficient sampling of the space to check the MRE. Table 6.5 gives the cases so chosen in this work. The Response Surface Equation (RSE) developed above is used to predict the responses for these new cases and arrive at the MRE distribution by comparing it to the corresponding experimental capacities. Figure 6.8 shows the MRE distribution for both 1.1 Ah and 3.2 Ah cells. For the 1.1 Ah cell, one outlier increased the error bounds as well as the standard deviation. Hence this datum was excluded, and the corresponding MRE distributions are given in Figure 6.8. It can be seen that the upper and lower bounds of error for the 1.1 Ah cell are 5.45 % and -7.669 %, and the mean and standard deviation are -0.2 and 3.716. For the 3.2 Ah cell, the MRE statistics were even poorer, but when two outliers were excluded in the new data, the statistics got better with error bounds as 7 % and -9.47 %, mean and standard deviation were respectively 0.67 and 4.33. Even though it is understandable to see an MRE with poorer statistics than MFE, in our case, the statistics are comparable. Definitely a better RSE could lead to a better MRE. The predictive capability of the assumed model is probably reduced because of the inclusion of low temperature data such as at 0 ^{o}C. So higher order terms need to be employed to improve the predictability or narrow the design space if it is known the range of operation is narrower than considered here.

6.3.2.5. Response Surface Equation

Figure 6.9 shows the response surface of capacity as a function of the rate of discharge and temperature for both the commercial cells.

6.3.2.6. Analysis of the influence of the independent variables

Sensitivity Analysis

Sensitivity is a measure of the contribution of an independent variable to the total variance of the dependent data. Scatter plots and Pareto plots are used in this work. Pareto plots help in the prioritization of the independent variables according to their relative contribution to the variance in the response. These plots also help us in determining variables to focus on to reduce maximum uncertainty. Scatter plots have a global scope and are qualitative in nature [1]. Figure 6.10 shows the Pareto plot for both the commercial cells. This plot gives the relative influence of the variables and the interaction between variables on the response which is capacity of the cell in our case. The influence of the individual variables on the response can be viewed either in Figure 6.11, in a Scatter plot matrix, or in Figure 6.12 in the prediction profiler. The prediction profiler gives the change in capacity of the cell with respect to temperature or rate of discharge alone while the other variable remains fixed at a value within the range of interest. One can then obtain simulated responses using the RSEs created for, say 5000 runs, by using a random uniform distribution on temperature as well as rate of discharge within the design range. Random noise can also be added on the capacity values. In this case random noise with a standard deviation of 0.0436 for the 1.1 Ah cell and 0.1199 for the 3.2 Ah cell is added to the responses. The resulting capacity distribution is shown in Figure 6.13. The corresponding cumulative distribution function (CDF) is shown in Figure 6.14. These plots can be used in decision making process about avoiding undesired operating conditions. Desirability functions can also be used to arrive at optimal settings of operation to achieve the desired objective.

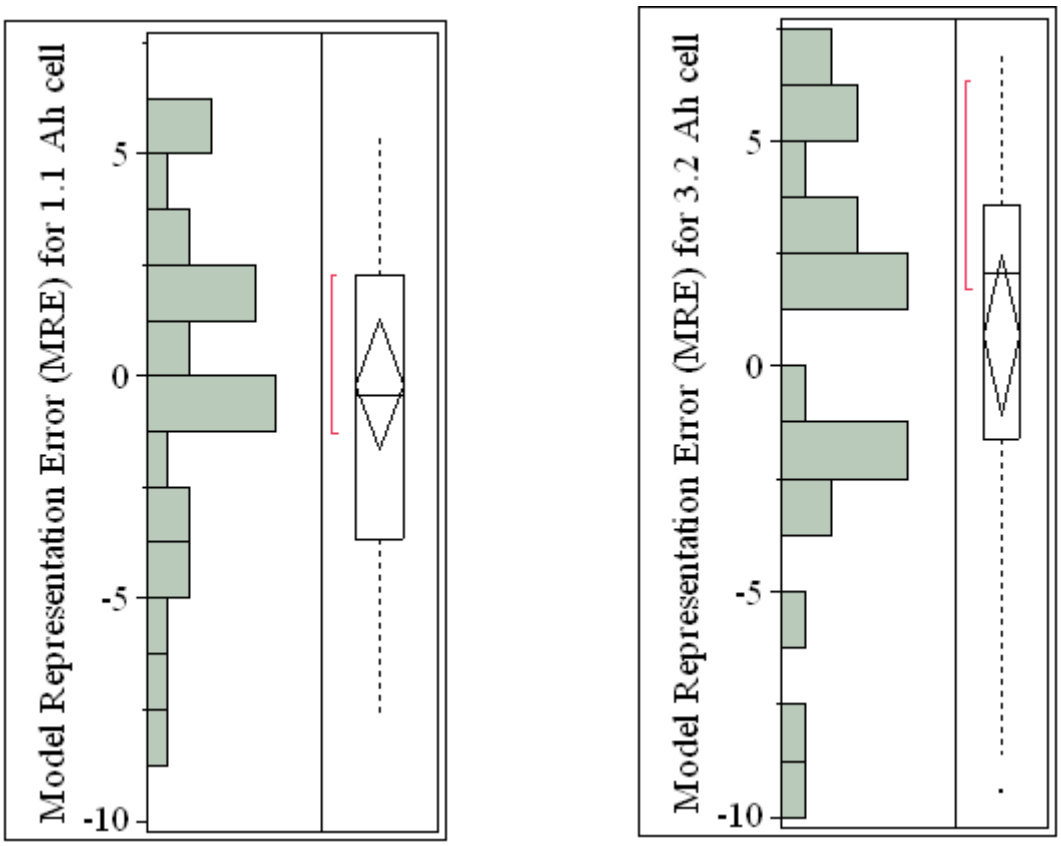

Figure 6.8. Model Representation Error (MRE) for (a) 1.1Ah cell (b) 3.2Ah cell.

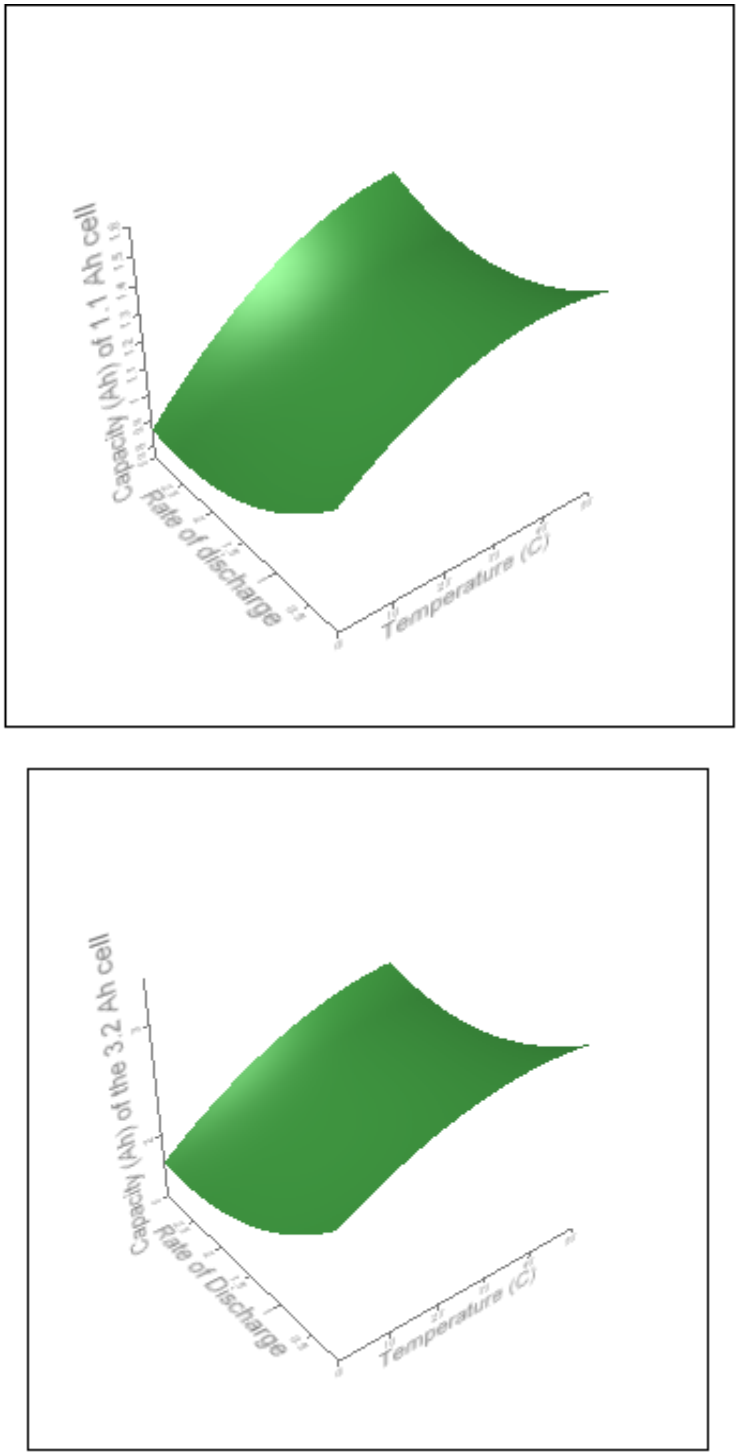

Figure 6.9. Response surface profiler of capacity as a function of temperature of operation and rate of discharge for (a) 1.1 Ah cell (b) 3.2 Ah cell.

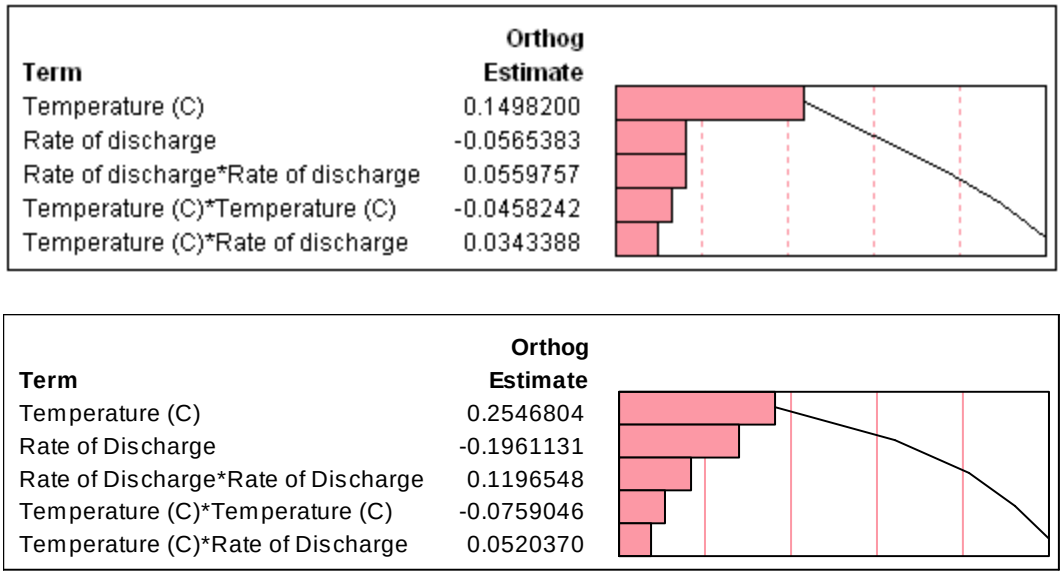

Figure 6.10. Pareto plot for the influence of temperature and rate of discharge on capacity of (a) 1.1Ah cell (b) 3.2 Ah cell.

6.4. Conclusions and Future Work

The Response Surface Equations when used outside the design range will give greater error. Hence in order to obtain good RSEs in such a case, one might have to expand the design range. When the design space is expanded too much, the design of experiments will have to be populated sufficiently using clever design of experiments to obtain good RSEs. Several other performance metrics like power, specific energy should also be studied and multiple RSEs can be created. This methodology can also be extended to understand the influence of variables such as electrode thickness and porosity on the capacity by using data from physics-based models to develop response surface equation. Finally, the RSM can be extended to study degradation in batteries by having number of cycles or storage time as one of the independent variables of interest. The interaction of temperature with cycle life and calendar life on capacity will also be of significance. Thus, a framework is established and illustrated for a high fidelity, computationally fast modeling approach using Response Surface Methodology for transferring

the knowledge about lithium ion batteries from experiments and physics-based models to the vehicle level system models [17].

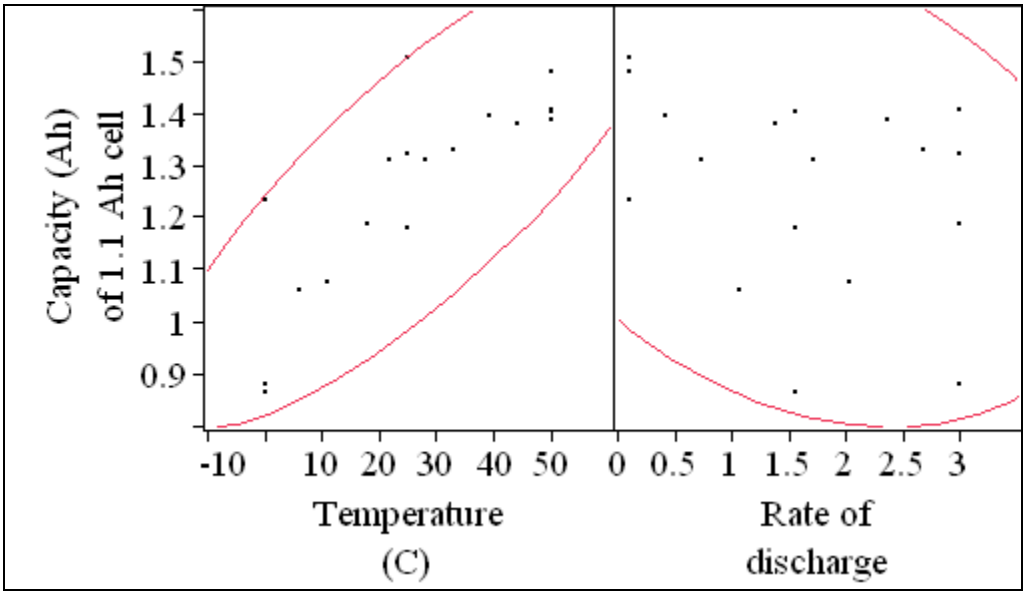

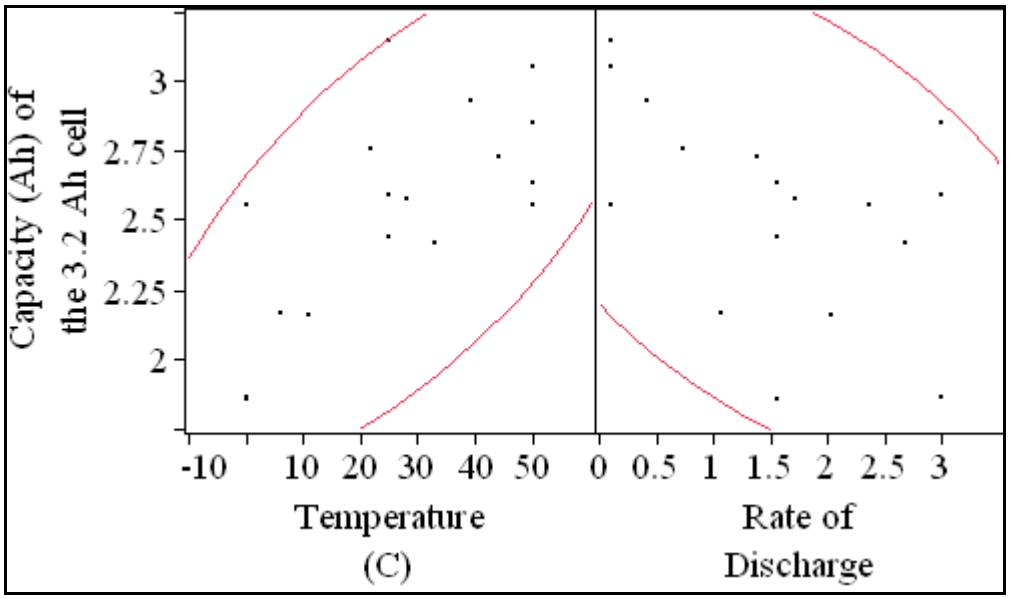

Figure 6.11. Scatterplot Matrix for (a) 1.1Ah cell (b) 3.2Ah cell.

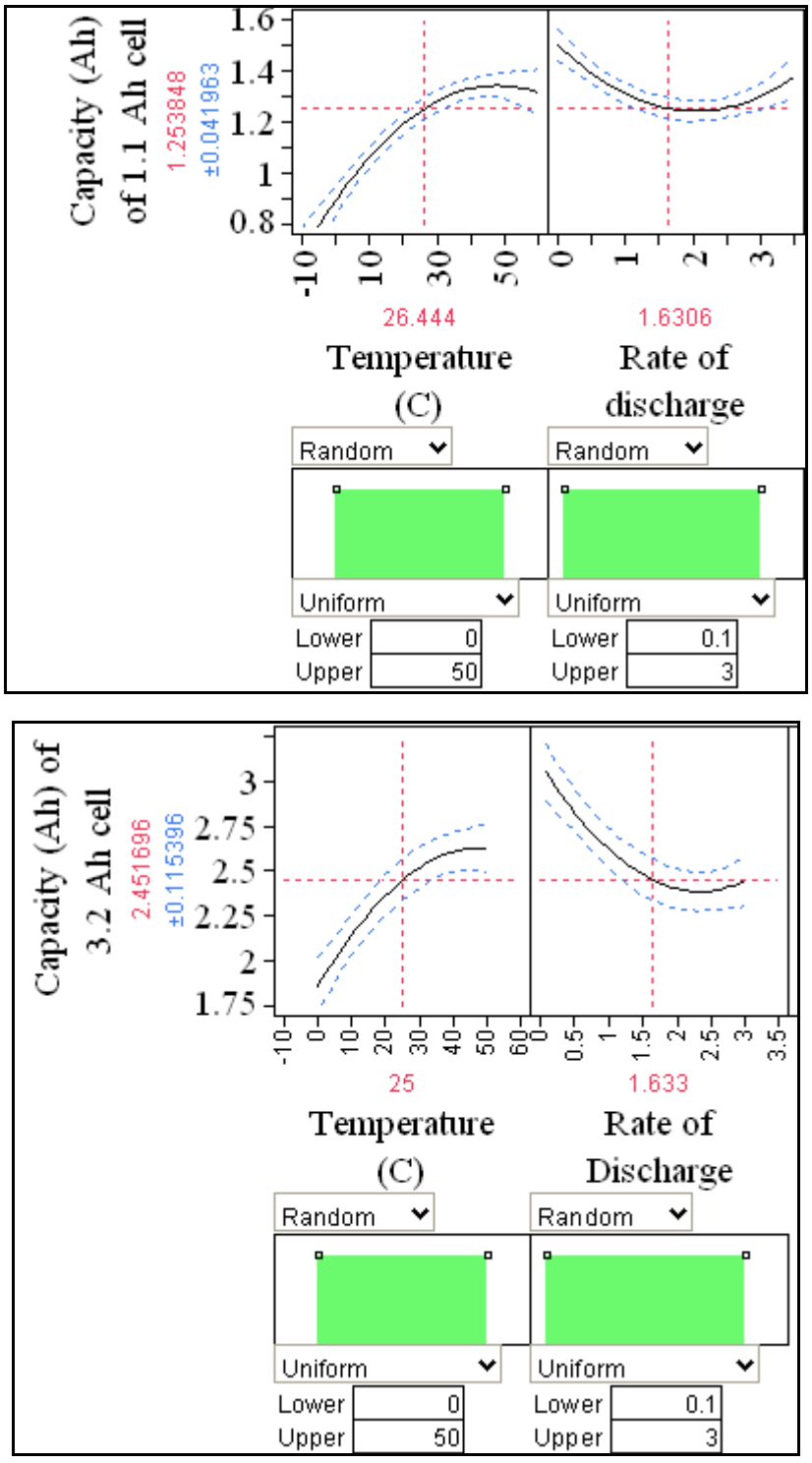

Figure 6.12. Prediction profiler for (a) 1.1Ah cell (b) 3.2 Ah cell.

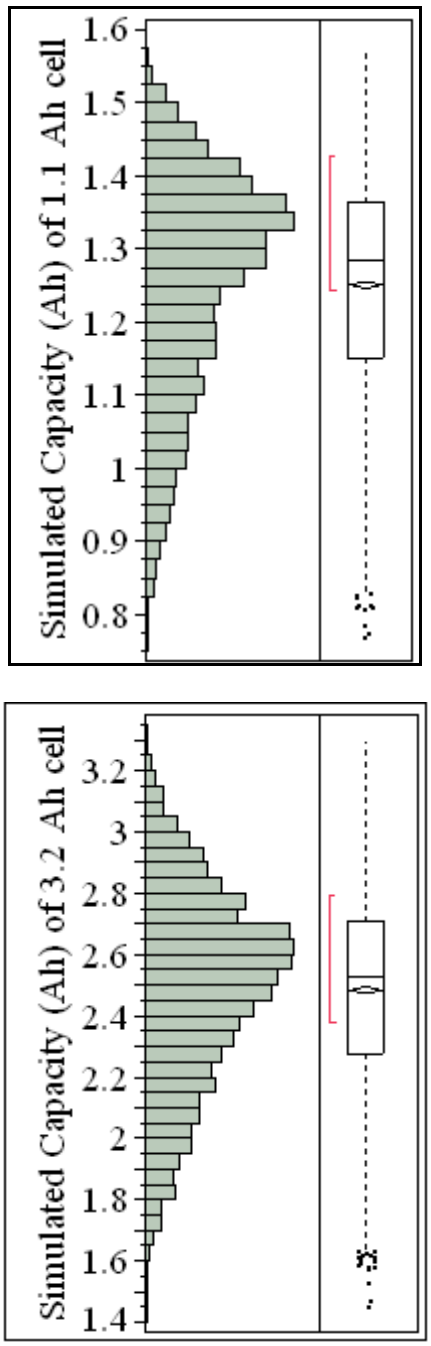

Figure 6.13. Simulated capacities of 5000 random cases accounting for uncertainties for (a) 1.1Ah cell (b) 3.2 Ah cell.

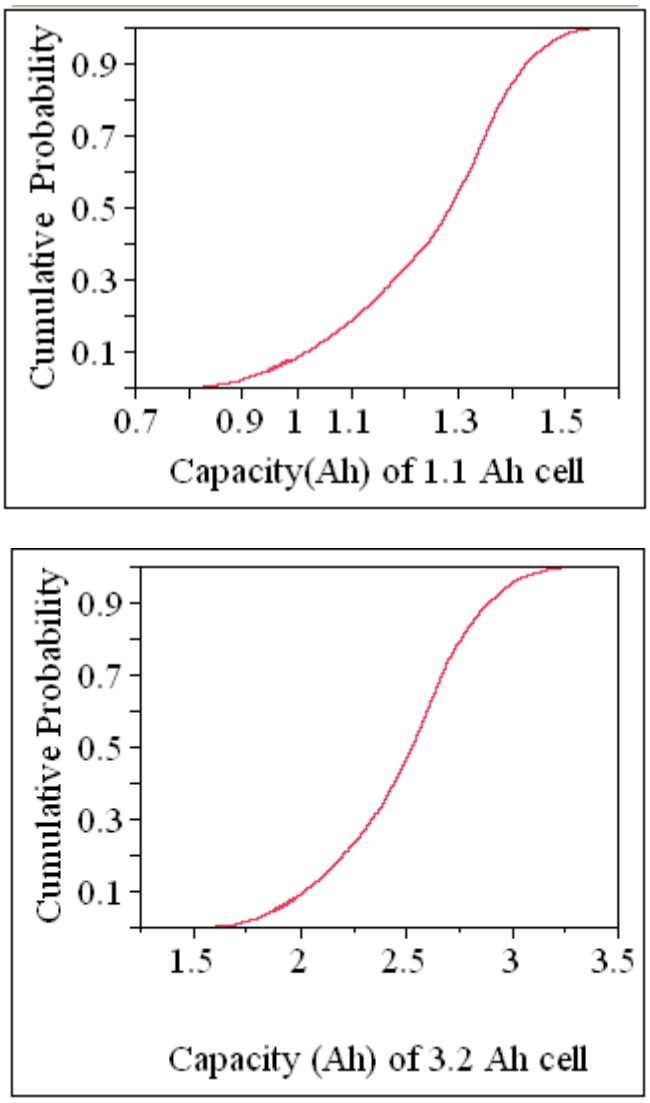

Figure 6.14. CDF plots for (a) 1.1Ah cell, CDF plots (b) 3.2Ah cell.

6.5. References

[1] Rajeswari Chandrasekaran, Wu Bi, Thomas F Fuller, *J.Power Sources* 182 (2008) 546-557.

[2] M.J. Kim, H. Peng, *J. Power Sources* 165 (2) (2007) 819– 832.

[3] W. Na, B. Gou, *J. Power Sources* 166 (2) (2007) 411– 418.

[4] Bor Yann Liaw, G. Nagasubramanian, R. G. Jungst, D. H. Doughty, *Solid State Ionics* 175 (2004) 835–839.

[5] http://www.transportation.anl.gov/modeling_simulation/PSAT/index.html

[6] Parthasarathy M. Gomadam, John W. Weidner, Roger A. Dougal, Ralph E. White, *J. Power Sources* 110 (2002) 267–284.

[7] Long Cai, Ralph White, *J.Electrochem.Soc.* 156 (3) (2009), A154-A161.

[8] Godfrey Sikha, Ralph E. White, and Branko N. Popov, *J.Electrochem.Soc.* 152 (8), A1682-A1693, (2005).

[9] B.Bhikkaji, T.Soderstrom*, Int.J.Control*, 74 (2001), 1543.

[10] Shriram Santhanagopalan and Ralph E. White, ECS Transactions (2007), 3(27, Lithium-Ion Batteries), 243-256.

[11] Dimitri N.Mavris, Oliver Bandte, Daniel A. DeLaurentis, *J.Aircraft*, 36(1), 1999.

[12] Godfrey Sikha, Branko N. Popov, Ralph E. White *J. Electrochem. Soc.* 151 A1104 (2004).

[13] Rajeswari Chandrasekaran, Godfrey Sikha, Branko N. Popov, *J.Applied Electrochemistry* (2005) 35, 1005–1013.

[14] Pankaj Arora, Ralph E. White, Marc Doyle , *J. Electrochem. Soc.* 145 3647 (1998).

[15] D.Bernardi, E. Pawlikowski, J. Newman, *J. Electrochem. Soc.*, 132 (1), 5-12 (1985).

[16] Karthikeyan Kumaresan, Godfrey Sikha, Ralph E. White, *J. Electrochem. Soc.* 155 A164 (2008).

[17] Rajeswari Chandrasekaran, Jonathan Denis, Michael Skinner, Thomas F. Fuller, Abstract # 457c (ID :133925Technical talk at the 2008 AIChE Annual Meeting: Philadelphia, PA (# P133925, Conference Proceedings on CD-ROM-ISBN 978-0-816910-1050-2).

CHAPTER 7

LITERATURE REVIEW, MODELING TECHNIQUE & TOOL FOR ANALYSIS OF SILICON NEGATIVE ELECTRODES

7.1. Introduction

The demand for lightweight, high-capacity, lithium-ion batteries for portable electronic devices, hybrid-electric vehicles, and large-scale energy storage, has led to intense interest in new positive and negative electrode materials that can store energy more densely [1]. Silicon is one such example for the negative electrode in lithium-ion batteries [2]. The theoretical value for energy density is 4200 mAh/g when $Li_{22}Si_5$ is the fully lithiated phase [3]. Earlier studies on Li-Si system were at high temperatures [4]. It is only recently that Li-Si systems have been investigated at room temperature [5]. Under these conditions, for all intents and purposes $Li_{15}Si_4$ is the fully lithiated phase attainable through an electrochemically driven solid state amorphization process [6] because formation of $Li_{22}Si_5$ phase may be kinetically hindered. Hence at room temperature, the maximum energy density is 3579 mAh/g for all practical purposes [7]. Even this lower value is far above that of graphite (372 mAh/g), which is currently used as the negative electrode for most rechargeable lithium cells.

7.2. Issues with silicon and efforts to overcome

Electrochemical cycling of Li-alloy electrodes is mostly associated with large volume changes (atleast > 100%) unlike that of insertion electrodes that have been studied so far such as Li_xC_6, $LiCoO_2$, $LiMn_2O_4$, $LiFePO_4$, etc. with < 10% volume changes [8]. At room temperature 250% [9] -280% [10] volume expansion is encountered in Li-Si system. Whereas the promise for Li-Si system is great, due to huge volume changes, good cycle life and high rate capability have

not yet been achieved, partly because of loss of electrical contact [9], [11]. Furthermore, insufficient space for volume changes in the silicon electrode upon lithium insertion/de-insertion and phase changes cause stresses that lead to pulverization and further contribute to irreversible capacity loss. At room temperature, slow kinetics [12], the low value of the diffusion coefficient of lithium in silicon [13] and its low electronic conductivity [14] are additional barriers. It is known that electrical contact between particles, electrical contact with the current collector, a proper solid electrolyte phase (SEI) layer, electrode porosity, binder chemistry and electrolyte degradation all affect cell performance. Now, with shrinking electrode-particle sizes [15], thin films [16], nano architectures and geometries [2] , [17], use of carbon along with silicon [18], alternate binders such as sodium carboxymethyl cellulose (CMC) [19], some of the problems have been overcome and lithium-silicon systems show promise for practical applications. Kasavajjula *et al.* have extensively reviewed the experimental efforts by different research groups to mitigate these issues [20].

7.3. Phase transitions at room temperature

For a lithium-silicon electrode at high temperature, crystalline phase transitions [4] follow the thermodynamic phase diagram [21], [22]; and hence the equilibrium potential *vs.* composition curve is used for modeling Li(Si)/FeS_2 cells at high temperature [23]. Recent reports [7], [24], [25], [26] suggest that when starting with crystalline silicon the alloying of lithium at room temperature proceeds through an amorphous phase transition that is associated with isotropic volume expansion [27]. A metastable phase is formed from an electrochemically driven solid state amorphization process instead of the crystallization process [6]. Kinetic arrest, similar to that found in glass formation [28], may prevent the amorphous alloy phase, a-Li_xSi, from crystallizing to the equilibrium phase in any reasonable time scale [29]. If lithiation is continued

below around 50 mV (all potentials are referenced to Li/Li^+), a-Li_xSi suddenly crystallizes to $Li_{15}Si_4$ [7]. The final amorphous phase composition, just before crystallization, was found from NMR studies [30] to be a-$Li_{3.4\pm0.2}Si$. Chevrier and Dahn [25] argue that since a-Li_xSi does not form any other crystalline phases, the final composition should be close to a-$Li_{3.75}Si$, corresponding to crystalline $Li_{15}Si_4$. During de-lithiation, an amorphous transition occurs resulting in a-Si. So even though one observes two sloping plateaus (crystalline Si→ a-Li_xSi→$Li_{15}Si_4$) [24] during the first lithiation, a single sloping curve is observed in subsequent cycles in either direction as long as the potential is restricted to values greater than 50 mV. To this end, better cycling performance has been reported when the potential is restricted to greater than 50 mV [7], [31] or 70 mV for particles larger than 500 nm [25]. However recent work with novel binders has shown that good cycle life can be obtained even if lower potentials (10 mV) are reached during lithiation [32]. Neither the amorphous phase nor the crystalline $Li_{15}Si_4$ phase observed at room temperature appears in the recent phase diagrams for the Li-Si system [21], [22] (contrasting earlier work by Sharma and Seefurth [33]).

7.4. Potential gap in potential *vs.* composition curve at room temperature

Chevrier and Dahn used density functional theory to calculate the potential *vs.* composition curve at equilibrium (absence of an electric field or polarization) at room temperature for amorphous silicon lithiation [25]. This may be called a pseudo-thermodynamic *vs.* composition curve since it is based on a metastable amorphous phase transition. Their prediction is more suited for modeling lithium-silicon system at room temperature than the thermodynamic potential *vs.* composition curve measured at high temperature [4]. Key *et al.* [30] observed that the open-circuit potential value of a lithium-silicon electrode after a full discharge continued to rise even after 320 hour at room temperature. They attributed this to the reactivity

of the metastable phase with the electrolyte and subsequent loss of lithium. They also observed that the relaxation of the open-circuit potential to 170 mV after a full discharge took nine days without a binder and a month with CMC as the binder. Ryu *et al.* [14] observed that the open-circuit potential after a twelve hour relaxation period during galvanostatic discharge still changes with applied pressure. Recently, Sethuraman *et al.* [34] demonstrated the use of multi-beam optical sensor technique to measure stress evolution in a silicon thin-film electrode and concluded that it was comparable to the polarization losses during lithiation and de-lithiation.

However, Chevrier and Dahn claimed earlier [25] that they don't observe any obvious hysteresis, since all the configurations in their calculations yielded similar formation energies from which potential was calculated. But the authors have neglected entropy and pressure terms in their expression for formation energy, which may be needed to understand the influence of hysteresis. Also, the accuracies as mentioned by the authors [25] are on the order of 0.1V, whereas hysteresis offset voltages of the order of 50 mV [35] have been observed in cobalt hydroxide containing nickel-hydroxide electrodes. It is acknowledged that the hysteresis observed in NiOOH electrode does not suggest anything about Li-Si system, but just cautions that the prediction of hysteresis can sometimes be limited by the level of accuracy that is attainable. More recent work by Chevrier and Dahn [36] discussed the limitations of their calculations in not being able to predict the potential gap observed in Li-Si even at significantly low rates. It was suggested that it could largely be due to the formation energies not taking into account the hysteresis arising from bond-breaking activation energies or due to electrolyte decomposition. The authors also suggested that a very small contribution could be from diffusion effects on the formation energies.

Hysteresis refers to the phenomenon where a change in direction of an independent variable causes a dependent variable to fail to retrace the values through which it passed in the forward process [35]. Hysteresis during lithium insertion into and extraction from high capacity disordered carbon has been observed before [37], [38] and there are suggestions that ascribe this to large charge transfer resistance and slow diffusion of lithium during de-lithiation [37]. At high temperature, the diffusivities of lithium in different lithium-silicon crystalline phases are of the same order of magnitude [4]. If this observation can be extrapolated to room temperature lithiation and delithiation of amorphous silicon as is considered here, then solid phase diffusivity should not be a function of lithium concentration and this possibility for explaining potential gap can be ruled out. Even at very low rates a potential difference between the lithiation and de-lithiation curve for most of the amorphous range of the lithium silicide alloy has been observed [7], [24], [39], [12]. Fuller *et al.* [40] point out that the different relaxation processes in lithium-ion insertion cells can have widely varying time constants. As mentioned before, because of the changes occurring during relaxation, the history of the cell is important for its performance. However, at significantly low rates, the transients after current-interruption discussed in their paper should not be measurable. At low rates, hysteresis from charge transfer resistance, for instance should be small or cease to exist. Similarly, even though porosity and tortuosity change considerably in silicon electrodes [41], neither these nor pore microstructural changes alone can account for the potential gap observed in silicon electrodes.

In silica [42] a kinetically hindered first-order transition between the low-density amorphous and the high-density amorphous phases occurs. This transition leads to two different curves in pressure-volume graph, one during compression and one during decompression. Dudney *et al.* [43] suggested that in amorphous or nanocrystalline $Li_xMn_{2-y}O_4$ cathodes at

potentials above 3V true hysteresis occurs even though the structural basis for this is unknown. Hysteresis in solid state reactions has been reviewed for many systems [44]. Hysteresis in disordered carbon has been interpreted as the rectification of the lithiated carbon in the presence of electrolyte, similar to that of the n-type semiconductors under anodic polarization [37].

Thermodynamic treatment of true hysteresis has been done using domain theory [45], whereas attempts for thermodynamic treatment of metastable states with slow relaxation processes have used an equivalent equilibrated state [46]. Presaich's model was used for a macroscopic understanding of the hysteresis by Ta and Newman in nickel hydroxide electrodes [35], even though these models do not lend any insight as to the specific molecular-scale causes of hysteresis.

7.5. Use of cyclic voltammetry (CV) and microelectrodes to verify presence of hysteresis

Levi and Aurbach [47] suggested a modified Frumkin intercalation isotherm for capturing the intrinsic hysteresis in the potential-composition curves for lithiated graphite electrodes, which reflects the dynamics of phase transition very close to thermodynamic control. The current observed in the voltammetry of a single electrode particle (~ microelectrode) is orders of magnitude less than that observed in typical electrode experiments. Verbrugge and Koch [48] experimentally studied lithium intercalation in a single carbon fiber electrode because in a microelectrode technique the solution phase resistance is negligible. Guilminot *et al*. [49] concluded that an "ultramicroelectrode with cavity" (UMEC) is a better technique than a porous rotating disk electrode (RDE) to characterize fuel-cell electrocatalysts using cyclic voltammetry because interference from the binder is avoided.

7.6. Volume changes in silicon electrodes

Volume changes in porous electrodes can be manifested in two ways: porosity changes and/or changes in porous composite silicon negative electrode dimensions during lithiation/ de-lithiation. Beattie *et al.* [11] have shown through simple model and experiments that silicon composite electrodes with less than 20% by volume of silicon cycle well. A highly porous electrode can accommodate the huge (~ 270%) volume expansion with little or negligible electrode particle movement. This means, even though the volume expansion of the individual silicon electrode particles with lithiation is large (and hence porosity changes are significant), the absolute volume expansion of the composite electrode is subdued [11]. This is important, because unless suitable binder is used or extra space is provided, changes in composite electrode dimensions lead to poor cycling capability.

Theoretical treatment of volume changes in porous electrodes is available in literature [50-58]. Newman and Tiedemann [50] reviewed the methodology to include porosity changes with extent of reaction at each location within the electrode by material balance on solid phase. Gu *et al.* [51] used the macroscopic treatment to analyze Ag/AgCl porous electrodes with sparingly soluble reactants. Evans *et al.* [52] modeled the lithium/thionyl primary chloride cell with porosity changes and a reservoir to supply electrolyte as it is consumed at the cathode. Pollard and Newman [53] modeled porosity changes in lithium-aluminum iron sulfide battery at high temperature. Bernardi and Newman [23], [54] modeled Li (alloy) iron disulfide cells at high temperatures. Sikha *et al.* [55] analyzed the effect of porosity on the capacity fade of a lithium-ion battery. Porosity changes due to both intercalation reaction and side reaction is considered for evaluating initial cell performance. Since porosity changes due to side reactions dominate capacity fade and that due to intercalation reaction can be assumed to be reversible (*i.e.* changes

in porosity during charging is reversed during discharging), former is considered for cycle life. Gomadam and Weidner *et al.* [56] modeled volume changes in porous electrodes which includes both changes in pore volume fraction and in electrode dimensions. The authors introduced a term called swelling coefficient (g) which has to be determined experimentally. For g=0, the volume changes are entirely reflected as porosity changes and for g=1, the volume changes result solely in changes in electrode dimensions, keeping the porosity constant.

Porosity changes can arise when the molar volume of the product of the main reaction [53] or that of the side reaction is larger than that of the reactants [55]. In the former case, this can lead to a change in particle size if the product is not precipitated separately. The effective transport properties such as diffusion coefficient of Li ions in the salt (*i.e.* solution phase) in the negative electrode matrix, conductivities in the solution and matrix phase as well as the interfacial area per unit electrode volume are dependent on porosity [55]. Usually, the solid electrode material is more conductive than the electrolyte. Hence as porosity decreases, the current flows through a more tortuous path in the electrolyte phase [54] and leads to a higher ionic resistance (or internal resistance [53]) and increased polarization of the system. Variations in porosity are usually greater at the electrode-separator interface [55]. Decreased porosity also leads to steeper concentration gradients [55]. All these lead to a sharp reduction in cell voltage [53] and hence the system can reach the cut-off potential even before the pore volume fraction drops to zero [56]. Thus the system could be ionically limited when the volume changes are manifested as solely porosity changes with no change in electrode dimensions. Hence, increasing the initial porosity increases the cell voltage as well as utilization (i.e. larger operating time before the pores are completely filled for g=0) [54], [56]. Moreover, usually the rate of change of average porosity decreases with cycling due to the fact that, as more reaction product is formed,

it hinders the side reaction rate because of the decrease in the interfacial area. Changes in porosity also affect the rate capability with cycling, especially at higher rates of discharge [55].

But, Pollard and Newman suggested that in reality, porosity variations may not be as acute as predicted [53] because the electrodes could swell or expand, i.e. undergo change in porous electrode dimensions. This expansion could occur by compaction of separator or displacement of can walls or motion of electrodes relative to one another during a particular charge or discharge and they suggested that such a change in electrode dimensions might be a prerequisite for successful operation of battery packs with high electrode capacities in electric vehicles [53]. But changes in porous electrode dimensions can lead to short circuit and flexible can wall might pose a challenge for mechanical integrity of the batteries in an automobile application. This problem can be circumvented by improved mechanical construction of the electrodes wherein they are constrained at the faces and edges to prevent expansion and designing electrodes with high initial porosity [54]. A methodology to account for the permanent changes in electrode dimensions that occurred in first few cycles and also the reversible expansion in subsequent cycles with available experimental data is available in literature [54]. The change in thickness of the electrodes was related to initial porosity.

Pollard and Newman [53] evoked pseudo-steady state approximations to evaluate the solid concentration since the time needed for solid phase diffusion was much smaller than the time needed for complete utilization of the electrode particle. Even though the actual particle size might have changed with greater molar volume of Li_2S as compared to the reactants, this is not considered in their model. Contribution of convection to the spatial variation of electrolyte concentration in the cell sandwich mainly arises from the influx or squeezing of the electrolyte as the porosity changes. Convection has been neglected in some literature [55], which is valid for

the electrode system under consideration and galvanostatic rate of operation employed, whereas others [23], [51-54] have included and the order of magnitude of the velocity is estimated to be small [53]. When porosity changes are due to formation of precipitates, access to solid electrode particles could be hindered. Strictly speaking, one has to then consider the transport through the outer precipitate before diffusion inside the particle is possible. Alternately, Sikha *et al.* [55] have indirectly included this effect by varying the solid phase diffusion coefficient as side reaction products are formed. Gomadam and Weidner [56] analyzed volume changes for the special case of uniform current distribution. In reality, charge balance in matrix and solution phases and mass balance for all species should be solved along with their model to obtain reaction rate distribution and obtain results comparable with experimental data. Moreover, most work used dilute solution theory for their systems whereas for lithium ion systems, as done in reference [55] concentrated solution theory has to be used.

The next section provides a brief overview of the modeling technique and tool employed in this thesis for analysis of lithium insertion/ de-insertion in silicon electrodes.

7.7. Finite Element Method

COMSOL [59] is the software used to develop both the particle model in Chapter 8 and the cell sandwich model for lithium-silicon electrodes in Chapter 9. COMSOL uses the Finite Element Method (FEM) to solve coupled multiphysics phenomena. Finite element method is one wherein the difficulty of solving large complex geometric problems is transformed from a differential equation approach to an algebraic problem. The building blocks or finite elements have all the complex equations solved for their simple shape [60]. The finite element models are defined by grid points located in three-dimensional space. Location of these grid points are defined by coordinate systems. Also, grid point displacements and other properties may for convenience

require a different coordinate system from that used to locate the grid points. Different coordinate systems used in FEM analysis include fundamental, local, element, displaced and material coordinate systems. The way finite element analysis (FEA) obtains desired unknown parameters in the finite element model is by minimizing energy functional. An energy functional consists of all the energies associated with the particular finite element model. From law of conservation of energy, this functional must be zero. The accuracy of the calculations generally increases as the number of elements in the model increases. Matrices and matrix methods were included in the FEM analysis to organize large numbers of algebraic equations. The number of unknowns in the matrix equation for one element equals the number of grid points in the element times the number of degrees of freedom per grid point. The matrix equation for the finite element model is an assembly of the matrix equations of all its finite elements. In order to save computational time, the computer program resequences the matrix rows and columns to move the nonzero entries in the N by N stiffness matrix along the matrix diagonal. Solution types of FEM analysis include steady-state static solution, transient solution, eigenvalue problem.

7.8. References

[1] J.Graetz, C.C.Ahn, R.Yazami, B.Fultz, *Electrochem.Solid-State.Letts.*, 6 (9) (2003), A194-A197.

[2] C. K. Chan, H. Peng, G.Liu, K.McIlwrath, X.F.Zhang, R.A.Huggins, Y.Cui, *Nature Nanotech.*, 3 (2008), 31-35.

[3] Robert A, Huggins, R.A., *J.Power Sources*, 81-82 (1999), 13-19.

[4] C.J.Wen, R.A.Huggins, *J.Solid.State Chem.*, 37 (1981), 271-278.

[5] D.Larcher, S.Beattie, M.Morcrette, K.Edström, Jean-Claude Jumas, Jean-Marie Tarascon, *J.Mat.Chem.*, 17 (2007), 3759-3772.

[6] Pimpa Limthongkul, Young-Il Jang, Nancy J. Dudney, Yet-Ming Chiang, *Acta Materialia*, 51 (2003), 1103–1113.

[7] M. N. Obrovac, L.Christensen, *Electrochem.Solid- State Letts.*, 7 (5) (2004), A93-A96.

[8] M.Winter, J.O. Besenhard, M.E. Spahr, P.Novák, *Adv. Mater.*, 10(10) (1998), 725-763.

[9] Z.Chen, L.Christensen, J.R.Dahn, *Electrochem.Comm.*, 5 (11) (2003), 919-923.

[10] M.N.Obrovac, Leif Christensen, Dinh Ba Le, J.R.Dahn, *J.Electrochem.Soc.*, 154 (9) (2007), A849-A855.

[11] S.D. Beatie, D.Larcher, M.Morcrette, B.Simon, J.M.Tarascon, *J.Electrochem.Soc.*, 155(2) (2008), A158-A163.

[12] Model-Experimental Studies on Next-generation Li-ion Materials, Venkat Srinivasan, OVT Merit Review, May 21, 2009.

[13] E.M.Pell, *Phys.Rev.*119 (4) (1960), 1222-1225.

[14] J.H.Ryu,J.W.Kim,Y.Sung,S.M.Oh, *Electrochem.Solid-State.Letts.*, 7(10) (2004), A306-A309.

[15] A. Magazinski, P. Dixon, B. Hertzberg, A. Kvit, J. Ayala, G. Yushin, *Nature Materials*,14 March 2010, DOI:10.1038/NMAT2725.

[16] J.P.Maranchi, A.F.Hepp, P.N.Kumta, *Electrochem.Solid-State Lett.*, 6 (2003), , A198-A201.

[17] T.Song, J.Xia, J.Lee, D.Lee,M.Kwon, J.Choi, J.Wu, S.Doo, H.Chang, W.Park, D. Zang, H.Kim, Y.Huang, K.Hwang, J.Rogers, U.Paik, DOI: 10.1021/nl100086e, *Nano Lett.* (ASAP).

[18] L.F.Cui, Y.Yang, C.M.Hsu, Y.Cui, *Nano Lett.*, 9 (9) (2009), 3370-3374.

[19] Juchen Guo , Chunsheng Wang, *Chem. Commn.*, 46 (2010), 1428–1430.

[20] U.Kasavajjula, C.Wang, A.J.Appleby, *J.Power Sources*, 163 (2007), 1003-1039.

[21] H.Okamoto, *Bulletin of Alloy Phase Diagrams*, 11(3) (1990), 306-312.

[22] M.H.Braga,L.F.Malheiros,I.Ansara, *J.Phase Equilibria*, 16 (4) (1995),324-329.

[23] Dawn Bernardi, John Newman, *J.Electrochem.Soc.*, 134 (6) (1987), 1309-1318.

[24] T. D. Hatchard, J. R. Dahn, *J. Electrochem.Soc.*, 151 (6) (2004), A838-A842.

[25] V.L. Chevrier, J. R. Dahn, *J.Electrochem.Soc.*, 156 (6) (2009) A454-A458.

[26] L. Y. Beaulieu, K. W. Eberman, R. L. Turner, L. J. Krause, J. R. Dahn, *Electrochem Solid-State Letts.*,4 (9) (2001), A137-A140.

[27] A. Timmons, J. R. Dahn, *J.Electrochem.Soc.*, 154 (5) (2007), A444-A448.

[28] Valerie J. Anderson, Henk N.W.Lekkerkerker, *Nature*, 416 (2002), 811-815.

[29] W.L.Johnson, *Mat. Sci. Engg.*, 97 (1988), 1-13.

[30] B.Key, R.Bhattacharyya, M.Morecrette, V.Seznec, J.M.Tarascon,C.P.Grey, *J. Am. Chem. Soc.*, 131 (26) (2009),9239–9249.

[31] M. N. Obrovac, L. J. Krause, *J. Electrochem.Soc.*, 154(2) (2007), A103-A108.

[32] A.Magasinski, B.Zdyrko, I.Kovalenko, B.Hertzberg, R.Burtovyy, T.F. Fuller, I.Luzinov, G.Yushin, *ACS Applied Materials and Interfaces* (submitted).

[33] Ram A. Sharma and Randall N. Seefurth, *J.Electrochem.Soc.*, 123(12) (1976), 1763-1768.

[34] V.Sethuraman, M.J. Chon, M.Shimshak, V.Srinivasan, P.R. Guduru, *J. Power Sources*, 195(15) (2010), 5062-5066.

[35] K.Podolske Ta, John Newman, *J.Electrochem.Soc.*, 146 (8) (1999), 2769-2779.

[36] V.L.Chevrier, J.R.Dahn, *J. Electrochem.Soc.*, 157 (4) (2010), A392-A398.

[37] Norio Takami, Asako Satoh, lakahisa Ohsaki, Motoya Kanda, *J. Electrochem. Soc.*, 145 (2) (1998), 478-482.

[38] Edward Buiel, J.R. Dahn, *Electrochim. Acta* 45 (1999), 121-130.

[39] L.Baggetto, R.A.H.Niessen, F.Roozeboom, P.H.L.Notten, *Adv.Funct.Mat.*, 18 (2008), 1057-1066.

[40] Thomas F.Fuller, Marc Doyle, John Newman, *J. Electrochem.Soc.*, 141(4) (1994).

[41] R.Chandrasekaran, A.Magasinski, G.Yushin, T.F.Fuller, 217th ECS meeting, Vancouver, Canada, April 2010.

[42] Daniel J. Lacks, *Phys.Rev.Letts.*, 84 (20) (2000), 4629-4632.

[43] N.J.Dudney, J.B.Bates, C.D.Evans, ORNL/CP-102734, April 1999.

[44] T. B. Flanagan, C.-N. Park W. A. Oates, *Prog. Solid State. Chem.*, 23 (1995), 291-363.

[45] D.H. Everett, W.I.Whitton, *Trans.Faraday Soc.*, 48 (1952), 749.

[46] Daniel Kivelson, Howard Reiss, *J.Phys.Chem.B.*, 103 (1999), 8337-8343.

[47] M.D.Levi, D.Aurbach, *J.Phys.Chem.B*, 101 (1997), 4630-4640.

[48] Mark W. Verbrugge, Brian J.Koch, *J.Electrochem.Soc.*, 143(1) (1996), 24-31.

[49] Elodie Guilminot, Audrey Corcella, Marian Chatenet, Fre´de´ric Maillard, *J.Electroanal.Chem.*, 599 (2007), 111–120.

[50] John Newman, William Tiedemann, *AIChE Journal*, 21(1) (1975), 25-41.

[51] Hiram Gu, Douglas N.Bennion, John Newman, *J.Electrochem.Soc.*, 123(9) (1976), 1364-1370.

[52] T.I.Evans, T.V.Nguyen, R.E. White, *J.Electrochem.Soc.*, 136 (2) (1989), 328-339.

[53] Richard Pollard, John Newman, *J.EIectrochem. Soc.,* 128(3) (1981), 491-502.

[54] Dawn Bernardi, Ellen M. Pawlikowski, John Newman, *J.EIectrochem. Soc.*, 135(12) (1988), 2922-2931.

[55] Godfrey Sikha, Branko N. Popov, Ralph E. White, *J. EIectrochem. Soc.*, 151 (7) (2004), A1104-A1114.

[56] Parthasarathy M. Gomadam, John W. Weidner, *J. EIectrochem. Soc.*, 153 (1) (2006), A179-A186.

[57] R.C.Alkire, E.A.Grens II, C.W.Tobias, *J.Electrochem.Soc.*, 116 (1969), 1328.

[58] J.S. Dunning, D.N.Bennion, J. Newman, *J.Electrochem.Soc.,* 120 (1973), 906.

[59] http://www.comsol.com/

[60] What Every Engineer Should Know About Finite Element Analysis, edited by John R. Brauer, ISBN 0-8247-7832-4.

CHAPTER 8

ANALYSIS OF LITHIUM INSERTION / DE-INSERTION IN SILICON ELECTRODE PARTICLE AT ROOM TEMPERATURE

8.1. Introduction

The differences between lithium-silicon and graphite systems suggest that the electrode and cell design will need to be altered. A detailed mathematical model is vital for understanding the performance at the cell level, optimization, effective scale-up, and improvement of cycle life. Existing models of lithium-ion cells are based on porous electrode theory, and transport of electrolyte is accounted for using concentrated solution theory [1], [2] [3]. Transport in the solid phase and charge transfer kinetics at the electrode surface are also included in these models. An expression for the open-circuit potential *vs.* composition is used to evaluate the overpotential. It is worthwhile to investigate if the same approach is valid for modeling the Li-Si system at room temperature. It is to be noted that the equilibrium potential *vs.* composition curve that was used at high temperature cannot be used for modeling Li-Si system at room temperature for reasons discussed in Chapter 7, and a pseudo-thermodynamic potential *vs.* composition curve should be used. Further, a potential gap is observed even when cycled at low rates such as C/1000.

The implications of the offset voltage due to hysteresis are two-fold. First, the round-trip energy efficiency of the battery with a silicon electrode would be lower than 100 % even at very low rates [4]. Second, the state of charge, which is an indicator of the stored energy of the battery pack, will be more difficult to determine, perhaps increasing the complexity of control algorithms [5]. Hence, it is necessary to analyze if hysteresis is present in Li-Si system at room temperature. Accordingly, if needed, pseudo-thermodynamic potential *vs.* composition curve has to be further modified before pursuing cell level model.

There is either a slow relaxation process whose time constant is orders of magnitude higher than the time scale of experiments leading to an apparent hysteresis or there is a true hysteresis that has to be considered in lithium-silicon system at room temperature [6]. True hysteresis requires stable, reproducible, and time-independent behavior, such as that observed in magnetism or adsorption isotherms [7], [8]. A hypothesis with the semiconductor nature of silicon is discussed below.

The rate of the electrode process depends on the electronic structure of the semiconductor electrodes. When a semiconductor such as silicon is used as the electrode material, two exchange current densities have to be distinguished for the exchange of electrons with the conduction band and valence bands respectively [9] due to the significant energy gap and the diffuse double layer (space-charge type) [10]. The potential difference applied to interfacial reactions is not just the applied or easily measured potential but should be corrected for potential variations within the space charge region of the semiconductor. Newman and Thomas-Alyea [11] also suggest that anodic transfer coefficients are smaller for electron reactions that are favored in the cathodic direction and are larger for hole reactions that are favored in the anodic direction. These conclusions apparently describe the interaction of the semiconductor space-charge region with the interface and not just the kinetics of the interfacial reactions. All these will have to be further verified by experiments in Li-Si electrodes. However, these indicate another possibility to explain the potential gap that has been observed between lithiation and de-lithiation curves.

The small hysteresis (~ 10 mV) [12], [13], [14], negligible volume change [12] and relatively facile kinetics for lithium intercalation/de-intercalation in graphite make it markedly different from the Li-Si system. Hence it is sensible to investigate hysteresis in the Li-Si system. The objective is to clarify the impact on cell performance and to identify the proper treatment for

future modeling efforts of full cells. Cyclic voltammetry is a useful technique in this regard. In cyclic voltammetry, the potential difference between the corresponding peaks in the cathodic and anodic directions due to kinetic hysteresis (relaxation effects in the timescale of the experiment) should tend to zero [16] as the scan-rate is lowered. The peak potential separation due to true (or thermodynamic hysteresis) such as that observed by Levi and Aurbach [15] in lithiated graphite electrodes and that due to apparent hysteresis with very long relaxation time constants as compared to the experimental timescale exist even under low scan rates. This weakens the mirror symmetry of the peaks to an extent [16].

Among other concerns with silicon electrodes, it is known that the diffusion coefficient of lithium in silicon [17] is orders of magnitude less than that in carbon based electrodes [18]. Recent advancements in nanostructures and nano architectures have facilitated transport of lithium in silicon at room temperature [19], [20], [21], [22] by reducing the diffusion path length, though transport is still less facile than in carbon. The kinetics of lithium insertion in silicon is also reported to be slower as compared to that in carbon [23]. Knowledge of the solid phase diffusion coefficient and kinetic parameters is vital to understanding the performance at the cell level through modeling efforts discussed before. Since few data are available on the solid state diffusion coefficient of lithium in silicon and the kinetic parameters, methods to determine kinetic and transport properties of lithium insertion/de-insertion are desired.

Microelectrode techniques [24] are one possibility where cyclic voltammetry and other experiments can be made on a single silicon electrode particle [25]. Physico-chemical parameters may be inferred by comparing the data with a corresponding single particle model [26]. Hence, it is believed that microelectrode technique reduces greatly the distortion of cyclic voltammetric

behavior due to ohmic resistance, which is found in studies of porous electrodes. Lithium intercalation in single-fiber carbon microelectrodes have been modeled before [27].

A single particle model that neglects volume changes has also been reported for spinel particles under potentiodynamic control [26]. Volume changes due to the intercalation of lithium in a carbon fiber have been studied previously under potentiodynamic control [28]. Christensen and Newman [29] have studied stress in single micron-sized particle. In both Verbrugge and Koch's [27] and Botte's work [28], constant current densities were used for the flux boundary condition at the surface of the particle, and the associated error might have been less doing so because of the small volume changes. However, in the present work, this has to be modified because the volume changes in Li-Si system are ~ 250% [30]-280% [31] at room temperature.

In this work, lithium insertion/de-insertion in a single silicon electrode particle is modeled under potentiodynamic and galvanostatic control. The results are compared with experimental data and justification is provided to employ a pseudo-thermodynamic potential (with path dependence) based on metastable phase transitions for further modeling of lithium-silicon systems at the cell level. The exchange current densities are also obtained for lithiation and de-lithiation and the possibility of kinetics at semiconductor (silicon) electrode leading to path dependence is hypothesized. Alternatively, kinetic hysteresis involving unequal values of transfer coefficients that could lead to the potential gap is analyzed. The limitations of this mechanism and the need for further experiments to deduce kinetic parameters are discussed. The present work will help to better understand the influence of solid phase transport and kinetic properties during lithium insertion/de-insertion in a single silicon electrode particle with volume changes under either a galvanostatic or potentiodynamic control. This model and knowledge

thereof can then be used in a full cell-sandwich model of practical lithium-ion cells with composite silicon negative electrodes.

8.2. Model Development

A schematic of a lithium-silicon composite electrode / separator / lithium foil electrode cell [1] and single particle of lithium-silicon electrode is given in Figure 8.1. The following assumptions are made for the single-particle model: (i) Only radial diffusion occurs; (ii) Butler-Volmer kinetic expression governs the charge transfer reaction at the electrode/electrolyte interface; (iii) Double layer capacitance and any side reactions are neglected; (iv) the Li^+ concentration in the electrolyte phase is constant; (v) The particle is a solid sphere; (vi) Amorphous lithiation/ de-lithiation is considered; (vii) Isotropic volume change (uniform radial growth/shrinkage) [32]; (viii) the particle size is small enough so that fracture does not occur [33]. This assumption is further explained below.

In thin films of amorphous alloys, it has been proposed that the capacity loss occurs because contact is lost due to expansion/contraction of the particles and the associated volume changes and not due to pulverization that occurs in crystalline films [34]. It has been shown that below a certain thickness [34], among many other factors, crystallization to $Li_{15}Si_4$ also does not occur in thin films (irrespective of the potential). Mechanical degradation is counteracted by the use of thin layers of alloys with small particle size materials ("submicro- or nanomaterials") [35]. Hence neglecting stress is valid in this work.

(ix) The final assumption is that the electrochemical reaction that occurs at the surface of the particle is considered as

$$Li^+ + e^- + Si_{4/15} \underset{k_b}{\overset{k_f}{\rightleftharpoons}} LiSi_{4/15} \qquad (1)$$

and this can be thought of as:

$$Li^+ + e^- \rightleftharpoons Li \qquad (2)$$

$$Li + Si_{4/15} \rightleftharpoons LiSi_{4/15} \qquad (3)$$

Material balance on Li is given in Equation (4) (detailed discussion is given in Appendix C.1),

$$\frac{\partial c}{\partial t} + \frac{1}{r^2}\frac{\partial}{\partial r}\left(r^2\left(-D_{Li}\frac{\partial c}{\partial r}\right)\right) = 0 \qquad (4).$$

The initial and boundary conditions are

$$\left.\begin{array}{ll} c = 0 & @\ t = 0 \quad \text{(lithiation)} \\ c = c_{280\%} = 81923\ \text{mol/m}^3 & @\ t = 0 \quad \text{(de-lithiation)} \end{array}\right\} \qquad (5)$$

$$D_{Li}\frac{\partial c}{\partial r} = -\frac{i'}{nF} \qquad @ r = R_p(t) \qquad (6)$$

$$\frac{\partial c}{\partial r} = 0 \ @\ r = 0 \qquad (7)$$

where $i' = i\left(\frac{R_{p_0}}{R_p(t)}\right)^3$

Charge transfer kinetics at the surface of the particle for reaction (1) is assumed to be described by the Butler-Volmer equation.

$$i = \left(i_0\left\{\exp\left(\frac{\alpha_a F\eta}{RT}\right) - \exp\left(\frac{-\alpha_c F\eta}{RT}\right)\right\}\right) \qquad (8a)$$

where

$$i = \frac{I}{4\pi\left(R_p(t)\right)^2} \qquad (8b)$$

and where i_0 is the exchange current density given by

$$i_0 = F\ k\ (c_e)^{\alpha_a}\ \left(c_{\max_0} - c_s'\right)^{\alpha_a}\left(c_s'\right)^{\alpha_c} \qquad (9)$$

where $c_{\max_0} = \frac{N_{tot}}{\frac{4}{3}\pi {R_{p_0}}^3}$, $c_s' = c_s\left(\frac{R_p(t)}{R_{p_0}}\right)^3$.

k represents the product of the forward and backward rate constants in reaction (1) each raised to a power depending on the transfer coefficients for the charge-transfer reaction at the electrode surface.. It should be noted that since two different curves are used for U, k can have different values depending on the path followed. A wide range of exchange current density values has been reported in literature and is the range analyzed in this work [23], [36], [37], [38], [39]. N_{tot} is the total number of moles of Li that can be inserted in the silicon electrode based on the mass of the bare silicon electrode particle and a maximum molar Li:Si ratio of 3.75:1 (as a first approximation, the final composition considered is $Li_{15}Si_4$; c_e is the concentration lithium in the electrolyte; c_s is the concentration of Li in the solid phase at the surface of the particle, and α_a, α_c are the anodic and cathodic transfer coefficients respectively. The kinetic expression and the flux are slightly modified from earlier modeling studies [1] as discussed in Appendix C.1.

The overpotential η is defined as

$$\eta = \varphi_1 - \varphi_2 - U(x_s), \quad \text{where } x_s = \frac{\frac{4}{3}\pi\left(R_p(t)\right)^3}{N_{tot}} c_s \qquad (10)$$

φ_1 is the metal potential, φ_2 is the solution potential, and U is the pseudo-thermodynamic potential (dependent on surface composition, x_s), which includes a contribution from hysteresis as discussed before. The open-circuit potential formulation for nickel metal hydride batteries had an empirical expression to capture the salient features of the varying voltage hysteresis [5]. Ta and Newman [40] allowed the two loops of the potential composition curve to be offset by a constant value. In this work, two experimental curves from the literature [38] are employed to reflect hysteresis. When analyzing the alternate mechanism where variation in transfer coefficients explains the potential gap, U represents a single curve with no path dependence, as discussed later. The Li/Li^+ reference electrode is assumed to be placed in the electrolyte adjacent

to the electrode particle. Arbitrarily, the solution phase potential is assumed to be zero at the reference electrode, and the metal potential in the particle is assumed to be invariant with radial distance from the center of the particle.

For a crystallization process accompanying charge transfer, the overpotential associated with nucleation, growth at kinks, screw dislocations, *etc*. have been discussed [9]; and similarly, the current-overpotential relation could be modified if growth and formation of an amorphous phase is found to be the rate determining step. For now, it is simplified by noting that η includes an overpotential that is associated with the formation and growth of the amorphous Li-Si alloy phase from original Si electrode.

The potential U as a function of x of the lithium-silicon electrode from different sources is given in Figure 8.2. At high temperatures, there are multiple plateaus in the thermodynamic potential *vs.* composition curve due to the equilibrium between any two crystalline phases (shown in Figure 8.2 for comparison purposes only) [41], [42]. At room temperature, however, only a sloping region is seen [34], as shown with the Galvanostatic Intermittent Titration Technique (GITT) experiment lithiation curve [38] in Figure 8.2. The corresponding de-lithiation curve is also seen in Figure 8.2. As can be noted, the hysteresis phenomenon is reflected by the potential difference between these two curves. These two room-temperature curves are used for simulations in this work. Also shown in Figure 8.2 is the potential *vs.* composition curve derived by Chevrier and Dahn [43] from first principles simulation. This curve is used to semi-quantitatively demonstrate the need to include hysteresis in Li-Si system. This curve is also used to analyze an alternate plausible mechanism of asymmetric transfer coefficients to explain the observed potential gap.

Finally, since this is a moving boundary problem as seen in equations 6, 8b, 9 and 10; the radius at any time *t* is given by (11), and the initial condition is given by (12). The expression for the molar volume of the alloy electrode in equation 11 is based on the work by Obrovac *et al.* [31]

$$\left.\begin{aligned} \frac{R_p(t)}{R_{p_0}} &= \left(1+\frac{3.75\ \overline{V}_{Li} < x >}{\overline{V}_{Si}}\right)^{1/3} \qquad \text{(lithiation)} \\ \frac{R_p(t)}{\left(3.8^{1/3}\right)R_{p_0}} &= \left(1-\frac{3.75\ \overline{V}_{Li}(1- < x >)}{\left(\overline{V}_{Si}+3.75\ \overline{V}_{Li}\right)}\right)^{1/3} \quad \text{(de-lithiation)} \end{aligned}\right\} \qquad (11)$$

$$\left.\begin{aligned} R_p(t) &= R_{p_0} @\ t=0 \qquad \text{(lithiation)} \\ R_p(t) &= \left(3.8^{1/3}\right)R_{p_0} @\ t=0 \qquad \text{(de-lithiation)} \end{aligned}\right\} \qquad (12)$$

The initial radius during de-lithiation corresponds to a-$Li_{3.75}Si$, which is accompanied by a 280 % volume expansion. The expression for radius growth and the initial condition during CV scan, starting from bare silicon electrode is the same as that for lithiation. Equations (11) and (12) are solved with respect to fixed co-ordinates. $\langle x \rangle$ is the dimensionless volume average concentration in the entire particle and is given as

$$\langle x \rangle = \begin{cases} \left(\frac{|I|t}{nFN_{tot}} \right) & \text{(lithiation)} \\ 1\text{-} \left(\frac{|I|t}{nFN_{tot}} \right) & \text{(de-lithiation)} \end{cases} \quad (13)$$

$$= \frac{\frac{4}{3}\pi \left(R_p(t) \right)^3}{N_{tot}} \langle c \rangle \quad (14)$$

where,

$$\langle c \rangle = \frac{\left(\int_0^{R_p(t)} c \left(4\pi r^2 \right) dr \right)}{\frac{4}{3}\pi \left(R_p(t) \right)^3} \quad (15)$$

Similarly, local dimensionless concentration or state of charge (x) is given by

$$x = \frac{\frac{4}{3}\pi \left(R_p(t) \right)^3}{N_{tot}} c = \left(\frac{c}{c_{280\%}} \right) \left(\frac{R_p(t)}{\left(3.8^{1/3} R_{p_0} \right)} \right)^3 \quad (16)$$

Though equations 13 and 14 are equal, it is easier to use (14) to evaluate <x> for CV simulations since I is no longer constant. From equations (1)-(3), the moles of Li in a mole of $Si_{4/15}$ vary between 0 and 1 (given by <x> in Eqn. (13) and Eqn. (14) over the entire particle), and the final composition of the amorphous phase considered is $Li_{3.75}Si$. Hence the '3.75' multiplication factor appears in the expression for radius in Eqn. (11). It should be noted that an exact correlation between local concentration and radial growth will not be seen since radial growth is based on <x> over the entire particle which is in line with the assumption of isotropic volume change made earlier.

8.2.1. Simulation conditions

The results and discussions are presented for two different modes of operation: (a) galvanostatic control, and (b) potentiodynamic control. The first most closely represent battery

operation, the second allows comparison to experimental data in small cells or microelectrode studies.

During galvanostatic control, the current (I) is held constant and potential evaluated. The current is negative for lithiation and positive for de-lithiation of the silicon electrode. Lithiation is stopped when dimensionless surface concentration of Li (x_s) reaches one. Alternately, one could stop the lithiation based on a specific cut-off potential (*e.g.*, 50 mV). At the 10 C-rate, the overpotential is high, and the cut-off potential is attained quickly, and the simulations would stop. The primary idea for now is to analyze the concentration profile for single silicon electrode particle with volume changes, so the former stop condition is chosen. Moreover, even though a potential less than 50 mV is attained during galvanostatic simulations, a phase boundary problem (a-Li_xSi to crystalline $Li_{15}Si_4$) is not considered because that is needed mainly for analysis of stress [44], which is neglected in present work due to small particle size. De-lithiation is stopped when the concentration of lithium at the surface of the particle reaches zero. The total capacity of the particle with an initial radius R_{p0} determines the C-rate for the galvanostatic lithiation/ de-lithiation process. The parameters used in the simulation are given in Table 8.1.

For potentiodynamic control,

$$\varphi_1 = V_{app} = V_0 + \upsilon t \qquad (17)$$

V_0 is the initial applied potential and υ is the potential scan rate. The scan rate is negative for cathodic sweep and positive for anodic sweep direction. The current is calculated and is negative for lithiation and positive for de-lithiation. The potential sweep direction is changed from cathodic to anodic when V_{app} reaches 0 V. It is to be noted that, for some cases, the cathodic sweep was carried to slightly negative potential before switching direction. This ensures that the switch is made when the potential difference between the U values in lithiation and de-lithiation

directions is close to zero. If the switch from cathodic to anodic sweep is made when the potential difference between U values is few hundred millivolts (*i.e.*, when $<x> < 1$), a sudden increase in overpotential is induced leading to a current spike. This is an artifact that is not observed in experiments. The reason for this is not known. It could be due to a phenomenon (such as double layer charging, *etc.*) with a time constant approximately equal to that for the main reaction to follow the two different U *vs.* x curves without any artifacts. Alternately, the reason could be that the movement along the lithiation or the de-lithiation branch occurs only if the potential is less than a given value on the lithiation branch or exceeds a given value on the de-lithiation branch. Another reason could be that apart from the outer or boundary U *vs.* x curve, inner or scanning curves are necessary to describe the system to access the potentials between the boundary curves as proposed by Srinivasan *et al.* [45] for nickel hydroxide electrodes.

8.3. Results and discussions

8.3.1. Galvanostatic control

Figure 8.3. shows the dimensionless concentration profiles at the 10 C-rate of lithiation (C-rate is constant current of 9.44 x 10^{-16} A, *i.e.*, 0.083 A/m^2, when normalized to initial surface area for particle size of radius 30 nm). It is to be noted that the lithiation might be stopped even earlier when based on a specific cut-off potential as mentioned before. The concentration gradients are more pronounced at 10 C-rate than at C-rate. This can be understood by comparing the time constant for diffusion with the time corresponding to the C-rate at which the particle is lithiated using the following dimensionless parameter.

$$S_s \approx \left(\frac{{R_{p_0}}^2 |I|}{D_{Li} n F N_{tot}} \right) \qquad (18)$$

When the diffusion time constant is larger than the time corresponding to the C-rate at which the particle is lithiated, concentration gradients develop inside the particle. In other words, for S_s<<1, there are no diffusion limitations in the solid. During lithiation at the 10 C-rate, for a particle with initial radius of 30 nm and for the diffusion coefficient in Table 8.1, S_s is 2.5, whereas at the 1 C-rate, S_s is still lower (~0.25). Since the particle is growing, the diffusion limitations increase with lithiation whereas the current density is decreasing. Hence S_s ~ 1.60 at 10 C-rate (using the detailed equation in Appendix C.2) corresponding to 280% volume expansion (*i.e.*, towards the end of lithiation). As the lithiation rate increases or the initial radius of the particle increases, solid phase diffusion limitations become significant and can be evaluated using equation 18. Also, a wide range of diffusion coefficient values have been reported in the literature [17], [19], [20], [21], [46]. It is paramount to correctly determine the solid phase diffusion coefficient for lithium in silicon. The performance at other diffusion coefficient values can also be analyzed using equation 18. Thus, this analysis provides guidance for the design of electrodes.

In addition to diffusion limitations on rate capability, mechanical stress arises from the non-uniform dilation of the particles. An advantage of nanostructured materials is that their relaxation times for diffusion are short, owing to their small dimensions and hence the concentration of lithium is more uniform when cycled at moderate rates as observed in this work. Therefore, strains due to alloying and diffusion dissipate much more quickly than in bulk materials [47]. Even though stress is neglected in the present work, the concentration profiles provide insight into scenarios in which stress would be significant. At high rates, since the concentration difference is higher, stress will also be also higher [29] and as lithiation proceeds, stress in the particle will also drop.

Elaborating on the validity and limitations of the model before moving further, this model is accurate for nanoparticles even with the simplifications involved. However, for micron sized particle, the actual transport limitations within the particle might differ when the convective term is also included in the flux boundary condition (Appendix C.1). Moreover, the potential reaches 0V at 140 seconds at 10 C-rate (figure not shown) and hence only 40% capacity can be inserted for all practical purposes. Experimental data [48] at the 8C rate show that ~ 28 % capacity can be lithiated before reaching 0V. The difference can be partly explained in that at high rates the solution phase resistance also becomes significant and is not accounted for in this particle model.

Figure 8.4 shows the concentration profiles during de-lithiation at the 10 C-rate starting from maximum allowable value of $<x>$, *i.e.*, unity. De-lithiation is stopped when the surface concentration reaches zero. Rate capability effects are not seen for rates below 5C. Again, this can be understood by comparing the time constant for diffusion with the time corresponding to the C rate at which the particle is de-lithiated. During de-lithiation, for a particle with an initial radius of 47 nm (corresponding to 280% volume expansion) and for the diffusion coefficient in Table 8.1, S_s~1.60 for 10 C-rate (from Appendix C.2) and an order of magnitude lesser for C-rate. It is to be noted that the concentration gradient increases towards the end of de-lithiation (S_s~2.5) because de-lithiation is stopped when the surface concentration is zero, while the interior of the particle still remains unutilized. This also means that at the end of de-lithiation, the contractions are most non-uniform. This is consistent with Christensen and Newman's suggestion that crack formation is due to tensile rather than compressive stress [29], and so fracture would most likely occur at the center of the particle during lithiation, and at the surface of the particle during de-lithiation [29].

Figure 8.5 gives the electrode potential *vs.* <*x*> during lithiation (and de-lithiation) at different rates. Equation 8a can be simplified to Equation 19 for the case of equal transfer coefficients (α_a=α_c=0.5) to evaluate the overpotential in galvanostatic simulations. The electrode potential is obtained using equation 10 and the *U vs. x* curve assumed in this work. It is observed that at C/40 rate, the electrode potential curve follows *U vs. x* for lithiation (and de-lithiation). It can be seen that the overpotential increases with the rate of lithiation. The *k* values ($2.5\times10^{-9}(m/s)\ (mol/m^3)^{-\alpha_a}$ for lithiation curve and $1\times10^{-9}(m/s)\ (mol/m^3)^{-\alpha_a}$ for de-lithiation curve) chosen for galvanostatic simulations result in i_0 ~ (O (10^{-2}) A/m^2. But experiments with silicon nanowires [49] at the C-rate showed capacities similar to the simulation results at C-rate when the *k* value for lithiation is adjusted to $1\times10^{-9}(m/s)\ (mol/m^3)^{-\alpha_a}$ instead of $2.5\times10^{-9}(m/s)\ (mol/m^3)^{-\alpha_a}$. Alternatively, solution phase and matrix phase limitations could have caused the decrease in achievable capacity in composite electrode in experiments even without adjusting the value of *k*. If the kinetics is further limited [23], the over potentials from simulations are significantly higher and quickly reach negative potentials, contrary to what is observed in experiments. This could mean that the exchange current density values might have to be re-visited for the case of nanoparticles. The potential *vs*. composition curve employed also influences the accurate estimation of kinetic parameters. The kinetics of lithium insertion/de-insertion in silicon system is still at least two orders of magnitude smaller than that in carbon. Figure 8.5 gives insight into the ability of silicon electrodes to perform in high power applications and the influence of electrode kinetics and solid phase transport on its performance.

$$\eta = \frac{RT}{0.5F}\, arc\sinh\left(\frac{I}{2i_0 4\pi\left(R_p(t)\right)^2}\right) \qquad (19)$$

The lithiation step could limit the deliverable capacity because it cannot be allowed to proceed below 0 V to avoid plating of lithium; and as seen from Figure 8.5, only 60 % capacity is realized even at the 2 C-rate with this criterion for terminating the charge. The effects on rate capability are less pronounced during de-lithiation as compared to lithiation, partly because the potential at which de-lithiation is terminated is not a limiting factor in a cell with lithium foil as the counter and reference electrode as studied here. But in a cell where Li-Si electrode is used as the negative electrode with another positive insertion electrode, the useful capacity that is available from de-lithiation of silicon electrode can be limited by cell cut-off potential. Moreover, at higher rates, the rate capability effect becomes significant due to solid phase diffusion limitations.

8.3.2. Potentiodynamic control

Before proceeding with the simulation discussions, in-house experimental CV data at a potential sweep rate of 25 μV/s on a coin cell with silicon composite electrode are given in Figure 8.6 for further comparison. In Figure 8.6a the electrode is made of HF-cleaned nano-Si powder (21.54%) with CMC binder (14.84%), pure black (49.79%) and carbon (13.84%) [50]. The intensity of Si peaks is prominent as HF cleaning has diminished the intensity of C peaks (concluded from comparison with as-received sample). In Figure 8.6b, the electrode is C-Si granule whose preparation and performance is discussed elsewhere [48]. The peak locations are quite similar to others that are found in literature [51], [38]. The cathodic peak at 0.2 V (vs. Li/Li^+ ref.) and anodic peak at around 0.5 V (vs. Li/Li^+ ref.) are prominently seen in other in-house electrodes with different binders as well, with and without the presence of vinylene carbonate (VC) additives in the electrolyte [52]. A small cathodic peak at ~ 0.05 V is seen in

some cases as well. Finally, from subsequent post mortems of the cell, it was noted that particle fracture did not occur under these conditions.

Figure 8.7 shows the cyclic voltammogram at three different scan rates using the parameters in Table 8.1. These may be compared with experimental data. In order to do so, the appropriate kinetic rate constant (and the exchange current density) has to be determined in this work. The exchange current density values reported in literature vary by orders of magnitude for lithium –silicon system. However, for the *U vs. x* employed in this work, the kinetic rate constant *k* in exchange-current density expression gives a better comparison to experimental data in terms of peak position and peak separation for values of $2.5\times10^{-9}(m/s)\ (mol/m^3)^{-\alpha_a}$ for lithiation and $1\times10^{-9}(m/s)\ (mol/m^3)^{-\alpha_a}$ for de-lithiation directions respectively. This yields i_0~O (10^{-2}) A/m^2 at room temperature (the exact value of exchange current density varies between lithiation and de-lithiation direction). These agree with the conclusions from galvanostatic simulations. Since the particle size changes with time, the current has been normalized with respect to initial surface area of the particle to yield current density values shown in Figure 8.7. Peak current value at 25 μV/s corresponds to roughly a 0.64 C-rate for the 30 nm particle. In the potential range that is being studied, two cathodic peaks and one anodic peak are seen, and this asymmetry is due to the different *U vs. x* curves used for lithiation and de-lithiation to reflect the hysteresis. As expected, with increasing scan rate, the peak height increases. The anodic peak potential shifts to more positive values and the cathodic peak potential to slightly more negative values with increase in scan rate reflecting that the charge transfer kinetics is sluggish.

The influence of the kinetic rate constant is studied in Figure 8.8 for two different particle sizes. The smaller the kinetic rate constant, the greater the shift in corresponding peak potentials away from each other. The peak positions (*i.e.*, the anodic peak at around 0.5 V and the cathodic

peaks at 0.2 V (and around 0.03-0.05 V)) and the corresponding peak separation seem to agree more with in-house experimental CV data in Figure 8.8 for the kinetic rate constants 2.5 x 10^{-9} $(m/s)\,(mol/m^3)^{-\alpha_a}$ (lithiation) and 1 x 10^{-9} $(m/s)\,(mol/m^3)^{-\alpha_a}$ (de-lithiation) than for the corresponding constants an order of magnitude lesser, irrespective of particle size. This comparison is fine for a first approximation since experimental data were collected in a composite electrode with an average particle size of few hundreds of nanometers whereas the CV simulations were performed on a single particle of 30 nm or 60 nm in this work The exact values of the current cannot be compared because of the actual differences in capacity of the experimental electrodes and that of the simulations. Kinetics, as analyzed in this study, is still sluggish in comparison with the carbon electrode whose exchange current density for lithiation reaction is of the order of 10 A/m^2 at room temperature. Figure 8.9 is the CV for different values of the cathodic and anodic transfer coefficients (α_c and α_a respectively) for the electrode kinetics. The scan rate is 25 μV/s and lithiation kinetic rate constant is 2.5 x 10^{-9} $(m/s)\,(mol/m^3)^{-\alpha_a}$ and the de-lithiation kinetic rate constant is 1 x 10^{-9} $(m/s)\,(mol/m^3)^{-\alpha_a}$. The anodic peak height increases and peak potential decreases (less overpotential) with an increase in α_a. But the cathodic peak potential shifts to less positive potential with an increase in α_c, and the peak height remains almost unchanged. This anomaly could partly be due to the shape of the *U vs. x* curve. Both of these indicate that relatively, the anodic transfer coefficient has a stronger influence on the charge transfer kinetics. These further suggest that kinetics has a significant influence on the rate constant and the scan rates employed in CV simulations. A plot of the anodic peak current density (peak @ 0.5 V) and cathodic peak current density (the peak at 0.2 V is considered) *vs.* square root of scan rate ($\upsilon^{1/2}$) for transfer coefficient values of 0.5 is provided in the inset in Figure 8.7 for five different scan rates: 100, 25 15, 10, 1 μV/s. The plot is non-linear. For a

reaction of the type O + $ne^- \Leftrightarrow$R with reversible kinetics, the following expression has been suggested [53], [54], [55] for the peak current (I_p) at room temperature:

$$I_p = \left(2.69 \times 10^5\right) n^{3/2} A D_O^{1/2} C_O \upsilon^{1/2}$$

And for irreversible kinetics,

$$I_p = \left(2.99 \times 10^5\right) \alpha^{1/2} A D_O^{1/2} C_O \upsilon^{1/2}$$

When the rest of the parameters are constant, a plot of I_p *vs.* $\upsilon^{1/2}$ (and peak current density *vs.* $\upsilon^{1/2}$) is linear. For quasi-reversible kinetics, non-linearity is observed. But when A is changing, I_p *vs.* $\upsilon^{1/2}$ may exhibit non-linearity in other regimes as well, and thus complicate the analysis. However, earlier it was observed in Figure 8.7 that the peak potential is a function of sweep rate, which further confirms that the charge transfer kinetics for Li-Si system is less facile.

The diffusion coefficient used in present work (10^{-18} m^2/s) is based on the work of Pell [17]. There is a large range of diffusion coefficient values reported as mentioned before. Hence, a parametric study was carried out for a 30 nm particle at a scan rate of 25 μV/s with the following values for diffusion coefficient: (10^{-18}, 10^{-16}, 10^{-14}, 10^{-12} m^2/s). Since the particle sizes are small (R_{p0}=30 nm) and the scan rate is low, the peak CV currents are of the order of 0.64 C-rate only and this leads to $S_s \sim 0.16$ for $D_{Li}=10^{-18}$ m^2/s from equation 18 and still lesser for higher diffusion coefficients. Hence, the cyclic voltammograms remain unchanged with variation in solid phase diffusion coefficients, whereas the electrode kinetics has a greater influence on the CV as discussed before. But as discussed in the galvanostatic simulations section, the exact value of the diffusion coefficient is significant at high rates of cycling.

For larger particles, irrespective of the kinetic rate constants, the peak current values increase because the total lithium storage capacity increases. The peak current density is also almost doubled as seen in Figure 8.8. The total surface area varies by a factor of four between the two sizes of particle chosen here, and the peak current varies by an order of magnitude. If diffusion limitations were a significant factor, these observations would have varied. For any given kinetic rate constant, the anodic and cathodic peaks shift to slightly more positive and more negative potentials respectively with increase in particle size, which suggests the slight increase in overpotential with increased diffusion path within the particle.

8.3.3. Analysis of hysteresis from CV

Potentiodynamic experiments have been used to analyze the existence of hysteresis in nickel hydroxide electrodes [40]. The existence of potential gap independent of the sweep rate implied hysteresis existed in their system because if the potential gap was due to mass transfer limitations, then it should have been a function of sweep rate. In Li-Si system, the effect of sluggish kinetics is superimposed on the effect of hysteresis on the peak potential separation for a vast range of sweep rates and hence semi-quantitative analysis is being made.

If a single potential *vs*. composition curve (neglecting hysteresis phenomena), such as that proposed by Chevrier and Dahn (Fig 8.2) is used, the peak potential locations in both anodic and cathodic directions simultaneously (and thus the peak separation) do not agree with experimental data in Figure 8.6 for any value of exchange current density (including the kinetic rate constants considered in this work) for equal values of anodic and cathodic transfer coefficient values of 0.5 at the same scan rate. For k=1x10^{-9}, the anodic and cathodic peaks were at 0.5 V and 0.3 V respectively as seen in Figure 8.10. For k= 1x10^{-10} and α_a =0.5, α_c=0.5, the anodic and cathodic peaks were at 0.6 V and 0.2 V respectively (figure not shown). It is to be

noted that only one expression for exchange current density (and hence one value for kinetic rate constant) is used since there is no path dependence.

From equation 10, the expression for peak potential separation can be derived as given below.

$$\left(\varphi_{1,c} - \varphi_{1,a}\right) = (\eta_c - \eta_a) + (U_c - U_a) + (\varphi_{2,c} - \varphi_{2,a}) \qquad (20)$$

Since solution potential at the reference electrode is assumed to be zero,

$$(\varphi_{2,c} - \varphi_{2,a}) = 0 \qquad (21)$$

Thus yielding the expression for peak potential separation with intrinsic hysteresis

$$\Delta\varphi_1 = \left(\varphi_{1,c} - \varphi_{1,a}\right) = (\eta_c - \eta_a) + (U_c - U_a) \qquad (22)$$

If a single potential *vs.* composition curve is used (no path dependence), then

$$(U_c - U_a) = 0 \Rightarrow \Delta\varphi_1 = (\eta_c - \eta_a) \qquad (23)$$

If hysteresis is included, then contribution from overpotential is not over predicted leading to better comparison. As discussed in the previous sections, the peak positions of the anodic and cathodic peak and the corresponding peak potential separation obtained in the CV simulations at 25 μV/s in Figure 8.7 using the *U vs. x* composition curve from GITT experiments shown in Figure 8.2 agree better with the experimental data in Figure 8.6 than without the inclusion of hysteresis. The exact value of the kinetic rate constant will vary depending on the accuracy of the pseudo-thermodynamic potential *vs*. composition curve that is used. As discussed before, different values of exchange current density have been reported. But Figure 8.7 in comparison with experimental data in Figure 8.6 suggests that the exchange current density could be in the order of 10^{-2}-10^{-3} A/m^2 at room temperature. It is also noted that the exact value of the kinetic rate constant used for lithiation and de-lithiation were different (2.5 x10^{-9}

$(m/s)\,(mol/m^3)^{-\alpha_a}$ for lithiation and $1\text{x}10^{-9}$ $(m/s)\,(mol/m^3)^{-\alpha_a}$ for de-lithiation) and this led to slightly different exchange current density values for the forward and backward reaction even though the order of magnitude remains same. Path dependence of potential *vs.* composition curve was essential to obtain correct results to compare with experimental CV data in terms of peak separation.

It was seen in Figure 8.9 that the anodic transfer coefficient has a greater influence on the peak position and peak height as compared to the cathodic transfer coefficient. Hence, a parametric study was carried out by varying the kinetic rate constant and the transfer coefficients with single potential *vs.* composition curve neglecting hysteresis phenomena (Chevrier and Dahn in Fig 8.2). It is noted that for k=1x10^{-10} and α_a =0.7, α_c=0.3 or for k=0.6 x 10^{-10}, α_a =0.8, α_c=0.2, a reasonable fit in terms of peak potential location and peak separation is obtained as seen in Figure 8.10. For symmetric coefficients the peak location and separation did not match with experimental observation as discussed before. This suggests the possibility of an alternative mechanism wherein the potential gap between lithiation and de-lithiation curves is explained by kinetic hysteresis due to sluggish kinetics and asymmetric transfer coefficients as opposed to path dependence in the *U vs. x* curves. In Figure 8.10 the curves corresponding to asymmetric coefficients look different from the one for symmetric coefficient because the direction of sweep is switched at 0V (if allowed to go further negative potentials, the curve shapes will be similar).

To further explore this possibility, the *U vs. x* de-lithiation curve from GITT experiments is used for both forward and reverse direction and the kinetic parameters, namely, k, α_a, α_c were varied and CV obtained at 25 μV/s. It is observed in Figure 8.11 that for k=1x10^{-10} and α_a =0.7, α_c=0.3 or k=2.5 x 10^{-10}, α_a =0.6, α_c=0.4, a reasonable fit in terms of peak potential and peak separation is obtained. For symmetric coefficients, i.e. α_a =0.5, α_c=0.5, the peak locations were

similar to that observed with *U vs. x* curve from Chevrier and Dahn (discussed in previous paragraph), and thus the peak separation did not match with experimental data for any value of kinetic rate constant. The small peak in the cathodic direction at ~1V is due to the small plateau in the *U vs. x* de-lithiation curve from GITT experiments around x=0. It is not seen in the de-lithiation direction because the simulation is stopped at 1 V. These should be considered as mere artifacts with no significance attached as these data are an approximation from literature and not obtained in-house.

Thus, the simulations indicate the two different mechanisms or ways in which potential gap observed in Li-Si system can be captured in future modeling efforts. The first one is the existence of path dependence in the pseudo-thermodynamic potential *vs.* composition curve. This gives a reasonable fit with experimental data for $\alpha_a = \alpha_c = 0.5$, without much tuning of parameters. This mechanism can explain the existence of potential gap even at C/1000 rates. The second mechanism involves a slightly lower kinetic rate constant ($k \sim$ O (10^{-10}) (m/s) $(mol/m^3)^{-\alpha_a}$) with $\alpha_a \sim 0.7$ and $\alpha_c \sim 0.3$ to obtain the desired peak potential separation with single *U vs. x* curve. The asymmetric transfer coefficients might tempt one to evoke the theory of semiconductor electrochemistry to explain the potential gap, subject to verification from experiments. The disadvantage is that the cathodic and anodic transfer coefficients must be obtained from experiments from current-potential relationship and not deduced. Moreover, kinetic hysteresis is dependent on scan rate and hence at significantly low scan rates, the potential gap due to this hysteresis should cease to exist. To verify this, CV at a scan rate of 25 x 10^{-8} V/s using *U vs. x* de-lithiation curve from GITT experiments for both forward and reverse direction was obtained for $k = 1 \times 10^{-10}$, $\alpha_a = 0.7$ and $\alpha_c = 0.3$. The peak current was ~ C/38 and the potential gap was ~ 33 mV. The potential gap increased to 74 mV for $\alpha_a = 0.5$ and $\alpha_c = 0.5$. Hence, at C/1000 rates, the

potential gap due to kinetic hysteresis will cease to exist contrary to experimental observations. The kinetic hysteresis can exist at C/1000 rates only if the kinetic rate constant is deduced to be orders of magnitude lesser than analyzed in this work for nanoparticles. Hence, experiments in Li-Si system are needed to find the transfer coefficients and the kinetic rate constant before establishing kinetic hysteresis as the cause for the potential gap. Therefore, unless otherwise proven, for all modeling purposes, justification has been provided in this work for the necessity to include path dependence in the pseudo-thermodynamic potential *vs*. composition (*U vs. x*) curve for Li-Si system.

In-house data will provide metastable pseudo-thermodynamic potential *vs*. composition curve in the future. A methodology should be sought to separate the contribution of kinetics and hysteresis to the peak potential separation and provide a complete quantitative analysis.

8.4. Conclusions

A single particle model for the case of amorphous lithiation/de-lithiation of silicon electrode that accounts for volume changes is developed [56]. Both potentiodynamic and galvanostatic modes of operation have been discussed. It is shown that the pseudo-thermodynamic potential *vs.* composition curve with hysteresis (path dependence) is necessary to compare with experimental observations in cyclic voltammograms. Two different exchange current density values are used to fit our peak locations in anodic and cathodic directions in cyclic voltammograms respectively. Experiments are needed in future to verify the contribution of different phenomena such as stress, side reactions, semiconductor nature of silicon electrode to hysteresis. It has been quantitatively shown that even though the kinetic parameters can be tuned to fit with experimental data and lead to the conclusion that kinetic hysteresis is the cause for the potential gap in Li-Si system, this mechanism cannot explain the potential gap at low

rates. Hence accurate prediction of kinetic parameters, namely, exchange current density, anodic and cathodic transfer coefficients is needed to further verify kinetic hysteresis in Li-Si system. Influence of different parameters is investigated during CV scan and their influence on the solid phase concentration profile and corresponding growth of particle is understood. Knowledge about influence of solid phase diffusion coefficient, kinetic rate constant, particle size and path dependence of pseudo-thermodynamic potential serve as a starting point to understand silicon electrodes and thus help design of better electrodes. Future work on composite lithium-silicon electrodes will further provide insight into how these electrodes can be made more efficient.

Table 8.1. Baseline Parameters used in the simulation

Parameters	Value
R_{p0}	30 nm
D_{Li}	10^{-18} m^2/s [17]
α_a, α_c	0.5
k (Units: $(m/s)\ (mol/m^3)^{-\alpha_a}$)	2.5 x 10^{-9} (lithiation) , 1 x 10^{-9} (de-lithiation)
c_e	1000 mol/m^3
$\overline{V}_{Li}$	9 x 10^{-6} m^3/mol [31]
$\overline{V}_{Si}$	1.2 x10^{-5} m^3/mol [31]

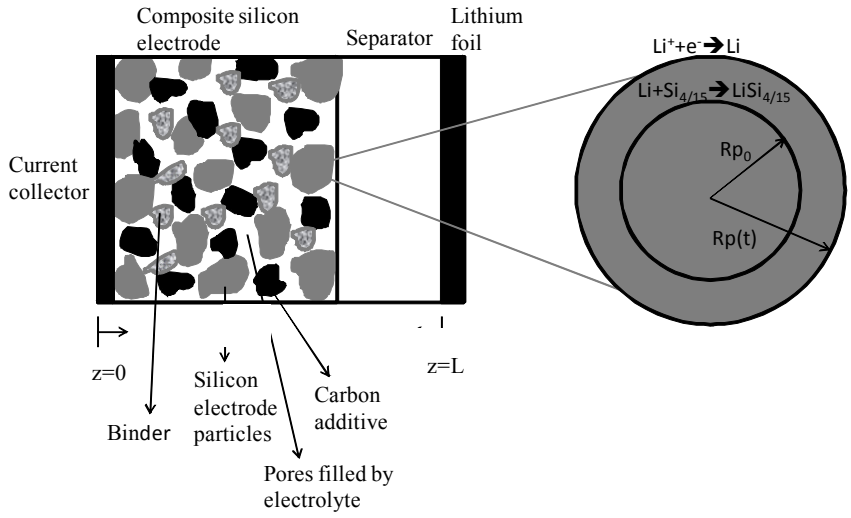

Figure 8.1. Schematic of a lithium-silicon composite electrode/separator/lithium foil electrode cell and single particle of lithium-silicon electrode.

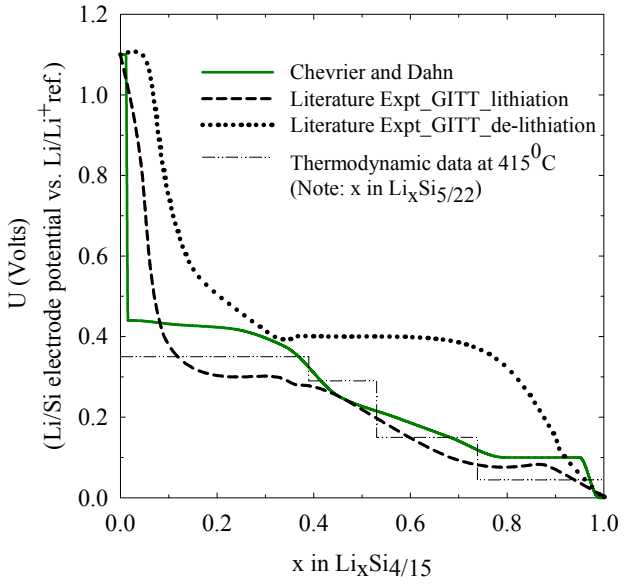

Figure 8.2. Pseudo-Thermodynamic potential (*U vs.* Li/Li^+ ref.) *vs. x* (composition) curve of Li/Si electrode at room temperature. Note: At x=0 and x=1, the graph is extrapolated for simulation purposes. Also shown for reference, the thermodynamic potential curve (at 415°C) for which x varies from 0 to 1 in $Li_xSi_{5/22}$.

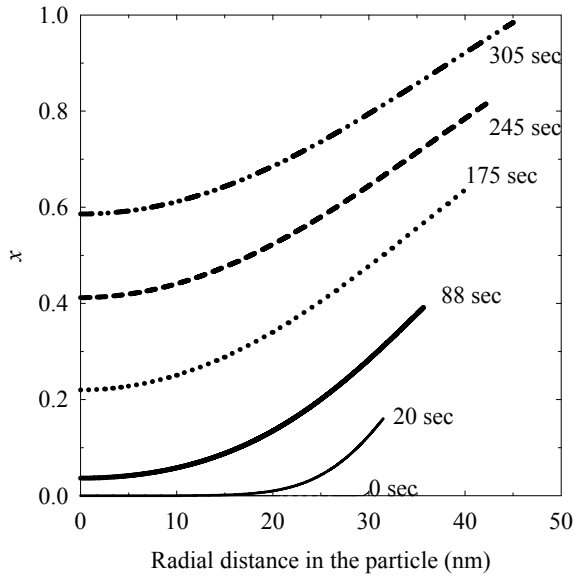

Figure 8.3. Dimensionless Li concentration (x) profiles inside the particle during lithiation at 10 C- rate (D_{Li}=10^{-18} m^2/s, k (lithiation curve) = 2.5 x 10^{-9} $(m/s)\ (mol/m^3)^{-\alpha_a}$).

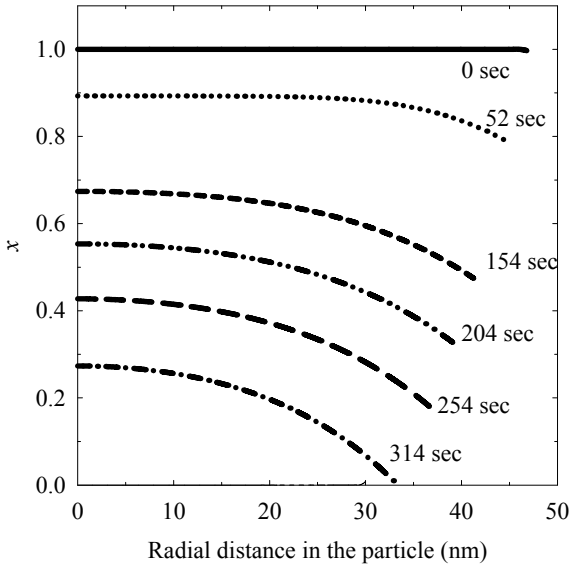

Figure 8.4. Dimensionless concentration (x) profile in a shrinking particle de-lithiated at 10 C-rate (D_{Li}=10^{-18} m^2/s, k (de-lithiation curve) =1 x10^{-9} $(m/s)\ (mol/m^3)^{-\alpha_a}$).

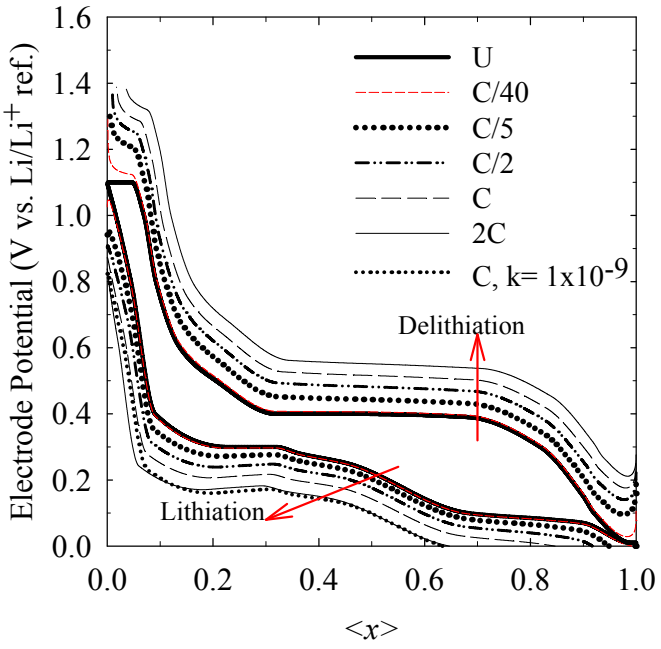

Figure 8.5. Electrode potential *vs.* dimensionless volume average concentration (<*x*>) at different rates of lithiation (curves below the potential gap) and de-lithiation (curves above the potential gap) for D_{Li}=10^{-18} m^2/s, k (lithiation curve) = 2.5 x10^{-9} $(m/s)\,(mol/m^3)^{-\alpha_a}$, k (de-lithiation curve)= 1 x10^{-9} $(m/s)\,(mol/m^3)^{-\alpha_a}$ (i_0~ O (10^{-2} A/m^2). *U vs. x* for lithiation (and de-lithiation) based on GITT experiments from Figure 8.2 is provided for comparison.

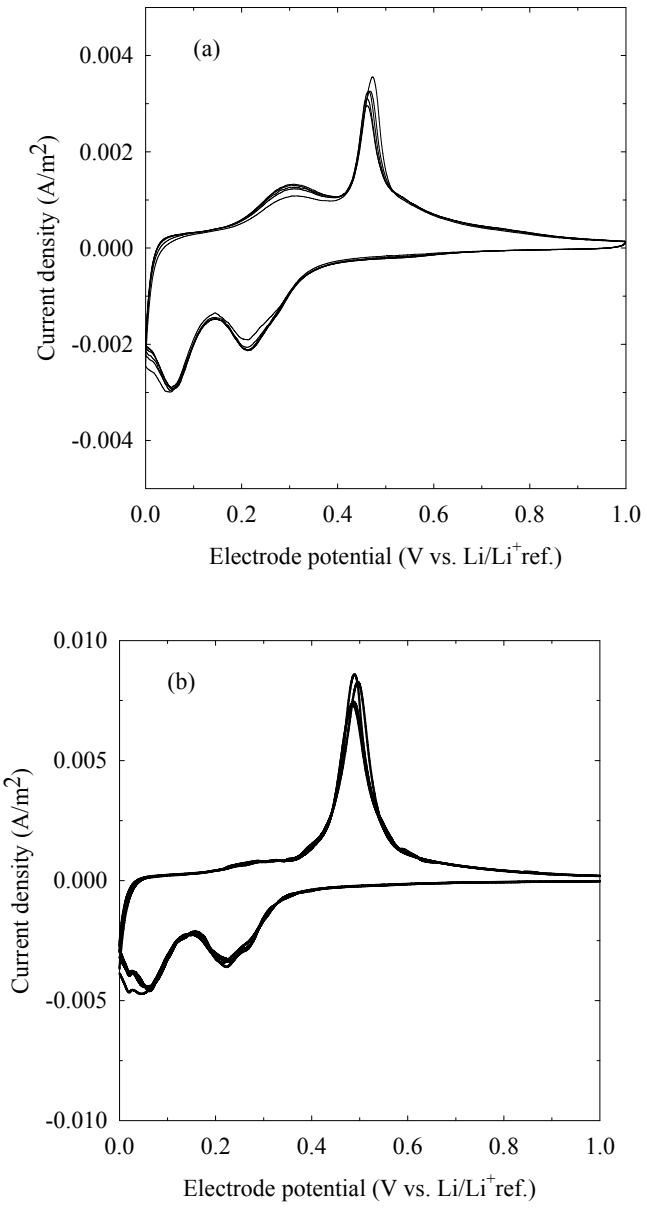

Figure 8.6. Experimental CV curve of lithium-silicon electrode full cell at a scan rate of 25 μV/s (a) CMC binder [50] (b) C-Si granules with PAA binder (preparation described elsewhere) [48].

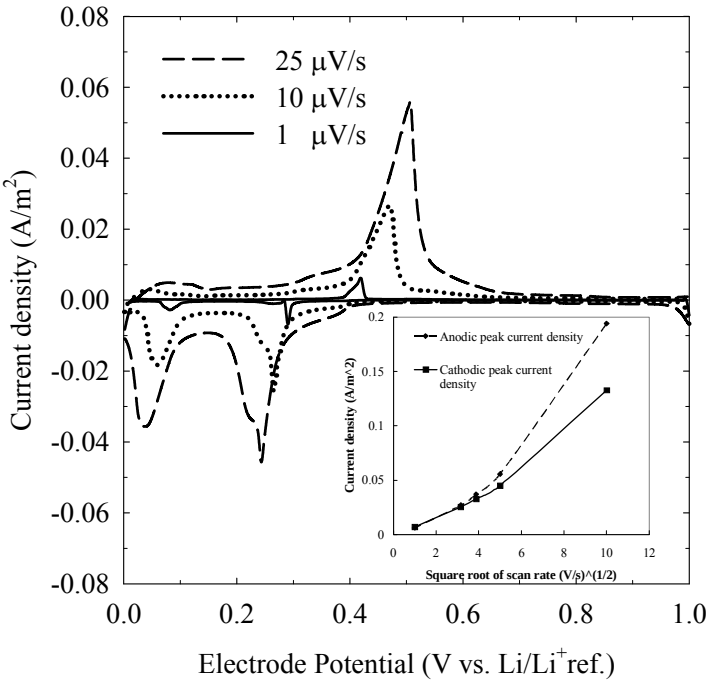

Figure 8.7. CV of the silicon electrode particle at three different scan rates (D_{Li}=10^{-18} m^2/s, k (lithiation curve) =2.5 x 10^{-9} $(m/s)\,(mol/m^3)^{-\alpha_a}$, k (de-lithiation curve) =1 x10^{-9} $(m/s)\,(mol/m^3)^{-\alpha_a}$). Note: The current density in the plot is obtained by normalizing the response current at each time step with respect to the initial surface area of the particle of radius 30 nm. Inset: Peak current density *vs.* square root of scan rate for anodic peak and cathodic peak at approximately 0.5 V and 0.2 V respectively.

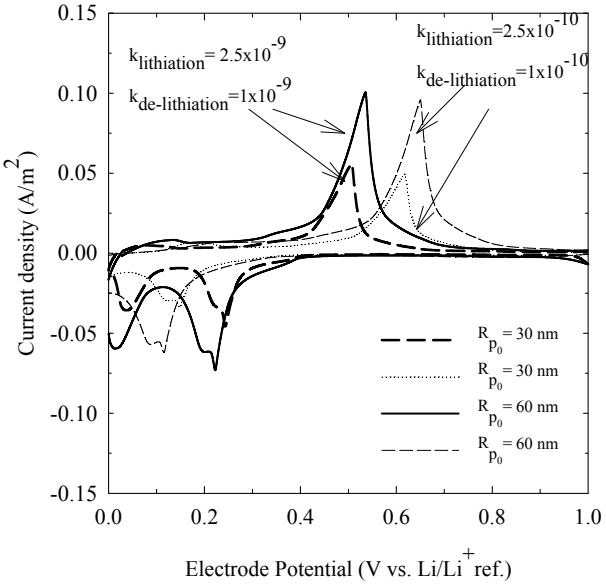

Figure 8.8. CV for varying kinetic rate constants for two different particle sizes at scan rate of 25 μV/s. $k_{lithiation}$ denotes the *k* value corresponding to *U vs. x* curve for lithiation and $k_{de\text{-}lithiation}$ denotes the *k* value corresponding to *U vs. x* for de-lithiation. Note: The current density in the plot is obtained by normalizing the response current at each time step with respect to the initial surface area of the particle (with corresponding radius).

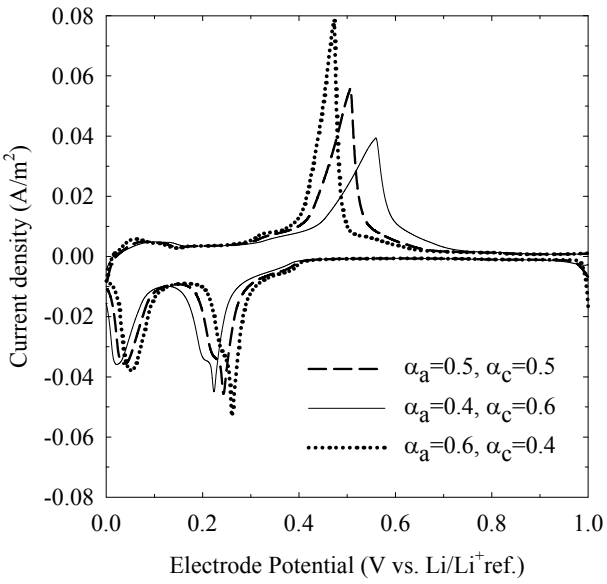

Figure 8.9. CV for different values of transfer coefficients for particle of radius 30 nm for υ=25 μV/s for k= 2.5 x 10^{-9} $(m/s)\,(mol/m^3)^{-\alpha_a}$ (lithiation curve) and k=1 x10^{-9} $(m/s)\,(mol/m^3)^{-\alpha_a}$ (de-lithiation curve). Note: The current density in the plot is obtained by normalizing the response current at each time step with respect to the initial surface area of the particle of radius 30 nm.

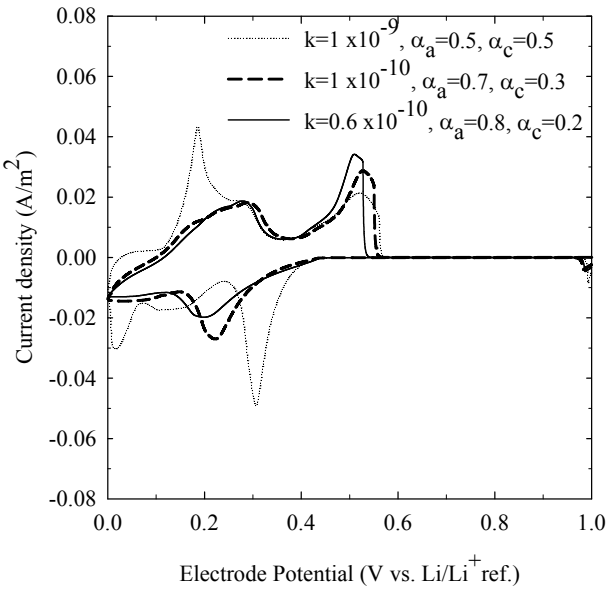

Figure 8.10. CV Simulations for scan rate of 25 μV/s based on the first principles simulation data from Chevrier and Dahn (Fig 8.2). The current density in the plot is obtained by normalizing the response current with respect to the initial surface area of the particle of radius 30 nm.

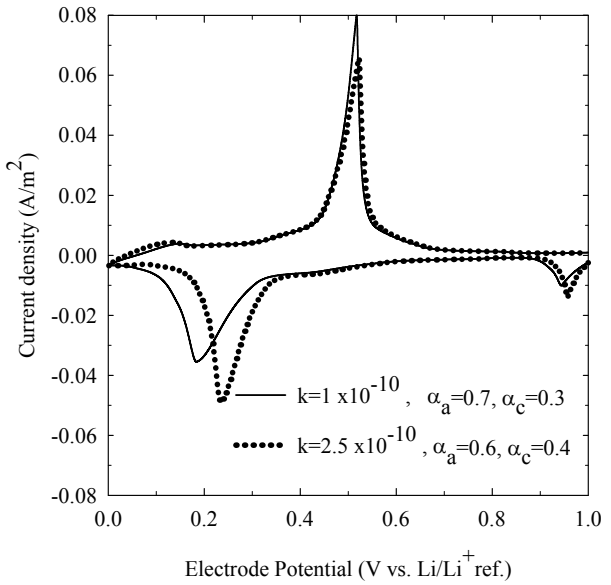

Figure 8.11. CV Simulations for scan rate of 25 μV/s with *U vs. x* from GITT experiment de-lithiation curve (Fig 8.2.) for both forward and reverse directions. The current density in the plot

is obtained by normalizing the response current at each time step with respect to the initial surface area of the particle of radius 30 nm.

8.5. References

[1] Thomas F. Fuller, M. Doyle, J. Newman*, J. Electrochem. Soc.*, 141(1) (1994), 1-10.

[2] Rob Darling, J. Newman, *J. Electrochem. Soc.*, 145 (1998), 990-998.

[3] Godfrey Sikha, Ralph E. White, *J. Electrochem. Soc.*, 155 (12) (2008), A893-A902.

[4] V. Srinivasan, V. Sethuraman, J. Newman, Abstract #607, 214th ECS Meeting, Hawaii.

[5] Mark Verbrugge, Edward Tate, *J.Power Sources,* 126 (2004), 236-249.

[6] D.H. Everett, W.I.Whitton, *Trans.Faraday Soc.*, 48 (1952), 749.

[7] IUPAC Recommendations, *Pure Appl. Chem.*, 57 (1985), 603.

[8] IUPAC Recommendations, *Pure Appl Chem.*, 66 (1994), 1739.

[9] Klaus J. Vetter, Electrochemical Kinetics-Theoretical Aspects, Academic Press, 1967.

[10] Tibor Erdey-Grúz, Kinetics of Electrode Processes, Wiley-Interscience,1972.

[11] Newman and Thomas-Alyea, Electrochemical Systems, Third Edition, John Wiley and Sons, Inc.

[12] T.Ohzuku, Y.Iwakoshi, K.Sawai, *J.Electrochem.Soc.*, 140 (9) (1993),2490-2498.

[13] Rachid Yazami,Yvan Reynier, *J.Power Sources*, 153 (2006), 312-318.

[14] Joongpyo Shim, Kathryn A. Striebel, *J.Power Sources*, 130 (2004), 247-253.

[15] M.D.Levi, D.Aurbach, *J.Phys.Chem.B*, 101 (1997), 4630-4640.

[16] Wu-Shou Zhang, Xin-Wei Zhang, Xian-Geng Zhao, *J.Electroanal.Chem.*, 458 (1998), 107–112.

[17] E.M.Pell, *Phys.Rev.*119 (4) (1960), 1222-1225.

[18] P.Yu, B. Popov, J. A. Ritter, R. E. White, *J.Electrochem.Soc.,* 146 (1) (1999), 8-14.

[19] T.L. Kulova, A.M. Skundin, Yu.V. Pleskov, E.I. Terukov, O.I. Kon'kov, *J.Electroanal.Chem.*, 600 (2007), 217–225.

[20] N. Ding , J. Xu, Y.X. Yao , G. Wegner , X. Fang , C.H. Chen , I. Lieberwirth, *Solid State Ionics*, 180 (2009), 222-225.

[21] K.Yoshimura J.Suzuki K.Sekine, T.Takamura, *J.Power Sources*, 174 (2007), 653-657.

[22] T.Song, J.Xia, J.Lee, D.Lee,M.Kwon, J.Choi, J.Wu, S.Doo, H.Chang, W.Park, D. Zang, H.Kim, Y.Huang, K.Hwang, J.Rogers, U.Paik, *Nano Lett.* (ASAP), (2010), DOI: 10.1021/nl100086e.

[23] Model-Experimental Studies on Next-generation Li-ion Materials", Venkat Srinivasan, OVT Merit Review, May 21, 2009.

[24] Hironori Ura, Tatsuo Nishina, Isamu Uchida, *J. Electroanal. Chem.,* 396 (1995), 169-173.

[25] Qingfang Shi, Daniel A. Scherson, *Electrochem.Solid.State Letts.*, 8 (2) (2005), A122-A124.

[26] D. Zhang, B. Popov, Ralph White, *J. Electrochem.Soc.,* 147 (3) (2000), 831-838.

[27] Mark W. Verbrugge, Brian J.Koch, *J.Electrochem.Soc.,* 143(2) (1996), 600-608.

[28] Gerardine Botte, *Electrochim.Acta*, 50 (2005), 5467-5658.

[29] John Christensen, John Newman, *J.Solid State Electrochem.*, 10 (2006), 293-319.

[30] Z.Chen, L.Christensen, J.R.Dahn, *Electrochem.Comm.,* 5 (11) (2003), 919-923.

[31] M. N. Obrovac, Leif Christensen, Dinh Ba Le, J. R. Dahn, *J.Electrochem. Soc.*, 154 (9) (2007), A849-A855.

[32] A. Timmons, J. R. Dahn, *J.Electrochem.Soc.*, 154 (5) (2007) , A444-A448.

[33] Huggins, R.A., W.D. Nix, *Ionics*, 6 (2000), 57.

[34] T. D. Hatchard, J. R. Dahn, *J. Electrochem.Soc.*, 151 (6) (2004), A838-A842.

[35] Martin Winter, Jürgen O. Besenhard, Michael E. Spahr, Petr Novák, *Advanced Materials*, 10 (10) (1998), 725-763.

[36] L.Baggetto, R.A.H.Niessen, F.Roozeboom, P.H.L.Notten, *Adv.Funct.Mat.,* 18 (2008), 1057-1066.

[37] L. Baggetto, R.A.H. Niessen, P.H.L. Notten, *Electrochim. Acta* 54 (2009), 5937–5941.

[38] L. Baggetto, J.F.M. Oudenhoven, T. Van Dongen, J.H. Klootwijk , M. Mulder, R.A.H. Niessen, M.H.J.M. de Croon, P.H.L. Notten, *J.Power Sources* 189 (2009), 402-410.

[39] Dawn Bernardi, John Newman, *J.Electrochem.Soc.*, 134 (6) (1987), 1309-1318**.**

[40] Kathryn P. Ta, John Newman, *J.Electrochem.Soc.,*146 (8) (1999), 2769-2779.

[41] Robert A, Huggins, R.A., *J.Power Sources*, 81-82 (1999), 13-19.

[42] M.Green, E.Fielder, B.Scrosati, M.Wachtler, J.S.Moreno, *Electrochem.Solid-State Letts.,* 6 (5) (2003), A75-A79.

[43] V.L. Chevrier, J. R. Dahn, *J.Electrochem.Soc*., 156 (6) (2009) A454-A458.

[44] S. Renganathan, G. Sikha, S. Santhanagopalan, R.E. White, *J.Electrochem.Soc.*, 157 (2) (2010), A155-A163.

[45] V. Srinivasan, J.W. Weidner, J.Newman, *J.Electrochem.Soc.*, 148 (9) (2001), A969-A980.

[46] Riccardo Ruffo, Seung Sae Hong, Candace K. Chan, Robert A. Huggins, Yi Cui, *J. Phys. Chem. C* 113 (2009), 11390–11398.

[47] J.Graetz, C.C.Ahn, R.Yazami, B.Fultz, *Electrochem.Solid-State.Letts.*, 6 (9) (2003), A194-A197.

[48] A. Magasinski, P. Dixon, B. Hertzberg, A. Kvit, J. Ayala and G. Yushin, *Nature Materials*, 9(4) (2010), 353-358.

[49] C. K. Chan, H. Peng, G.Liu, K.McIlwrath, X.F.Zhang, R.A.Huggins, Y.Cui, *Nature Nanotech.*, 3 (2008), 31-35.

[50] Alexandre Magasinski, Gleb Yushin, personal communication.

[51] W.Liu, J. Wang, H.Wu, D.Shieh, M.Yang, N. Wua**,** *J.Electrochem.Soc.*, 152 (9) (2005), A1719-A1725.

[52] A.Magasinski, B.Zdyrko, I.Kovalenko, B.Hertzberg, R.Burtovyy, T.F. Fuller, I.Luzinov, G.Yushin, *ACS Applied Materials and Interfaces (submitted).*

[53] Allen J.Bard, Larry Faulkner, Electrochemical Methods- Fundamentals and Applications, Second Edition, Pg 242-243.

[54] Noel and Vasu, Cyclic Voltammetry and Frontiers of Electrochemistry, Oxford & IBH Publishing Co. Pvt. Ltd., India.

[55] Richard S.Nicholson, *Anal.Chem*. 37 (11) (1965) 1351-1355.

[56] Rajeswari Chandrasekaran, Alexandre Magazinski, Gleb Yushin, Thomas F.Fuller, *J.Electrochem.Soc.,* 2010 (accepted).

[57] Transport Phenomena, Bird, Stewart, Lightfoot, John Wiley and Sons Ltd., 1994.

[58] John Newman, Thomas W.Chapman, *AIChE Journal*, 19 (2) (1973), 343-348.

[59] Jake Christensen, *J.Electrochem.Soc.*, 157 (3) (2010), A366-A380.

CHAPTER 9

ANALYSIS OF THE LITHIUM-ION INSERTION SILICON COMPOSITE ELECTRODE / SEPARATOR / LITHIUM FOIL CELL

9.1. Introduction

In this work**,** porosity changes in a lithium-silicon composite electrode and the impact of porosity changes on cell performance is analyzed assuming electrode dimensions remain constant. The concept of reservoir is introduced for the first time in lithium-ion battery systems for room temperature applications to accommodate the electrolyte that gets squeezed out during lithiation of silicon electrode so that it can be available for subsequent de-lithiation.

9.2. Model Development

A schematic of a lithium-silicon composite electrode / separator / lithium foil electrode cell with extra head-space called reservoir is given in Figure 9.1.

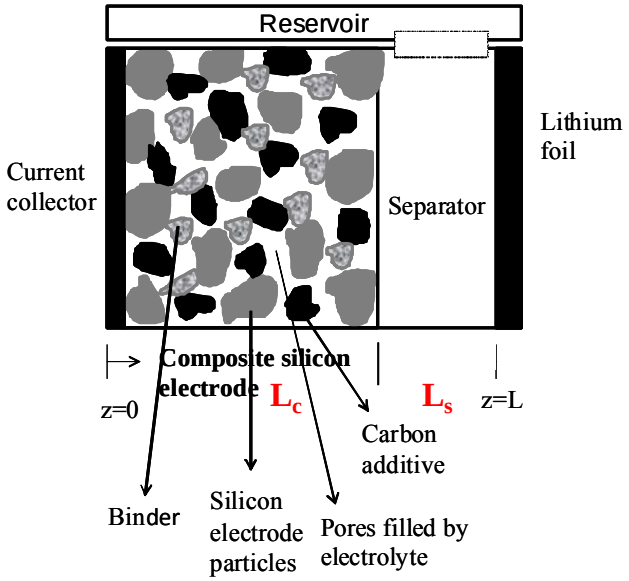

Figure 9.1. Schematic of a lithium-silicon composite electrode / separator / lithium foil electrode cell with reservoir accessible from above the separator.

In insertion electrode cells studied so far, volume changes were not important and hence ignored. The decrease in porosity due to side reactions in carbon/separator/$LiCoO_2$ lithium insertion cell [1] was much less than in the present study; and hence, no extra additional space was provided to accommodate the displaced solution phase volume. But extra space is needed to accommodate the volume of the solution phase that gets squeezed out due to significant porosity changes during lithiation of silicon electrode. The concept of reservoir has been used earlier but in a different context [2], [3], [4], [5]. It was used to replenish the electrolyte as it gets used up in the formation of precipitates during a reaction. Hence the reservoir was part of the cell sandwich. In the present work, reservoir acts solely to accommodate the displaced volume of solution and is placed above the cell sandwich as shown in the figure. In the present model, it is considered that the reservoir is accessible from above the separator alone. The reason is, if the electrode also has access to reservoir, the electrode material has freedom to change in dimension back and forth with cycling and thus may be a problem for its mechanical integrity in the long run. Higher initial porosity is chosen for silicon composite electrode than that has been used for other insertion electrodes (with negligible volume changes) in earlier models of lithium-ion batteries. The reason is that the high initial porosity provides ample space for the expanding electrode particles with no (or minimal) dimensional changes in the composite electrode. Hence, modeling volume changes in silicon composite electrode in terms of porosity changes alone is a valid assumption in this work.

The reaction that occurs at the silicon electrode is:

$$Li^+ + Si_{4/15} + e^- \rightleftarrows LiSi_{4/15}, \qquad (1)$$

which can be thought of as

$$Li^+ + e^- \rightleftarrows Li \quad \text{(at the surface of the silicon particle)} \qquad (2)$$

$$Li + Si_{4/15} \rightleftarrows LiSi_{4/15} \quad \text{(alloying process)} \qquad (3)$$

The reaction that occurs at the lithium foil is:

$$Li \rightleftarrows Li^{+} + e^{-} \qquad (4)$$

One dimensional transport of lithium ions across the cell sandwich is considered. The silicon composite electrode consists of carbon as the inert conducting material, pores filled with electrolyte, binder and silicon insertion electrode particles. The macro-homogenous approach [6] is used to model the porous electrode wherein the essential features of an actual electrode are accounted for without going into the exact geometric detail. The solid matrix and the electrolyte phase are treated as superposition of two continua. Transport in the electrolyte phase (both in the separator and in the porous electrode) is modeled using concentration solution theory as done in literature [7], [8], assuming a binary electrolyte and a solvent. In concentrated solution theory, the driving force for mass transfer is the gradient in electrochemical potential.

$$c_i \nabla \mu_i = \sum_{j \neq i} K_{ij} (\mathbf{v}_j - \mathbf{v}_i) \qquad (5)$$

Where K_{ij}'s are the frictional coefficients describing interaction between species i and j. Equations of this form can be written for each ionic species and the solvent, although one of these equations will be redundant. Fluxes can be obtained by inverting these equations and that requires a choice of the frame of reference for the fluxes. In previous lithium ion cell sandwich models, the solvent was chosen as the reference species and its velocity was taken as zero. In this work, as relative volume of liquid to solid (due to changing particle size) within pores changes, a convective flow of liquid into or out of the electrode results. Hence solvent velocity cannot be taken as zero. Convection plays a role in the transport of the species across the cell sandwich due to changes in porosity. Hence, superficial volume average velocity is chosen as the reference as

was done in other systems earlier [9], [10], [11]. The fluxes of the ionic species in solution phase in terms of the volume average velocity ($\boldsymbol{v}^{\square}$) is then given by

$$\mathbf{N}_{+} = -\upsilon_{+} D(c) \nabla c + \frac{\mathbf{i} t_{+}^{0}}{z_{+} F} + \upsilon_{+} c \boldsymbol{v}^{\square} \qquad (6)$$

$$\mathbf{N}_{-} = -\upsilon_{-} D(c) \nabla c + \frac{\mathbf{i} t_{-}^{0}}{z_{-} F} + \upsilon_{-} c \boldsymbol{v}^{\square} \qquad (7)$$

c is the concentration of the electrolyte ($c = c_i / \upsilon_i$). The K_{ij}'s can be related to the transport properties $D\ (c), t_{+}^{0}$, κ. Data for varying transport properties are taken from existing literature [12], [13] for $LiPF_6$ in organic solvent. If these fluxes are to be written for species in solution phase within pores of a porous electrode

$$\frac{\mathbf{N}_{+}}{\varepsilon} = -\upsilon_{+} D(c) \nabla c + \frac{\mathbf{i} t_{+}^{0}}{z_{+} F} + \upsilon_{+} c \frac{\boldsymbol{v}^{\square}}{\varepsilon}$$

i.e.

$$\mathbf{N}_{+} = -\upsilon_{+} \varepsilon D_{eff} \nabla c + \frac{\mathbf{i}_2 t_{+}^{0}}{z_{+} F} + \upsilon_{+} c \boldsymbol{v}^{\square} \qquad (8)$$

Similarly

$$\mathbf{N}_{-} = -\upsilon_{-} \varepsilon D_{eff} \nabla c + \frac{\mathbf{i}_2 t_{-}^{0}}{z_{-} F} + \upsilon_{-} c \boldsymbol{v}^{\square} \qquad (9)$$

where $D_{eff} = D(c)\ \varepsilon^{0.5}$ (10)

is called the effective diffusivity accounting for the actual path length of the species. In this work, data for bulk diffusion coefficient of the salt ($LiPF_6$) as a function of its concentration at 294 K (~ room temperature) in organic solvent (PC/EC/DMC) are taken from literature [12] and are provided in the Appendix D.

A material balance on the electrolyte in the porous electrode [14] (for constant partial molar volume of the electrolyte, i.e. $\nabla.\overline{V}_e = 0$) gives

$$\frac{\partial(\varepsilon c)}{\partial t} = \nabla.(\varepsilon D_{eff}\nabla c) - c_0\overline{V}_0\frac{\mathbf{i}_2.\nabla t_+^0(c)}{z_+\upsilon_+F} - \nabla.(c\mathbf{v}^{\square}) + c_0\overline{V}_0\frac{aj_n(1-t_+^0)}{\upsilon_+} \qquad (11a)$$

ε is the porosity of the composite silicon electrode. It is to be noted that as the electrode gets lithiated/ de-lithiated, the porosity also varies and hence ε should also be determined from the model. At this point, we assume that the solvent concentration is constant, which implies that the partial molar volume of the electrolyte is zero [7] and thus equation 11a simplifies to

$$\frac{\partial(\varepsilon c)}{\partial t} = \nabla.(\varepsilon D_{eff}\nabla c) - \frac{\mathbf{i}_2.\nabla t_+^0(c)}{z_+\upsilon_+F} - \nabla.(c\mathbf{v}^{\square}) + \frac{aj_n(1-t_+^0)}{\upsilon_+} \qquad (11).$$

j_n is the pore-wall flux averaged over the interfacial area, relative to the velocity of the pore wall and in the direction pointing into the solution. The pore-wall flux, j_n, is related to the divergence of the current flow in the electrolyte phase through Faraday's law

$$aj_n = -\frac{as_i}{nF}i_n = -\frac{s_i}{nF}\nabla.\mathbf{i_2} \qquad (12)$$

In the separator region, the porosity remains constant (ε_s) and it is considered that the volume of the liquid phase that gets squeezed out by the porosity changes in the insertion electrode goes to the reservoir.

Now, the material balance on the electrolyte in the separator region is

$$\varepsilon\frac{\partial(c)}{\partial t} = \nabla.(\varepsilon D_{eff}\nabla c) - \frac{\mathbf{i}_2.\nabla t_+^0(c)}{z_+\upsilon_+F} - \nabla.(c\mathbf{v}^{\square}) \qquad (13)$$

It is to be noted that in the separator, $\mathbf{i_2}$=I. Here ε denotes the porosity of the separator and is constant.

In most of the earlier modeling works, the transference number of the lithium ion has been taken to be constant for lack of reproducible experimental data [8]. However, importance of transference number has been discussed by Doyle *et al.* [15] for lithium-ion systems. The authors used a fitted expression for transference number of lithium ions in polymer electrolyte system [7]. Furthermore, in recent years, experiments to measure transference number as a function of concentration are available in literature [12], [13]. Hence, it is worthwhile to investigate the case of varying transference number with concentration. Since, the noise level in the determination of the Li^+ transference number as a function of concentration is significant using Hittorf method, Valøen and Reimers [12], used a constant value of 0.38, which will be used in simulations with constant transference number in the present work. However, for the cases with varying transference number (t_+^0), the expression provided by Nyman *et al.* using the system $LiPF_6$ in EC: EMC (3:7) (valid between the concentration range 0.2-2 mol/l) at room temperature [13] will be used. The corresponding plot is shown in Appendix D.

For a single electrode reaction, a material balance on the solid phases shows how the porosity changes with the extent of reaction at each location within the electrode [14], [6].

$$\frac{\partial \varepsilon}{\partial t} = \sum_{solid\ phases} \frac{s_i M_i}{\rho_i n F} \nabla . \mathbf{i_2} \qquad (14)$$

which, in the present work, reduces to (see Appendix D)

$$\frac{\partial \varepsilon}{\partial t} = -s_+ \frac{\nabla . \mathbf{i_2}}{F} (-\tilde{V}_{Si_{4/15}} + \tilde{V}_{LiSi_{4/15}}) = aj_n (\tilde{V}_{LiSi_{4/15}} - \tilde{V}_{Si_{4/15}}) = -\frac{as_+}{F} i_n (\tilde{V}_{LiSi_{4/15}} - \tilde{V}_{Si_{4/15}}) \qquad (15)$$

where $\tilde{V}_{LiSi_{4/15}}$ and $\tilde{V}_{Si_{4/15}}$ are the molar volumes of $Li_xSi_{4/15}$ and $Si_{4/15}$ respectively. Since, for simplicity, the species in reaction (1) are written as $LiSi_{4/15}$ and $Si_{4/15}$, the molar volumes considered in the above expression are 4/15th of $\tilde{V}_{Li_{3.75}Si}$ and $\tilde{V}_{Si}$ respectively. If the initial solid

phase concentration is non-zero, then instead of the molar volume of the silicon electrode, one would use $\left(\tilde{V}_{LiSi_{4/15}}\right)_{initial}$ (see Appendix D). See also Appendix D for the case of de-lithiation.

Expression for $\tilde{V}_{LiSi_{4/15}}$ is based on the work by Obrovac *et al.* [16]

$$\tilde{V}_{LiSi_{4/15}} = \frac{4}{15}\left(\overline{V}_{Si} + 3.75 < x > \overline{V}_{Li}\right) \qquad (16)$$

If the molar volumes in equation 15 were constant, then porosity is a linear function of utilization or time. In such a case, porosity is independent of direction of current. However, as seen from equation 16, the molar volume of the alloy electrode is a linear function of state of charge or utilization. Hence, rate of change of porosity is proportional to the state of charge (or degree of lithiation) or utilization, which is a linear function of time. This implies that porosity is a second-order function of time and hence porosity is dependent on the direction of current as well. In other words, porosity is path dependent. Thus, porosity changes can be expected to contribute to the potential gap (voltage hysteresis) observed in silicon electrodes. This gap in porosity values between lithiation and delithiation is independent of the galvanostatic rate. However, the authors have observed from preliminary data that unless the path dependence of *U vs.* x is included, the porosity changes alone cannot explain the observed voltage hysteresis.

The total current density is conserved, i.e. it either flows through the solution phase ($\mathbf{i_2}$) or the matrix phase of the silicon insertion material ($\mathbf{i_1}$).

$$I = \mathbf{i}_1 + \mathbf{i}_2 \qquad (17)$$

In the present work, I is negative during lithiation of silicon electrode (i.e. discharge of the full cell) and is positive during de-lithiation of the silicon electrode.

Current flowing in the matrix phase is governed by Ohm's law

$$\mathbf{i}_1 = -\sigma_{eff}\nabla\Phi_1 \qquad (18)$$

where σ_{eff} is the effective conductivity of the matrix given by

$$\sigma_{eff} = \sigma_b(1-\varepsilon-\varepsilon_{bf})^{1.5} \qquad (19)$$

σ_b is taken to be a constant bulk conductivity of 33 S/m for the silicon electrode.

At the current collector/insertion electrode interface, the current flows in the solid matrix only (i.e. $\mathbf{i_2}$=0). Hence,

$$\nabla\Phi_1 = -I/\sigma_{eff} \quad @\ z=0 \qquad (20)$$

At the electrode/separator interface, the current is entirely carried in the solution phase and hence,

$$\nabla\Phi_1 = 0 \quad @\ z=L_c \qquad (21)$$

The boundary conditions in the solution phase are that the flux of each species is equal to zero at the cathode/current collector boundary. This leads to

$$\nabla c = 0 \quad @\ z=0 \qquad (22)$$

The variation of potential in the electrolyte is given by

$$\mathbf{i_2} = -\kappa_{eff}\nabla\Phi_2 + \frac{2\kappa_{eff}RT}{F}\left(1+\frac{\partial \ln f_A}{\partial \ln c}\right)\left(1-t_+^0\right)\nabla \ln c \qquad (23)$$

where Φ_2 is measured with a lithium reference electrode in solution. Most of the earlier works neglected the non-ideality of the electrolyte since activity coefficient data had not been reported [8]. The salt activity co-efficient (f_A) as a function of concentration in lithium-battery electrolytes has been measured in recent years [12], [13], [17] and Kumaresan *et al.* [18] captured this non-ideality in their thermal model for lithium-ion cells. In the present work, the results will be discussed for the baseline case of ideal solution as well as for the case where thermodynamic factor $\left(1+\frac{\partial \ln f_A}{\partial \ln c}\right)$ varies with concentration [13]. The corresponding plot from

literature [13] is given in Appendix D. In the above equation effective conductivity is used to account for transport within the porous media.

$$\kappa_{eff} = \kappa(c)\varepsilon^{1.5} \qquad (24)$$

Salt conductivity as a function of concentration is taken from literature for $LiPF_6$ in PC/EC/DMC at room temperature [12]. The corresponding plot is given in Appendix D. This is similar to that discussed by Doyle *et al.* for pure liquid electrolyte of $LiPF_6$ in EC: DMC (2:1) for concentration between 0.2-1.5 mol/l [19].

The flux and concentration of each species and the potential in the solution phase are taken to be continuous between the separator and the composite cathode material. From equation 22 and the condition that $\mathbf{i_2}$=0 at current collector/electrode interface,

$$\nabla\Phi_2 = 0 \quad @\ z = 0 \qquad (25)$$

Since we are interested in potential differences, the potential of the solid lithium phase at the lithium foil boundary is arbitrarily set to zero.

$$\Phi_1 = 0 \qquad @\, z = L_c + L_s \qquad (26)$$

The other boundary conditions involve the flux of lithium ions equaling the net transfer of lithium ions at the interface

$$\mathbf{N}_+ = \frac{I}{F} \quad @\ z = L_c + L_s \qquad (27)$$

The kinetics for the insertion reaction (equation 1) at the silicon composite electrode can be represented by

$$i_n = \left(i_0 \left\{ \exp\left(\frac{\alpha_a F \eta}{RT} \right) - \exp\left(\frac{-\alpha_c F \eta}{RT} \right) \right\} \right) \qquad (28)$$

where

$$i_0 = F\ k\ (c)^{\alpha_a}\ \left(c_{\max} - c_s\right)^{\alpha_a} \left(c_s\right)^{\alpha_c} \qquad (29)$$

The overpotential η appearing in Equation (28) is defined as

$$\eta = \Phi_1 - \Phi_2 - U(x_s) \qquad (30)$$

where $U\ (x_s)$ is the open-circuit potential of silicon composite electrode as a function of the amount of lithium inserted. x_s denotes the surface composition (c_s/c_{max}) and can also be thought of as the stoichiometric coefficient of Li in silicon electrode defined by $Li_xSi_{4/15}$. The plot of U *vs.* x for lithium-silicon electrode is given in Figure 9.2. The discussion about U being strictly a pseudo-thermodynamic potential and that it is path dependent can be found elsewhere [20].

At the lithium foil, the kinetics follows the Butler Volmer kinetics and is given by

$$I = -i_{01}\left[\exp\left(\frac{\alpha_{a1} F \eta_{s1}}{RT}\right) - \exp\left(-\frac{\alpha_{c1} F \eta_{s1}}{RT}\right)\right] \qquad (31)$$

where i_{01} is the exchange current density for the reaction (4) at the lithium foil, taken to be a constant in this work. The overpotential η_{s1} is given by

$$\eta_{s1} = \Phi_1 - \Phi_2 - U' \qquad (32)$$

U' is the open circuit potential of lithium foil for reaction (4) referenced with respect to Li/Li^+ electrode placed in the adjacent solution. Hence, U'=0. And together with equation (26) gives,

$$\eta_{s1} = -\Phi_2 \qquad (33)$$

It can be seen that for a galvanostatic operation, Φ_2 is constant at the lithium foil.

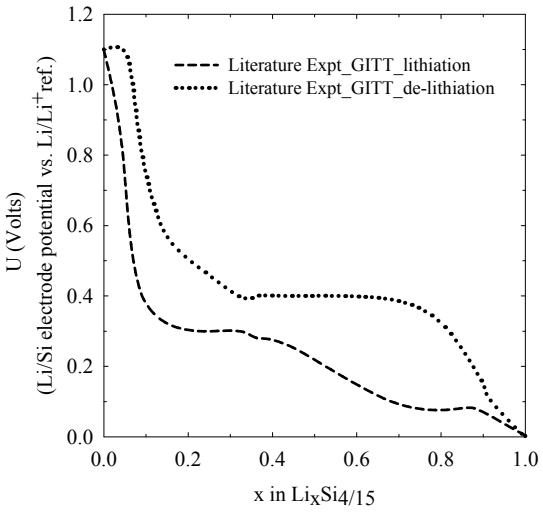

Figure 9.2. *U vs. x* for $Li_xSi_{4/15}$ electrode

The active electrode material is assumed to be made up of spherical silicon particles of radius R_s with diffusion being the mechanism of transport within the particle. The particle radius is taken to be in the nanometer regime so that neglecting stress will be a reasonable assumption to begin with. Strictly speaking, particle with varying radius has to be modeled due to huge volume changes associated with lithiation /de-lithiation. Also transport due to convection (*i.e.* bulk movement due to volume changes) should also be included within the particle. Solid phase transport and insertion kinetics were studied by Chandrasekaran *et al.* [20] earlier in lithium-silicon electrode particle with volume changes. Their studies showed that for nano particles transport due to bulk movement can be neglected at low to moderates of lithiation and diffusive flux dominates the transport. The authors concluded that the advantage of nanostructured materials is that their relaxation times for diffusion are short and hence the concentration of lithium is more uniform when cycled at moderate rates. Moreover, from their potentiodynamic studies, it was evident that slow kinetics has a greater influence on peak locations in cyclic voltammograms than diffusion coefficient or particle size. Hence, from all these, modeling solid phase transport within a particle of constant size considering diffusion as the mechanism of

transport is a valid first approximation. It is to be noted that the effect of changes in particle size is captured in terms of porosity changes in composite electrode.

The direction normal to the surface of the particles is considered to be the *r*-direction.

$$\frac{\partial c_s}{\partial t} + \frac{1}{r^2}\frac{\partial}{\partial r}\left(r^2 \left(-D_s \frac{\partial c_s}{\partial r} \right) \right) = 0 \qquad (34)$$

where c_s represents the concentration of lithium in the solid particle phase. From symmetry,

$$\frac{\partial c_s}{\partial r} = 0 \qquad @\ r = 0 \qquad (35)$$

The second boundary condition is provided by a relationship between the pore-wall flux across the interface and the rate of diffusion of lithium ions into the surface of the insertion material.

$$j_n = -D_s \frac{\partial c_s}{\partial r} \qquad @\ r = R_s \qquad (36)$$

Since spherical electrode particles are considered in this work, specific interfacial area 'a' is given by

$$a = 3\ \frac{(1 - \varepsilon - \varepsilon_{bf})}{R_{sp}} \qquad (37)$$

For the Li-Si system, 'a' will not remain constant because of porosity changes and also change in particle size with lithiation. Even though material balance in solid phase is solved for a constant particle size of radius R_s, expression provided by Chandrasekaran *et al.* [20] can be used to evaluate the changing particle size (R_{sp}) in equation 37.

To describe the bulk flow motion and solve for $\boldsymbol{v}^{\square}$, an overall material balance (i.e. continuity equation or conservation of volume) is needed as done in literature for porous electrode [2], [9], [10], [14]. Assuming a constant partial molar volume of the electrolyte $(\nabla . \overline{V}_e = 0)$,

$$\frac{\partial \varepsilon}{\partial t} + \nabla . \boldsymbol{v}^{\square} = -\frac{s_+}{nF}\left[\frac{\overline{V}_e t_-^0}{\upsilon_+}\right]\nabla . \mathbf{i_2} - \overline{V}_e \frac{\mathbf{i_2}.\nabla t_+^0}{z_+ \upsilon_+ F} \qquad (38)$$

Re-arranging equation 38 gives the generic expression for $\nabla . \boldsymbol{v}^{\square}$.

Substituting equation 15 in equation 38 and integrating, one gets (for n=1),

$$\boldsymbol{v}^{\square} = \frac{s_+}{F}(-\tilde{V}_{Si_{4/15}} + \tilde{V}_{LiSi_{4/15}})\,\mathbf{i_2} - \frac{s_+}{nF}\left[\frac{\overline{V}_e(1-t_+^0)}{\upsilon_+}\right]\mathbf{i_2} - \frac{s_+}{nF}\left[\frac{\overline{V}_e \int (1-t_+^0)}{\upsilon_+}\right]\nabla . \mathbf{i_2} - \overline{V}_e \frac{t_+^0}{z_+ \upsilon_+ F}\mathbf{i_2} - \overline{V}_e \frac{\nabla t_+^0}{z_+ \upsilon_+ F}\int \mathbf{i_2}$$

(39)

Again if the initial solid phase concentration is non-zero, then instead of the molar volume of the silicon electrode, $\left(\tilde{V}_{LiSi_{4/15}}\right)_{initial}$ appears in the above equation. See Appendix D for the case of de-lithiation.

For a constant transference number and for *n*=1, equation 38 can be re-arranged to get $\nabla . \boldsymbol{v}^{\square}$.

$$\nabla . \boldsymbol{v}^{\square} = -\frac{\partial \varepsilon}{\partial t} - \frac{s_+}{F}\left[\frac{\overline{V}_e t_-^0}{\upsilon_+}\right]\nabla . \mathbf{i_2} = -\frac{\partial \varepsilon}{\partial t} - \frac{a s_+}{F}\left[\frac{\overline{V}_e t_-^0}{\upsilon_+}\right] i_n \qquad (40)$$

Again using equation (15) for $\frac{\partial \varepsilon}{\partial t}$ in equation (40) and integrating as suggested in literature [2], [14], yields expression for $\boldsymbol{v}^{\square}$ in the porous electrode as

$$\boldsymbol{v}^{\square} = \frac{s_+}{nF}\left[(\tilde{V}_{LiSi_{4/15}} - \tilde{V}_{Si_{4/15}}) - \frac{\overline{V}_e(1-t_+^0)}{\upsilon_+}\right]\mathbf{i_2} \qquad (41)$$

with the boundary condition that both $\boldsymbol{v}^{\square}$ and $\mathbf{i_2}$ vanish at plane of symmetry or the backing plate.

In the present work, since $\overline{V}_e$ is considered negligible, equations (38) or (40) and (39) or (41) simplifies respectively to equations

$$\nabla . \boldsymbol{v}^{\square} = -\frac{\partial \varepsilon}{\partial t} \qquad (42)$$

$$\boldsymbol{v}^{\square} = \frac{s_+}{nF}\left[(\tilde{V}_{LiSi_{4/15}} - \tilde{V}_{Si_{4/15}})\right]\mathbf{i_2} \qquad (43)$$

In the separator region, since porosity is constant and the solution phase current density is constant during galvanostatic operation, equation 38 reduces to

$$\nabla.\boldsymbol{v}^{\square} = -\overline{V}_e \frac{\mathbf{i}_2.\nabla t_+^0}{z_+ \upsilon_+ F} \qquad (44)$$

yielding

$$\boldsymbol{v}^{\square} = -\overline{V}_e \frac{t_+^0}{z_+ \upsilon_+ F}\mathbf{i}_2 - \overline{V}_e \frac{\nabla t_+^0}{z_+ \upsilon_+ F}\int \mathbf{i}_2 \qquad (45)$$

which reduces to $\boldsymbol{v}^{\square}=0$ when $\overline{V}_e \sim 0$, irrespective of whether the transference number is constant or not.

It is to be noted that even though, in the present work, it is assumed that the partial molar volume of electrolyte is zero, more recently non-zero values have been treated. Nyman *et al.* calculated constant partial molar volumes of 59 x10^{-6} and 87 x 10^{-6} m^3/mol for the salt ($LiPF_6$) and the solvent mixture (EC: EMC) respectively [13]. The authors plotted solvent concentration as a function of the salt concentration. Stewart and Newman [17] provided an expression for the density of solution of $LiPF_6$ in EC as a function of salt concentration. If a constant non-zero value of partial molar volume of the electrolyte is to be used, then, equation 38 can be multiplied by 'c' and substituted in equation 11a to obtain the simplified material balance in electrolyte as shown below, similar to the one provided by Newman and Tiedemann [14].

$$\varepsilon \frac{\partial(c)}{\partial t} = \nabla.(\varepsilon D_{eff} \nabla c) - \boldsymbol{v}^{\square}.\nabla c + (c_0 \overline{V}_0 - c\overline{V}_e)\left(\frac{aj_n(1-t_+^0)}{\upsilon_+} - \frac{\mathbf{i}_2.\nabla t_+^0(c)}{z_+ \upsilon_+ F}\right) \qquad (46)$$

The above equation can then used with equation (38) and (39) and other equations to solve for unknown variables.

The unknown variables are c, Φ_1, Φ_2, c_s, j_n, ε, i_2, $\boldsymbol{v}^{\square}$ and are solved for using the equations listed in Table 9.1 with the appropriate initial and boundary conditions using

COMSOL multiphysics software. The mesh size and tolerances are adjusted as needed. Table 9.2 gives the values of different baseline parameters used in the galvanostatic simulations.

Table 9.1. Equations used in the simulation

Variable	Equation	Boundary condition & Initial condition
Li-Si Electrode		
c	$\frac{\partial(\varepsilon c)}{\partial t} = \nabla.(\varepsilon D_{eff}\nabla c) - \frac{\mathbf{i_2}.\nabla t_+^0(c)}{z_+\upsilon_+ F} - \nabla.(c\boldsymbol{v}^{\square}) + \frac{aj_n(1-t_+^0)}{\upsilon_+}$	$\nabla c = 0 \quad @\ z = 0$; $c = c_{initial}\ @\ t = 0$
ε	$\frac{\partial \varepsilon}{\partial t} = \sum_{solid\ phases} \frac{s_i M_i}{\rho_i nF} \nabla.\mathbf{i_2}$	$\varepsilon = \varepsilon_0\ @ t = 0$
$\mathbf{\Phi}_2$	$\mathbf{i_2} = -\kappa_{eff}\nabla\Phi_2 + \frac{2\kappa_{eff}RT}{F}\left(1+\frac{\partial \ln f_A}{\partial \ln c}\right)\left(1-t_+^0\right)\nabla \ln c$	$\nabla\Phi_2 = 0 \quad @\ z = 0$
$\mathbf{\Phi}_1$	$\nabla\Phi_1 = -\frac{(I\text{-}\mathbf{i_2})}{\sigma_{eff}}$	$\nabla\Phi_1 = -I/\sigma_{eff} \quad @\ z = 0$; $\nabla\Phi_1 = 0 \quad @\ z = L_c$
$\mathbf{i_2}$	$aj_n = -\frac{s_i}{nF}\nabla.\mathbf{i_2}$; $a = 3\ \frac{(1-\varepsilon-\varepsilon_{bf})}{R_{sp}}$; $R_{sp} = R_{p0}\left(1+\frac{3.75\ \overline{V}_{Li} < x >}{\overline{V}_{Si}}\right)^{\frac{1}{3}}$; $< x >= c_{s_{avg}}/c_{\max}$	$\mathbf{i_2} = 0\ @ z = 0$; $\mathbf{i_2} = I\ @ z = L_c$
j_n	$j_n = -\frac{s_i}{nF}\left(i_0\left\{\exp\left(\frac{\alpha_a F(\Phi_1-\Phi_2-U(x_s))}{RT}\right)-\exp\left(\frac{-\alpha_c F(\Phi_1-\Phi_2-U(x_s))}{RT}\right)\right\}\right)$ where $i_0 = F\ k\ (c)^{\alpha_a}\ \left(c_{\max}-c_s\right)^{\alpha_a}\left(c_s\right)^{\alpha_c}$	-
$\boldsymbol{v}^{\square}$	$\nabla.\boldsymbol{v}^{\square} = -\frac{\partial \varepsilon}{\partial t}$; $\boldsymbol{v}^{\square} = \frac{s_+}{nF}\left[(\tilde{V}_{LiSi_{4/15}} - \tilde{V}_{Si_{4/15}})\right]\mathbf{i_2}$ (also see Appendix D)	$\boldsymbol{v}^{\square} = 0$ @ z=0

Table 9.1. continued

c_s	$\frac{\partial c_s}{\partial t}+\frac{1}{r^2}\frac{\partial}{\partial r}\left(r^2\left(-D_s\frac{\partial c_s}{\partial r}\right)\right)=0$; $j_n=-D_s\frac{\partial c_s}{\partial r}$ @ $r=R_s$; $c_s=c_{s_{initial}}$ @ $t=0$; $\frac{\partial c_s}{\partial r}=0$ @ $r=0$	-
Separator		
c	$\varepsilon_s\frac{\partial(c)}{\partial t}=\nabla.(\varepsilon_s D_{eff}\nabla c)-\frac{\mathbf{i}_2.\nabla t_+^0(c)}{z_+\upsilon_+F}-\nabla.(c\mathbf{v}^{\square})$	$\mathbf{N}_+=\frac{I}{F}$ @ $z=L_c+L_s$ $c=c_{initial}$ @ $t=0$
Φ_2	$I=-\kappa_{eff}\nabla\Phi_2+\frac{2\kappa_{eff}RT}{F}\left(1+\frac{\partial\ln f_A}{\partial\ln c}\right)\left(1-t_+^0\right)\nabla\ln c$	$I=-i_{01}\left[\exp\left(-\frac{\alpha_{a1}F\Phi_2}{RT}\right)-\exp\left(\frac{\alpha_{c1}F\Phi_2}{RT}\right)\right]$ @ $z=L_c+L_s$

Table 9.2. Values for parameters

Parameter	**Value**
D_s	10^{-16} m^2/s [21]
R_s	60 nm (for $c_{s_{initial}}$=0, i.e. bare silicon electrode), to be adjusted for other values of $c_{s_{initial}}$; for de-lithiation, for consistency, R_s is the same value as that for lithiation.
T	298 K
ε_0	0.6 (lithiation, if $c_{s_{initial}}$=0), 0.26 (de-lithiation); For $c_{s_{initial}}$=1000 mol/m^3, ε_0=0.5812 (assumed))
ε_{bf}	0.172
σ_b	33 S/m

Table 9.2. continued

$c_{s_{initial}}$	10000 mol/m^3 (lithiation) ($soc_{initial}$= $c_{initial}$/c_{max} =0.032); 280000 mol/m^3 (de-lithiation)
L_c, L_s	25 μm
i_{01}	12.6 A/m^2 [7]
z_+	1
t_+^0	0.38 (for constant transference number calculations)
s_+	-1
$\overline{V}_e$	0 (assumed based on [7])
I	51.48 A/m^2 (for 1 C-rate) (negative for lithiation and positive for de-lithiation).
$c_{initial}$	1000 mol/m^3
k	10^{-13} (m/s) (mol/m^3)$^{-0.5}$ (assumed)
c_{max}	311307.4 mol/m^3 (calculated , [20])

9.3. Results and Discussions

Porosity changes under three different cases are analyzed. Firstly, the results for constant transference number and an ideal electrolyte are discussed (variation of activity coefficient with concentration is neglected). The second case corresponds to that of a non-ideal electrolyte. The third case analyses the system for varying transference number and non-ideal electrolyte. The analysis is carried out for de-lithiation as well. Stop condition for galvanostatic lithiation is that

the cell potential should reach zero. Stop condition for de-lithiation is that the state of charge at the separator/electrode interface should drop to 0.03 (corresponds to the arbitrary initial condition for lithiation). For lack of actual data, the kinetic constant during de-lithiation is taken to be the same as that during lithiation. But, as discussed earlier [20], the kinetic rate constant might be lesser during de-lithiation than during lithiation. This parameter can be adjusted by fitting cyclic voltammogram simulations of a cell sandwich with actual experimental data.

Figure 9.3 gives the cell potential as a function of utilization of the silicon electrode for galvanostatic discharge of the cell (lithiation of the silicon electrode) and galvanostatic charge (de-lithiation of silicon electrode) at different current densities. The corresponding pseudo-thermodynamic potential *vs.* composition curves are also given [20]. The utilization is

$$u = \frac{\int_0^{L_{neg}} soc_{avg}\, dx}{\int_0^{L_{neg}} dx} \qquad (47)$$

where

$$soc_{avg} = \frac{c_{s_{avg}}}{c_{\max}}$$

where $c_{s_{avg}}$ is the solid phase concentration averaged over the entire particle

$$c_{s_{avg}} = \frac{\int_0^{R_p} c_s\, dr}{\int_0^{R_p} dr}$$

It can be seen that until C/5 rate, the electrode is utilized to a great extent before the cut off potential is reached. However, at higher rates such as C and 2C rates, the cut off potential is reached before the electrode can be utilized. Sluggish kinetics contributes to the overpotential in

silicon electrodes more than that observed in conventional electrodes for lithium ion cells. Also, at high rates, ohmic drop is higher. Moreover, as the porosity is reduced, the effective solution phase conductivity decreases and the ohmic drop further increases, all of which leads to quickly reaching the cut-off potential of zero volts against lithium reference. The potential *vs.* composition curve remains the same at a given galvanostatic lithiation rate for all three cases analyzed here (constant transference number and ideal electrolyte, non-ideal electrolyte and constant transference number and varying transference number and non-ideal electrolyte) and hence curves for the first two cases are not provided in Figure 9.3 for purpose of clarity. The potential *vs.* composition curve at C/10 rate for the case with thinner, less porous electrode with same capacity as the baseline case is also given. The lesser utilization (0.7) achieved here as compared to that at C/10 rate of the baseline case is because, the pores get completely filled in the thinner electrode with lower initial porosity at the separator/electrode interface as will be shown later. This leads to a sharp reduction in voltage as seen here in Figure 9.3. During de-lithiation, most of the electrode is utilized if there are no restrictions on the maximum porosity that is allowed. Also, in a real cell when silicon electrode is used as the negative electrode with another positive insertion electrode, cell potential limitations could further limit the de-lithiation of the silicon electrode.

The concentration profiles of the electrolyte over the time scale of a full discharge cycle are depicted in Figure 9.4 at C-rate, 2 C-rate and C/10-rate for the case of varying transference number and non-ideal electrolyte. At the rates analyzed here, the limiting current phenomenon is not observed at any location within the silicon electrode, which will drive the electrolyte concentration to zero (until the cut-off potential is reached). The concentration profile is quickly established compared to the time of discharge especially at C-rate and 2C-rate. The variation in

porosity at C-rate and 2C-rate are not high enough either to have much influence on the concentration profile. At C/10-rate, since utilization is high, corresponding porosity changes influence the local composition changes and so the concentration profile is established for the entire time of lithiation. At the rates considered here, the concentration profiles and the porosity profiles (Figure 9.5) are almost the same for the case of ideal electrolyte with constant transference number, non-ideal electrolyte with constant transference number and the case of non-ideal electrolyte varying transference number and hence figures not repeated for the first two cases. In conventional electrodes, at still higher rates, lithium ion transference number, initial salt concentration, salt diffusion coefficient and electrolyte conductivity all could lead to severe transport limitations within the electrolyte phase, resulting in high concentration overpotential, limiting the performance and ultimately leading to failure. However, in silicon electrodes, it is observed that due to kinetic (along with ohmic) limitations, the cell potential reaches zero at high rates (~ 3C) at low state of charge (~0.2) before any notable drop in porosity or transport limitations could be observed.

Porosity variations are mostly uniform across the silicon electrode at C rate and slight gradients are observed at 2 C-rate as seen in Figure 9.5. At high rates (C-rate and 2C-rate), the system reaches the cut-off potential even before the pore volume fraction drops to lower values. However, at low rates (for e.g. C/10 rate), the electrode is utilized to a great extent before the pores can get completely filled. As porosity decreases, the effective solution phase conductivity decreases in the silicon electrode and this leads to increased polarization of the system. This is in agreement with literature as well [3], [5]. Thus high initial porosity for silicon electrodes seems to be advantageous in terms of better utilization when lithiated at low rates and not so much when done at higher rates.

For verification, porosity profile and concentration profile for a galvanostatic lithiation at C- rate, 2C-rate and C/10 rate for thinner silicon electrodes with same capacity as before (which implies lower initial porosity) are given in Figure 9.6 and Figure 9.7 respectively. Comparing Figure 9.5 and Figure 9.6, it is seen that at C-rate and 2C-rate, the thinner electrode with lower initial porosity can be utilized to almost the same extent as the thicker electrode with high initial porosity since kinetic limitations are predominant. However, at C/10 rate, the pores of the thinner electrode get completely filled at the electrode/separator interface and thus limit the cell utilization to 0.7 (Figure 9.3) as opposed to the higher utilization (>0.9) of the thicker electrode with higher initial porosity. If the electrode dimensional changes are allowed, then the cell utilization may be higher even with lower initial porosity; however due to issues such as short circuit or mechanical integrity which need to be understood better, this option is not explored and discussed further. In Figure 9.7, the compositional changes are accentuated than in Figure 9.4 due to the higher porosity changes in the thinner, less porous electrodes. Due to the low porosity, the transport limitations play a role in these electrodes and hence the concentration gradients are steeper and are established for the entire time of lithiation.

One might argue that with spherical electrode particles of uniform size (as assumed in this model for solid phase mass transport), there is a lower limit to the pore volume fraction that is possible based on the packing structure (and associated packing density) [22] and hence low porosities as attained in Figure 9.6 will not be possible. Thus one should start with higher initial porosities. This argument is acknowledged and the present work serves to provide a guideline to optimize electrode design parameters based on application (i.e. *C*-rate required) rather than provide exact values for initial porosity or thickness. But it is to be noted that for irregular particles shapes and varied particle size distribution, such low porosities might be permissible.

With the above arguments, one is tempted to analyze the performance of an electrode with the same thickness as that used in Figure 9.4 and 9.5 but with a lower initial porosity (i.e. higher capacity than before). Figure 9.8 gives the porosity and concentration profiles at C-rate and C/10-rate. Steeper concentration gradients are also developed than in Figure 9.4 (due to lower porosity) and Figure 9.6 (due to increased thickness of the electrode). Moreover, the concentration profile does not develop as fast as that discussed for the case of high initial porosity. It can be seen that the porosity drops to lower values at electrode/separator interface than the rest of the electrode (i.e. porosity gradients are prominent), which means the electrolyte conductivity is also decreased leading to a significant potential drop. At C-rate, lithiation is stopped when cell potential reaches zero much before the back of the electrode can be utilized. At C/10 rate, large concentration gradient at the end of lithiation is observed. This is because of the influence of the complete plugging of pores at the electrode/separator interface which also limits the cell performance. At 2 C-rate, the electrode utilization is only 0.14 with an initial porosity of 0.3 and thickness of 25 microns (figure not given) whereas as seen in Figure 9.3, with an initial porosity of 0.58, this goes up to ~ 0.45. The utilization (as observed from lithiation time in Figure 9.8) is lower than compared to electrodes of same thickness with high initial porosity or thinner electrodes of similar porosity at other rates as well. Thus, a trade-off between utilization, capacity, weight and volume of the electrodes should be arrived at based on the load demand and application in terms of thickness and porosity of the electrodes.

The importance of diffusion in the solid can be assessed from the dimensionless parameter

$$S_c = \frac{R_s^{\,2}\,|I|}{D_s F(1-\varepsilon_0-\varepsilon_{bf})c_{\max}L_c} \qquad (48)$$

The diffusion time (R_s^2/D_s), using the parameters in Table 9.2, is ~38 seconds and will increase to 76 seconds even if the increase in radius towards the end of lithiation is considered. At C-rate, the (theoretical) lithiation time is 3600 seconds. Hence solid phase diffusion limitations are not expected until high rates such as 10 C-rate is considered. Hence concentration profiles within the solid are not provided here for the rates considered in this work.

An analogous parameter can be calculated relating the time constant for transport of the electrolyte to the time of discharge

$$S_s = \frac{\left(L_s + L_c\right)^2 |I|}{D(c)\, F(1-\varepsilon_0-\varepsilon_{bf})c_{\max} L_c} \qquad (49)$$

At C –rate, this ratio turns out to be ~0.002, which implies solution phase concentration limitations are not expected until significantly high rates are employed for the same thickness of the electrode and separator. Alternately, if the thicknesses are increased solution phase limitations can appear at low/medium rates of lithiation itself. It should be noted that the solution phase limitations are slightly higher than that calculated above due to influence of varying porosity on effective diffusion coefficient.

Next, to analyze the relative importance of ohmic and kinetic limitations in current distribution in the porous electrode (especially when concentration of electrolyte is nearly constant such that concentration effects are negligible), Newman [6] considers the dimensionless current density and exchange current density values and these are discussed by Doyle *et al.* [7] for lithium battery systems. If either of these parameters is significantly larger than unity, then ohmic drop dominates the current distribution in the porous electrode. If one calculates these parameters for lithium-silicon electrodes in the present work, δ ~ 0.063 (for C-rate), ν ~0.085 (see Appendix D). Hence kinetic limitations are important in lithium-silicon electrodes at the

beginning of lithiation. In the present work, this analysis can only be taken as a first approximation because two of the assumptions that are made in the original work are not applicable for silicon electrodes, namely, the pore volume is not constant throughout the thickness of the silicon electrode and the fluid velocity is not zero in the electrode. Towards the end of lithiation, due to very low pore volume fraction, ohmic limitations also could be seen, especially at rates above 1 C. Of course, towards the end of lithiation, concentration effects also could come into effect and hence the analysis is not straightforward.

One can see from equation 37, that 'a' depends on both radius of the electrode particle and the porosity. The radius of the particle increases during lithiation, tending to decrease 'a' and the porosity decreases with lithiation, tending to increase 'a'. Figure 9.9 shows the specific interfacial area ('a') across the silicon electrode during lithiation at C-rate and 2 C-rate for the case of non-ideal electrolyte and varying transference number. As seen from the figures, the specific interfacial area initially decreases with lithiation and then increases.

Figure 9.10 gives the porosity profile at C-rate and 2C-rate for the case of varying transference number in a non-ideal electrolyte. During galvanostatic de-lithiation, the porosity of the silicon electrode is uniform across the electrode at the rates considered here. Analyzing the concentration profiles during de-lithiation (Figure 9.11), it is seen that the concentration gradients at 2 C-rate is higher than at C-rate as expected. Unlike in lithiation, the concentration profiles take considerable time to develop because of the low initial porosities during de-lithiation. Increase in porosity with de-lithiation leads to increased solution phase conductivity whereas the electrode conductivity decreases. Overall one can see that while using silicon electrode, lithiation in silicon electrode limits its performance.

Implications for full cell: So far, analysis has been presented for silicon electrode when used with lithium foil. However, in real world applications, silicon is used as the negative electrode in conjunction with a positive electrode and most likely an intercalation electrode. In such a case, since the positive electrode, say for e.g. $LiCoO_2$, does not undergo significant volume changes, a constant porosity will be chosen and since the theoretical specific capacity is lesser than that of silicon electrode, a thicker positive electrode will be needed to match the capacity of negative electrode. This implies that at higher rates, one has to determine if solution phase limitations in the positive electrode or the kinetics at the silicon electrode limits the cell performance. However, for applications that do not require higher rates, this system should be well utilized. Also, it should be understood that lithiation of silicon electrode could limit the available capacity. All these analyses are the subject of a future investigation.

9.4. Conclusions

Cell sandwich model for lithium-silicon composite electrode/separator/lithium foil is developed [23]. Porosity changes have been included in the model. The concept of reservoir is introduced for accommodating the electrolyte that gets displaced during the operation of the cell. It is shown quantitatively that at low rates, high initial porosity leads to high (almost complete) electrode utilization during lithiation of silicon electrode whereas with low initial porosity, the pores get completely filled at the separator/electrode interface leading to a sharp reduction in cell potential and the cell performance is thus limited . At higher rates, thicker, porous electrodes and thinner, less porous electrodes lead to similar utilization because silicon electrodes are limited by electrode kinetics before any transport limitations could be seen. It is also shown that utilization is reduced if one attempts to increase the capacity of the electrode for the same thickness by reducing the porosity. This is due to increased transport limitations. Future work can

quantitatively explore the relative merits of allowing electrode dimensional changes as opposed to porosity changes in silicon electrodes and also develop 2 D model to consider flow in and out of the reservoir and its impact on the performance of the cell. Also knowledge form this study should be carried further to analyze dual lithium insertion cell for real world applications.

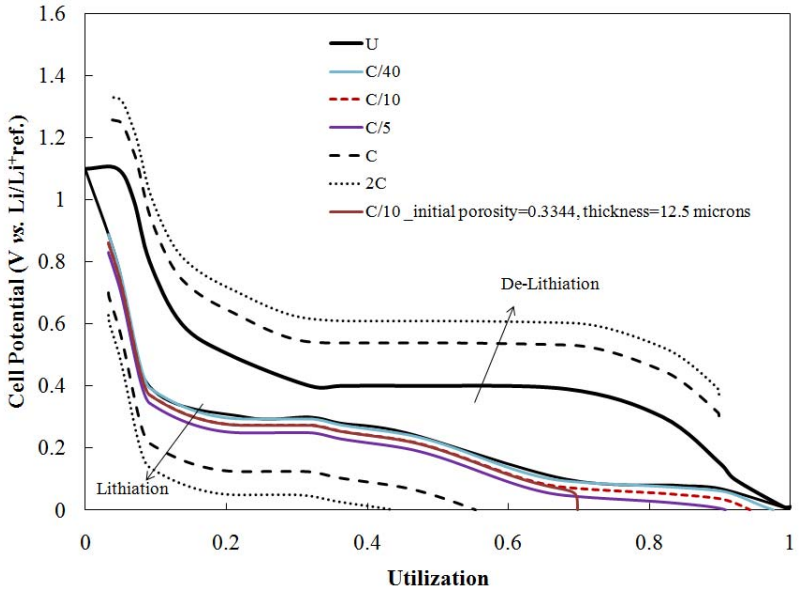

Figure 9.3. Cell Potential vs. utilization during lithiation of silicon electrode

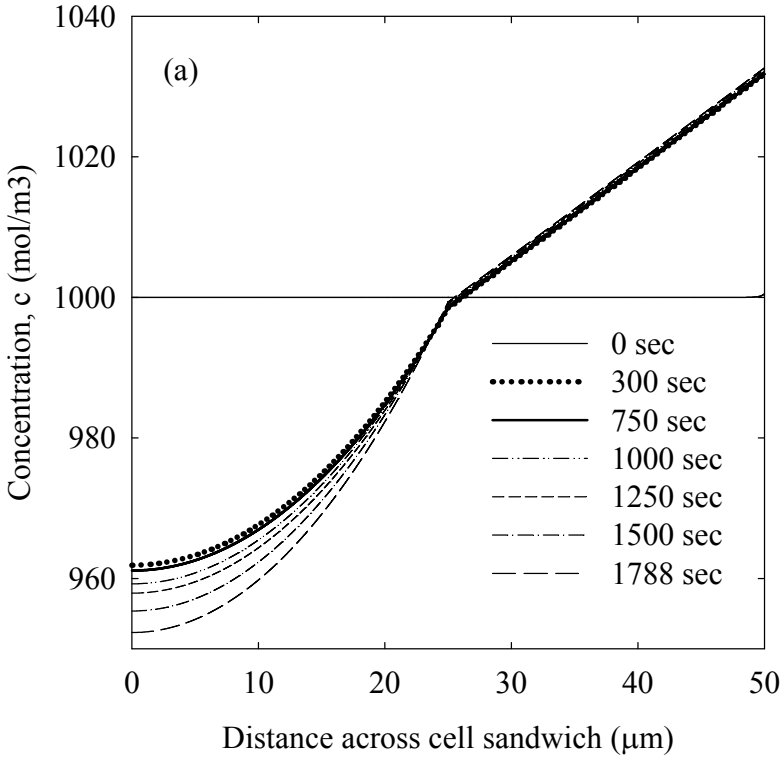

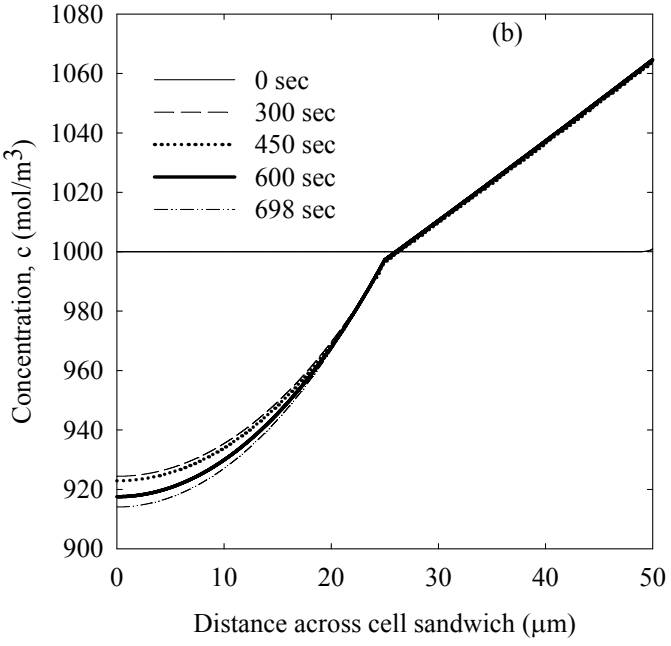

Figure 9.4. Concentration profile across cell sandwich during lithiation of silicon electrode for varying t_+^0, non-ideal electrolyte @ (a) C- rate ; (b) 2 C –rate; (c) C/10 –rate.

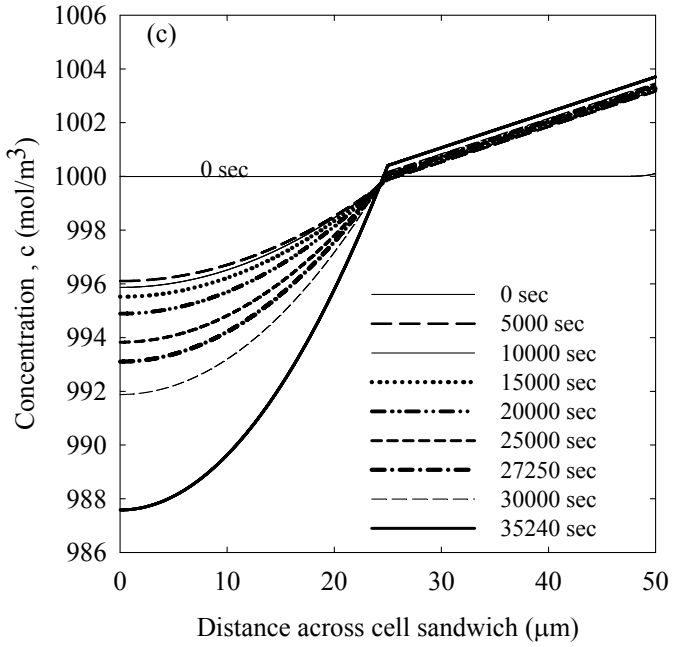

Figure 9.4. continued

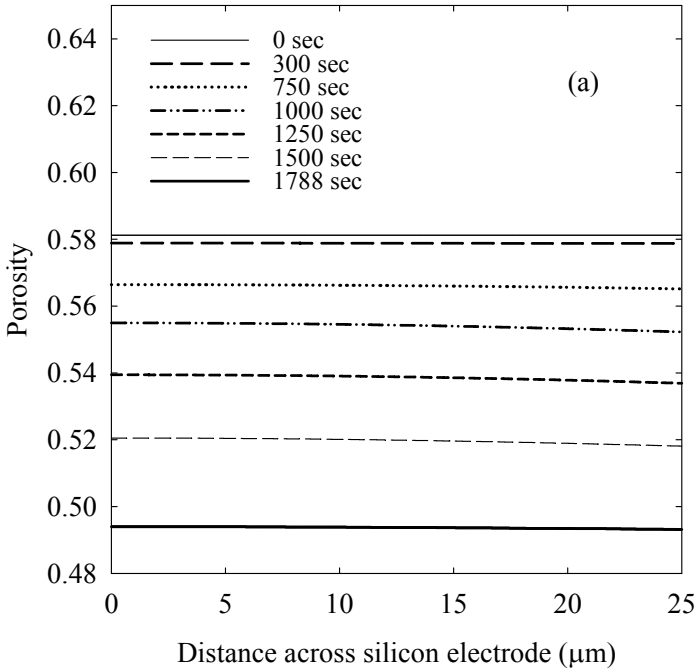

Figure 9.5. Porosity profile across silicon electrode during lithiation for varying t_+^0, non-ideal electrolyte @ (a) C- rate; (b) 2 C –rate; (c) C/10 –rate.

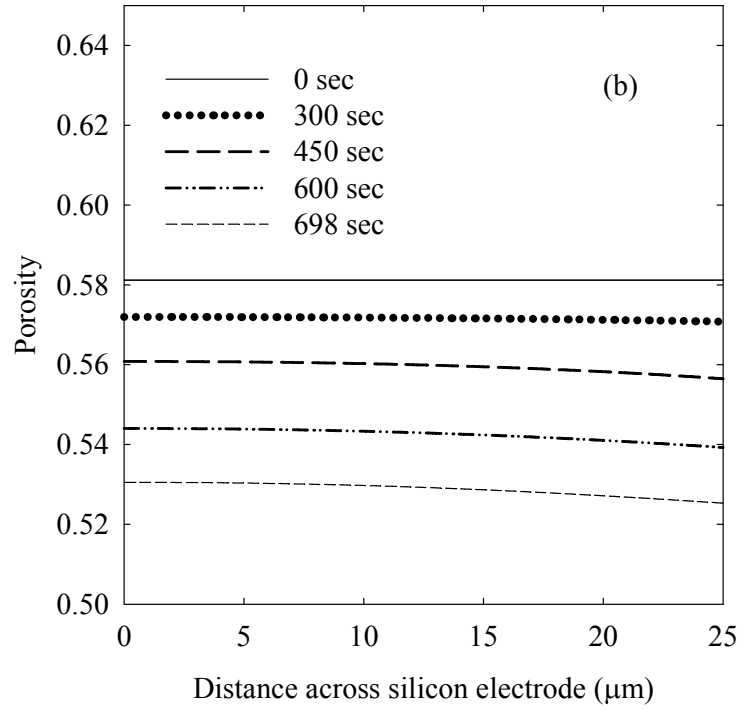

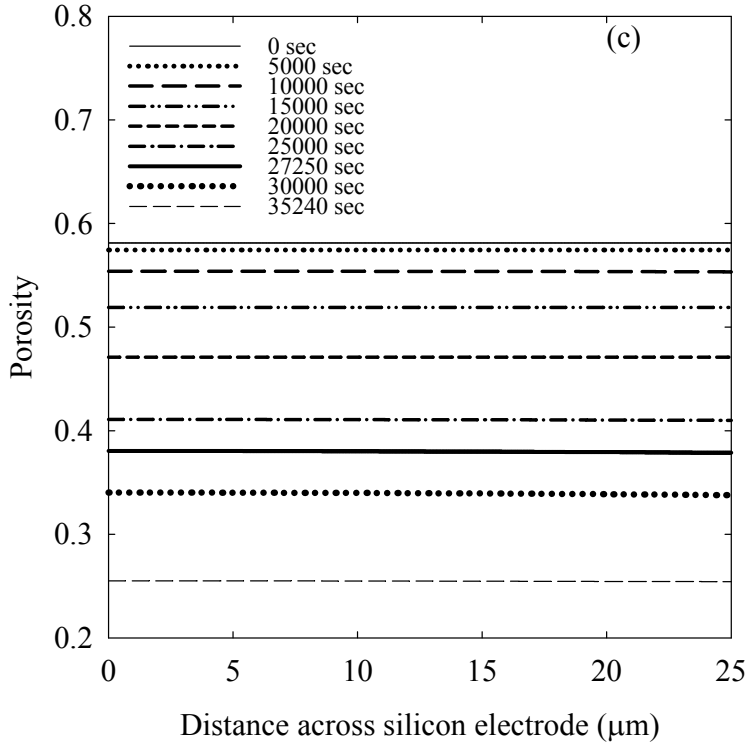

Figure 9.5. continued

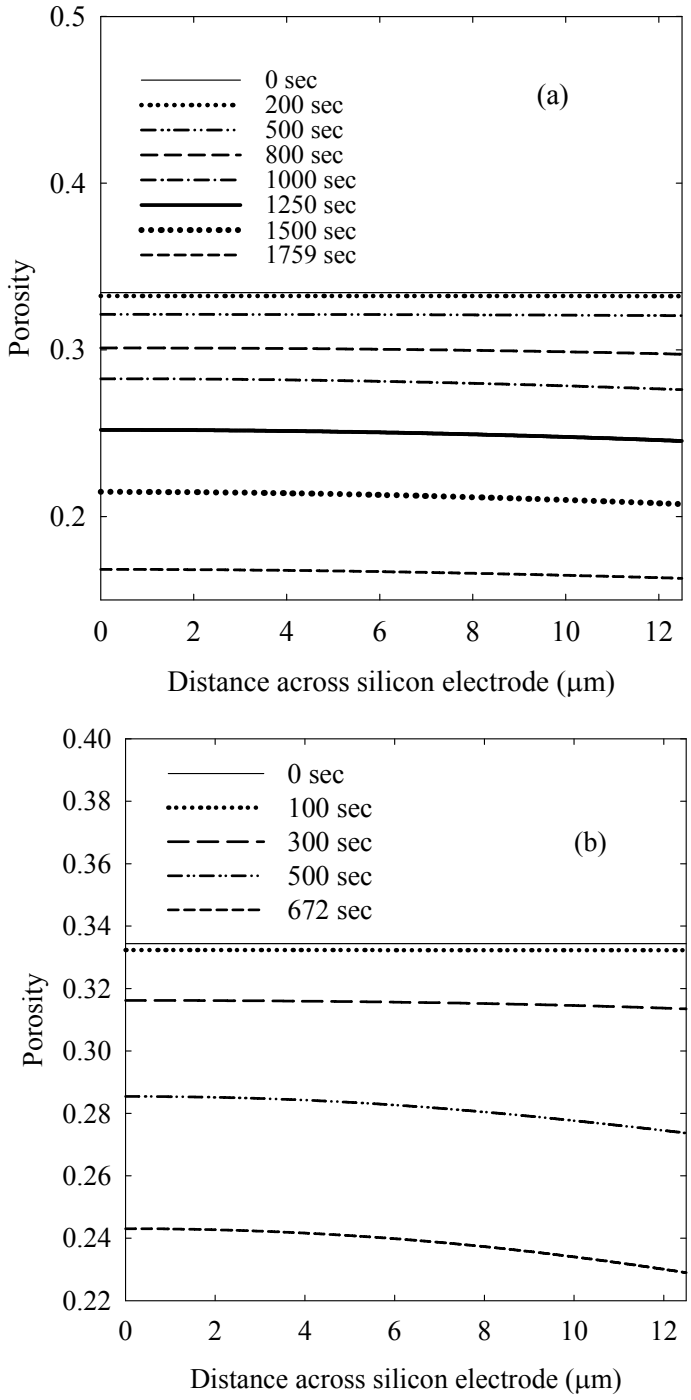

Figure 9.6. Porosity profile across silicon electrode during lithiation with initial porosity of 0.3344 and thickness 12.5 microns (designed for same total capacity as in Figure 9.4 and 9.5) for varying t_+^0, non-ideal electrolyte @ (a) C- rate ; (b) 2 C –rate; (c) @ C/10 –rate.

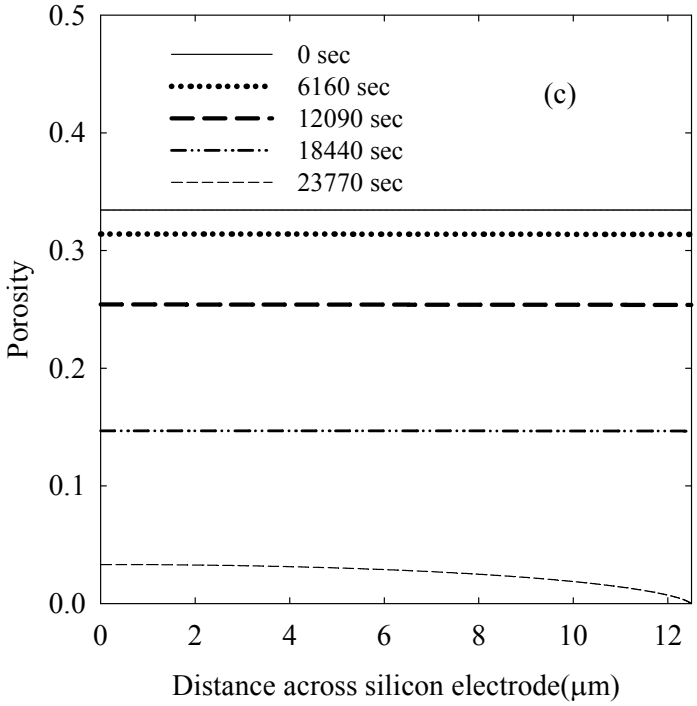

Figure 9.6. continued

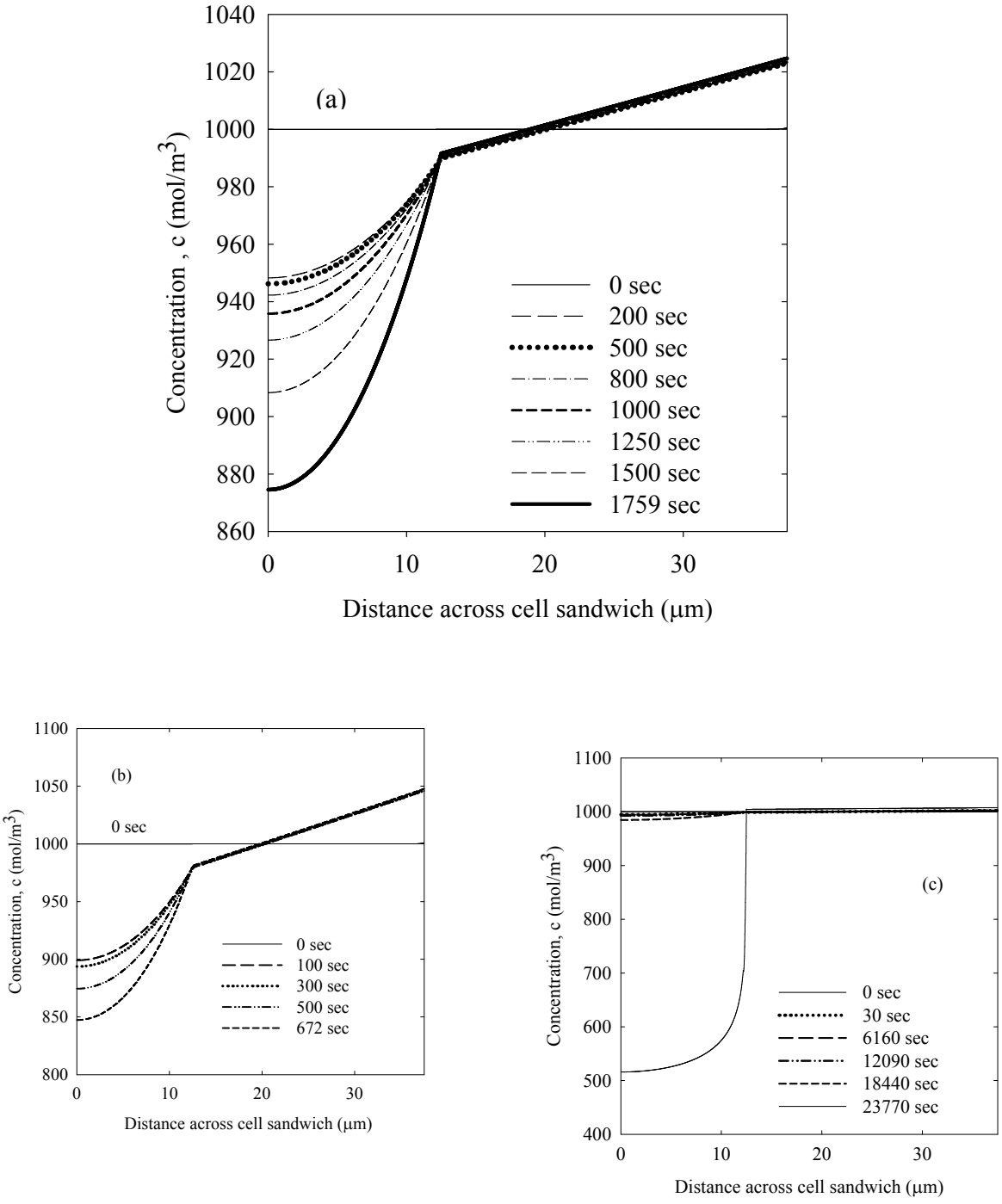

Figure 9.7. Concentration profile across silicon electrode during lithiation with initial porosity of 0.3344 and thickness 12.5 microns (designed for same total capacity as in Figure 9.4 and 9.5) for varying t_+^0, non-ideal electrolyte @ (a) C- rate ; (b) 2 C –rate; (c) C/10 –rate.

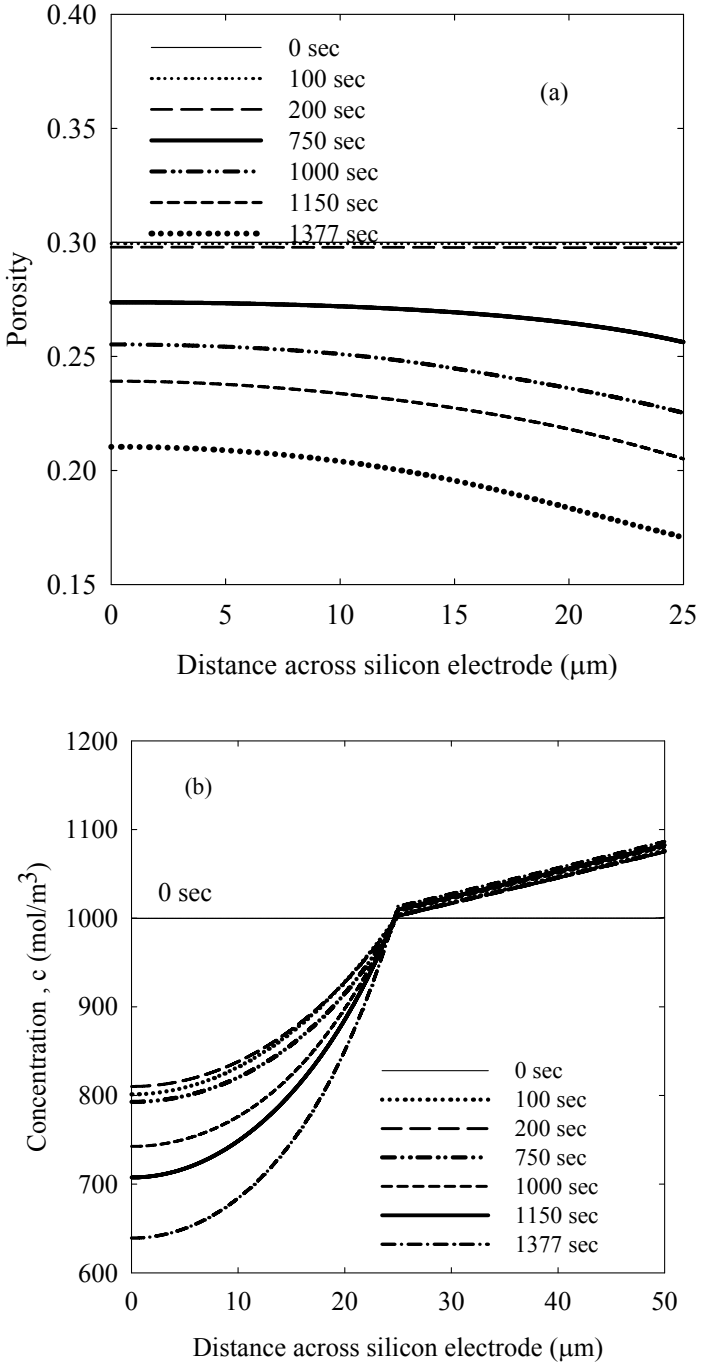

Figure 9.8. (a) Porosity profile at (a) C-rate; (c) C/10-rate; Concentration profile at (b) C-rate ; (d) C/10-rate during lithiation of silicon electrode with non-ideal electrolyte and varying transference number, starting with an initial porosity of 0.3 and thickness 25 microns.

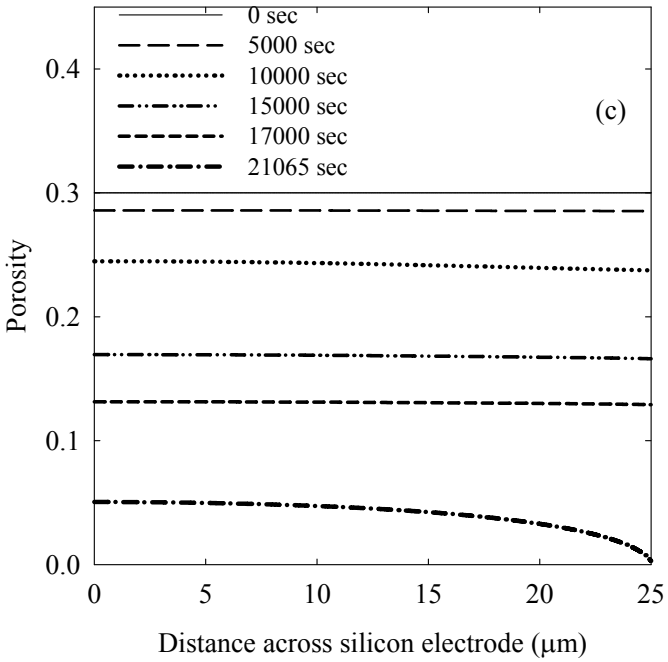

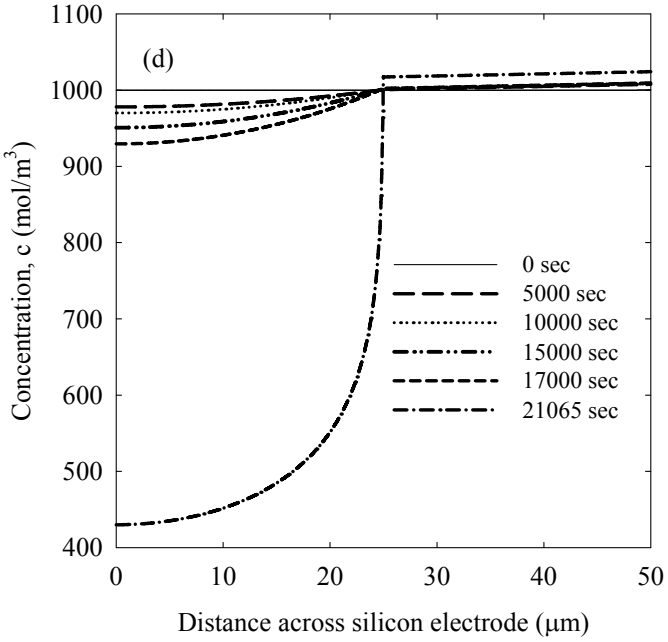

Figure 9.8. continued

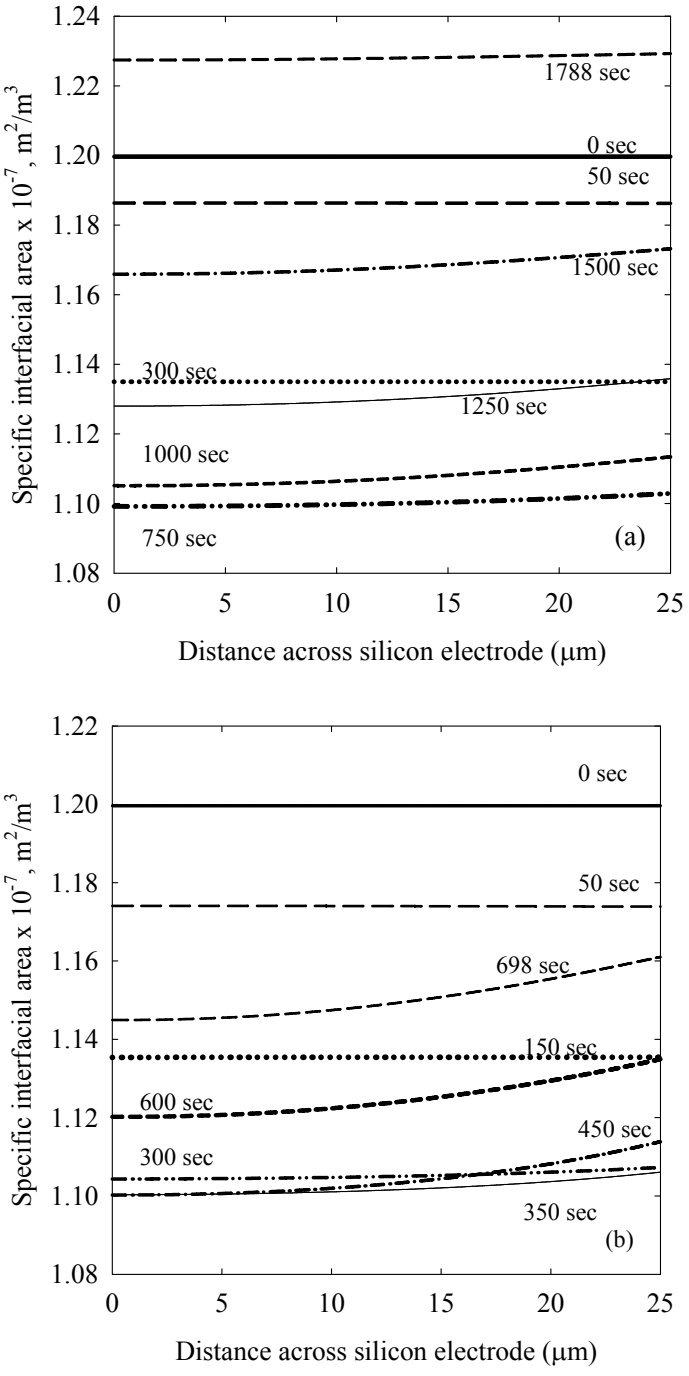

Figure 9.9. Variation of specific interfacial area across silicon electrode during lithiation for non-ideal electrolyte for the case of varying transference number @ (a) C-rate (b) 2 C-rate.

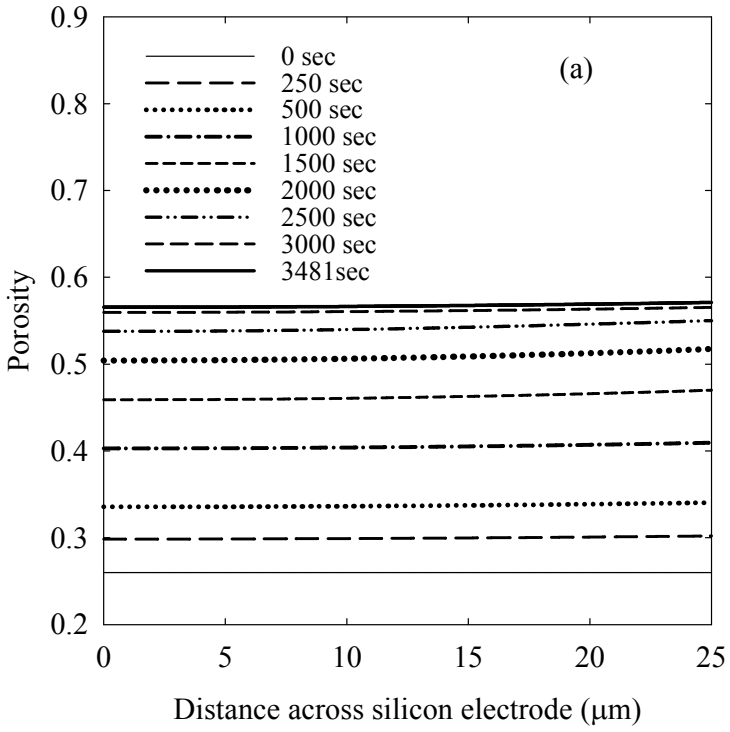

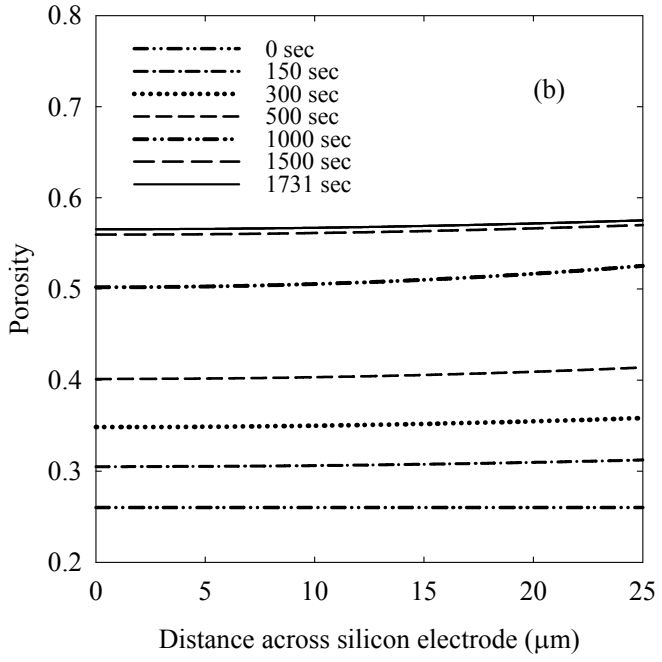

Figure 9.10. Porosity profile during de-lithiation for the case of varying transference number in non-ideal electrolyte (a) C-rate (b) 2C -rate

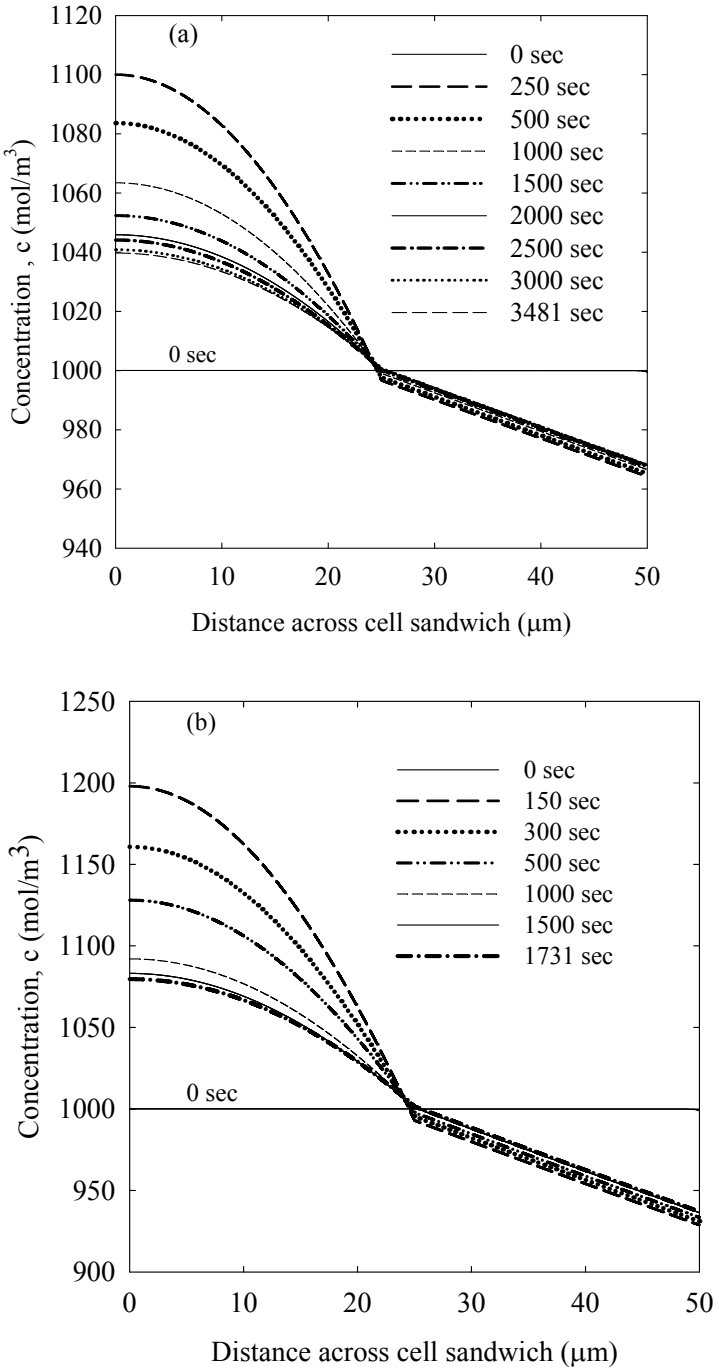

Figure 9.11. Concentration profile during de-lithiation for the case of non-ideal electrolyte, varying transference number @ (a) C-rate; (d) 2 C-rate

9.5. References

[1] Godfrey Sikha, Branko N. Popov, Ralph E. White, *J. EIectrochem. Soc.,* 151 **(**7) (2004) A1104-A1114.

[2] T.I.Evans, T.V.Nguyen, R.E. White, *J.Electrochem.Soc.*, 136 (2) (1989), 328-339.

[3] Richard Pollard, John Newman, *J.EIectrochem. Soc.,* 128(3) (1981), 491-502.

[4] Dawn Bernardi, John Newman, *J.EIectrochem. Soc.*, 134 (1987), 1309-1318.

[5] Dawn Bernardi, Ellen M. Pawlikowski, John Newman, *J.EIectrochem. Soc.*, 135(12) (1988) 2922-2931.

[6] Newman and Thomas-Alyea, Electrochemical Systems, Third Edition, John Wiley and Sons, Inc.

[7] Marc Doyle, Thomas F.Fuller, John Newman, *J.Electrochem.Soc.*, 140 (6) (1993), 1526-1533.

[8] Thomas F. Fuller, M. Doyle, J.Newman, *J. Electrochem. Soc.*, 141(1), 1994, 1-10.

[9] John Newman, Thomas W.Chapman, *AIChE Journal*, 19 (2) (1973), 343-348.

[10] Hiram Gu, Douglas N.Bennion, John Newman, *J.Electrochem.Soc.*, 1364-1370, 123(9) 1976.

[11] T.I.Evans, T.V.Nguyen, R.E. White, *J.Electrochem.Soc.*, 136 (2), 1989, 328-339.

[12] Lars Ole Valøen, Jan N. Reimers, *J.Electrochem.Soc.*, 152(5), A882-A891 (2005).

[13] Andreas Nyman, Mårten Behm, Göran Lindbergh, *Electrochim.Acta*, 53 (2008) 6356-6365.

[14] John Newman, William Tiedemann, *AIChE Journal*, 21(1), 1975, 25-41.

[15] Marc Doyle, Thomas F.Fuller. John Newman, *Electrochim.Acta*, 39(13), 2073-2081, 1994.

[16] M.N.Obrovac, Leif Christensen, Dinh Ba Le, J.R.Dahn, *J.Electrochem.Soc.,* 154 (9) (2007), A849-A855.

[17] Sarah Stewart, John Newman, J.*Electrochem.Soc.*, 155(6), A458-A463 (2008).

[18] K.Kumaresan, G.Sikha, R.E. White, *J.Electrochem.Soc.*, 155(2), A164-A171,(2008).

[19] M.Doyle, J.Newman, A.S.Gozdz, C.N. Schmutz, J.M.Tarascon, *J.Electrochem.Soc.*, 143 (1996) 1890.

[20] Rajeswari Chandrasekaran, Alexandre Magazinski, Gleb Yushin, Thomas F.Fuller, *J.Electrochem.Soc.*, 2010 (accepted).

[21] N. Ding , J. Xu, Y.X. Yao , G. Wegner , X. Fang , C.H. Chen , I. Lieberwirth, *Solid State Ionics*, 180 (2009), 222-225.

[22] S.D.Beattie, D.Larcher, M. Morcrette, B.Simon, J.M.Tarascon, *J.Electrochem.Soc.*, 155(2) A158-A163 (2008).

[23] Rajeswari Chandrasekaran, Thomas F.Fuller, *J.Electrochem.Soc.*, (manuscript soon to be submitted).

CHAPTER 10

CONCLUSIONS AND RECOMMENDATIONS

This dissertation has contributed significantly in both mitigating durability issues in Pt catalyst in PEMFC at hybrid system level by controls approach and analyzing silicon electrodes from physics-based models for optimization of performance and effective scale-up.

10.1. RSM Methodologies for electrochemical systems

The first part of this thesis has provided the framework to make trade-offs between performance and durability in electrochemical energy storage and energy conversion devices. The need to have robust design methodologies as part of degradation mitigation efforts in the early design phases is established. Surrogate models using Response Surface Methodologies are a step in this direction. Surrogate models were developed in this thesis for platinum catalyst dissolution in PEMFC. It is shown quantitatively in this dissertation from response surface models that upper fuel cell potential is the dominating factor affecting Pt stability. Hence it is proven quantitatively in this dissertation that for a small loss in efficiency, Pt loss can be reduced by orders of magnitude in a fuel cell/battery hybrid system. Surrogate models were also developed to capture the influence of rate capability and temperature on performance of lithium ion batteries. This is important because most battery models in system models do not include their influences effectively.

Future work should focus on creating surrogate models for other durability issues as well in PEMFC such as carbon corrosion, membrane degradation, etc. Surrogate

models for capacity fade of batteries should also be developed. As and when the influence of the degradation of one component on the durability of the other is established in PEMFC (and in batteries) from experiments or detailed simulations, these should be used to create the response surface models reflecting the same so that this knowledge can be used in higher level system models to arrive at valuable trade-offs between cost, performance, durability, etc. An advantage of using RSM methodologies is that interaction between different degradation phenomena and their collective influence at the hybrid vehicle system level can be established with high fidelity without adding complexity and computational time.

However simple second order polynomials used in RSM might not depict the true picture for all cases due to complexities of the system. In such a case, either higher order RSEs should be used or other surrogate modeling techniques be adopted.

10.2. Modeling of silicon negative electrodes

In the second part of the thesis, physics-based models of composite silicon negative electrodes for lithium ion batteries have been developed for fundamental understanding and to guide electrode design for better performance.

In this doctoral work, lithium insertion/de-insertion in silicon electrodes at room temperature is analyzed. From the particle model with volume changes, path dependence of the pseudo-thermodynamic potential *vs.* composition curve for lithium-silicon electrodes at room temperature is established and justified by comparing simulated and experimental cyclic voltammograms. The need to use two different kinetic rate constants in the expression for exchange current density for lithiation and de-lithiation is discussed and incorporated in the work. Advantage of nanoparticles in facilitating transport of

lithium within silicon is quantitatively shown from galvanostatic simulations, in spite of the low diffusion coefficients of lithium in silicon at room temperature. Parametric CV study with different diffusion coefficient values was carried out, due to the disparity in literature values and to further corroborate the advantage of nano-materials. At high rates, concentration gradients develop and the results shown in this dissertation have profound implications for stress. Sluggish kinetics is established. However, it is discussed from the results of both constant current and potential sweep simulations, that really low values found in literature for exchange current density might not be applicable for nanoparticles. Anodic transfer coefficient that appears in the Butler-Volmer kinetic expression is found to have a stronger influence than the cathodic transfer coefficient on the cyclic voltammograms. Lithium insertion kinetics is found from this dissertation to be the dominant factor limiting cell performance. This work stresses the need for experimental efforts to accurately determine the solid phase diffusion coefficient of lithium in silicon and the kinetic parameters (exchange current density and transfer coefficients) for charge transfer kinetics for the lithium insertion in silicon nanoparticles without interference from other components of the electrode. It is shown in this dissertation that one might reason kinetic hysteresis as another plausible mechanism to explain path dependence in potential *vs.* composition curve. However, this work cautions that unless asymmetric transfer coefficients and really slow kinetics than found in this work is established, kinetic hysteresis cannot account for the potential gap observed at rates such as C/1000. At such really slow kinetics, one expects a really poorer performance than observed from experiments. This contradiction should also be sorted out. This dissertation suggests that

apart from stress and side reactions, semiconductor nature of the silicon electrodes could contribute to the potential gap, subject to further verification from experiments.

The particle model should further be extended to include stress as well as side reactions on the surface of the silicon electrode particle. The problem one might encounter here is the unavailability of extensive data on side reactions on the surface of silicon negative electrodes. The scientific community is urged to work in this field. Also, the need to further corroborate stress simulations results with actual experimental data would mean that one needs to have accurate in-situ techniques to measure stress under different operating conditions. Influence of temperature on charge transfer kinetics and solid phase transport should be studied as well. The particle model should be extended to study other particle shapes because in real manufacturing conditions for high volume applications, there might be some variation in particle shapes and sizes. If this particle model is to be used for micron sized particles, then convective flux at the boundary condition has to be included.

The knowledge from the particle model is then used to develop the cell sandwich model for lithium insertion/de-insertion from silicon electrodes at room temperature. This model analyzes the porosity changes during lithiation/ de-lithiation in silicon negative electrodes. It has been verified that porosity changes alone cannot explain the observed potential gap and hence the pseudo-thermodynamic potential *vs.* composition curve with path dependence from single particle modeling work has been used to simulate the potential gap observed in experiments. The exchange current density's order of magnitude is the same from both cell model and particle model. It is shown how the specific interfacial area varies with both varying porosity and the changing radius of the

silicon electrode particle. The influence of varying porosity on transport properties is also included in this dissertation. The influence of initial porosity (and hence the thickness for same capacity) on electrode performance at different rates is studied. It is found that at medium and high rates, kinetics limits the cell performance with silicon electrodes comprising nanoparticles of active material and the porosity does not vary much. Hence higher initial porosity does not offer real advantage in terms of improving performance, but just ensures that the final porosity during lithium insertion is higher than or equal to that dictated by packing density based on particle shape. However, for low-rate applications, thicker electrodes (*i.e.* higher initial porosity for the same capacity) lead to better utilization of active material. If the initial porosity is low, the pores get plugged at separator/electrode interface and the cell potential drops to zero and limit cell performance. During de-lithiation, the performance is only limited by the initial state of charge that is possible from the previous lithiation step and the final porosity value that might be dictated by initial electrode design. Again no solid phase limitations were observed for nanoparticles. No solution phase limitations were observed at low to medium rates. If kinetics is improved by some surface treatment, then thickness and porosity will play even more significant factor in determining cell performance. It can be seen that silicon electrode's performance is limited by it's lithiation step. The concept of reservoir is introduced for the first time for lithium ion batteries to accommodate the electrolyte that gets squeezed out during lithiation of silicon negative electrodes.

Future work should include the growing particle in the cell sandwich model, especially if bigger particles (micron-sized) are used in the electrode. The cell model should be extended to include the electrode dimension change in the silicon electrodes

along with porosity changes. Detailed 2D model will be needed to capture the movement of electrolyte into and out of the reservoir. The cell performance model should then be extended to capture the capacity fade due to formation of poor solid electrolyte interphase (SEI) at the silicon electrode. A comprehensive model should finally be developed that combines the volume changes, capacity fade due to irreversible loss of lithium as mentioned above stress in silicon electrodes and finally thermal effects. Finally, to be directly applicable to real world applications, the Li-Si electrode has to be modeled with a positive insertion electrode in a cell sandwich and understand the limitations in either electrode that limit cell performance. Challenges will be to get actual data for several parameters that get introduced with increasing complexity of the model as fewer fundamental studies on properties of Li-Si system for battery applications is available. Hence this dissertation urges the material scientists and chemists to contribute this knowledge to the community to help guide better electrodes for hybrid and all-electric vehicles.

APPENDIX A

CHAPTER 4 SUPPLEMENTARY MATERIAL

The supplementary materials in this Appendix are from Reference [1] in this Appendix.

Appendix A.1. Vehicle Design

Table A.1. Vehicle design parameters

Parameters	**Value**
Density of air ($\rho_{a)}$	1.2 kg/m^3
Acceleration of gravity, g	9.81 m/s^2
Aerodynamic drag coefficient (C_d)	0.26
Frontal Area (F_{area})	2.2 m^2
Coefficient of rolling resistance (C_{rr})	0.007

Vehicle Model Equations

$$P_{d-total} = P_v + P_{rr} + P_{ad} + P_{acc}$$
$$P_v = m_v \times v \times a$$
$$F_{rr} = C_{rr} \times m_v \times g$$
$$P_{rr} = F_{rr} \times v$$
$$F_{ad} = \frac{1}{2} \times \rho_a \times v^2 \times C_d \times F_{area}$$
$$P_{ad} = F_{ad} \times v$$
$$P_{acc} = 1000(Watts)$$
$$m_{bv+pp} = 1450kg$$
$$m_v = m_{bv+pp} + m_b + m_{fc}$$

Maximum Power demand =110 kW

Table A.2. Nomenclature

Symbol	**Description**
$P_{d\text{-}total}$	Total power demand of the vehicle (Watt)
P_v	Power demand of the vehicle due to vehicle velocity (Watt)
P_{rr}	Power to overcome rolling resistance (Watt)
P_{ad}	Power to overcome aerodynamic drag (Watt)
P_{acc}	Accessory power demand (Watt)
m_v	Net mass of the vehicle (kg)
v	Velocity of the vehicle
a	Acceleration of the vehicle (m/s^2)
F_{rr}	Force of rolling resistance (N)
F_{ad}	Force due to aerodynamic drag (N)
m_{bv+pp}	Base mass of vehicle +passenger payload (kg)
m_b	Mass of battery (kg)
m_{fc}	Net mass of fuel cell stack system (kg)

Appendix A.2. Fuel Cell

Table A.3. Fuel Cell System Design Specifications

Compressed hydrogen tank pressure	70 MPa
Weight of fuel cell stack/rated power	2.6 kg/kW
P_{fc_rated} (Rated Fuel cell power)	90 kW
u_{H_2} (Hydrogen Utilization Factor)	90%
A_{MEA} (Area of 1 MEA of PEMFC)	200 cm^2
m_{sub} (mass of FC subsystem)	150 kg
Number of hydrogen tanks	4
Compressibility factor (Z)	1.57
Safety factor (to calculate hydrogen storage volume)	1.13
$m_{H2\_tanks\_net}$ (Net mass of all hydrogen tanks)	77.054 kg (Basis: http://www1.eere.energy.gov/hydrogenandfuelcells/pdfs/33098_sec3.pdf))
m_{H2} (Mass of hydrogen in tank at start of simulation)	5.4 kg
MW_{H_2} (Molecular weight of hydrogen)	0.002 kg/mole
F (Faraday's constant)	96485 coulombs/mole
n (for H_2)	2

N_{MEA} (Number of PEMFC MEA needed) = 427

$$m_{fc} = 2.6 * P_{fc\_rated} + m_{H_2\_\text{tank}} + m_{H_2} + m_{sub}$$

Weight percent of hydrogen: $\dfrac{m_{H_2}}{m_{H_2} + m_{H_2\_\text{tanks}\_net}} = 6.54\%$

Hydrogen used= $\dfrac{1}{u_{H_2}} \int_0^t \dfrac{N_{\text{MEA}}\ i\ A_{\text{MEA}}}{n\ F\ MW_{H_2}} dt$

Appendix A.3. Battery

Battery Model Equations

$$OCP_{pos} = 4.19829 + 0.0565661 \tanh(-14.5546\, y + 8.60942) - 0.0275479 \left(\frac{1}{((.998432 - y)^{0.492465})} - 1.90111 \right)$$

$$-0.157123\, e^{(-0.04738\, y^8)} + 0.810239\, e^{(-40\,(y - 0.133875))}$$

$0.4 < y < 0.9981$

[2]

$$OCP_{neg} = \frac{(1.997 + 2.472 \times x)}{1 + 31.823 \times x}$$ [3]

$$OCP_{cell} = OCP_{pos} - OCP_{neg}$$

η_v = quadratic function of battery current density (Assumed parameters)

$V_{cell} = OCP_{cell} - \eta_v$

Relation between State of charge of the battery and intercalation co-efficients of the individual electrodes

During Discharge Process,

If anode is the limiting electrode,

$$SOC = \frac{x - x_{min}}{(x_{max} - x_{min})}$$

and

$$y = (1 - SOC) \times (y_{max} - y_{min}) + y_{min}$$

If cathode is the limiting electrode,

$$SOC = \frac{y_{max} - y}{(y_{max} - y_{min})}$$

Faraday's law used to update individual electrodes state of charge

$$m_b = w_{Li-cell} \times n_{Li}$$

$$Energy\ of\ battery\ (Joules) = \left(\int_0^t V_{cell} \times n_{Li} \times I_{bat} \times dt \right)$$

Table A.4.

Variables	**Description**
y	Intercalation co-efficient of the positive electrode
x	Intercalation co-efficient of the negative electrode
OCP_{pos}	Open circuit potential of positive electrode (Volts)
OCP_{neg}	Open circuit potential of negative electrode (Volts)
OCP_{cell}	Open Circuit potential of individual cell (Volts)
η_v	Overpotential of individual lithium ion cell (Volts)
V_{cell}	Individual lithium ion cell voltage (Volts)
m_b	Net Mass of the batteries in series (kg)

Table A.5. Battery Design Parameters

Parameter	**Value**
Mass of one lithium ion cell ($w_{Li\text{-}cell}$)	0.908 kg (Yardney website)
Number of lithium ion cells ($n_{Li)}$	53
y_{max}	0.9972
y_{min}	0.179
x_{max}	1
x_{min}	0.1
Initial state of charge	0.8 (Variable input parameter)
Maximum Power from battery (P_{b_max})	20 kW
Capacity of individual lithium ion cell	25 Ah

Appendix A.4. DC/DC Converter

DC/DC Converter Model Equation

$$y = 0.6077x^6 - 1.7325x^5 + 1.1629x^4 + 0.7525x^3 - 1.3222x^2 + 0.6276x + 0.8707$$

y : *Fractional efficiency*

x : *Fraction of input power*

Appendix A.5. Power sharing algorithm

Power sharing algorithm for the Baseline Model

If $P_{traction} >= 0$ & $P_{acc}>0$

  If $P_{traction} + P_{acc} > P_{FC\text{-}rated}$

    $P_{traction} + P_{acc} = P_{FC\text{-}rated} + P_{batt}$ (if battery has sufficient capacity)

  Else if $P_{FC\text{-}min} < P_{traction} + P_{acc} < P_{FC\text{-}rated}$

    If SOC >= 0.6

      $P_{traction} + P_{acc} = P_{FC}$

    Else if SOC <0.6

      $P_{traction} + P_{acc} + P_{batt\_charge} = P_{FC} = P_{FC\text{-}rated}$

End
Else if $P_{traction} + P_{acc} <= P_{FC\text{-}min}$
If SOC <0.4
$P_{traction} + P_{acc} + P_{batt\_charge} = P_{FC} = P_{FC\text{-}rated}$
Else if 0.4<= SOC<0.45
$P_{traction} + P_{acc} = P_{FC}$
Else if 0.45<= SOC <1
$P_{traction} + P_{acc} = P_{batt}$
End
End
Else if $P_{traction} < 0$ & $P_{acc}>0$
If $P_{traction} + P_{acc} <0$
If SOC <1
$P_{batt\_charge} = P_{traction} + P_{acc}$
End
Else $P_{traction} + P_{acc} >0$
If SOC >=0.7
$P_{batt} = P_{traction} + P_{acc}$
Else SOC <0.7
$P_{FC} = P_{acc}$
$P_{batt\_charge} = P_{traction}$
End
Else
$P_{FC}=0$
$P_{batt}=0$ (Battery discharge power for the accessories load and the battery charge power from regenerative braking are the same).
End
End

Table A.6.

Term	**Explanation**
$P_{traction}$	Traction Power Demand (Watts)
P_{acc}	Accessories Power Demand (Watts)
P_{FC_rated}	Rated Fuel Cell Power (Watts)
P_{FC}	Fuel Cell Power (Watts)
P_{batt}	Battery Discharge Power (Watts)
P_{batt_charge}	Battery Charge Power (Watts)

A.6. References

[1] R.Chandrasekaran, W.Bi, T.F.Fuller, *J.Power Sources*, 182 (2008) 546–557.

[2] Marc Doyle, Newman, Antoni S. Gozdz, Caroline N. Schmutz and Jean-Marie Tarascon, *J. Electrochem. Soc*., 143(6),1996.

[3] Godfrey Sikha, Branko N. Popov and Ralph E. White, *J.Electrochem.Soc.*, 151 (7) A1104-A1114, 2004.

APPENDIX B

CHAPTER 6 SUPPLEMENTARY MATERIAL: DESIGN OF A HYBRID VEHICLE

This Appendix appears as proceedings [1]* for the poster presentation by R.Melsert at the IEEE Energy 2030 conference in November 2008. Co-authors in this work are R.Chandrasekaran, T.Bandhauer, T.F.Fuller and Jerome Meisel.

B.1. Abstract

As part of the Ecocar: The Next Challenge student competition, the Georgia Tech (GT) team is designing a hybrid vehicle to be integrated into a production stock 2009 Saturn Vue. The team chose to use E85 in a spark-ignition engine with lithium ion batteries and employ GM's 2-mode hybrid transmission (2-MT). The preliminary results in terms of performance, emissions, and fuel economy are presented.

B.2. Introduction

As the price of conventional transportation fuels increase, the concerns and effects of climate change become more defined, and the vulnerability of the transportation system created by its dependence on petroleum become more evident, government, industry and consumers are increasingly searching for methods to meet our transportation needs in a more intelligent and sustainable manner. One avenue is the use of hybrid-electric vehicles, which use on-board electrical storage to help recover energy and to deliver power in a more systematic and controlled manner. A step further is to allow this electrical storage system to be charged by grid electricity, or become a plug-in hybrid,

allowing for an energy source that is independent from petroleum based transportation fuels.

B.3. Architecture Selection Process

Extensive literature search and fundamental understanding was developed prior to the selection of the team's hybrid architecture.

B.3.1. Degree of hybridization

One of the challenges in the design of a hybrid vehicle is to determine the values of the peak power outputs of the engine and the electric motor. The percentage of peak power delivered by the electric motor, also called the degree of hybridization, has important implications as to the overall vehicle operation and performance. Vehicles with relatively low power electric motors, sometimes referred to as 'mild-hybrids', generally only use the electrical system to recover a portion of the braking energy and then use that energy to power the vehicle accessories. The other end of the spectrum is full electric vehicles, which have no engine on-board and only use grid electricity to perform all operations

B.3.2. Hybrid Configurations

Figure B.1. presents some of the different hybrid configurations investigated [2]. These are parallel, series, series-parallel and split (complex) configurations. The GM 2-mode hybrid transmission is an example of a split configuration. The major advantages over series and parallel architectures obtained in using the 2-MT are summarized as follows [3].

- Smaller electric motors and a smaller battery pack can be used.

- Higher efficiencies (i.e. lower fuel consumption) over a wide range of driving schedules can be achieved.
- A strong pure mechanical energy path exists between the engine and the driven wheels without the need for battery electric energy, as in the Toyota THS-II powertrain in the Prius.

B.3.3. Fuel Selection and Well-to-Wheel Influence

The GT team decided to choose the fuel from the options given: E10, E85, B20, gaseous hydrogen, and electricity, based on a review of their effect on several factors such as performance, range, emissions, WTW energy use, and WTW green house gas (GHG) emissions. E10 does not result in significant improvements in WTW GHG emissions or WTW energy use compared to gasoline, and B20 has many of the same issues with criteria pollutants as conventional diesel fuel. Though only moderate modifications are required for a gasoline engine to be able to be use gaseous hydrogen, our team did not choose this design because of the increase in emission of WTW GHG's compared to gasoline and because of the range issues arising due to lower volumetric energy density of hydrogen when stored as a gas.

The GT team chose the fuel which best meets the demands of this competition, which we feel is E85. The E85 will be combusted in a dedicated ethanol engine, as opposed to a flex-fuel engine, and as a result this engine will never have to operate on pure gasoline, or any other low octane fuel. This engine can now employ an increased compression ratio to take advantage of E85's high octane rating. The compression ratio is arguably the most influential parameter when determining engine efficiency and its increase will directly lead to an increase in vehicle mileage. It is understood that

increasing the compression ratio of an engine will in turn generally increase the amount of NOx produced. However, the total amount of NOx released (g/mile) may still be decreased if the decreased fuel consumption per distance traveled is greater than the increased NOx production per unit fuel combusted. If this emission rate is too high, alternative mitigation methods such as exhaust gas recirculation, lean combustion, or additional catalytic treatment will be considered.

For on-board energy storage, this team has chosen to use lithium ion batteries. These batteries have high power and energy densities compared to other battery chemistries as shown in Figure B.2 [4]. Their light weight ensures that the added mass to the vehicle does not significantly affect the performance and mileage.

Table B.1. compares different lithium ion chemistries available in the market [5]. The good characteristics of iron phosphate chemistries are high stability and non-toxicity, good specific capacity, flat voltage profile, cost effectiveness and improved safety. Disadvantages are a lower voltage than other cathodes, poor Li diffusion ($D_{Li} \sim 10^{-13}$ cm^2/sec) and poor electronic conductivity ($\sim 10^{-8}$ S/cm). However, A123 Systems employs nanophosphate [6] materials (US patent # 7,338,734) which help overcome some of the poor characteristics. Also, A123System's technology enables smaller pack sizing [7]. A123's 32157 M1HD cell is being used in the Saturn Vue PHEV development program [8]. As a result of the above arguments, the GT Ecocar team has decided to use the lithium ion batteries donated by A123 Systems for on-board energy storage.

B.3.4. Motors

The different types of motors that could be considered for hybrid applications are induction motors (IM), switched reluctance motors (SRM) and permanent magnet motors

(PMM). Rahman, Ehsani, and Butler [9] discuss the advantages and disadvantages of these motors for different types of hybrids. The authors concluded based on their preliminary studies on wide speed rangeability and energy efficiency, PMM is a suitable motor for a 50% hybridized car because of its superior efficiency in the constant torque regime. However, for a 20% hybridized car, SRM may be a better choice for its extended speed rangeability and a sufficiently good efficiency (equal or better than IM) at constant power. Georgia Tech Ecocar team will use a PMM motor for its hybrid architecture.

B.3.5. Engines

The GT team has decided that the best engine option is to convert a 1.8L production gasoline GM engine to a dedicated E85 engine. This decision was reached by trading off the improved performance aspects of a larger (higher peak power) engine with the superior efficiency of a smaller displacement engine. With the peak power of the electric motors (~110 kW) sufficient to provide acceptable performance in conjunction with the engine over a wide range of loads and vehicle speeds, the engine power need only be large enough to supply sustained steady-state loadings. We calculate the max steady-state loading (hill climb with trailer tow and high accessory load) to be 75-100 kW. Our 1.8L dedicated E85 engine is sufficient to provide this power, with a peak of ~105 kW on gasoline and 115-125 kW on E85.

B.4. Modeling and Simulation

The desired architecture of the GT team comprises a front wheel drive (FWD) hybrid with an E85 fueled spark-ignition engine and lithium ion battery pack combined with a 2-Mode (split) hybrid transmission configuration, as shown in Figure B.3. A vehicle model was developed using the Powertrain Systems Analysis Toolkit (PSAT)

software developed by Argonne National Lab (ANL). Component models were obtained from ANL, GM, and other sponsors as part of the EcoCAR competition. A first approximation PSAT model was developed by the GT team for the A123 batteries with the available data provided by A123 Systems. The powertrain is composed of a 1.8L (or 1.6L) E85 fueled 120 kW peak power engine, a 50 kW peak power permanent magnet motor (Motor 2) and a 60 kW peak power permanent magnet motor (Motor 1), and modules of lithium ion batteries. The peak power and efficiency of the gasoline engine were scaled by 15% and 7% respectively to account for the increased power output and efficiency of E85 vs. gasoline combustion. The urban dynamometer driving schedule (UDDS), Highway Fuel Economy Driving Schedule (HWFET), and High Acceleration Aggressive Driving Schedule (US06) were used as the test cycles. Vehicle acceleration was simulated over 0-60 mph, 50-70 mph, and rest to ¼ mile acceleration tests. A parametric study with respect to the number of battery modules was performed.

B.5. Results and Discussions

Tables B.2., B.3., B.4. show the mileage and emissions results corresponding to a 1.8 L engine for varying numbers of battery modules. In addition to the mileage and emissions results, acceleration simulations were performed with this vehicle architecture to ensure that the peak combined powers examined represented a viable vehicle. This simulation was also performed using a varying number of battery modules. The results of this simulation, shown in Table B.5., demonstrate that not only is this hybrid vehicle viable, but it has superior acceleration to the conventional vehicle under all circumstances tested. Even though the max power of the motors is 110 kW, this amount of power can not be passed through the motors if the batteries have a limiting power lower than this.

Therefore, the peak power of the electric system is the minimum of the peak power of the motor or the battery pack (less some inversion and transmission losses). As the number of battery modules increases, the peak power of the electric system as a whole increases. However, due to the increased vehicle mass from the additional battery modules, there is almost no change in the fuel economy, vehicle acceleration and even the greenhouse gas emissions.

As the peak power of the electric system increases, its ability to power the vehicle without assistance from the engine also increases. This means that as the degree of hybridization increases, the electric motor can handle higher loads and therefore the vehicle can operate in the electric only range at higher loads (higher vehicle speed, greater angle of climb, greater acceleration, etc.). In addition to the engine operating for a shorter duration over a driving cycle, it also avoids operating under low load conditions, where it is the least efficient. Internal combustion engines are generally most efficient under maximum load and moderate rotational speed. In conventional vehicles, engines must operate continuously to deliver all of the vehicles needs, independent of the total load. With a hybrid vehicle the electrical powertrain may supply all of the needs of the vehicle under low loads, enabling the engine to turn off completely and only engage when a higher load is demanded and more efficient operating conditions exist. The increased degree of hybridization also allows for higher power energy recovery. With the peak power of the electric system increased, kinetic energy from the vehicle can be transferred to the battery pack at a higher rate, allowing for a greater percentage of total braking energy to be recovered, especially under high braking loads.

In order to decide amongst the two sizes of spark-ignition engines considered (1.8L vs. 1.6L), the above tests were repeated on the smaller displacement engine. Tables B.6., B.7., B.8., B.9. present the PSAT results for 1.6L engine with the same varying number of battery modules. Tables B.6.-B.8. show that there is modest improvement in fuel economy and WTW GHG emissions when using the 1.6L versus the 1.8L engine. Also, Table B.9. shows that there is almost no change in the vehicle acceleration. The lower peak engine power (85 kW on gasoline, 95-100 kW with E85) may present problems under long duration high load steady state conditions. However, the results of this study demonstrate that the use of the 1.6L engine deserves further investigation.

B.6. Conclusions

This paper has discussed the hybrid vehicle that is being developed by the Georgia Tech Ecocar team and the reasoning behind the architecture, fuel, and component selection. The effect of the size of the spark-ignition engine and that of the electric motor on fuel economy, emissions, and performance under different drive cycles and conditions is presented. It has been observed that a higher number of battery modules improve vehicle acceleration, mileage, and GHG emissions up until the peak power of the battery pack is approximately equal to that of the electric motor. This study was performed by the Georgia Tech EcoCAR Challenge team (www.ecocar.gatech.edu). The EcoCAR Challenge (www.ecocarchallenge.org) is a collegiate advanced vehicle technology competition sponsored by the US DOE and General Motors that allows students to redesign a production vehicle in order to achieve increased fuel economy, and decreased pollutant and green house gas emissions, while maintaining vehicle performance and functionality.

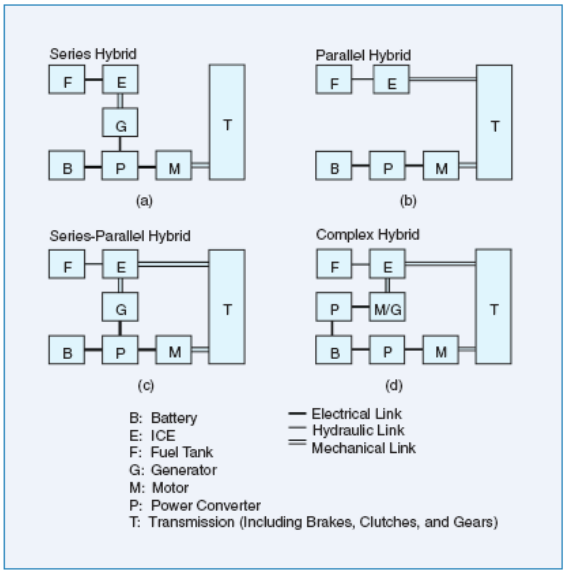

Figure B.1. HEV configurations [2]

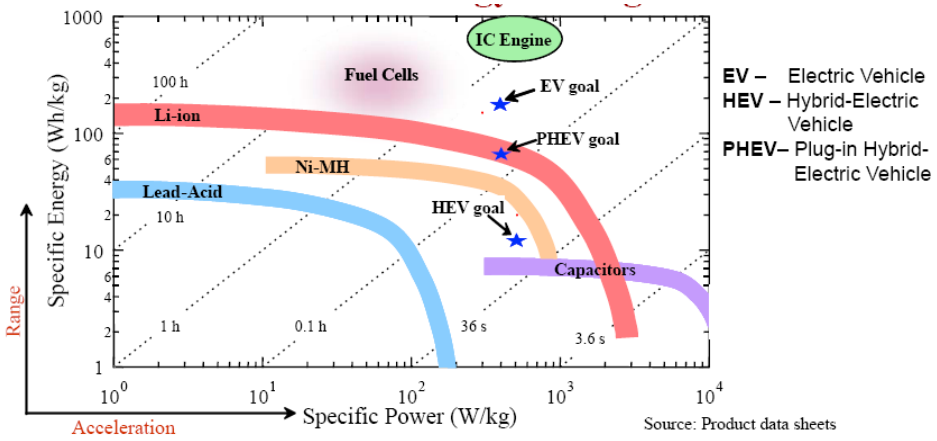

Figure B.2. Comparison of different battery chemistries [4]

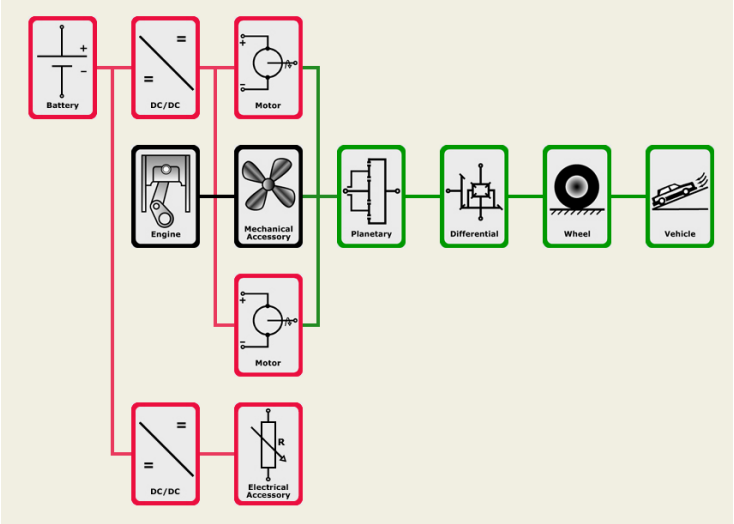

Figure B.3. Powertrain configuration in PSAT

Table B.1. Lithium ion battery chemistries [5]

Theoretical values for a battery system relative to graphite anode and $LiPF_6$ electrolyte

Material	Δx	mAh/g	avg V	Wh/kg	Wh/l
$LiCoO_2$	0.55	151	4.00	602	3073
$LiNi_{0.8}Co_{0.15}Al_{0.05}O_2$	0.7	195	3.80	742	3784
$LiMn_2O_4$	0.8	119	4.05	480	2065
$LiMn_{1/3}Co_{1/3}Ni_{1/3}O_2$	0.55	153	3.85	588	2912
$LiFePO_4^*$	0.95	161	3.40	549	1976

*Typically diluted with 10% carbon for electronic conductivity

Table B.2. PSAT parametric simulation results of the UDDS test with 1.8L engine

Number of A123 Battery Modules	3	8	10	12
Fuel economy (mpgge)	36.78	36.77	36.11	35.72
GHG emissions, Tank-to-Wheel (g/mile)	253.76	253.65	258.4	261.02
Vehicle mass (kg)	1821	1872	1893	1913

Table B.3. PSAT parametric simulation results of the HWFET test with 1.8L engine

Number of A123 Battery Modules	3	8	10	12
Fuel economy (mpgge)	36.58	36.14	36.19	36.09
GHG emissions, Tank-to-Wheel (g/mile)	254.97	258.04	257.69	258.43
Vehicle mass (kg)	1821	1872	1893	1913

Table B.4. PSAT parametric simulation results of the US06 test with 1.8L engine

Number of A123 Battery Modules	3	8	10	12
Fuel economy (mpgge)	24.02	21.99	21.39	21.73
GHG emissions, Tank-to-Wheel (g/mile)	388.33	424.09	436.1	429.03
Vehicle mass (kg)	1821	1872	1893	1913

Table B.5. PSAT parametric simulation results of the acceleration test with 1.8L engine

Number of A123 Battery Modules	3	8	10	12
Acceleration Time (0-60 mph, sec)	7.9	7.8	7.9	7.9
Acceleration Time (50-70 mph, sec)	4.1	4.1	4.1	4.0
Maximum Acceleration (m/s^2)	6.08	5.89	5.83	5.77
Acceleration Time (¼ mile, sec)	16	15.9	16.0	16.0

Table B.6. PSAT parametric simulation results of the UDDS test with 1.6L engine

Number of A123 Battery Modules	3	8	10	12
Fuel economy (mpgge)	39.23	38.79	38.48	38.34
GHG emissions, Tank-to-Wheel (g/mile)	228.54	231	233	234
Vehicle mass (kg)	1821	1872	1893	1913

Table B.7. PSAT parametric simulation results of the HWFET test with 1.6L engine

Number of A123 Battery Modules	3	8	10	12
Fuel economy (mpgge)	39.49	39.63	39.61	39.65
GHG emissions, Tank-to-Wheel (g/mile)	227	226	226	226
Vehicle mass (kg)	1821	1872	1893	1913

Table B.8. PSAT parametric simulation results of the US06 test with 1.6L engine

Number of A123 Battery Modules	3	8	10	12
Fuel economy (mpgge)	25.51	25.74	25.78	25.62
GHG emissions, Tank-to-Wheel (g/mile)	352	348	348	350
Vehicle mass (kg)	1821	1872	1893	1913

Table B.9. PSAT parametric simulation results of the acceleration test with 1.6L gasoline engine

Number of A123 Battery Modules	3	8	10	12
Acceleration Time (0-60 mph, sec)	8	7.7	7.7	7.8
Acceleration Time (50-70 mph, sec)	4.1	4.1	4.1	4.1
Maximum Acceleration (m/s^2)	6.07	5.90	5.84	5.78

B.7. References

[1] R.Melsert, R.Chandrasekaran, T.Bandhauer, T.F Fuller, J.Meisel, "Design of hybrid electric vehicle", Poster presented at IEEE Digest, Track T3, Sub-topic 3A, IEEE Energy 2030 Conference, November 17-18, 2008 (Proceedings available at Energy 2030 Conference, 2008. ENERGY 2008. IEEE, 17-18 Nov. 2008 Page(s):1 – 5; Digital Object Identifier 10.1109/ENERGY.2008.4781055).

[2] C. C. Chan, Y.S.Wong, IEEE Power and Energy Magazine, November/December 2004.

[3] Understanding GM Hybrid Electric Vehicles, Copyright 2006 Powertrain Group, General Motors Corp.

[4] Srinivasan, Venkat "Batteries for Vehicular Applications," available at berc.lbl.gov/venkat/Main_files/Status_of_Batteries_for_Vehicles.pdf, accessed October 11, 2008

[5]National Renewable Energy Laboratory, "Battery choices for different plug-in HEV configurations," available at www.nrel.gov/vehiclesandfuels/energystorage/pdfs/40378.pdf, Accessed October 9, 2008

[6] A123 Systems, "A123Systems Announces Patent Issuance for Nanophosphate™ Lithium Ion Battery Technology," available at www.a123systems.com/#/news/news110, accessed October 7, 2008

[7] A123 Systems, "Hybrid+ high usable energy," available at www.a123systems.com/#/applications/hev/hchart2, accessed October 7, 2008

[8] A123 Systems, "GM to use A123 Batteries for Saturn Vue Plug-In Hybrid Development Program," available at www.a123systems.com/#/news/news8, accessed October 7, 2008

[9] SAE technical paper series 2000-01-3062

* The only difference between the proceedings and the Appendix is that in the former, SOC correction was not done while SOC correction is done here and the corresponding values are shown in the tables.

APPENDIX C

CHAPTER 8 SUPPLEMENTARY MATERIAL

Appendix C.1.

Material balance on Li (Ref: [57], [58] in Chapter 8):

$$\frac{\partial c}{\partial t} + \nabla \cdot (N_{Li}) = 0 \qquad \text{(C-1)}$$

Neglecting pressure diffusion (i.e. stress neglected), thermal diffusion and other forced diffusion terms from the expression for flux, N_{Li} as a first approximation,

$N_{Li} = -\mathscr{D}_{\mathrm{Li}} \nabla c \left(1 + \frac{\partial \ln \gamma_{Li}}{\partial \ln \chi_{Li}} \right)_{T,p} + c v^{\square}$; where $v^{\square}$ is the volume average velocity (Ref: [58], [29], [57] in Chapter 8)

If $D_{Li} = \mathscr{D}_{\mathrm{Li}} \left(1 + \frac{\partial \ln \gamma_{Li}}{\partial \ln \chi_{Li}} \right)_{T,p}$, then above equation becomes

$N_{Li} = -D_{Li} \nabla c + c v^{\square}$ [57]

Hence $\frac{\partial c}{\partial t} + \nabla \cdot (-D_{Li} \nabla c + c v^{\square}) = 0$

$J_{Li} = -D_{Li} \nabla c$

J_{Li} is the molar flux of Li with respect to the volume average velocity, $v^{\square}$ (taken to be the reference velocity), i.e. J_{Li} is the diffusive molar flux.

So, $\frac{\partial c}{\partial t} + \nabla c \cdot v^{\square} + c \nabla \cdot v^{\square} + \nabla \cdot (J_{Li}) = 0$

Neglecting $c \nabla \cdot v^{\square}$ as a first approximation,

$$\frac{\mathrm{D}c}{\mathrm{D}t} + \nabla \cdot (J_{Li}) = 0 \qquad \text{(C-2)}$$

$$\text{where}\frac{\mathrm{D}c}{\mathrm{D}t}=\frac{\partial c}{\partial t}+\nabla c\cdot v^{\square}$$

and called the material or substantial derivative.

Initial and Boundary conditions:

$c=0 \qquad @\ t=0 \qquad$ (lithiation)

$\nabla c=0 \qquad @\ r=0$

$$J_{Li}=\frac{i}{nF}\ @r=R_p(t) \qquad \text{(C-3)}$$

This approximation, neglecting convective flux term at boundary condition is valid at low and moderate rates, especially in the case of (small) nano particles as discussed below.

- To understand the relative contribution of diffusive flux and convective flux to the total flux, the following dimensionless ratios are considered:

  <u>Ratio of diffusive flux to total flux:</u>

$$S_{D-T\ flux}=\left|\frac{-\left(\frac{R_p(t)}{R_{p_0}}\right)^3 D_{Li}\left.\frac{\partial c}{\partial r}\right|_{r=R_p(t)}}{\left(\frac{|I|}{nF4\pi R_p(t)^2}\right)}\right|\approx\frac{nF\left(\frac{R_p(t)}{R_{p_0}}\right)^3 D_{Li}\left(\frac{c_{280\%}-c_{r=0}}{R_p(t)}\right)}{\text{C-rate}\left(\frac{\frac{4}{3}\pi {R_{p_0}}^3\left(C_{tot}\rho_{Si}\right)}{4\pi R_p(t)^2}\right)}$$

  Assuming 280% volume expansion, $R_p(t)=1.56\,R_{p_0}, c_{r=0}\sim 0.5\ (c_{280\%})$ mol/m^3

$$S_{D-T\ flux}\approx\frac{0.5(1.56)^4\left(\frac{{R_{p_0}}^4}{{R_{p_0}}^6}\right)\left(D_{Li}\right)\left(c_{280\%}\right)}{\text{C-rate (28.8)}}\approx\frac{\left(\frac{0.5(1.56)^4}{{R_{p_0}}^2}\right)\left(D_{Li}\right)\left(c_{280\%}\right)}{\text{C-rate (28.8)}}$$

$$\boxed{S_{D-T\ flux}\approx\frac{8423}{\text{C-rate}}\left(\frac{D_{Li}}{{R_{p_0}}^2}\right)}$$

  For $R_{p0}=30\ nm$

$$S_{D-T\ flux}\approx\frac{9.36}{\text{C-rate}}$$

Thus it is seen that for small particles, at low rates, diffusive flux is relatively important. As the C-rate increases, convective flux facilitates transport. For bigger particles, the diffusion limitations are higher and hence the convective flux is important even at low rates for transport.

Ratio of diffusive flux to convective flux:

$$S_{D-C\ flux} = \left| \frac{-D_{Li} \left. \frac{\partial c}{\partial r} \right|_{r=R_p(t)}}{cv^{\square}} \right| \approx \left| \frac{-D_{Li} \left(\frac{c_{280\%} - c_{r=0}}{R_p(t)} \right)}{c_{280\%} \left(\frac{3}{4\pi} \right)^{\frac{1}{3}} \left(\frac{V_p^{1/3} - V_{p_0}^{1/3}}{\Delta t} \right)} \right|$$

Assuming 280% volume expansion, $R_p(t) = 1.56\ R_{p_0}, c_{r=0} \sim 0.5\ (c_{280\%})$ mol/m^3

$$S_{D-C\ flux} \approx \frac{0.5 D_{Li} \left(\frac{c_{280\%}}{1.56 R_{p_0}} \right)}{c_{280\%} \left(\frac{3}{4\pi} \right)^{\frac{1}{3}} \left(\frac{4}{3}\pi \right)^{\frac{1}{3}} R_{p0} \left(\frac{(3.8^{1/3} - 1)}{\left(3600 \sec \frac{1\text{C-rate in Amperes}}{|I|} \right)} \right)}$$

$$S_{D-C\ flux} \approx \frac{D_{Li}}{R_{p0}^{\ 2}} \left(\frac{1}{\text{C-rate}} \right) \left(\frac{0.5 \times 3600}{1.56 \times \left(3.8^{1/3} - 1^{1/3} \right)} \right)$$

$$\boxed{S_{D-C\ flux} \approx \frac{D_{Li}}{R_{p0}^{\ 2}} \left(\frac{2059}{\text{C-rate}} \right)}$$

For $R_{p0} = 30\ nm,\ S_{D-C\ flux} \approx \left(\frac{2.287}{\text{C-rate}} \right) = 2.287$ for C-rate & 0.2287 for 10 C-rate

Thus, for small particles, importance of convective flux increases at higher rates of lithiation/ de-lithiation. Hence it is justified to neglect the convective flux term in (C-3) for small particles, especially at low to moderate rates. For bigger particles, (e.g. micron sized particles), diffusion limitations are significant and convective transport

is important even at low rates. It was also verified independently that the ratio of convective flux to total flux remains almost constant at ~ 4.

- Since lithiation/de-lithiation decides particle growth, as a first approximation, the transport problem is solved in terms of concentration in the (Lagrangian) reference frame in COMSOL and is associated with the geometry. Change in particle size is calculated with respect to the spatial frame in COMSOL which is fixed in space (i.e. fixed co-ordinates).
- (C-1) is with respect to fixed co-ordinates. (C-2) is with respect to the Lagrangian reference frame. Moreover it is to be noted that if an equation of the type $\frac{\partial c}{\partial t} + \nabla \cdot (J_{Li}) = 0$ is used as the governing equation in reference frame in COMSOL, it actually refers to $\frac{\mathrm{D}c}{\mathrm{D}t} + \nabla \cdot (J_{Li}) = 0$. In other words, the physical significance of the reference time derivative is that it denotes the material derivative.
- Concentration of Li is moles of Li/volume of the particle. The molar volume of the Li-Si electrode and hence the volume of the particle changes with lithiation/de-lithiation. As mentioned before the transport problem is solved in terms of concentration in the reference frame to evaluate the varying volume of the particle with respect to the fixed co-ordinates. Hence, as first approximation, the concentration is normalized with respect to the initial volume of the particle. (Christensen (Ref: [59] in Chapter 8) has introduced $\left(\frac{R}{R_0} \right)^2$ at the flux boundary condition before to relate the pore-wall flux computed in dualfoil domain to the

current density at the particle surface). If $c' = c\left(\frac{R_p(t)}{R_{p_0}}\right)^3$ is used instead of c in (C-2),

the equation remains unchanged as shown here :

$$\frac{\mathrm{D}c'}{\mathrm{D}t} + \nabla \cdot (J'_{Li}) = 0$$

$$\frac{\mathrm{D}}{\mathrm{D}t}\left(c\left(\frac{R_p(t)}{R_{p_0}}\right)^3\right) + \nabla \cdot \left(-D_{Li}\nabla\left(c\left(\frac{R_p(t)}{R_{p_0}}\right)^3\right)\right) = 0$$

$$c\frac{\mathrm{D}}{\mathrm{D}t}\left(\left(\frac{R_p(t)}{R_{p_0}}\right)^3\right) + \left(\frac{R_p(t)}{R_{p_0}}\right)^3 \frac{\mathrm{D}c}{\mathrm{D}t} + \left(\frac{R_p(t)}{R_{p_0}}\right)^3 \nabla \cdot \left(-D_{Li}\nabla c\right) = 0$$

$$\left(\frac{3c\left(R_p(t)\right)^2}{{R_{p_0}}^3}\right)\left(\frac{\mathrm{D}R_p(t)}{\mathrm{D}t}\right) + \left(\frac{R_p(t)}{R_{p_0}}\right)^3 \frac{\mathrm{D}c}{\mathrm{D}t} + \left(\frac{R_p(t)}{R_{p_0}}\right)^3 \nabla \cdot \left(-D_{Li}\nabla c\right) = 0$$

It is to be noted that $\frac{\mathrm{D}R_p(t)}{\mathrm{D}t}$ is zero; hence the above equation becomes

$\left(\frac{R_p(t)}{R_{p_0}}\right)^3 \frac{\mathrm{D}c}{\mathrm{D}t} + \left(\frac{R_p(t)}{R_{p_0}}\right)^3 \nabla \cdot \left(-D_{Li}\nabla c\right) = 0$ **or** $\frac{\mathrm{D}c}{\mathrm{D}t} + \nabla \cdot \left(-D_{Li}\nabla c\right) = 0$ which is (C-2).

However (C-3) is modified to

$$J_{Li}' = -D_{Li}\nabla c' = \frac{i}{nF} \quad @\, r = R_p(t)$$

$$i.e.\ J_{Li} = -D_{Li}\nabla c = \frac{i}{nF}\left(\frac{R_{p_0}}{R_p(t)}\right)^3 \quad @\, r = R_p(t)$$

$$\text{or } J_{Li} = -D_{Li}\nabla c = \frac{i'}{nF} \quad @\, r = R_p(t) \qquad \text{(C-4)} \ ; \quad \text{where } i' = i\left(\frac{R_{p_0}}{R_p(t)}\right)^3$$

- Concentration terms in equation 9 in Chapter 8 have also been normalized with respect to initial volume of the particle for the above reason.
- Local and average x values were obtained by the ratio of moles (concentration multiplied by volume) to maximum number of moles of Li that can be inserted. This

leads to equality shown in equations (13)-(14) in Chapter 8. The usual way of calculating x as the ratio c/c_{max} ($c/c_{280\%}$) is avoided. The reason is molar volume of the electrode (and hence total concentration) is not constant. This is also the reason for the formula for x_s in equation 10.

Eqn. (C-2) and (C-4) yield Eqn. 4 and Eqn. 6 in Chapter 8 respectively.

Appendix C.2.

$$S_s = \frac{\left(\frac{|I|}{\left(4/3\right)\pi R_p(t)^3} \times \frac{R_p(t)^2}{D_{Li}} \right)}{\left(\frac{nFN_{tot}}{\left(4/3\right)\pi R_{p_0}{}^3} \right)} = \left(\frac{\left(R_p(t)\right)^2 |I|}{D_{Li} nFN_{tot}} \right) \left(\frac{R_{p_0}}{R_p(t)} \right)^3$$

APPENDIX D

CHAPTER 9 SUPPLEMENTARY MATERIAL

Appendix D.1.

Transport properties and activity coefficient as a function of salt concentration

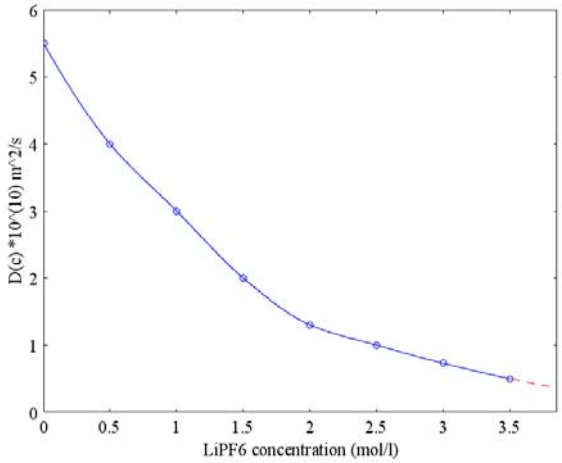

Figure D.1. Diffusion coefficient of $LiPF_6$ in organic solvent (EC/PC/DMC: 27/10/63, volume %) at 294 K (~ room temperature)

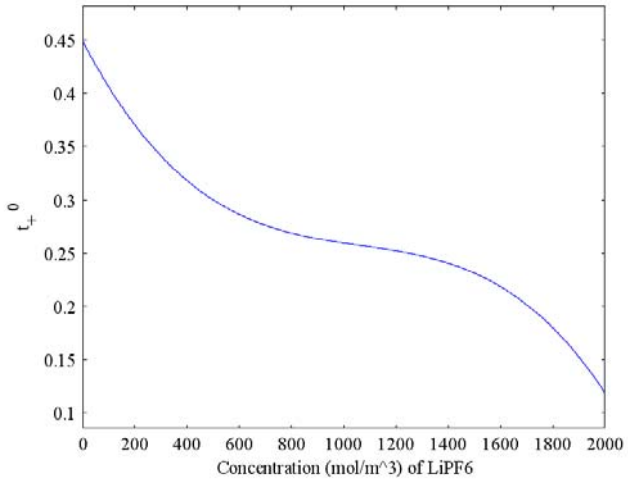

Figure D.2. Transference number of lithium ions (from $LiPF_6$ salt) in organic solvent (EC/EMC:: 3:7) at room temperature.

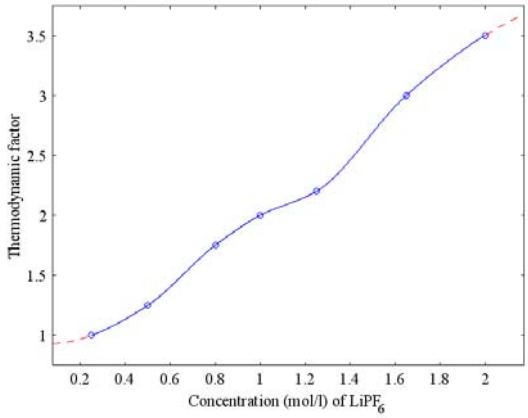

Figure D.3. Thermodynamic factor $\left(1+\frac{\partial \ln f_A}{\partial \ln c}\right)$ as a function of salt ($LiPF_6$) concentration in organic solvent (EC/EMC:: 3:7)

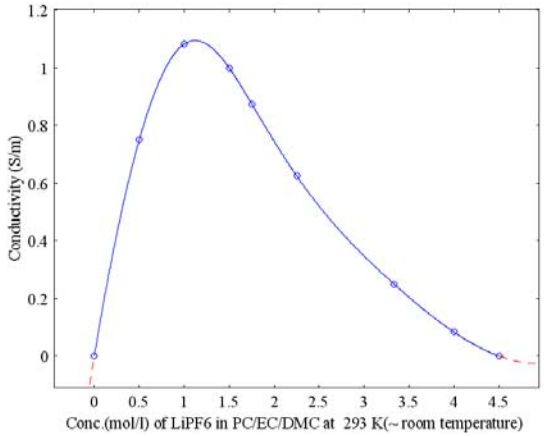

Figure D.4. Conductivity of salt ($LiPF_6$) as a function of salt concentration in organic solvent (PC/EC/DMC) at 293 K (~ room temperature).

Appendix D.2.

$$\frac{\partial \varepsilon}{\partial t} = \sum_{solid\ phases} \frac{s_i M_i}{\rho_i n F} \nabla . \mathbf{i_2}$$

$$\frac{\partial \varepsilon}{\partial t} = \frac{s_{Si_{4/15}} M_{Si_{4/15}}}{\rho_{Si_{4/15}} n F} \nabla . \mathbf{i_2} + \frac{s_{LiSi_{4/15}} M_{LiSi_{4/15}}}{\rho_{LiSi_{4/15}} n F} \nabla . \mathbf{i_2}$$

$s_{Si_{4/15}} = s_{Li^+} = -s_{LiSi_{4/15}} = -1; \quad n = 1;$ For simplicity, $s_{Li^+} = s_+$

$$\frac{\partial \varepsilon}{\partial t} = -s_+ \frac{\nabla . \mathbf{i_2}}{F} (-\tilde{V}_{Si_{4/15}} + \tilde{V}_{LiSi_{4/15}}) = a j_n (\tilde{V}_{LiSi_{4/15}} - \tilde{V}_{Si_{4/15}}) = -\frac{a s_+}{F} i_n (\tilde{V}_{LiSi_{4/15}} - \tilde{V}_{Si_{4/15}})$$

If one starts with a non-zero solid phase concentration (i.e. $c_{s_{initial}} \neq 0$), then the above equation modifies to

$$\frac{\partial \varepsilon}{\partial t} = -s_+ \frac{\nabla . \mathbf{i_2}}{F}\left(-\left(\tilde{V}_{LiSi_{4/15}}\right)_{initial} + \tilde{V}_{LiSi_{4/15}}\right) = aj_n\left(\tilde{V}_{LiSi_{4/15}} - \left(\tilde{V}_{LiSi_{4/15}}\right)_{initial}\right) = -\frac{as_+}{F} i_n\left(\tilde{V}_{LiSi_{4/15}} - \left(\tilde{V}_{LiSi_{4/15}}\right)_{initial}\right)$$

where $\left(\tilde{V}_{LiSi_{4/15}}\right)_{initial}$ denotes the molar volume of the alloy electrode at initial conditions during lithiation and that corresponding to the state of charge used as stop condition during de-lithiation.

Appendix D.3.

Dimensionless current density, $\delta = \dfrac{\alpha_a FIL_c}{RT}\left(\dfrac{1}{\kappa_{eff}} + \dfrac{1}{\sigma_{eff}}\right)$

Dimensionless exchange current density, $\nu^2 = \dfrac{\left(\alpha_a + \alpha_c\right) Fai_0 {L_c}^2}{RT}\left(\dfrac{1}{\kappa_{eff}} + \dfrac{1}{\sigma_{eff}}\right)$

At initial conditions, $\sigma_{eff} \sim 4$ S/m, $\kappa_{eff} \sim 0.44$ S/m, $i_0 \sim 10^{-2}$ A/m^2, yielding $\delta \sim 0.063$ (for C-rate), $\nu \sim 0.085$ using values of other parameters as given in Table 9.2 or discussed in Chapter 9.